Dynamic identification of the Augusta hybrid base isolated building using data from full scale push and sudden release tests

by

Anastasia Athanasiou

A dissertation submitted in partial satisfaction of the

requirements for the degree of

Doctor of Philosophy in Structural and Geotechnical Engineering

Dottorato in Ingegneria Strutturale e Geotecnica, Ciclo XXVIII

University of Catania

Advisor

Professor Giuseppe Oliveto

2015

Abstract

Dynamic identification of the Augusta hybrid base isolated building using data from full scale push and sudden release tests

by

Anastasia Athanasiou

Doctor of Philosophy in Structural and Geotechnical Engineering

Dottorato in Ingegneria Strutturale e Geotecnica, Ciclo XXVIII

University of Catania

Advisor: Professor Giuseppe Oliveto

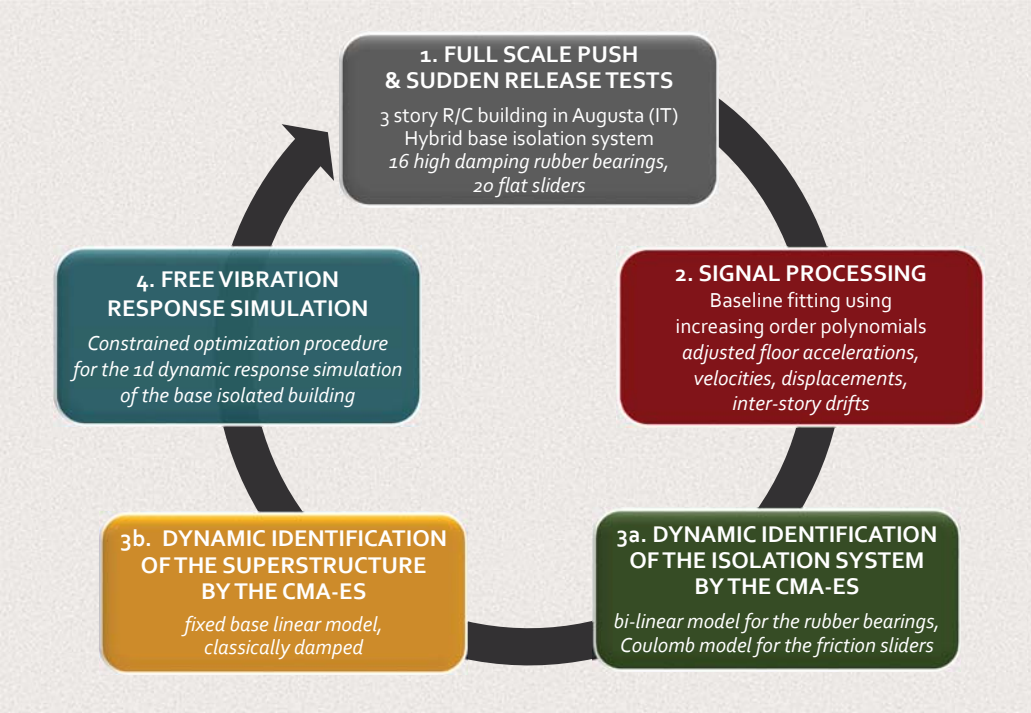

Graphical abstract

A three-story reinforced concrete building in Augusta (IT), isolated at the base and designed according to the provisions of the latest Italian seismic regulations, was subjected to a series of push and sudden release tests in March 2013. The Augusta isolation system is hybrid, consisting of 16 High Damping Rubber Bearings (HDRB) and 20 Low Friction Sliding Bearings (LFSB). The tests were characterized by a long quasi-static phase, where the building was pushed slowly to the desired displacement amplitude (sliding velocity $\approx 0.1mm/sec$, strain bearing demand $\gamma = 0.39-0.78$), and a dynamic phase where the building was left free to oscillate. The duration of the dynamic phase was utmost 1% the duration of the static phase. The recordings included the displacements at the isolation level and the floor accelerations. A baseline fitting scheme was developed for the removal of the low frequency noise in the records. Application of the adjustment scheme provided reliable estimates of the floor velocities and displacements. The advantage of the proposed signal processing method other than its simplicity, is its ability to account for boundary conditions, for instance initial and residual displacements. Once the signals obtained from all eight tests performed were adjusted, they were used in the identification of the non-linear isolation system and the flexible superstructure (linear in the range of interest). The identification was performed in the time domain using the Covariance Matrix Adaptation Evolution Strategy, a stochastic algorithm for difficult, non linear black-box optimization. The identification of the isolation system provided the mass of the rigid block, the bi-linear properties used in the mechanical representation of the rubber bearings and the sliding coefficient of friction for the Coulomb model used in the modelling of the sliders. The obtained parameters, showed that rubber bearing properties were closer to the corresponding static laboratory properties, therefore implying that after the long quasi-static phase the HDRBs did not have time to recover their dynamic properties. The identified sliding coefficient of friction was in average 1%, leading to significant energy dissipation. The identified superstructure properties were the distribution of the floor masses, the modal frequencies, damping ratios and mode shapes. The identified data for the isolation system and the superstructure were input in a synthesized model of the isolated Augusta building, for the dynamic response simulation of the structure. A constrained optimization algorithm was developed ad hoc for the time-step solution of the coupled equations of motion. The obtained simulated response of the Augusta building matched the experimental response, in terms of displacements, velocities and accelerations.

Contents

List of Figures

List of Tables

Acknowledgments

I am deeply grateful to my advisor, prof. Giuseppe Oliveto for his continuous guidance and support. He has been an excellent mentor. I would also like to thank Dr Mario Granata, Executive Director and Chief Design Engineer at SAP Studio Engineering, for sharing his expertise and passion for learning and prof. Felice Ponzo from the University of Basilicata for his important contribution in the realization of the Augusta experiments. I am much obliged to prof. Michael Constantinou and prof. Andrei Reinhorn for accepting me as a visiting scholar at SUNY, Buffalo and to prof. George Manolis from the Aristotle University of Thessaloniki for giving me the opportunity to study abroad.

I thankfully acknowledge the financial and technical support of ReLUIS (Italian National Network of University Earthquake Engineering Laboratories), through Project D.P.C - ReLUIS 2014-2016.

I would be remiss not to mention the faculty members, colleagues and staff who made DICAR a cordial working environment.

Finally, I could never thank enough my family and friends for their support and understanding.

Introduction

Base isolation, often cited as seismic or aseismic base isolation, is a passive vibration control technology for the earthquake protection of buildings, bridges, power plants and other structures. The basic concept of base isolation lies in the physical decoupling of the structure from the ground. This is succeeded interposing elements of low lateral and high vertical stiffness (isolators) between the superstructure and the foundation. The introduction of a layer of low lateral stiffness between the substructure and the superstructure aims to the elongation of the fundamental vibration period of the structure to a value that is away from the dominant frequencies of the expected earthquakes. The period shift to the velocity-sensitive region of the spectrum results to reduced pseudo-accelerations and consequently reduced floor acceleration and inter-story drift demands to the superstructure [1, 2]. When isolation is implemented in bridge construction, the primary design goals are the reduction of forces in the sub- and super-structures and the force redistribution between the piers and the abutments [3]. An effective base isolation system has sufficient energy dissipation capacity to prevent excessive displacement demands on the bearings and is stiff enough to prevent vibrations under frequent loads. Seismic isolation is also applied for the retrofitting of existing structures. An early example of seismic retrofitting in Italy by base isolation are the Solarino buildings [4].

Historical development of isolation systems

Early seismic protective systems can be found in antiquity. The Mausoleum of Cyrus II (Persia, 559-29BC) was a primitive sliding isolation system. In ancient Greek temples, the sliding-rocking motion of columns provided the structural system with flexibility. Wooden dowels covered by lead were used together with empolia to align the columns; the dowels provided the structure with the ability to absorb energy [5]. In modern times, early suggestions of isolation systems are found in the works of Jules Touaillon (*Improvement in buildings: isolation scheme consisting of double concave rolling balls, US Patent,1870*), prof. John Milne (*Base isolation of wooden house by ball bearings, Japan, 1876-1895*), K. Kawai (*Base isolation by timber logs, Japan, 1891*), Jacob Bechtold (*Earthquake-proof building built on a rigid base-plate which is mounted on balls of hard material, Germany, 1906*) and Dr. Johannes Calantarients (*Building construction to resist the action of earthquakes, where the sliding foundation was made of talk, England, 1909*). After the catastrophic Messina earthquake in 1908 in Italy, the Italian authorities considered the possibility of sliding isolation for the anti-seismic reconstruction of the area; however this option was rejected and the fixed-base design approach with height limitations and lateral force design requirements prevailed[1]. In 1921, Frank Lloyd Wright designed the Imperial palace hotel in Tokyo; the structure was supported on soft soil and performed well during the Kanto earthquake of 1923. The basic concepts and historical review of base isolation systems can be found in [1, 2, 6, 7, 8] and online at `http://nisee.berkeley.edu/lessons/kelly.html` (prof. Kelly, University of California, Berkeley) and `http://www.jssi.or.jp/english/` (Japanese Association of Base Isolation).

Modern applications of base isolation systems include a pendulum system without damping for the isolation of a three story building suspended from cables (Turkmenistan, 1955) a natural rubber bearing system for the isolation of a school in Skopje (Yugoslavia, 1969) and the GAPEC system consisting of steel laminated bearings (south France, 1977). The first isolated building in the United States was completed in 1986 and it was the Foothill

Communities Law and Justice Center in California. The building consisted of steel frames and was isolated by 98 laminated bearings. Nowadays, there are several thousands isolated buildings around the world, with Japan, USA, People's Republic of China, Russia and Italy being the leading countries in seismic isolation applications. In Japan, implementations increased significantly after the 1995 Kobe earthquake [9]. Analyses of seismographic records from base isolated buildings during recent strong ground shaking, such as the Northridge 1994 and Great Tohoku 2011 earthquakes, demonstrated the effectiveness of the method to maintain the structure safe and operational during and after the main shock [9, 10, 11, 12, 13]. Warn and Ryan in [7] noted that seismic isolation is being considered for the earthquake design of nuclear power plants in the United States .

Isolation hardware

A wide class of elastomeric and sliding bearings is available in the international market.

Rubber bearings

Elastomeric bearings consist of alternating layers of rubber and steel. The total thickness of the rubber provides to the isolator the low lateral stiffness ($G = 0.30 - 1.50MPa$ [14]), while the close spacing of the steel shims is responsible for the high vertical stiffness. Rubber is a material characterized by high elastic deformation, large elongation at break and nearly incompressibility - Poisson's ratio is between 0.498-0.499 [6]. Initially natural bearings were not reinforced by steel shims, and as a result horizontal ground motions were exciting rocking modes in the system [1]. The first evolution of the NRB bearings were the Low Damping natural and synthetic Rubber Bearings (LDRB). LDRB are characterized by low damping ratios ($< 6\%$ at $\gamma = 100\%$ [14]). The Lead Rubber Bearings (LRB) are similar to the LDRB and were introduced in the late '70s in New Zealand [1]. LRB include a lead plug that enhances energy dissipation through yielding; their hysteretic behaviour can be

described sufficiently using the bilinear model. In Japan 65% of the rubber bearings used are either NRB or LRB [9]. Temperature has a significant effect on the stiffness and energy characteristics of the LRB [6]. Nowadays, the High Damping Rubber Bearings (HDRB) have overtaken the LDRB and LRB. HDRB include damping in the elastomer (damping $10-20\%$ of critical at $\gamma = 100\%$). The behavior of HDRB is nonlinear viscoelastic at low strains and becomes nonlinear hysteretic at large strains [6]. The high stiffness of HDRB at small γ provides the structure with resistance against frequently occurring loads, such as small to moderate earthquakes and wind excitation. The bearing stiffness softens with increasing displacement amplitude, providing the system with the desirable flexibility. At extreme conditions ($\gamma > 250-300\%$) the rubber stiffens again; Villaverde describes this hardening behaviour as a 'safety valve against unexpectedly severe earthquakes' [8], while Becker, with reference to the Triple Friction Pendulum systems, comments that the hardening exhibited by the bearings at extreme loading may be used to reduce the velocity of the building at impact and to allow controlled yielding in the building immediately before impact [15]. HDRB combine flexibility with energy dissipation and they are easy to design and manufacture; however their mechanical properties depend on temperature, frequency and history of loading [6]. The shear force-displacement relationship in HDRB is usually described using the bilinear model. A clear advantage of the bilinear model over more complex models comes from its simple piecewise linear definition, that permits its adaptation to analytical formulations [16]. Naeim and Kelly suggest the combination of the bilinear model with a viscous damper for a more accurate representation of the hysteretic behavior relationship of the elastomeric bearing [1]. More complex smooth or polygonal hysteretic models exist, such as the Bouc-Wen model, models of smoothed plasticity based on the Bouc Wen model the hysteretic element developed by Kikuchi and Aiken [17, 18, 19, 20]. Due to their complexity, these models admit themselves substantially to numerical formulations and therefore have been incorporated in open source and commercial earthquake engineering software such as OpenSees(KikuchiLRBMaterial), 3D-BASIS(bi-directional smoothed plasticity model [19]) and SAP2000(Bouc-Wen model). The vertical force-displacement behaviour is

usually described by means of linear springs. Uplift is undesirable in isolation systems, however if expected, the vertical force-displacement behaviour should be modelled by means of non-linear models (see Figure 7-13 in [6] and Figure 2(b) in [7]).

Sliding bearings

Sliding isolators support the weight of the superstructure and provide seismic protection through the friction force developed in the sliding interface of the bearing, typically a polytetrafluorethylene (PTFE) - stainless steel interface. The coefficient of friction depends on the sliding velocity, apparent pressure, temperature, state and composition of the sliding surface [6, 21]. Several models for friction exist, that vary from the simple friction Coulomb model where the sliding coefficient is constant, to Stribeck and Constantinou's sophisticated models which account for variations in μ and stick-slip motion. While flat sliders are efficient in mitigating earthquake forces, they do not provide effective restoring force and hence may lead to large permanent displacements, especially when significant after-shocks occur shortly after the main event. Restoring force in pure sliding isolation systems can be achieved through geometry (Friction Pendulum, Zayas, 1985). 267 Friction Pendulum bearings where used for the isolation of the San Francisco's International Airport Terminal. The isolation system has a period of 3sec and reduced the seismic demand to the structure by 70%. The bearings were designed for lateral displacement of 508mm (20in) [22]. The most recent evolutions of the Friction Pendulum are the Double and Triple Pendulum bearing [23, 24, 25, 26]. The Triple Friction Pendulum (TFP) has an inner slider, two inner and two outer concave sliding surfaces. The adaptive stiffness and damping characteristics provide the system with independent pendulum response mechanisms (five sliding regimes) which are efficient over a wide range of strong ground motions [24, 27, 28]. A recent application of the TFP system is the 12-story San Bernardino Justice Center in California [29].

Additional information on the configuration and the mechanical properties of the rubber

and sliding bearings can be found in [1, 3, 6, 30]. and in the catalogues of major American, European and Japanese manufacturers; for a complete list see section 2.6 in [6].

Hybrid isolation systems

Hybrid Base Isolation Systems (HBIS) are common practice in Japan and in Italy, where flat sliders are combined with rubber bearings to achieve the desired period elongation and displacement demands. Typical applications of HBIS are the Mackay School of Mines at the University of Nevada at Reno [1], the PRADA Boutique Aoyama in Tokyo [31] and the Solarino and Augusta buildings in Sicily [32, 33]. A hybrid isolation system, consisting of lead rubber bearings and flat sliders was designed for the test program of a 5-story steel moment frame at the Hyogo Earthquake Engineering Research Center (E-Defense) of the National Institute for Earth Science and Disaster Prevention in Japan [34]. The experimental results indicated redistribution of axial load between the rubber and sliding elements. The hybrid design proved beneficial for the rubber bearings in terms of stability and post-buckling behaviour; nevertheless, it led to quite large tensile and compressive demands on the sliding bearings [34]. Much earlier, Kelly and Beucke demonstrated experimentally that sliding bearings may server as a fail-safe system for the isolation system if the bearings are subject to displacements beyond their design capacity [35]. Special attention should be given when flat bearings are used for energy dissipation, since their stick slip behavior may excite higher frequencies, potentially causing discomfort and damage to non-structural components and content [36].

Three dimensional isolation systems

In [7] Warn and Ryan after a detailed review of experimental performance of base isolated buildings conclude that 'the modern isolation systems can survive earthquakes larger than the design one through activation of ultimate limit state behaviours' and therefore point

the future research needs towards the 3D protection of the non-structural components and content of isolation buildings. For instance, the GERB system, a 3D isolation system which uses large helical springs, was found to be less effective in reducing horizontal accelerations due to the coupling of horizontal and vertical motion [1].

Dynamic identification

Dynamic identification is a highly effective tool for the detection of damage in Structural Health Monitoring, with applications to civil, mechanical, aerospace and other branches of engineering. In Structural Health Monitoring damage is defined as changes in the geometric and/or material properties of the system. These changes could be the result of extreme loading, aging, temperature, fatigue, manufacture and/ or installation errors etc. In structural engineering, dynamic identification is often synonymous to the time or frequency domain identification of the modal parameters of equivalent linear models used for the representation of the actual systems. The data used in the identification are usually ambient noise records instead of strong motion records, for the obvious reason that the probability of a monitored building to be excited by a earthquake during its nominal life is small. However, identification studies using earthquake data can be found in the literature and date back to the late '70 - early '80s. Beck and Jennings identified the parameters of a linear model for a high-rise buidling on the basis of the building's response during the 1971 San Fernando earthquake [37]. This study poses questions on the uniqueness of the optimal solution, the effect of noise on the modal approach, and the efficiency of equivalent linear models used in the simulation of non-linear system response. In [37] the identification is performed by means of an output-error method, where the function to be minimized is the (normalized) distance between identified and recorded response. Nowadays, the function to be minimized through the black-box optimization is known as the cost or objective or error function, while the population of trial systems as candidate solutions or offspring. More recently Stewart et al. performed identification analyses using the strong motion records from

four base-isolated buildings in California [38]. The authors used cumulative and recursive prediction error identification methods, CEM and RPEM respectively. The RPEM allows for the use of time-variation of the model used in the identification, while the CEM does not. The authors used an equivalent linear model to describe the isolation system and hence the identified parameters included the equivalent modal parameters of the base isolated building, i.e. fundamental-mode frequencies, damping ratios, and mode shapes. The authors observed frequency reduction (stiffness softening) with increasing ground motion amplitude and highlighted that the hysteretic action is strongly dependent on the shaking amplitude; consequently the fully softened isolator stiffness and damping values obtained from laboratory tests do not provide an accurate measure of actual isolator behavior. The same year, Nagarajaiah published the results he obtained from the modal identification of the base-isolated University of Southern California (USC) hospital, using the building's recordings during the 1994 Northridge earthquake [10, 39]. Nagarajaiah implemented parametric and non-parametric methods for the identification of an equivalent linear dynamic system. In [39] the optimal solution was defined as the solution providing the minimum weighted sum of squares of errors between the absolute magnitudes of the actual and desired frequency response function points. Oliveto et al. peformed the dynamic identification of a hybrid base isolated building in Solarino, Italy, using full scale free vibration tests [40]. The identification was done in the frequency domain and provided the optimal equivalent viscous models for the isolation system under the considered excitation. However, the identified linear models were unable to account for the period shortening with the decay of amplitude. The identification analyses of the Solarino isolation system were repeated in [41] with more detailed models for the description of the isolators. More specifically, the bi-linear model was used to model the HDRB and the Constant Coulomb Friction Model (CCFM) was used for the modelling of the friction sliders. In both [40] and [41] the least squares method was used for the identification. The least squares method introduced several complications to the inverse problem, since it required numerical approximation of the gradient and moreover interaction with the user during the iterative procedure. In the years that followed the

Covariance Matrix Adaptation Evolution Strategy, a state of the art algorithm for difficult non linear optimization [42], was applied to the Solarino identification study. The CMA-ES outperformed the previously used methods and improved the obtained solutions [43]. The implementation of the CMA-ES allowed for the consideration of more sophisticated models regarding the description of the isolation system, such as the trilinear model for the rubber bearings and the linear Coulomb model for the friction sliders [44].

Thesis outline

The present dissertation focuses in the dynamic identification of the mechanical properties of a hybrid base isolated building, in Augusta (Italy), from full scale, push and sudden release tests performed on the building. Chapter 1 provides information on the building and the performed tests, while Chapter 2 presents a baseline fitting method for the signal processing of the Augusta recordings. The proposed method is simple and can provide reliable velocities and displacements, provided that the signal does not contain significant amount of noise. Moreover, it ensures that initial and end conditions are met. The adjusted system response is used in the identification of the Augusta isolated building, see Chapter 3. This is a two stage identification, performed using the CMA-ES. In the first stage, the non-linear properties of the hybrid isolation system are identified. A bi-linear model is adopted for the rubber bearings and the standard Coulomb model is used for the description of the flat sliders. The optimal solution provided by the CMA-ES, corresponds to an isolation system whose velocity and displacement response matches the observed one. In the second stage of identification, the properties of the superstructure are identified. A linear, classically damped, fixed base model is considered for the description of the superstructure in the linear range of response. The system is excited at the base by the acceleration developed at the base isolation level. In this case, the optimal solution obtained by the identification attempts, is a linear system whose relative acceleration and velocity response matches the observed one. The identified properties of the isolation system and the superstructure are input in a synthesized model, which accounts for both the hysteretic base and the flexible superstructure. The response history analysis of the synthesized system is performed using an constrained optimization algorithm, developed ad hoc for the 1D dynamic response simulation of hybrid base-isolated buildings. Conclusive remarks and recommendations for future research are provided in the last chapter of this dissertation. An appendix relative to Chapter 2, can be found attached.

Chapter 1

The Augusta release tests

A residential building in the city of Augusta, Italy, was designed to withstand seismic action by means of a hybrid base isolation system. On March 2013, the Augusta building was subjected to a series of free vibration tests before being put into use. The release tests were performed at low amplitudes to ensure that no damage would occur in the building ($\gamma = 0.39 - 0.78$). A preliminary simulation of the system response of the building under the tests can be found in [33]. The experiments provided a handful of information that give light to the non-linear behaviour of the isolation system under real-time motions. In the following sections the output of the tests is used for the assessment of the isolation system and the validation of the existing models that are used to simulate the dynamic response of the structure.

1.1 The case study

The Augusta building consists of a basement, two storeys above the ground level and a penthouse. The structure is $35.70\,m$ long and $16.00\,m$ wide, the maximum height above the ground level is $10.50\,m$ and the basement story height is $3.60\,m$. Pictures of the building exterior are shown in Figure 1.1. The typical floor plan and sections of the building can be

a) 

b) 

Figure 1.1: a) and b) The Augusta building; aerial and South - East view.

seen in Figures 1.2 and 1.3. The foundation lies predominantly on deposits of stiff clay, i.e. a site of class B according to the Italian and European technical regulations [45, 46]. The building is isolated at the base; the isolators provide the structure with lateral flexibility so that the latter can withstand the horizontal forces induced during strong ground motion. The isolation plane runs along the top of the pillars of the basement storey slightly above the ground level and is composed by 16 High Damping Rubber Bearings (HDRB) and 20 Low Friction Sliding Bearings (LFSB), Figure 1.4.

The SI-N 500/150 antiseismic isolators and the multidirectional VASOFLONpot bearings VM 25/600/600 , VM 150/600/600 and VM 200/600/600 from FIP Industriale S.p.A. were selected for the High Damping Rubber Bearings (HDRB) and the Low Friction Sliding Bearings (LFSB) respectively. The HDRB (SI-N 500/150) have the following characteristics: total bearing height $312mm$, external diameter $500mm$, bonded diameter $480mm$, total rubber thickness $25 \times 6\,mm = 150\,mm$, steel height $24 \times 3\,mm = 72\,mm$, end plates $2 \times 20\,mm = 40\,mm$. The primary and secondary shape factors equal $S_1 = 20$ and $S_2 = 3.2$ respectively. S_1 is defined as the ratio of the compressed area, $\pi D^2/4$, divided by the area of lateral surface free to bulge, πDt. For circular bearings this relation simplifies to $S_1 = \frac{D}{4t} = 20$, where $D = 480mm$ is the bonded bearing diameter and $t = 6mm$ the single rubber layer thickness. S_2 is the aspect ratio, i.e. the bearing diameter $D = 480mm$ divided by the total rubber thickness $t_r = 150mm$, $S_2 = \frac{D}{t_r} = 3.2$.

The LFSB (VM 25/600/600 , VM 150/600/600 and VM 200/600/600) are characterized

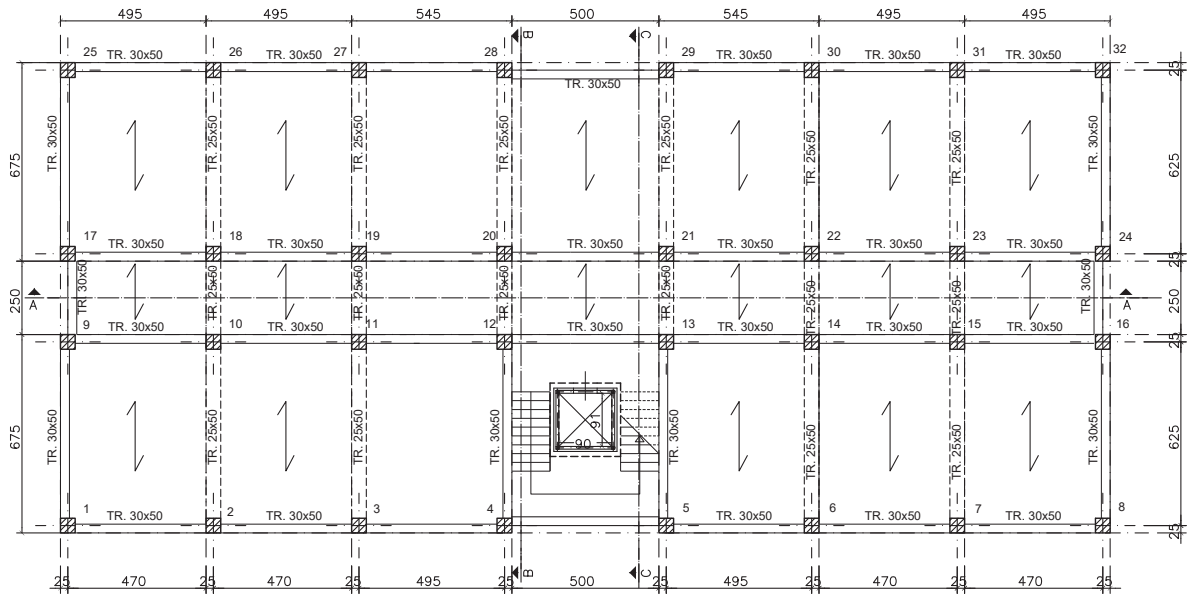

Figure 1.2: Typical floor plan of the Augusta building.

Table 1.1: Technical requirements for the seismic isolators of the Augusta isolation system, shown in Figure 1.4.

High Damping Rubber Bearings		*Low Friction Sliding Bearings*		
Vertical load in seismic condition	$1000\,kN$	*Type*	*Load*	*Displacement*
Damping ratio at $\gamma = 1$	$\xi = 15\%$	1	2000 kN	300 mm
Secant horizontal stiffness at $\gamma = 1$	$K_e = 1000kN/m$	2	1500 kN	300 mm
Vertical stiffness	$K_v > 800K_e$	3	250 kN	300 mm
Horizontal displacement at $\gamma = 2$	$d_c = 300mm$			

by maximum loading capacities that vary from 250 to $2000\,kN$. Tests performed by the manufacturer indicate very low values for the start-up, μ_s, and sliding coefficient of friction, μ_d:

- $0.31\% < \mu_s < 0.98\%$ and $0.24\% < \mu_d < 0.50\%$ for VM 25/600/600 at vertical loads varying from to $125 - 250kN$,

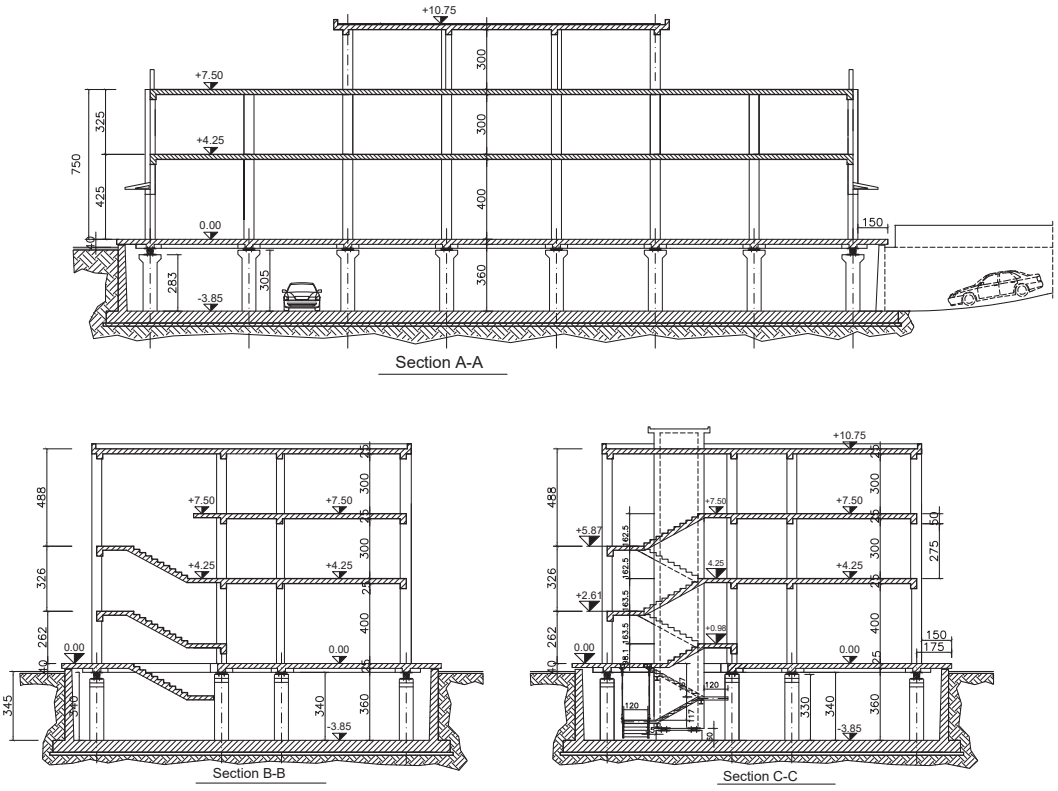

Figure 1.3: Sections of the Augusta building.

- $0.10\% < \mu_s < 0.30\%$ and $0.08\% < \mu_d < 0.15\%$ for VM 150/600/600 at vertical loads varying from to $750 - 1500kN$,
- $0.09\% < \mu_s < 0.24\%$ and $0.07\% < \mu_d < 0.14\%$ for VM 200/600/600 at vertical loads varying from to $1000 - 2000kN$.

Such small values of the friction coefficient are due to the lubrication of the PTFE and the very low testing velocity ($4mm/min$). For highly polished stainless steel and normal temperature conditions the coefficient of friction attains values of approximately 0.3%, though it could be somewhat higher at velocities relevant to seismic motions [6]. The technical characteristics of the HDRB and the LFSB used for the seismic isolation of the Augusta building are given in Table 1.1.

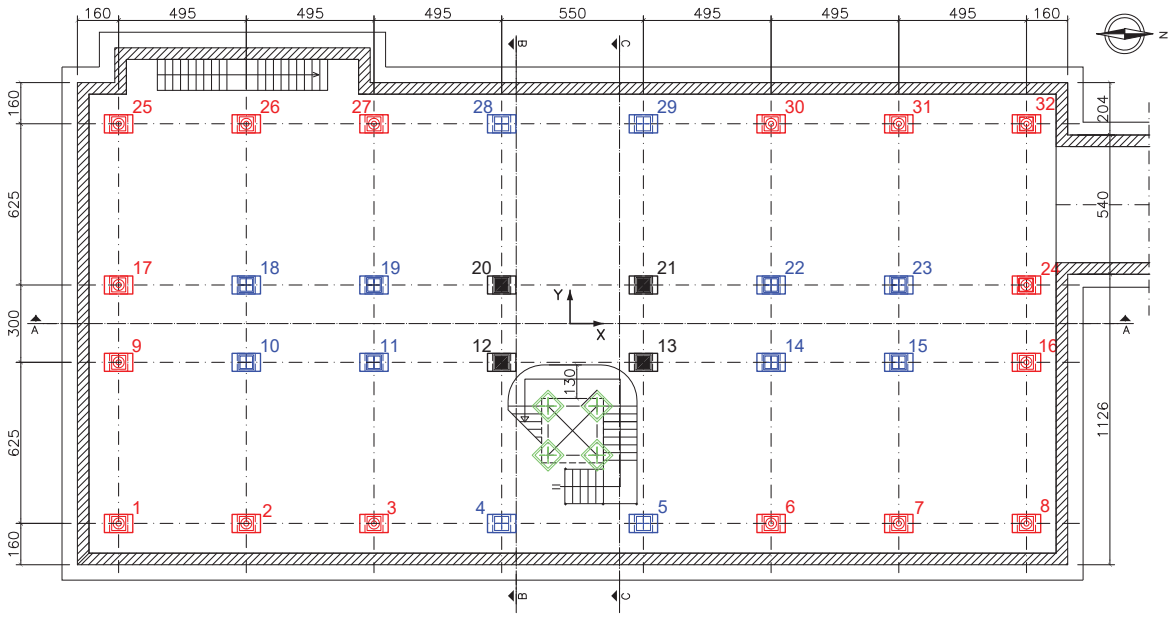

Figure 1.4: Plan view of the Augusta base isolation system. In red notation the High Rubber Damping Bearings (HDRB); in black, blue and yellow notation the Type 1, 2 and 3 Low Friction Sliding Bearings (LFSB).

1.2 Test description

A set of ten release tests, were performed on the Augusta building on March 2013 ($20/03 - 22/03/13$). During the tests the building was displaced statically from its initial position and then it was left to oscillate. The release tests were performed in low amplitudes to ensure that no damage would occur in the building; the imposed displacements varied from $5.8\,cm$ to $11.7\,cm$ ($\gamma = 0.40 - 0.80$). In tests 2 and test 7 there was no release of the building, therefore those tests shall not be considered herein. The testing timeline can be seen in Figure 1.5.

The testing apparatus consisted of the loading device, the measurement equipment and the data acquisition system. The loading device consisted of a reaction wall, a hydraulic jack, a sudden release device and a load cell [32]. The loading device can apply a maximum force of approximately $200\,tons$. The force was applied along the long direction of the building

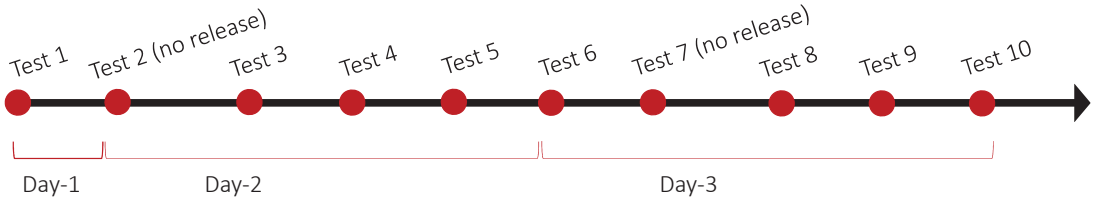

Figure 1.5: Augusta testing timeline (Days 1-3: 20-22 March 2013).

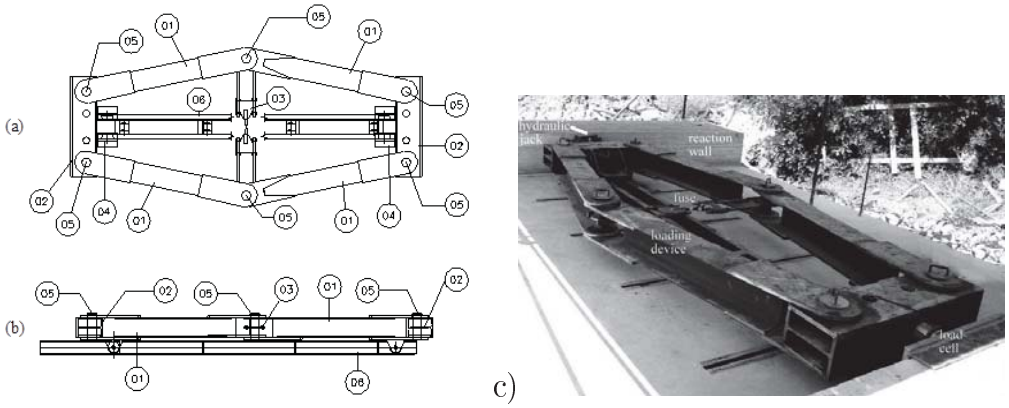

Figure 1.6: Loading device used in the Augusta experiments: a) plan and b) side views and c) device prototype. Figures are reproduced from [47].

(x-x direction, Figure 1.4) . The pushing and quick-release device was designed and built for the dynamic testing of another building in Solarino, in Eastern Sicily, retrofitted by means of base isolation in the beginning of the 21^{st} century. The device is shown in Figure 1.6.

The histories of the loading force, displacements and accelerations were recorded throughout the experiments. The loading force was measured by a NOVATECH model F205-CFR0K0 load cell [1], applied between the building and the head of the loading device. The horizontal and vertical accelerations were measured at the various floor levels using 16 channels, shown in a schematic layout in Figure 1.7 (c). The accelerometers used for the recording of the absolute acceleration response were the SA-107LN linear model developed by COLUMBIA Research Labs Inc. [2] and the wireless triaxial model POSEIDON developed

[1] http://www.novatechloadcells.co.uk/ds/f205.htm

[2] http://www.crlsensors.com/product.cfm?cat=force-balance&sub=linear-accelerometers&prod=sa-107ln

a) 

b) 

c) 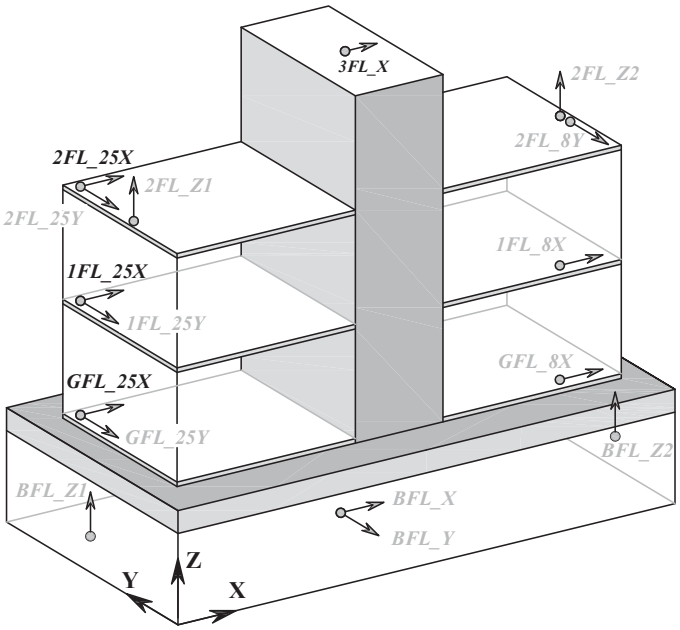

Figure 1.7: a) and b) Columbia and Poseidon accelerometers used in the Augusta experiments. c) Schematic accelerometers layout.

by LUNITEK [3], see Figures 1.7 (a) and (b). The horizontal displacements were measured at various positions below and above the isolation level through 15 channels, see Figure 1.9. The linear displacement sensor SLS320/400 developed by Penny and Giles [4] was used for the displacement measurements, see Figures 1.8.

[3] http://www.lunitek.it/listing/registratore-sismico-per-applicazioni-statichedinamiche/ (in italian)

[4] http://www.cw-industrialgroup.com/Products/Sensors/Linear-Position-Sensors/Linear-Displacement-Sensor-SLS320.aspx

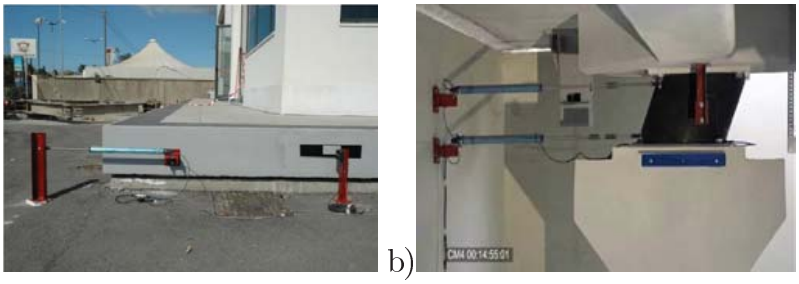

a) b)

Figure 1.8: Displacement sensors used in the Augusta tests for the measurement of the building displacements just above the isolation level, photo (a), and the measurement of the isolators deformations, photo (b).

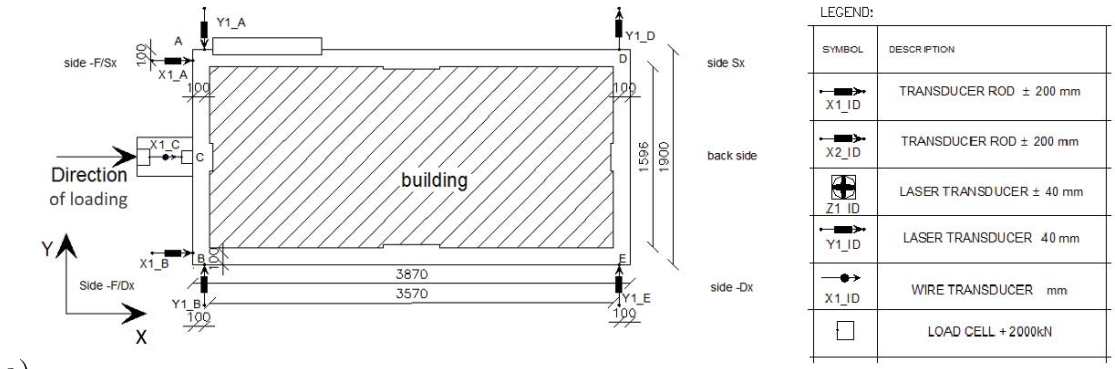

a)

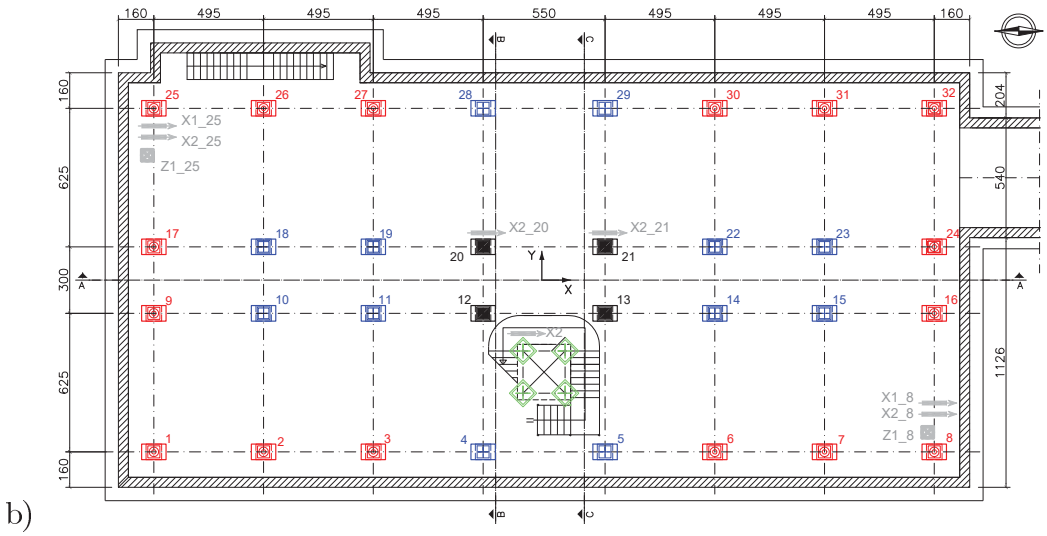

b)

Figure 1.9: Locations of the displacement sensors used in the Augusta experiments; (a) building exterior (see also photo 1.8 (a)) and (b) isolators 25 and 8 (see also photo 1.8 (b)).

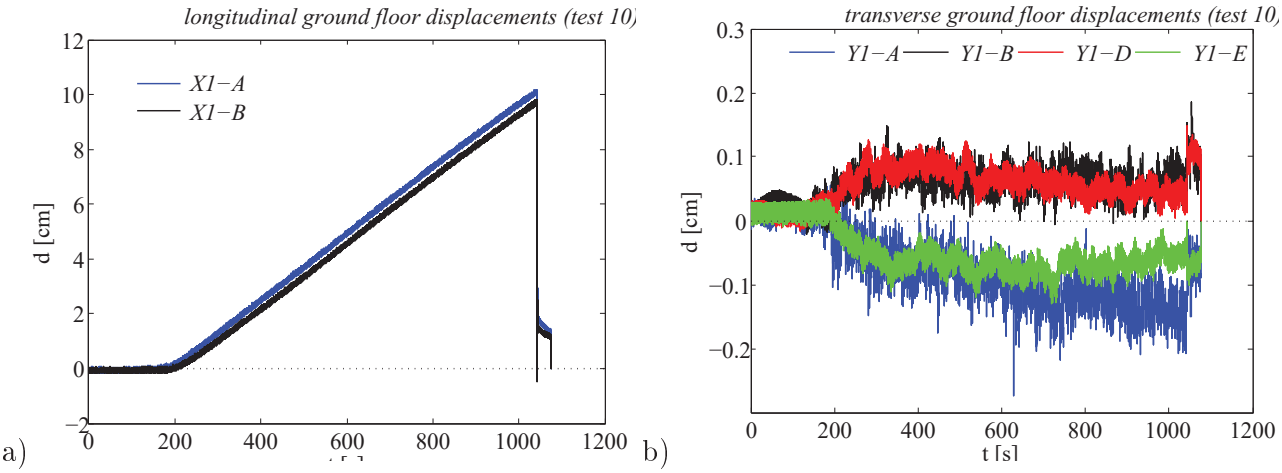

Figure 1.10: Longitudinal and transverse displacements measured at the corners of the Augusta building during free vibration test 10, sub-plots a) and b).

1.3 Displacement records

Figures 1.10 show the longitudinal and transverse displacements measured at the building corners during test 10 at the measuring stations *X1-A, X1-B, Y1-A, Y1-B, Y1-D, Y1-E* , see Figure 1.9 (a). Test 10 was among the tests with the higher energy input. Observation of Figure 1.10 (a) shows how the building was pushed statically for about $1000sec \sim 17min$ to arrive at a displaced position of $10cm$. As soon as the building was released it started oscillating; the free vibration response was damped rapidly and the system came to a rest with a residual displacement. The longitudinal displacements measured at the two front ends of the ground floor slab are somewhat different indicating rotation of the building. However, observation of sub-plot (b) shows how the transverse displacements are very small ($\sim 2mm$) with respect to the horizontal ones ($\sim 100mm$); hence the rotation introduced to the building by the uni-axial excitation can be considered negligible. It can be assumed that the small rotation of the building due to longitudinal excitation is the result of a small eccentricity of the loading force with respect to the center of rigidity of the isolation system. From the typical floor plan view shown in Figure 1.2, it can be seen how the presence of the reinforced concrete staircases and the elevator core introduces some asymmetry in the long

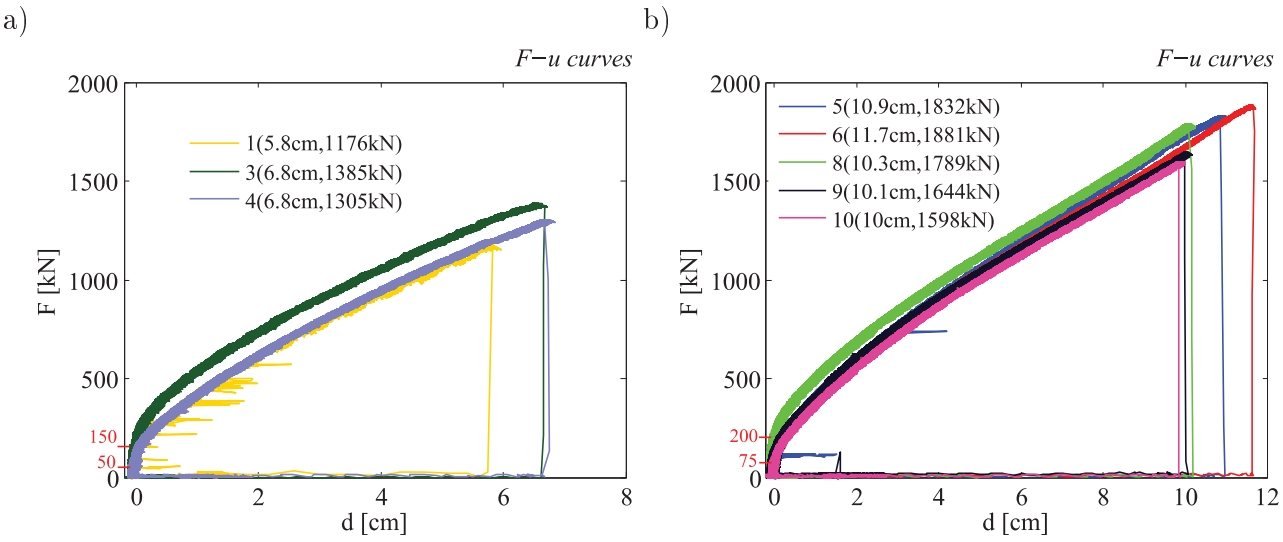

Figure 1.11: Experimental force-displacements curves; a) tests 1,3,4 and b) tests 5,6,8,10. The maximum displacement and force values are given within brackets next to the test identification number in the legend.

(x) direction.

Figures 1.11 show the loading force - longitudinal displacement[5] curves measured during the eight free vibration tests performed in the Augusta building. Sub-plot (a) refers to tests 1,3 and 4 that were tests of smaller initial displacement $(u_0 = 5.8 - 6.8cm)$ while sub-plot (b) refers to tests 5,6,8 and 10 that were tests of higher initial displacement $(u_0 = 10 - 11.7cm)$. It is interesting how the F-u curves resemble bilinear curves; in fact the loading force induced to the structure equals the static non-linear forces developed in the hybrid isolation system. The initial quasi-vertical branch of the F-u curves could provide an estimate of the start-up friction force. However this estimate is rather vague, the friction force could be as small as $50\,kN$ and as large as $200\,kN$, see Figures 1.11.

Figures 1.12 and 1.13 show the displacements as measured at the top of isolators 25 and 8, see Figure 1.9, during the free vibration part of the tests. In all tests, the system completed only one full cycle of motion before coming to rest with some residual displacement. Residual

[5]The displacement is evaluated as the average of the displacements measured at the building corners (channels X1-A and X1-B, see Figure 1.9 (a))

displacements vary from $0.27cm$ to $1.60cm$ and occur due to the non-linearity of the isolation system. A creep behaviour was observed after end of motion - this behaviour could be attributed to the elastomer. The magnitude of the residual displacement is not related to the initial input; systems that undergo larger deformations do not necessarily experience larger residual displacements. After every test the building was re-centred to the initial, zero displacement, equilibrium position by means of a simple re-centring mechanism.

The displacement diagrams can serve for an estimate of the damped period of vibration T_{1D} and the equivalent damping ratio ζ_{eq}, see Table 1.2. T_{1D} is read easily from the displacement traces as the time elapsed between the first and second positive peak (1st cycle of motion) or alternatively as the time elapsed between the first and second negative displacement peak. The equivalent damping ratio is evaluated by the logarithmic decrement method, see Eq. 1.1(a). Eq. 1.1(b) is the approximate solution to Eq. 1.1(a) and it is valid for damping ratios less than 20% [2]. For higher damping ratios the exact solution should be considered, see Eq. 1.1 (c). ζ_{eq}, as evaluated herein, is the total damping ratio, i.e. the sum of the equivalent damping ratios due to energy dissipation in the HDRB and the LFSB.

$$\delta = ln\frac{u_i}{u_{i+1}} = \frac{2\pi\zeta}{\sqrt{(1-\zeta^2)}} \qquad logarithmic\ \ decrement \tag{1.1a}$$

$$\zeta_{approx} = \frac{\delta}{2\pi} \qquad approximate\ \ solution\ \ valid\ \ for\ \ \zeta < 20\% \tag{1.1b}$$

$$\zeta_{exact} = \frac{\delta}{\sqrt{(4\pi^2+\delta^2)}} = \frac{\zeta_{approx}}{\sqrt{(1+\zeta^2_{approx})}} \qquad exact\ \ solution \tag{1.1c}$$

where u_i, u_{i+1} are two successive maxima (peaks); for the problem at hand that would be the first and second (positive) displacement peaks as read from the displacement diagrams shown in Figures 1.12 and 1.13.

Observation of Table 1.2 shows how the damped period of vibration increases with the displacement amplitude, implying softening of the effective stiffness with increasing strain

Table 1.2: Periods of vibration and equivalent damping ratios. First column: test number. Second column: initial displacement u_0. Third column: damped period of vibration T_{1D} measured as the time elapsed between the first and second positive peak (1st cycle of motion). Fourth column: damped period of vibration T'_{1D} measured as the time elapsed between the first and second negative displacement peak. Fifth column: approximate equivalent damping ratio ζ_{eq}, evaluated according to Eq. 1.1 (b). Sixth column: exact equivalent damping ratio ζ_{eq}^{exact}, evaluated according to Eq. 1.1 (c). ζ_{eq} (or ζ_{eq}^{exact}) is the total damping ratio due to energy dissipation in the rubber and friction devices. The tests are organized in terms of increasing initial displacement.

	$u_0[cm]$	$T_{1D}[sec]$	$T'_{1D}[sec]$	$\zeta_{eq}[\%]$	$\zeta_{eq}^{exact}[\%]$
Test 1:	5.83	1.45		20.0	19.2
Test 3:	6.81	1.75	1.5	26.6	25.7
Test 4:	6.85	1.75	1.55	19.6	19.2
Test 10:	10.02	1.95	1.65	20.4	20.0
Test 9:	10.11	1.95	1.65	21.3	20.8
Test 8:	10.33	1.95	1.60	26.0	25.2
Test 5:	10.88	1.90	1.55	22.0	21.4
Test 6:	11.66	1.95	1.65	20.8	20.4

amplitude, which is typical of isolated structures. On the other hand, the equivalent damping ratio does not show a clear trend, however it seems that the capacity of the isolation system to dissipate energy is similar for moderately low input motion ($\gamma = 0.5 - 0.8$). ζ_{eq} values approximately 20%, with the exception of tests 3 and 8 where $\zeta_{eq} \sim 25\%$. The simplified expression 1.1 (b) overestimates the equivalent damping ratio, however the differences between approximate and exact equivalent damping ratios are less than 4%.

A special comment should be made at this point on tests 3 and 8. Tests 3 and 8 followed the unsuccessful release tests 2 and 7, see Figure 1.5. The structure was not re-centered after test 7, and there is no information whether it was so after test 2. Therefore, the reliability of the results obtained from tests 3 and 8 is highly questionable.

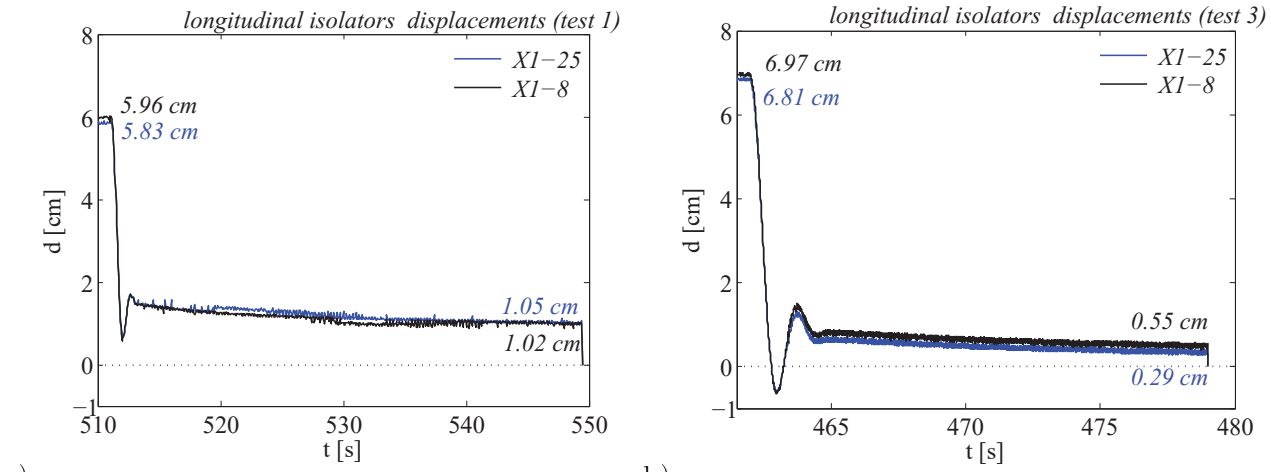

Figure 1.12: Sub-plots (a) to (d): Longitudinal isolators displacements recorded during tests 1, 3, 4 and 5 *(stations X1-25 and X1-8, see Figure 1.9 (b))*. The initial and residual displacements are given in the plots.

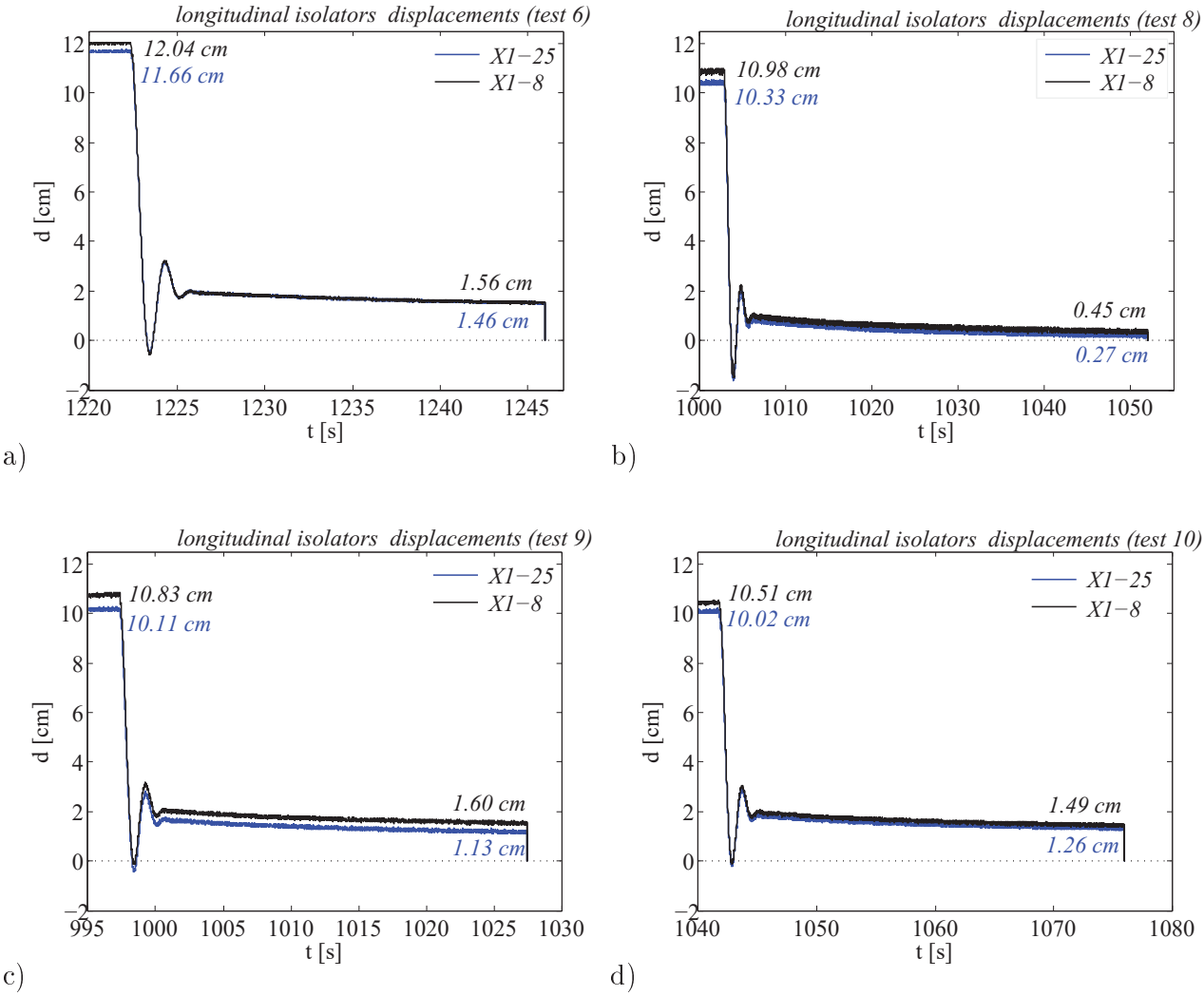

Figure 1.13: Sub-plots (a) to (d): Longitudinal isolators displacements recorded during tests 6,8,9 and 10 *(stations X1-25 and X1-8, see Figure 1.9 (b))*. The initial and residual displacements are given in the plots.

1.4 Acceleration records

Figures 1.14 to 1.16 show the longitudinal acceleration histories measured during tests 4 and 6 at the basement, ground floor, first floor, second floor and roof of the Augusta building, *(stations BFL-X, GFL-25X, 1FL-25X, 2FL-25X, 3FL-X, see Figure 1.7)*. The recorded response confirms that the introduction of the flexible isolation plane results to a reduction of the forces induced to the superstructure. In fact, the system response seems to be smaller at the upper floors. The fundamental period (isolation mode period) is evident in all floor signals. The signals contain also waveforms of higher frequency - these are generated because of the flexibility of the superstructure. The roof acceleration does not resemble very much the lower floor accelerations. The roof response contains wavelets which seem to be of a smaller frequency, compared to the high frequency wavelets observed in the lower floor signals. This is probably due to the irregularity of the structure in height and the low stiffness of the penthouse, Figure 1.1. Test 4 being a test of smaller initial displacement ($u_0 = 6.8cm$) result to lower acceleration records comparing to the ones obtained from test 6 (where $u_0 = 11.7cm$) . The foundation, lying beneath the isolation plane, did not experience any significant motion (maximum acceleration amplitude $< 0.10g$, see Figures 1.16 (a) and (b)).

1.4.1 Fourier amplitude spectra of the registered signals

The Fourier analysis of the recorded acceleration signals provides a valuable insight in the frequency content of the structural response. The Fourier amplitude spectra of the longitudinal acceleration signals recorded during tests 4 and 6 in the Augusta superstructure and shown in figures 1.14 and 1.15, are given in Figures 1.17 (a) and (b). Test 4 was one of the tests with the smallest initial displacement ($u_0 = 6.83cm$) while test 6 was the test with the highest initial displacement ($u_0 = 11.66cm$). The Fourier spectrum amplitudes of the accelerations recorded at the ground floor (just above the isolation plane) and at the upper floors are very similar in the neighbourhood of the fundamental frequency (isolation frequency), which is approximately equal to $f_{is} = 0.73\,Hz$ for test 4 and $f_{is} = 0.49\,Hz$

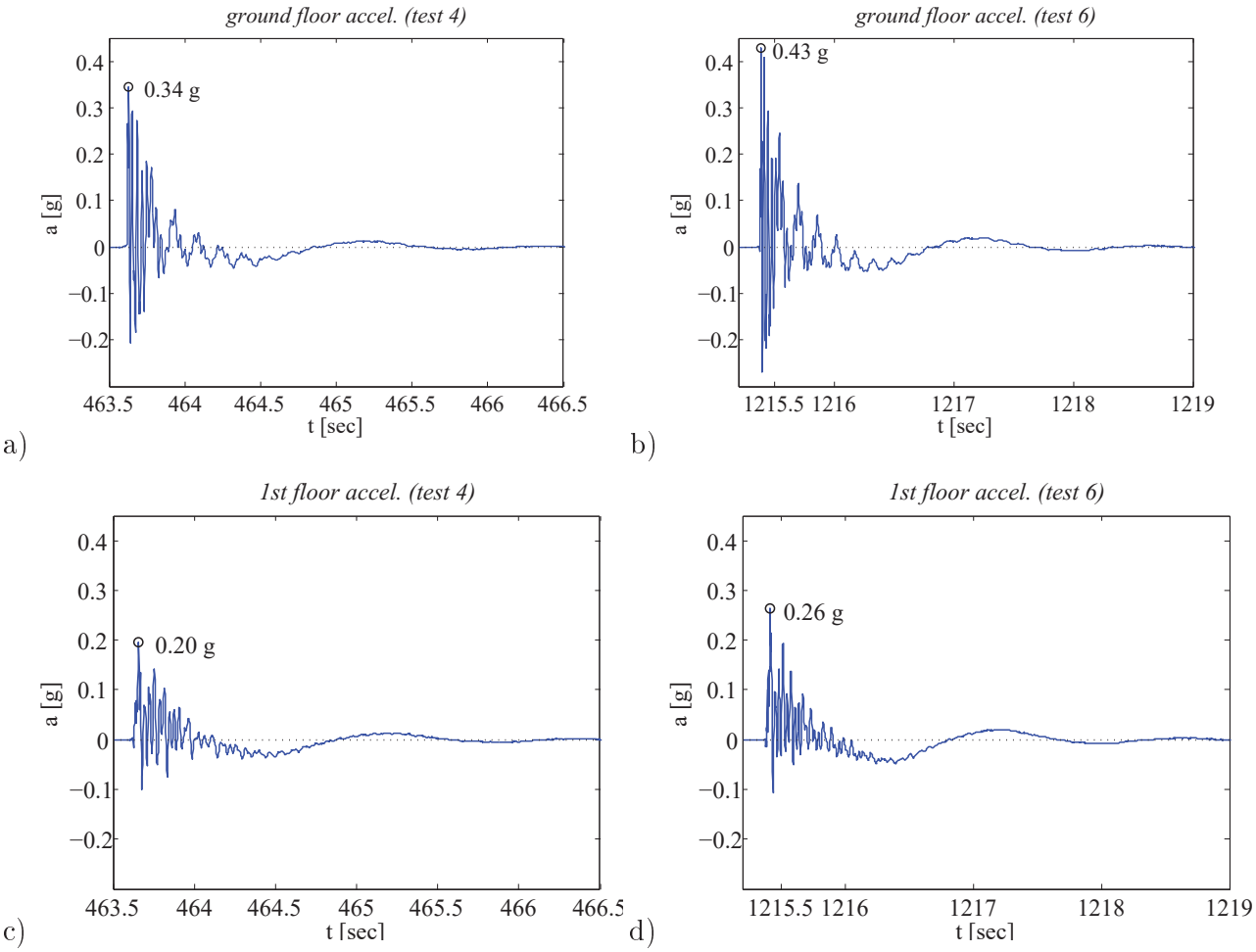

Figure 1.14: Sub-plots (a) to (d): Longitudinal acceleration signals recorded at the ground and first floor of the Augusta building during tests 4 and 6 *(stations GFL-25X, 1FL-25X, see Figure 1.7)*. The peak accelerations are given in the plots.

for test 6. The lengthening of the dominant period (shortening of the fundamental frequency) with increasing strain amplitude was evident also in the measured displacements, see Figures 1.12, 1.13 and Table 1.2. The following Fourier amplitude peaks, located in the higher frequency range, correspond to the higher modes of the system. Closer observation of Figures 1.17 shows that the frequencies that dominate the superstructure response are mainly four and approximately equal to: $f = 6.6\,Hz$, $13.9\,Hz$, $19.8\,Hz$, $32\,Hz$ for test 4 and $f = 6.4\,Hz$, $12.9\,Hz$, $18.8\,Hz$, $31.8\,Hz$ for test 6. One point seems really relevant here; not

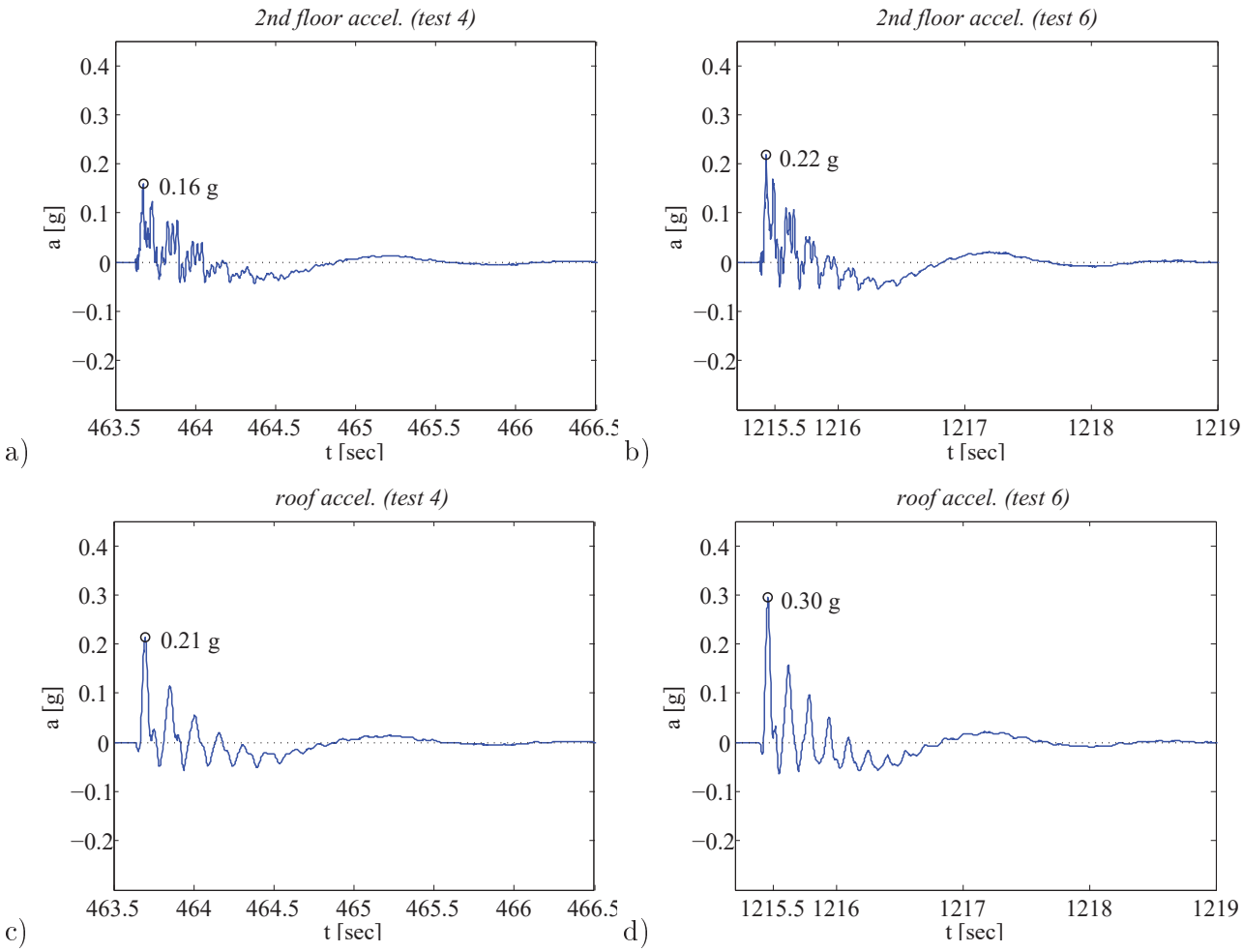

Figure 1.15: Sub-plots (a) to (d): Longitudinal acceleration signals recorded at the second floor and roof of the Augusta building during tests 4 and 6 *(stations 2FL-25X, 3FL-25X, see Figure 1.7)*. The peak accelerations are given in the plots.

only the isolation frequency becomes smaller as the initial displacement increases, but also the higher frequencies become smaller. The non-linearity of the isolation system causes a shift of the whole set of system frequencies. The ground floor and the first floor responses seem to be more sensitive to higher frequencies ($f \sim 19\,Hz$ and $f \sim 32\,Hz$), having relatively high Fourier amplitude peaks in those frequency ranges. These high frequency components however may be local due to the way the load was applied.

A comparison of the Fourier amplitude spectra of tests 4 and 6, confirms that larger

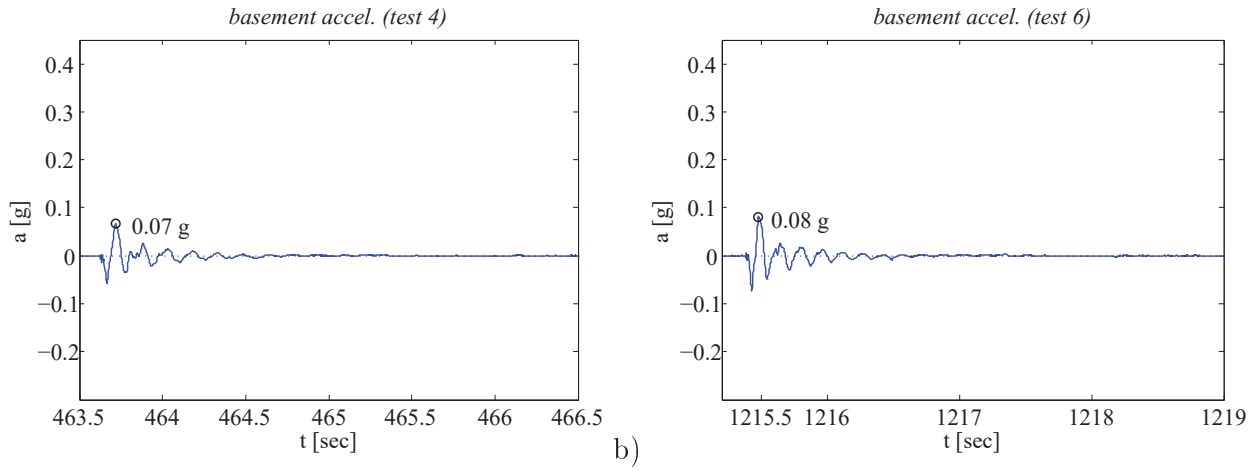

Figure 1.16: Longitudinal accelerations recorded at the Augusta basement during tests 4 and 6, sub-plots (a) and (b) *(station BFL-X see Figure 1.7)*. The peak accelerations are given in the plots.

initial displacements result to larger response amplitudes and shift of the fundamental frequency to the left. The Fourier spectrum of the foundation acceleration response is shown in Figure 1.18; the spectrum has a sharp peak in the proximity of $7\,Hz$, significantly above the fundamental frequency. This explains why the foundation did not exhibit any significant motion during the experiments.

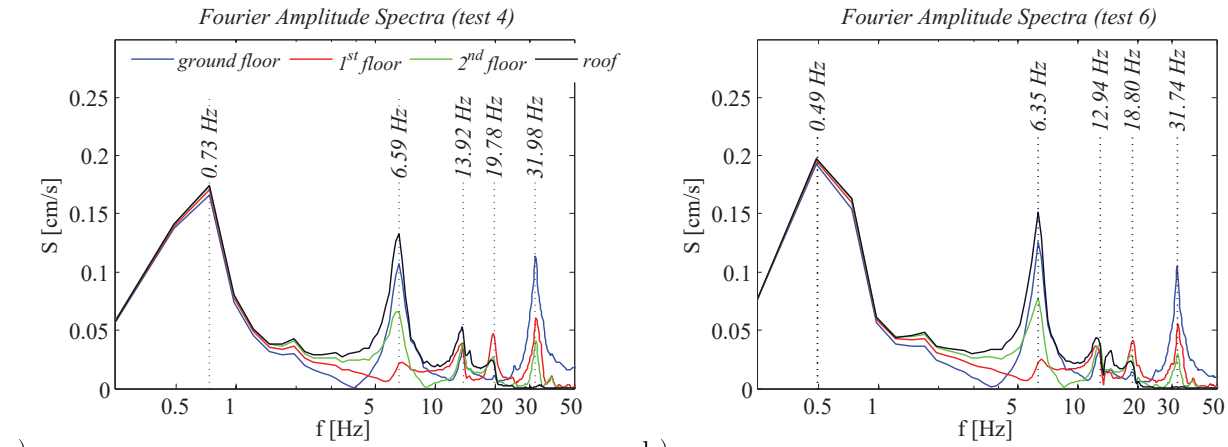

a) b)

Figure 1.17: Fourier amplitude spectra of the longitudinal acceleration signals recorded at the Augusta building during tests 4 and 6. Test 4 was among the tests with the smallest initial amplitude ($u_0 = 6.83cm$), while test 6 was the test with the highest initial displacement ($u_0 = 11.66cm$). The frequencies corresponding to the peak fourier amplitudes are also provided in the sub-plots.

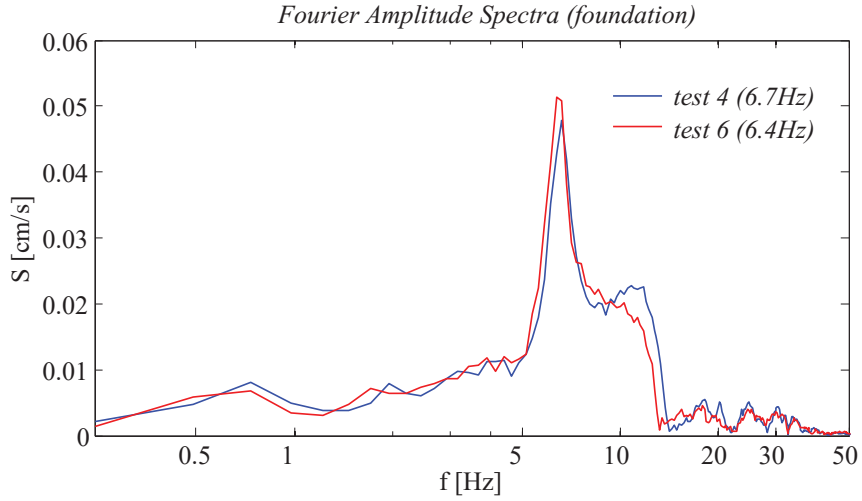

Figure 1.18: Fourier amplitude spectra of the longitudinal acceleration signals recorded at the Augusta basement during tests 4 and 6. Test 4 was among the tests with the smallest initial amplitude ($u_0 = 6.83cm$), while test 6 was the test with the highest initial displacement ($u_0 = 11.66cm$). The frequency corresponding to the peak fourier amplitude is given within brackets in the legend.

1.4.2 Record labelling

Not all the information provided by the experiments is relevant to the current study. The information that shall be used for calculation in the following chapters consists in

- ground floor displacements : namely the displacement measured at the top of isolator 25 (component X1-25,see Figure 1.9 (b))
- floor accelerations : namely the absolute floor accelerations measured at stations GFL-25X, 1FL-25X, 2FL-25X, 3FL-X (see Figure 1.7). Two digits shall be added in the component code name to indicate the test number, for instant GFL-25X-09 is the ground floor acceleration component (GFL) measured along the x axis at the position '25' (-25X) during test 9 (-09).

1.5 Conclusions

The data obtained from the free vibration Augusta experiments were presented briefly in this introductory section. The raw data will be processed in the following section according to the developed baseline fitting scheme to provide floor velocities, displacements and drifts which were not measured during the experiments. The processed data will be then used for the identification of the properties of the isolation system and the superstructure.

Chapter 2

Signal Processing

2.1 Introduction

Although the theoretical foundations of signal processing date back in the classical numerical analysis techniques of the 17th century [48], signal processing algorithms evolved much later, in the early '70s , along with the development of 'third-generation' computer hardware and the digitization of analog records. Signal processing aims to the removal of noise from the strong motion data and the extraction of valuable information, such as peak ground characteristics and response spectra. However, considering the arbitrary nature of the noise, it becomes clear that no method can recover the original, uncontaminated signal.

Noise causes distortion of the signal in a wide frequency range. The influence of noise is more dramatic in the low (<1Hz) and high (>25Hz) [1] frequency range, where the signal to noise ratio tends to be significantly lower. The signal to noise ratio (SNR) is defined as the ratio of the signal power to the noise power and it is a measure of the signal contamination. The lower the SNR, the more contaminated the data. Signals with very low SNR (<2), for instance signals of low amplitude, recorded from small or long distance earthquakes, are considered to be highly influenced by noise and therefore might be disregarded, since they

[1] $1Hz$ and $20Hz$ are indicative low and high frequency limits used in signal processing of strong motion.

are prone to provide meaningless information [49].

Low frequency noise originates in instrument errors, constant acceleration drifts, background noise and manipulation errors [50]. The effect of long period noise, which is basically the distortion of the reference baseline, cannot be detected easily in the acceleration record. However, once the acceleration is integrated to provide velocities and displacements its influence becomes clear; uncorrected accelerations generate un-physical velocities and displacements. Given the increased engineering interest towards performance based design strategies and also towards structures that respond in the long period range (high-rise buildings, bridges,isolated structures) the correction of records for low frequency noise becomes of major importance for the production of plausible displacements and realistic response spectra at the long period range. An overview of signal processing methodologies for the treatment of long period noise can be found in [51].

Low frequency noise can be treated using

- low cut (or high pass) filters, and/or
- baseline fitting schemes.

When low cut filters are applied to the signal, the signal components with frequencies below the selected cut-off frequency are removed. The generated response is very sensitive to the selection of the cut-off frequency. The choise of an appropriate cut-off frequency f_c can be done on the basis of the SNR ratio; the signal should be filtered in the frequency range $[0, f_c]$ where the SNR becomes significantly small [51].

Baseline fitting schemes can be considered as 'low-cut filters of unknown frequency characteristics' [51]. They consist in the adjustment of the distorted acceleration, velocity and displacement reference lines using straight or curved lines. In [50] Chiu presents a combination of baseline and filtering procedures for the effective removal of the long period noise. His algorithm provides reliable results and requires less computational effort than the established processing routine developed in the '70s by Trifunac and Lee [52]. Nonetheless, an essential limitation of the algorithm is its inability to account for permanent displacements.

2.2 Baseline fitting using higher order polynomial curves

A baseline fitting procedure is implemented for the **adjustment** of the acceleration signals recorded during the free vibration tests performed on the Augusta building. Herein the term 'signal adjustment' shall be used instead of the term 'signal correction'. The term 'correction' implies that the real signal is known and therefore can be recovered, that is seldom the case in reality [51]. The long period noise is removed from the acceleration, velocity and displacement traces by fitting the baseline with polynomial curves of increasing order, Eqs 2.1. The motion is adjusted in the time interval when the motion is essential - the definition of the duration of strong motion is given in section 2.3. The coefficients of the correction polynomials are evaluated using the boundary conditions, see Eq.2.2. The main advantage of the procedure suggested is that it accounts for the initial and end conditions, recovering permanent displacements, provided that the latter have been measured. For isolation systems, that are highly non-linear,the recovery of residual displacements is of utmost importance.

$$\ddot{u}(t) = \ddot{u}_{raw}(t+t_1) + 2p_2 + 6p_3\,t + 12p_4\,t^2 + 20p_5\,t^3 \tag{2.1a}$$

$$\dot{u}(t) = \int_0^t \ddot{u}_{raw}(\tau+t_1)\,d\tau + p_1 \; + 2p_2\,t + 3p_3\,t^2 + 4p_4\,t^3 + 5p_5\,t^4 \tag{2.1b}$$

$$u(t) = \int_0^t \int_0^{\tilde{\tau}} \ddot{u}_{raw}(\tau+t_1)\,d\tau\,d\tilde{\tau} + p_0 + p_1\,t + p_2\,t^2 + p_3\,t^3 + p_4\,t^4 + p_5\,t^5 \tag{2.1c}$$

where $\ddot{u}_{raw}(t)$ is the unprocessed acceleration record, t_1 is the time when the strong motion starts [1], $\ddot{u}(t), \dot{u}(t), u(t)$ are the processed acceleration, velocity and displacement histories,

[1]The signal adjustment refers to the time interval $(0, t_d)$ where the motion is significant. Hence the length of the adjusted response is significantly smaller than the length of the full record, since the full record includes pre- and post- event memories. The time interval $(0, t_d)$ where the motion is significant, corresponds to the time window (t_1, t_2) of the full record. t_1, t_2 are the start and end times of strong motion, estimated according to section 2.3.

and $p_i\,(i = 0, 1, ..5)$ are the polynomial coefficients evaluated from the boundary conditions, Eq.2.2. Since the number of available boundary conditions is equal to the number of the unknowns, the latter can be defined explicitly.

$$\ddot{u}(0) = \ddot{u}(t_d) = 0,\ \dot{u}(0) = \dot{u}(t_d) = 0,\ u(0) = u_0,\ u(t_d) = u_{res} \tag{2.2}$$

Eqs 2.2 describe the state of the system at the beginning ($t = 0$) and at the end of motion ($t = t_d$). When the motion starts from rest, the acceleration and velocity are zero. The displacement can be different than zero if the system starts moving from a displaced configuration (u_0), such as in the case of free vibration. When the motion ends, at time $t = t_d$, the acceleration and velocity drop back to zero, while the displacement can be non-zero (u_{res}), if the system is excited to its non-linear range. t_d is the duration of strong motion and it is defined in the section that follows.

Substitution of Eqs 2.2 in 2.1 leads to the following system of equations:

$$u(0) = u_0 \Rightarrow p_0 = u_0 \tag{2.3a}$$

$$\dot{u}(0) = 0 \Rightarrow p_1 = 0 \tag{2.3b}$$

$$\ddot{u}(0) = 0 \Rightarrow p_2 = -\frac{1}{2}\ddot{u}_{raw}(t_1) \tag{2.3c}$$

$$u(t_d) = u_{res} \Rightarrow p_0 + p_1\,t_d + p_2\,t_d^2 + p_3\,t_d^3 + p_4\,t_d^4 + p_5\,t_d^5 = u_{res} - \int_0^{t_d}\int_0^{\tilde{\tau}} \ddot{u}_{raw}(\tau + t_1)d\tau\,d\tilde{\tau} \tag{2.3d}$$

$$\dot{u}(t_d) = 0 \Rightarrow p_1 + 2p_2\,t_d + 3p_3\,t_d^2 + 4p_4\,t_d^3 + 5p_5\,t_d^4 = -\int_0^{t_d} \ddot{u}_{raw}(\tau + t_1)d\tau \tag{2.3e}$$

$$\ddot{u}(t_d) = 0 \Rightarrow 2p_2 + 6p_3\,t_d + 12p_4\,t_d^2 + 20p_5\,t_d^3 = -\ddot{u}_{raw}(t_d + t_1) \tag{2.3f}$$

Eqs 2.3 can be written in matrix form as follows:

$$\mathbf{A} \cdot \mathbf{p} = \mathbf{b} \tag{2.4}$$

where

$$\mathbf{A} = \begin{bmatrix} 1 & 0 & 0 & 0 & 0 & 0 \\ 0 & 1 & 0 & 0 & 0 & 0 \\ 0 & 0 & 1 & 0 & 0 & 0 \\ 1 & t_d & t_d^2 & t_d^3 & t_d^4 & t_d^5 \\ 0 & 1 & 2\,t_d & 3\,t_d^2 & 4\,t_d^3 & 5\,t_d^4 \\ 0 & 0 & 2 & 6\,t_d & 12\,t_d^2 & 20\,t_d^3 \end{bmatrix}, \mathbf{p} = \begin{pmatrix} p_0 \\ p_1 \\ p_2 \\ p_3 \\ p_4 \\ p_5 \end{pmatrix}, \mathbf{b} = \begin{pmatrix} u_0 \\ 0 \\ -\frac{1}{2}\ddot{u}_{raw}(t_1) \\ u_{res} - \int_0^{t_d}\int_0^{\tilde{\tau}} \ddot{u}_{raw}(\tau + t_1)d\tau\, d\tilde{\tau} \\ -\int_0^{t_d} \ddot{u}_{raw}(\tau + t_1)d\tau \\ -\ddot{u}_{raw}(t_d + t_1) \end{pmatrix} \tag{2.5}$$

Provided that the start and end times of strong motion are known, Eq. 2.4 describes a linear system of equations which can be solved for $\mathbf{p}$:

$$\mathbf{p} = \mathbf{A}^{-1} \cdot \mathbf{b} \tag{2.6}$$

The implementation of the proposed baseline fitting procedure requires that the initial and end conditions are known. While for systems responding in their linear range, the boundary conditions are easy to guess (the response is zero at the beginning and end of motion); for systems responding in their non linear range it is not so. For the boundary conditions to be known, the residual displacement should be known, i.e. measured.

2.3 Duration of strong motion

Accelerograms contain the information from the time that the induced motion exceeds the threshold trigger of the accelerometer, until the time that the recording returns to the level of the background noise. However, only some portion of the recorded vibration contributes significantly to the energy induced to the system and hence influences the system response. Duration and amplitude are the two major characteristics of any strong motion. The duration of strong motion plays a major role in the inelastic response of rigid and relatively weak structures and also in the dynamic response of structures with stiffness and strength degrading characteristics. While the amplitude of the motion is a property easily quantifiable, for instance the peak ground acceleration can be read immediately from the accelerogram, the duration of the motion cannot be determined straightforwardly. During the last 50 years, researchers have developed different methods for the evaluation of the strong motion duration t_d [53]:

- Bracketed durations (D_b): t_d is defined as the total time elapsed between the first and last excursions of a specified level of acceleration.
- Uniform durations (D_u): t_d is the sum of the time intervals during which the acceleration is greater than the selected threshold.
- Significant durations (D_s): t_d is the time interval during which the accumulation of energy is significant. Trifunac and Brady defined t_d as the time interval during which the integral of the squared acceleration, $\int a(t)^2 dt$, grows from 5 to 95% of its maximum value [54].

The procedure implemented herein for the evaluation of the durations of the motions recorded during the Augusta free vibration tests, lies conceptually in the third group of 'significant durations' methods. t_d is determined as the time interval during which the cumulative squared acceleration $CSA(t)$, Eq. 2.7(a), grows rapidly. For convenience, the

cumulative squared acceleration $CSA(t)$ is normalized to its maximum value $CSA(t_{max})$, Eq. 2.7(b). The motion is considered to be initialized at time t_1, when the rate of change of $CSA_n(t)$ becomes essentially different from zero, see Eq. 2.8 (a). The motion is thought to have ceased at time t_2, when the rate of change of $CSA_n(t)$ becomes negligible again, see Eq. 2.8 (b). The thresholds $\varepsilon_1, \varepsilon_2$ are very small quantities, of the order of magnitude of $O(-1)$ and $O(-4)$ respectively and should be chosen individually for every signal, to ensure reliable estimates of the times t_1 and t_2.

$$CSA(t) = \int_0^t [a(\tau)]^2 \, d\tau \tag{2.7a}$$

$$CSA_n(t) = \frac{CSA(t)}{CSA(t_{max})} = \frac{\int_0^t [a(\tau)]^2 \, d\tau}{\int_0^{t_{max}} [a(\tau)]^2 \, d\tau}, \quad 0 \leq CSA_n(t) \leq 1 \tag{2.7b}$$

$$motion \;\; starts \;\; at \;\; t = t_1 \;\; when \quad \frac{dCSA_n(t)}{dt}|_{t=t_1} > \varepsilon_1, \quad \varepsilon_1 = O(-1) \tag{2.8a}$$

$$motion \;\; stops \;\; at \;\; t = t_2 \;\; when \quad \frac{dCSA_n(t)}{dt}|_{t=t_2} < \varepsilon_2, \quad \varepsilon_2 = O(-4) \tag{2.8b}$$

Eqs 2.8 suggest that ε_1 is several orders of magnitude greater than ε_2. This can be justified as follows. ε_1 and ε_2 represent the slope of the cumulative squared acceleration curve at times t_1 and t_2. When the free vibration motion starts there is a rapid growth of the cumulative squared acceleration function, which is indicative of the amount of energy input to the system. The rapid growth of CSA or CSA_n translates to a significant change of slope at time t_1 ($\varepsilon_1 > 0$). During motion the initial input energy transforms to kinetic energy, elastic strain energy in the superstructure and dissipated energy in the isolation system. The kinetic energy and strain energy of the vibrating system are dissipated by various damping mechanisms [2]. The dissipation of the initial input energy marks the end of growth of the cumulative squared acceleration curve. Hence, versus the end of motion, at time t_2, the slope of CSA or CSA_n, is expected to be almost zero ($\varepsilon_2 \sim 0$).

2.3.1 Duration of the motion recorded at the base floor of the Augusta building during free vibration test 9

Figure 2.1(a) shows the acceleration trace recorded during test 9 at the ground floor of the Augusta building (component GFL-25X-09)[2]. The record is shown in the time interval $[1013.5, 1019]sec$ to facilitate the viewing of the strong part of the motion. The full length of the acceleration record in time is $1145sec \sim 19min$. Figure 2.1(b) shows the corresponding normalized cumulative squared acceleration, $CSA_n(t)$, estimated according to Eq. 2.7. Figure 2.1(c) shows the rate of change of $CSA_n(t)$. Figures 2.2 (a) and (b) are magnifications of Figure 2.1(c) in the time intervals where the strong motion starts and ceases. The time derivative of $CSA_n(t)$ was evaluated approximately, implementing the 'diff' function in MATLAB, [55], with the following syntax:

$$\frac{dCSA_n(t)}{dt} = diff(CSA_n, h) \tag{2.9}$$

where $h = 0.001sec$ is the time step.

The strong motion starts at time $t_1 = 1014.088sec$ when $dCSA_n(t)/dt$ becomes greater than $\varepsilon_1 = 10^{-1}$, see Figure 2.3(a). The motion stops at time $t_2 = 1017.419sec$, when $dCSA_n(t)/dt$ becomes smaller than $\varepsilon_2 = 5 \cdot 10^{-4}$, see Figure 2.2(b).

From Figure 2.2(b) it can be seen that the slope of the cumulative acceleration curve becomes less than the threshold even before $t_2 = 1017.419sec$. However, it is only the last time when the slope becomes less than ε_2 that is chosen as the ending time of the strong motion.

[2]for the record labelling the reader is referred to subsection 1.4.2

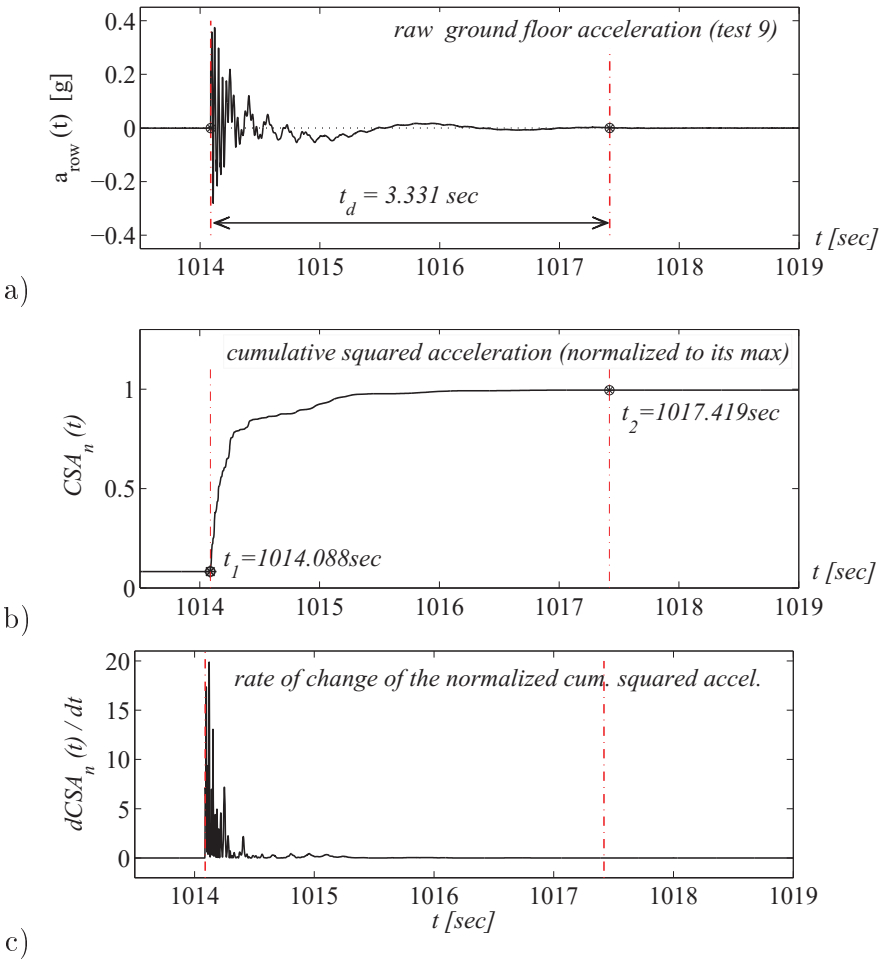

Figure 2.1: Estimation of the duration of strong motion, t_d, of the ground floor acceleration recorded in the Augusta building during test number 9 (component GFL-25X-09). a) Unprocessed acceleration, $a_{raw}(t)$, in the time window $[1013.5, 1019]sec$. b) Normalized cumulative squared acceleration, $CSA_n(t)$, evaluated according to Eq. 2.7. c) Rate of change of $CSA_n(t)$, evaluated according to Eq. 2.9. The essential part of motion lies between times $t_1 = 1014.088sec$ and $t_2 = 1017.419sec$, that is when $CSA_n(t)$ grows rapidly. The motion duration is $t_d = 3.331sec$. The start and end times of the strong part of the motion are marked in the plots with vertical dashed lines.

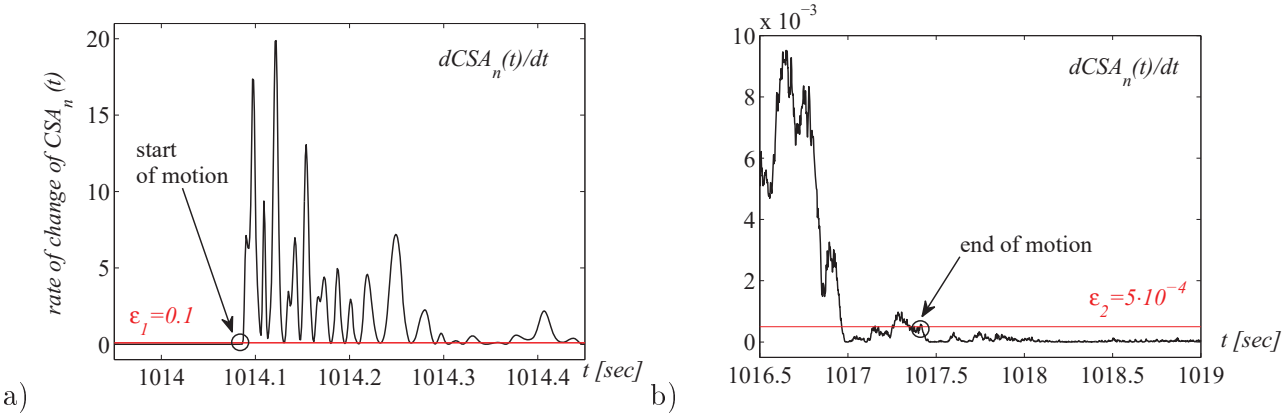

Figure 2.2: Rate of change of the cumulative squared acceleration, presented in larger time scale in Figure 2.1 (c). The plots (a) and (b) show the trace of $dCSA_n(t)/dt$ in the proximity of the start and end times of strong motion, $t_1 = 1014.088sec$ and $t_2 = 1017.419sec$ respectively. The strong motion starts when $dCSA_n(t)/dt$ becomes greater than $\varepsilon_1 = 10^{-1}$, while the motion stops when $dCSA_n(t)/dt$ becomes smaller than $\varepsilon_2 = 5 \cdot 10^{-4}$.

2.3.2 Calibration of the strong motion end time t_2

Figure 2.3 shows the velocity trace from integration of the unprocessed ground floor acceleration, shown in Figure 2.1 (a), in the time interval $[1014, 1030]sec$. A straight line is fitted between times $[1020, 1030]sec$ using the 'polyfit' function in MATLAB [55]; application of the 'polyfit' command provides the best fit, in a least-squares sense, for the velocity data in the range of interest. The linear trend observed in the velocity trace between $[1020, 1030]sec$ implies that the motion has already ended.

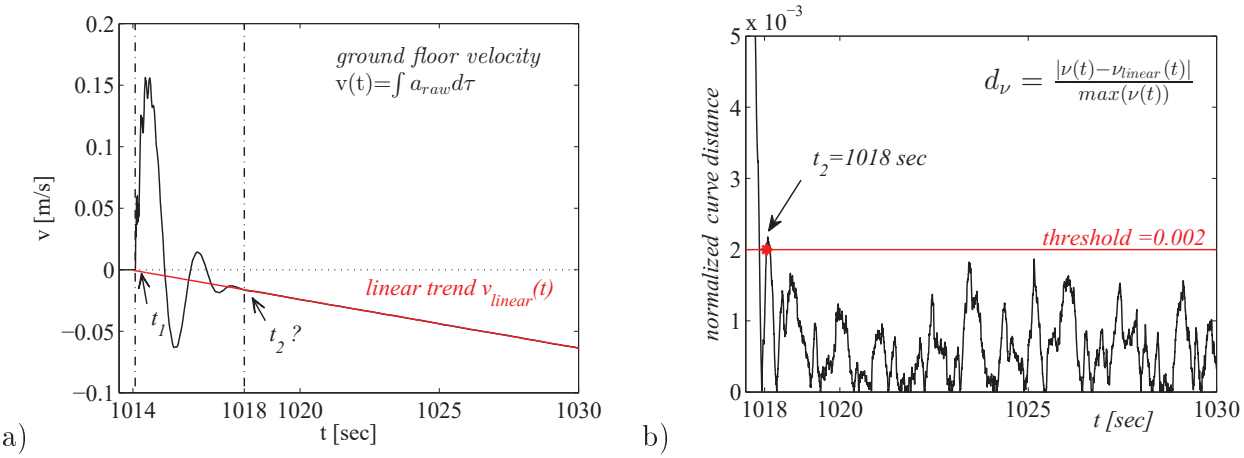

Figure 2.3: Calibration of the end time of the strong motion recorded at the ground floor of the Augusta building during test 9. a) Unprocessed ground floor velocity $\nu(t)$, estimated as the integral of the raw ground floor acceleration (black line). A straight line is fitted in the time interval $[1020, 1030]sec$. The line is extended until the start time $t_1 = 1014.088sec$ ($\nu_{linear}(t)$:red line). b) Distance between the velocity curves, $\nu(t)$ and $\nu_{linear}(t)$ in the time interval $[1017.5, 1030]sec$, evaluated as $d_\nu = |\nu(t) - \nu_{linear}(t)|/max(\nu(t))$, where $max(\nu(t)) = 0.156m/sec$ is the peak value of the unprocessed velocity. The motion is considered to cease at time $t_2 = 1018sec$, when the distance d_ν becomes smaller than a threshold, equal to $2 \cdot 10^{-3}$ for the considered record.

After cessation of motion the return of the signal to the background noise level causes a shift in the acceleration baseline that translates to a linear trend in the velocity. The fitted line is extended to the time interval $[1014, 1020]sec$. The motion is thought to have stopped when the velocity trace $\nu(t)$ distances from the linear trend $\nu_{linear}(t)$ by a very small quantity, ε_ν. The distance between the two curves is evaluated as $d_\nu = |\nu(t) - \nu_{linear}(t)|/max(\nu(t))$, where $max(\nu(t))$ is the peak unprocessed velocity in the essential time frame of motion. Setting a threshold of $\varepsilon_\nu = 0.002$, the end time for the ground floor acceleration recorded during test 9 is estimated to $t_2 = 1018sec$, somewhat greater than $t_2 = 1017.419sec$, that was the ending time found before using the $CSA_n(t)$ diagram. This output is considered more conservative, hence in the calculations that follow $t_2 = 1018sec$ for the ground floor acceleration.

2.4 Background noise

The part of the recorded motion preceding and following the main event is identified as pre- and post-event noise respectively, see Figures 2.4 (a) and (b). At time $t = 0sec$ the accelerometer is enabled and starts recording the background noise (wind,traffic effects, etc.). At time $t \sim 252sec$ the pushing device starts moving statically the building. The static motion influences the background noise; the noise in the interval $[252, 1014]sec$, although still of a very small amplitude, is amplified and has many acceleration spikes. At time $t \sim 1014sec$ the system is released and starts vibrating. At time $t \sim 1018sec$ the building stops vibrating and the record returns to the level of background noise. The pre-event noise in the interval $[0, 252]sec$ is very similar to the post-event noise, interval $[1018, 1144]sec$. The pre- and post-event noise is characterized by small amplitude ($< 10mg$) and broadband frequency content.

The Fourier Amplitude Spectra for the background noises are shown in 2.4 (c). For the evaluation of the FAS of pre- and post- event noise, two samples of records are considered in the intervals $[40, 140]sec$ and $[1040, 1140]sec$ respectively. The two FAS are almost identical in the frequency range $[0.25, 250]Hz$. Some differences arise in the low frequency range $[0, 0.25]Hz$, where the low frequency components of the post-event noise seem to be more powerful than the low frequency components of the pre-event noise.

The effect of low frequency noise is more critical than the effect of the high frequency noise in the evaluation of the response quantities of interest (velocities, displacements). High frequency components attenuate with integration and therefore shall be not treated herein. It is important to note at this point that the model of the main event noise might be different than the background noise model.

The need for removal of the low frequency noise becomes clear once the strong motion acceleration is integrated to provide velocities and displacements. Figure 2.5 shows the absolute acceleration signal $a_g(t)$, recorded at the ground floor of the Augusta building during free vibration test 9. $a_g(t)$ is integrated to generate total velocities $\nu_g(t)$ and displacements

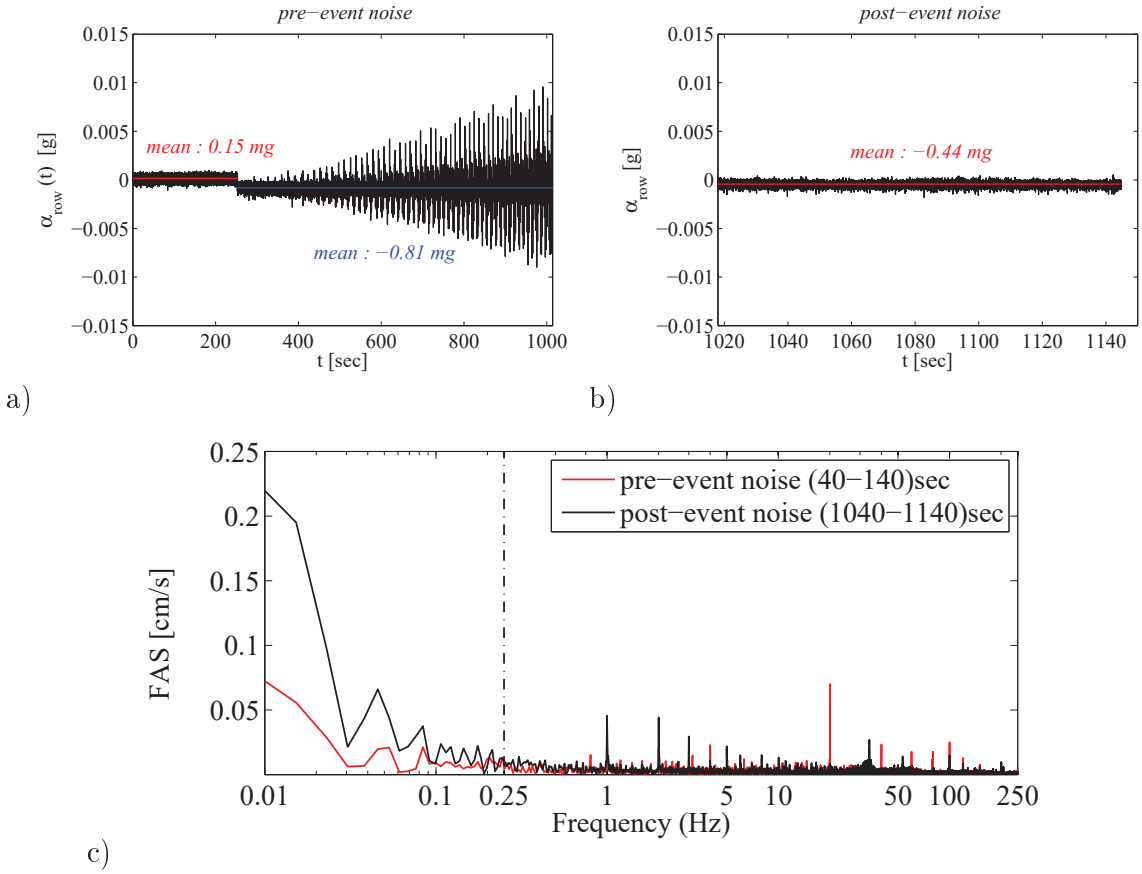

Figure 2.4: Background noise in the ground floor acceleration record obtained from the Augusta test 9. a) Pre-event noise (black line) and corresponding means in the intervals $[0, 252]sec$ (red line) and $[252, 1014.088]sec$ (blue line). b) Post-event noise (black line) and corresponding mean (red line). c) Fourier Amplitude Spectra of the pre- and post-event noise in the intervals $[40, 140]sec$ and $[1040, 1140]sec$, red and black lines respectively.

$u_g(t)$. The initial displacement, $u_0 = 10.1cm$, is added to the displacement trace obtained from integration to account for the displaced configuration of the system at $t = 0$. While the acceleration is negligible versus the end of the motion, the velocity is significantly lower than zero ($\nu(t_d) = -1.6cm/sec$) and the residual displacement is significantly higher than the observed one ($u(t_d) = 4.7cm$ against $u_{res}^{experimental} = 1.7cm$). The baseline shift in the acceleration trace after the end of strong motion, due to the presence of the post-event noise, translates to a linear trend in the velocity and a parabolic trend in the displacement after

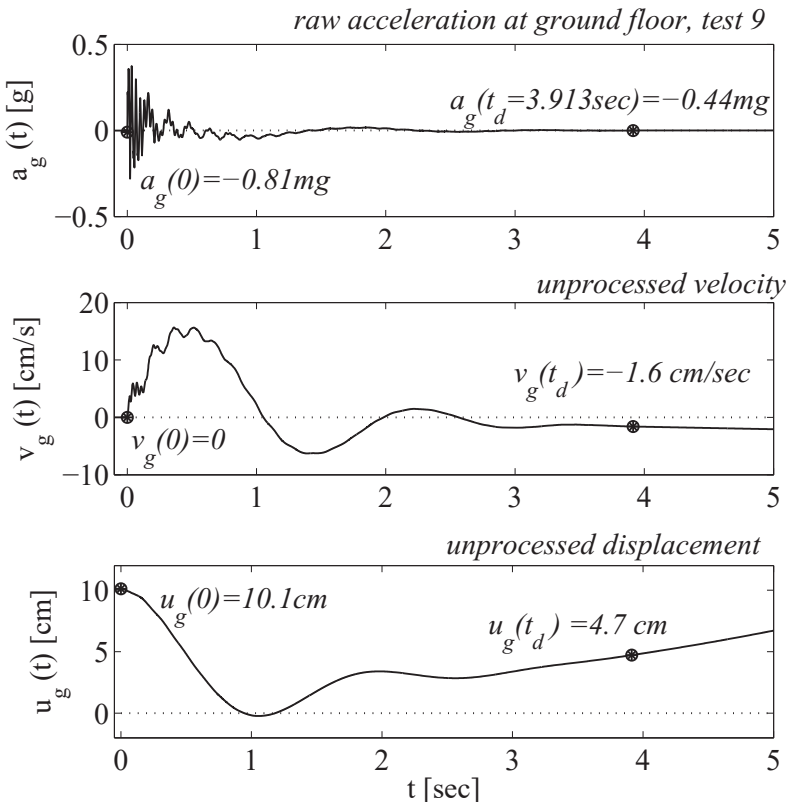

Figure 2.5: Unprocessed strong ground motion response for test 9. The raw acceleration $a_g(t)$ is integrated to provide the velocity and displacement traces $\nu_g(t)$ and $u_g(t)$. The initial response at time $t = 0$ and the estimated residual response at time t_d are provided.

the end of motion. The above results demonstrate how the long period noise, although not appreciable in the scale of the acceleration, is amplified upon numerical integration and leads to false velocities and displacements.

In the following section the acceleration response recorded at the ground floor, first floor, second floor and roof of the Augusta building during test 9, (components GFL-25X-09, 1FL-25X-09, 2FL-25X-09, 3FL-X-09, see Figure 1.7), is adjusted using the baseline fitting procedure presented in section 2.2. The predicted ground floor displacements are compared to the experimental ones to validate the effectiveness of the method.

2.5 Baseline fitting of the Augusta free vibration motion recorded during test 9

The ninth free vibration test performed on the Augusta isolated building was one of the tests with higher initial displacement ($u_0 = 10.1cm$). The longitudinal acceleration histories recorded at the ground floor and the upper floors during test 9 (components GFL-25X-09, 1FL-25X-09, 2FL-25X-09, 3FL-X-09, see Figure 1.7), are processed herein for the removal of the long period noise using the baseline fitting scheme presented in section 2.2.

2.5.1 Adjustment of the ground floor response

The longitudinal ground floor acceleration recorded during test 9 in the Augusta building and the corresponding adjusted acceleration are shown in comparison in Figure 2.6 (a). The two signals are practically one on the top of the other. The adjusted ground floor velocity is shown in Figure 2.6 (b). The predicted displacement, $u_g(t)$, is shown against the experimental one, $u_g^{exp}(t)$ in Figures 2.7 ; a very good matching is achieved between the two. The distance between $u_g(t)$ and $u_g^{exp}(t)$ is equal to $e^2 = 0.06\%$ and it is estimated according to the following formula:

$$e^2 = \frac{\sum_{i=1}^{N} \left(u_g^{exp}(i) - u_g(i)\right)^2}{\sum_{i=1}^{N} \left(u_g^{exp}(i)\right)^2} \tag{2.10}$$

where N is the number of the strong motion data points.

The boundary conditions are also provided in Figures 2.6. The adjusted acceleration and velocity at the beginning and end of motion are zero, $(a_g(0) = 0, a_g(t_d) = 0, \nu_g(0) = 0, \nu_g(t_d) = 0)$, while the initial and residual displacements are equal to $u_0 = 10.1cm$ and $u_{res} = 1.7cm$ respectively. The processing method ensures that the measured residual displacement is recovered. The noise removed from the main event in terms of acceleration, velocity and displacement can be seen in Figures 2.8 to 2.10.

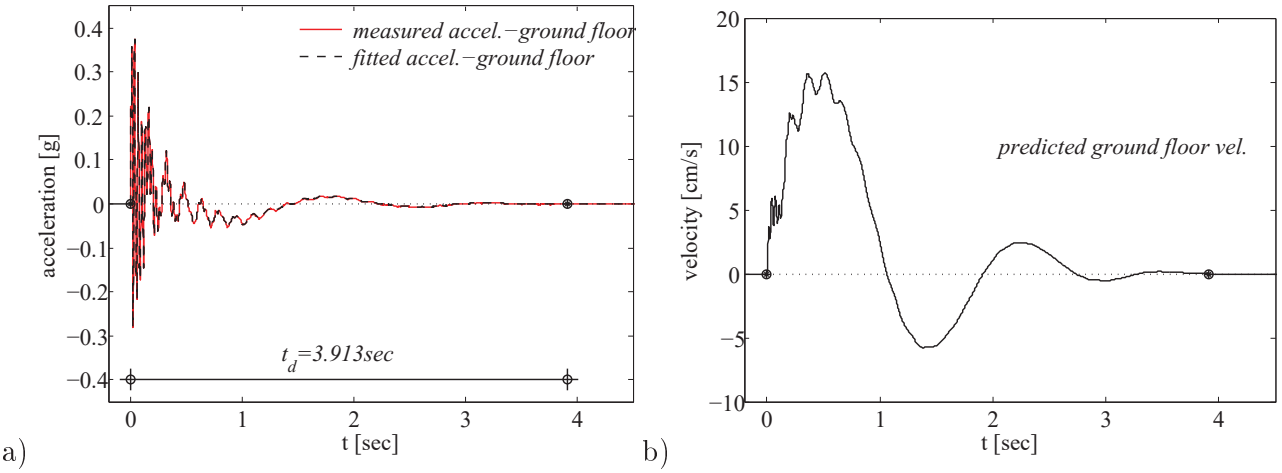

Figure 2.6: Adjusted ground strong motion response for the free vibration Augusta test number 9. a) Original (red line) and adjusted (black line) acceleration histories. b) Predicted ground floor velocity, obtained from integration of the adjusted acceleration trace. Black markers are plotted at the start and end times of motion.

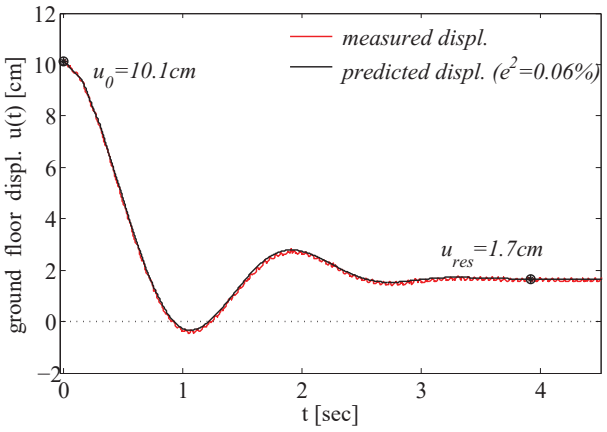

Figure 2.7: Predicted displacement history for test 9, obtained from integration of the generated velocity and implementation of initial and end conditions ($u_0 = 10.1cm, u_{res} = 1.7cm$). The generated displacement (black line) is compared to the measured displacement (red line); the two curves are practically one on the top of the other. Black markers are plotted at the start and end times of motion.

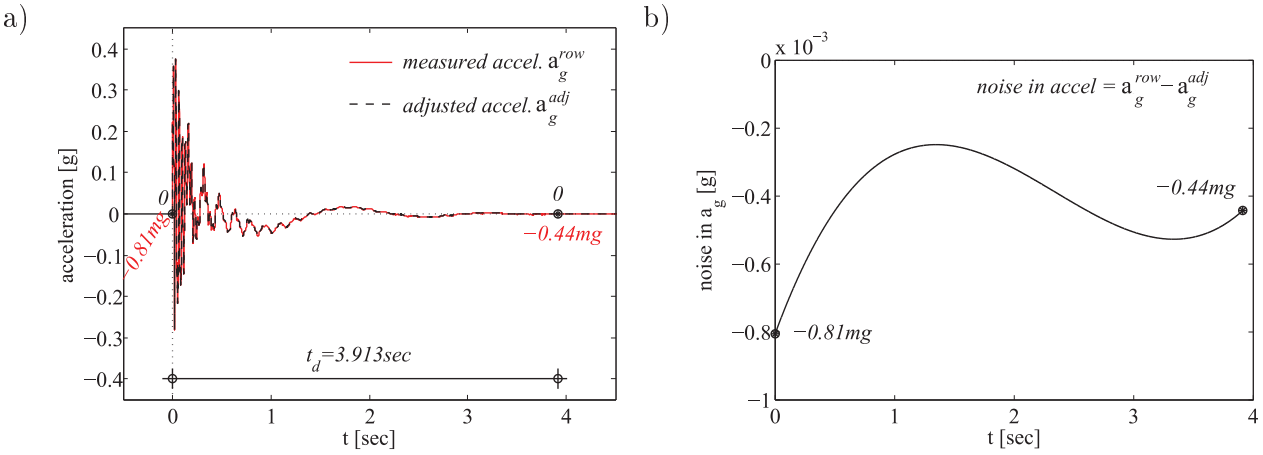

Figure 2.8: (a) Raw acceleration recorded at the ground floor of the Augusta building during test 9 (a_g^{raw}, red line) and corresponding adjusted acceleration (a_g^{adj}, black line). (b) Noise removed from the raw acceleration signal.

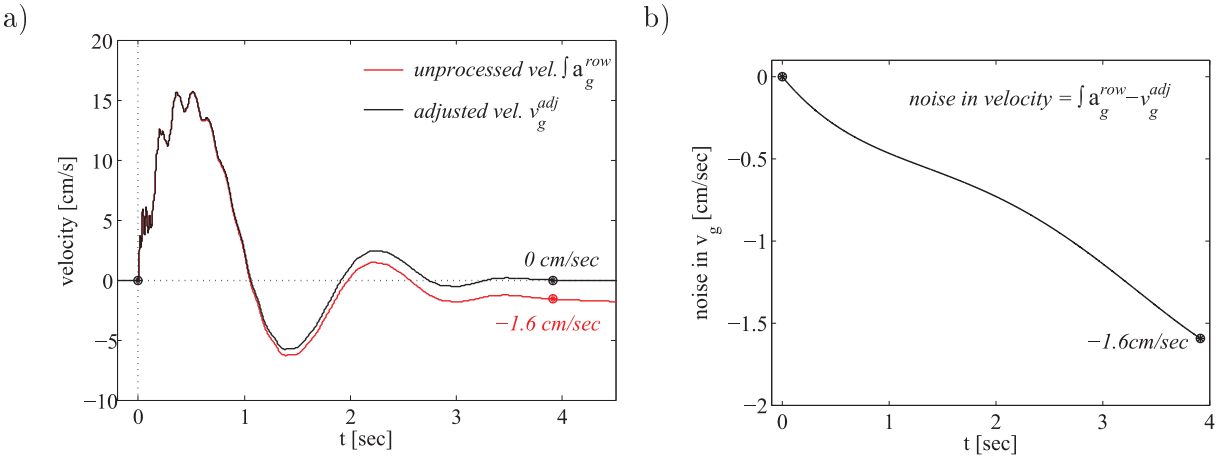

Figure 2.9: (a) Unprocessed ground floor velocity for test 9 ($\int a_g^{raw} dt$, red line) and corresponding adjusted velocity (ν_g^{adj}, black line). (b) Noise removed from the unprocessed velocity trace.

The noise removed from the acceleration is a long period waveform of very small amplitude ($< 1mg$). However once this noise is integrated it results to significant, erroneous residual velocities and displacements, see also Figure 2.5. Once the main event noise is extracted from the unprocessed signal, the adjusted response is recovered, see Figures 2.8(a),

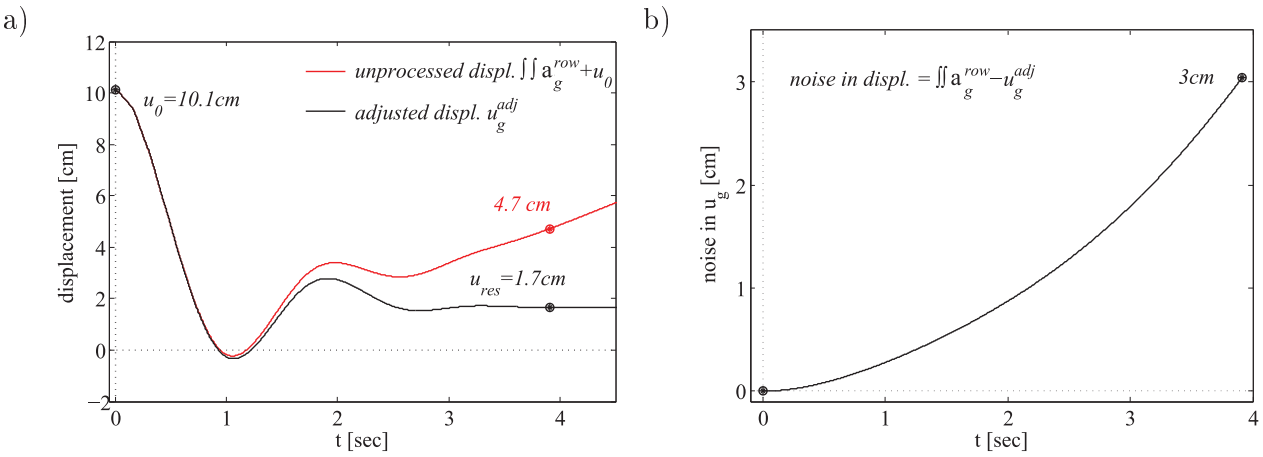

Figure 2.10: (a) Unprocessed ground floor displacement for test 9 ($\int\int a_g^{raw} d\tau dt + u_0$, red line) and corresponding adjusted displacement (u_g^{adj}, black line). (b) Noise removed from the unprocessed displacement trace.

2.9(a) and 2.10(a) . The noise removed from the raw signal for the adjustment of accelerations, velocities and displacements seems to be quite different from the observed pre- and post- event noise. While the background noise can provide a model for the main event noise, this model is incomplete, since the most important component of the noise is usually associated with the signal itself ('signal-generated noise') [51].

2.5.2 Adjustment of the absolute superstructure response

The baseline fitting scheme is applied to the acceleration signals recorded at the upper floors of the Augusta building during test 9 (components 1FL-25X-09, 2FL-25X-09, 3FL-X-09). Table 2.1 provides information on the start and end times, t_1 and t_2, and the duration, t_d, of longitudinal acceleration records obtained from test 9. The start times t_1 are evaluated from the corresponding cumulative squared acceleration diagrams, as discussed in section 2.3. The motion starts when the time derivative of $CSA_n(t)$ becomes greater than the selected threshold ε_1, that varies in the interval $1-12\%$ and is chosen individually for every

signal to ensure a reasonable estimate of the starting time t_1 [3], see Table 2.1. The end times t_2 are defined on the basis of the unprocessed velocity, to provide a more conservative estimate of t_2, as discussed in paragraph 2.3.2. Once the raw signals are integrated and the unprocessed velocity is retrieved, straight lines are fitted in the interval $[1020, 1030]$. The lines are extended to time $t = 1014sec$, see Figure 2.11(d). The distance between velocity curve and linear trend is calculated and normalized to the peak velocity; the motion is considered to have stopped when this distance, d_v, becomes smaller than a threshold ε_ν. ε_ν varies in the interval $0.1 - 0.2\%$ and as with ε_1, it is selected individually for each signal to ensure reliable estimates of t_2 [4], see Table 2.1.

The results of Table 2.1 show :

- A delay of motion as the waveform travels to the upper floors. The building is pushed statically to $u_0 = 10.1cm$. The base floor responds immediately at $t_1 = 1014.087sec$, while the upper floors respond fractions of seconds later, see Figure 2.11 (a). The same observation holds for the end of motion as well. The base floor stops moving at $t_2 = 1018sec$, while the upper floors continue to vibrate for a little longer. The base floor stops at $\approx 3.9sec$ while the upper floors stop at about $4sec$, see also Figure 2.11 (b). The start times are evaluated on the basis of the diagram of the rate of change of the normalized cumulative squared acceleration $CSA_n(t)$, see Figure 2.11(c). The end times are estimated on the basis of unprocessed absolute velocity traces, see Figure 2.11(d).

- The duration of strong motion is longer for the signals recorded at the upper floors

[3] Due to the motion propagation the ground floor is expected to respond first while the upper floors are expected to follow, $t_1(ground\,floor) < t_1(first\,floor) < t_1(second\,floor) < t_1(roof)$. At time t_1 the acceleration is very small ($< 0.01g$) but soon after its amplitude starts to increase significantly. The system undergoes free vibration and builds its maximum response during the first cycle of motion. Therefore, after initiation of motion, the rate of change of the cumulative squared acceleration becomes essentially higher than the selected threshold ε_1.

[4] The ground floor stops moving first, while the upper floors continue to vibrate until the motion is damped out. Hence $t_2(ground\,floor) \leq t_2(upper\,floors)$. After the motion ceases a linear trend is observed in the velocity trace, i.e. after time t_2 the distance d_ν tends to zero.

Table 2.1: Start, end times and duration of the main events recorded during free vibration test 9 in the Augusta superstructure. First column: acceleration record considered. Second and third columns: Start and end times t_1 and t_2 of the main event, evaluated according to the procedure presented in section 2.3. Fourth column: duration of strong motion, $t_d = t_2 - t_1$. Fifth and sixth columns: thresholds ε_1 and ε_ν used for the identification of times t_1 and t_2.

Acceleration record	$t_1[sec]$	$t_2[sec]$	$t_d = t_2 - t_1[sec]$	$\varepsilon_1[\%]$	$\varepsilon_\nu[\%]$
ground floor	1014.087	1018.000	3.913	1.0	0.10
first floor	1014.092	1018.049	3.957	2.0	0.10
second floor	1014.109	1018.170	4.061	10.0	0.20
roof	1014.122	1018.220	4.098	12.0	0.20

of the isolated building. This result is plausible; the isolation stops moving while the superstructure continues to vibrate, until the response is damped out.

- The time delays of the recorded signals can be used for the estimation of the wave propagation velocity ν_w. For instance $\nu_w = 4.25m/(1014.092-1014.087)sec = 4.25m/0.005sec = 850m/sec$ or $\nu_w = 10.25m/(1014.122 - 1014.087)sec = 10.25m/0.035sec = 292m/sec$ considering the propagation delays of the first floor and roof signal respectively, where $4.25m$ and $10.25m$ are the heights of the first floor and the superstructure. The resulting propagation velocities are small and very different to each other, with the larger velocity to seem more reliable. However, the subjectivity in the selection of the starting point of motion does not allow any better estimate of ν_w. It should be also mentionned that the position of the recording instruments might have affected the results (see Figure 1.7, section 1.2).

The adjusted absolute accelerations for the Augusta superstructure are shown in Figures 2.12 (a) to (d). The ground floor acceleration is shown again for completeness. The adjusted absolute velocities and displacements are shown in Figures 2.13(a) and (b). The total velocity and displacement response is very similar for all floors; implying that the superstructure behaves like a rigid body during dynamic motion. In fact, seismic isolation mitigates the

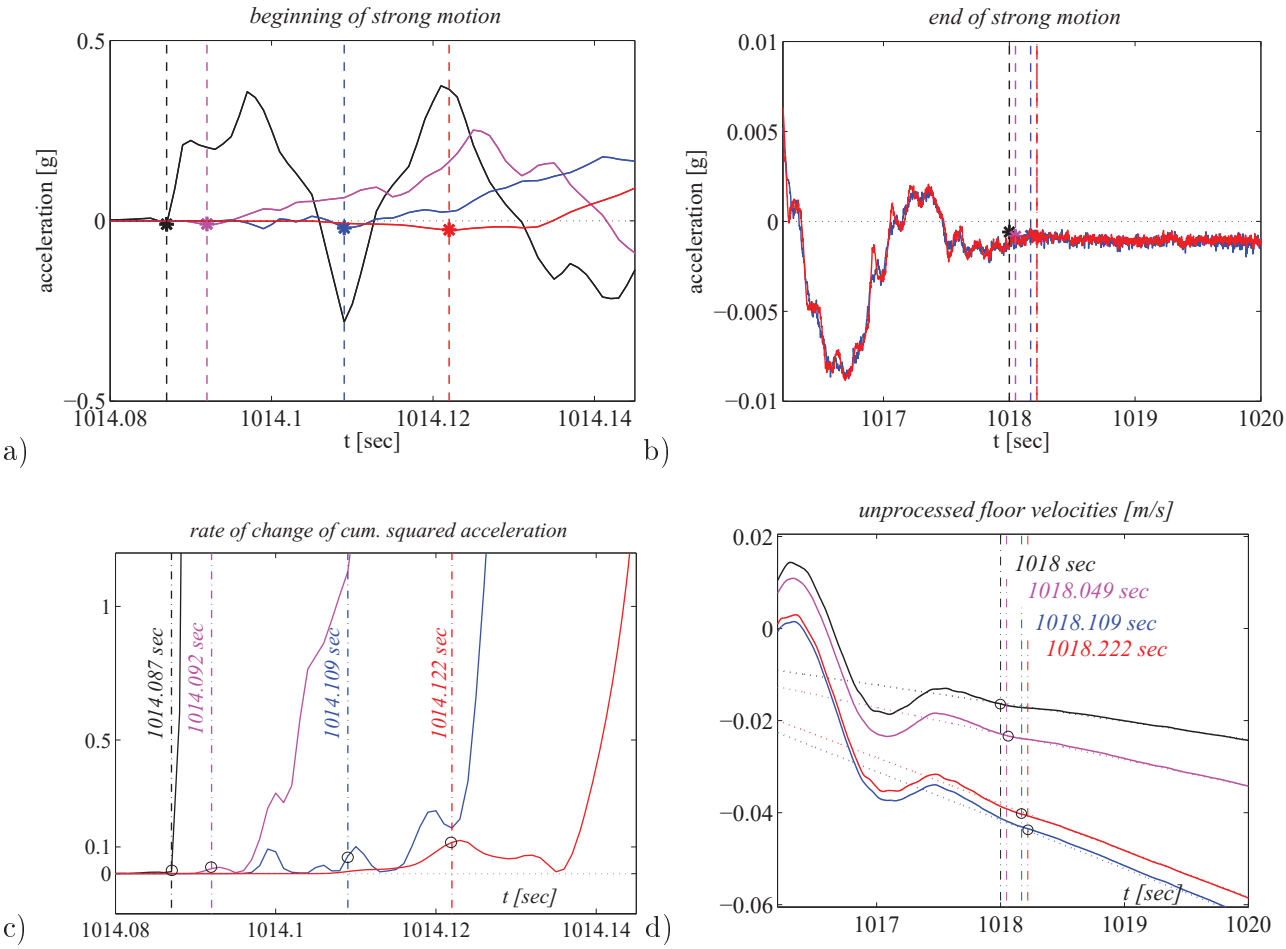

Figure 2.11: Delay of motion as the waveform travels to the upper floors of the Augusta isolated structure. Start and end times for the ground floor (black line), first floor (pink line), second floor (blue line) and roof(red line) acceleration records; sub-plots a) and b). Dashed lines are plotted at the times when the motion starts and ceases. c) Rate of change of the normalized cumulative squared accelerations . The motion starts when the $dCSA_n(t)/dt$ becomes greater than the threshold ε_1, see Table 2.1. d)Unprocessed absolute velocities, evaluated as the integral of the corresponding raw accelerations. Dotted lines indicate the linear velocity trend present due to noise. The motion stops when the velocity waveform starts to fit the linear trend.

risk by elongating the fundamental period of the structure and hence reducing the forces induced in the system and the vibrations of the superstructure.

Table 2.2 shows the peak superstructure response in terms of absolute floor accelerations,

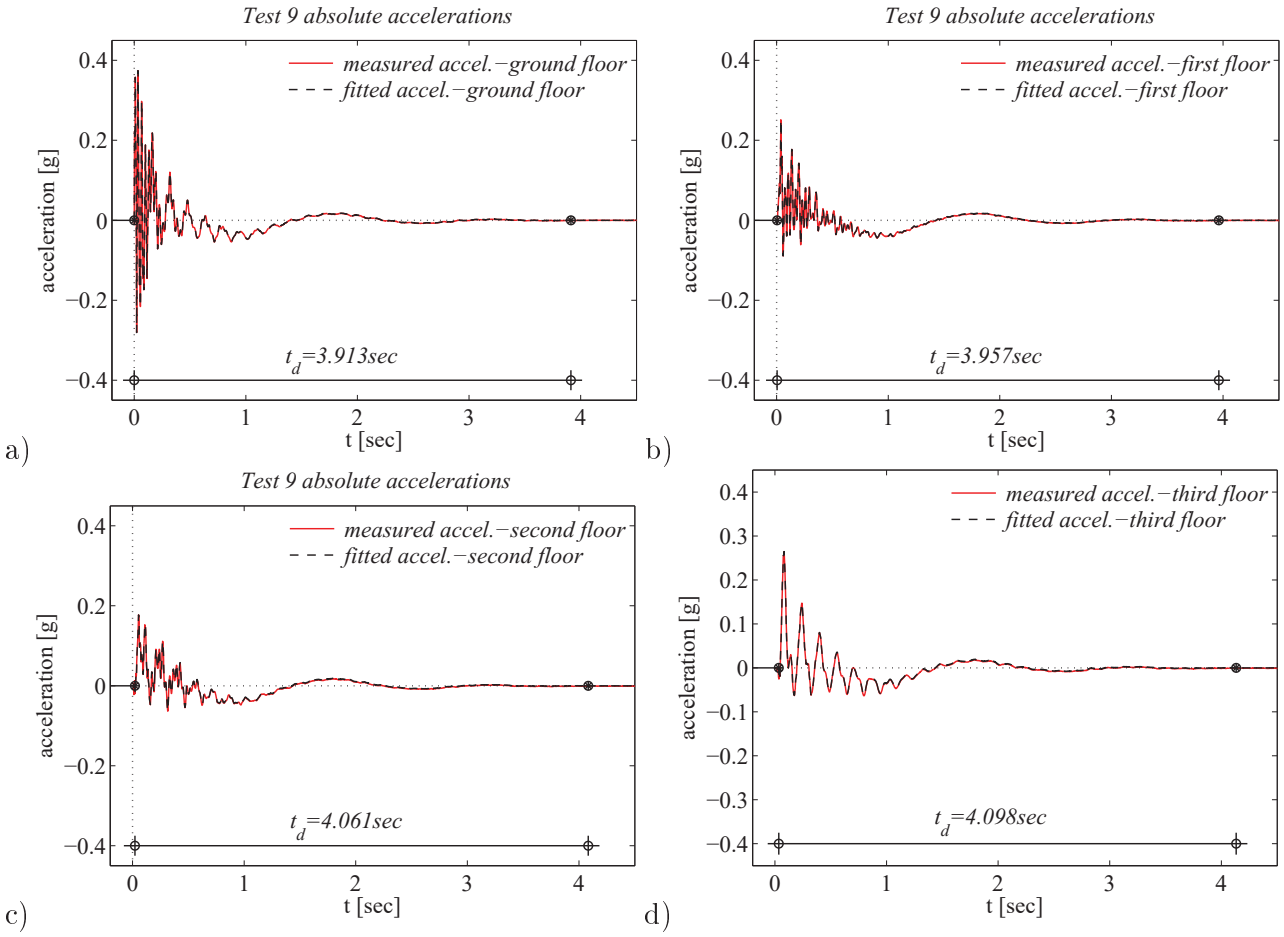

Figure 2.12: Absolute acceleration response of the Augusta superstructure for test 9: ground floor, first floor, second floor and roof response; sub-plots a), b), c), d) respectively. The raw signals are represented by red lines while the baseline fitted signals are shown by black lines. The times when motion starts and ceases are indicated by black markers. The duration of strong motion is also given.

velocities and displacements. The peak velocity and displacement response is similar for all floors; this fact enforces the belief that the superstructure responded as rigid body during the dynamic motion. The differences in the peak accelerations can be attributed to a wave propagation phenomenon. This phenomenon may be responsible for the high frequency content of the response and the spikes observed in the ground floor and first floor records, see Figures 2.12. It is important to highlight that peak accelerations can be read directly

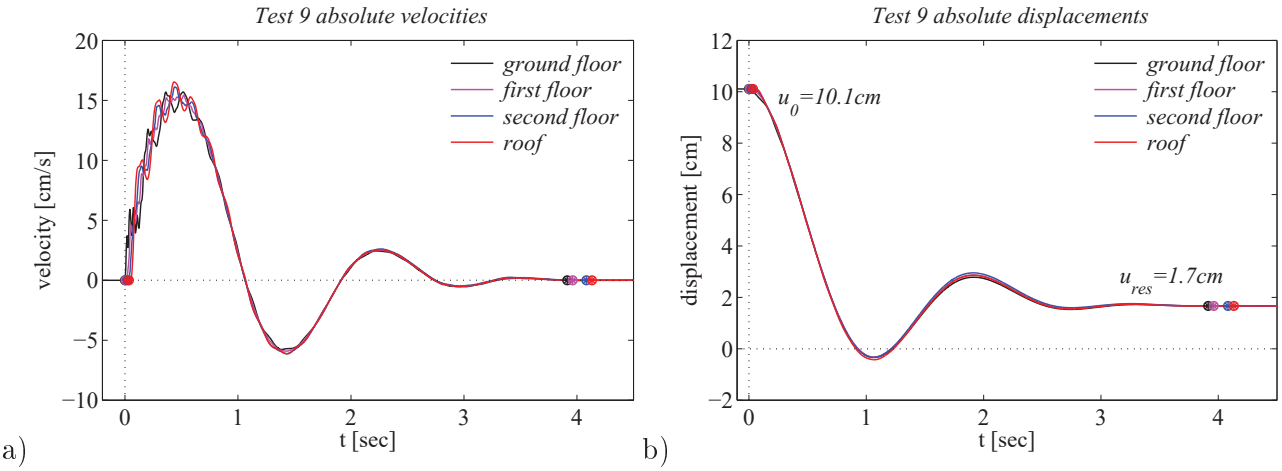

Figure 2.13: Adjusted absolute velocities and displacements at the ground floor, first floor, second floor and roof of the Augusta building during test 9; sub-plots a) and b) respectively. The times when motion starts and ceases are indicated by markers. The motion starts somewhat later and ends later at the upper floors.

Table 2.2: Peak superstructure response in terms of absolute acceleration, velocity and displacement under free vibration motion (test 9, $u_0 = 10.1cm$). First column: component considered. Second column: peak absolute acceleration response. Third column: peak absolute velocity response. Fourth column: peak absolute displacement response. The strong motion duration is given in the fifth column for completeness.

	Peak absolute response			
component	*accel.*$[g]$	*vel.*$[cm/sec]$	*displ.*$[cm]$	$t_d[sec]$
ground floor	0.374	15.70	10.11	3.913
first floor	0.252	15.43	10.11	3.957
second floor	0.177	16.12	10.11	4.061
roof	0.265	16.53	10.11	4.098

from the recordings, while peak floor velocities and displacements can be retrieved only after signal processing. The estimation of reliable velocity and the displacement traces with little computational effort is a major advantage of the baseline fitting scheme developed.

2.6 Estimation of the relative superstructure response under test 9

2.6.1 Estimation of the relative superstructure response from the processed absolute response

The adjusted absolute accelerations, velocities and displacements can be used to produce the relative, with respect to the base, accelerations, velocities and displacements and furthermore the inter-story drifts. The relative to the base response is evaluated according to the following formula:

$$r_i^{rel}(t) = r_i^{abs}(t) - r_g^{abs}(t) \tag{2.11}$$

where *'r(t)'* stands for the upper floor displacement, velocity and/or acceleration history. The superscript *'rel'* indicates the relative, with respect to the base, response; the superscript *'abs'* indicates the absolute response; the subscript *'i'* indicates the floor number ($i = 1, 2, 3$) and the subscript *'g'* indicates the base.

The relative accelerations for the Augusta superstructure under test 9 are shown in Figures 2.14 (a) to (c). The baseline fitted relative accelerations are practically on the top of the raw signals, indicating that the extracted noise is of a very small amplitude. The relative floor velocities and displacements are shown in Figures 2.15(a) and (b). The relative response is evaluated from the adjusted absolute response, see Figures 2.12 and 2.13, using Eq. 2.11.

Table 2.3 shows the peak superstructure response in terms of relative floor accelerations, velocities and displacements. Observation of Figures 2.14 and 2.15 and Table 2.3 shows that the motion amplitude increases as we move towards the upper floors; the relative response of the first floor in terms of acceleration/velocity/displacement is smaller in amplitude than the relative response of the second floor and so on. This result is in line with the theory; for such a small event the superstructure is expected to respond in the linear range and

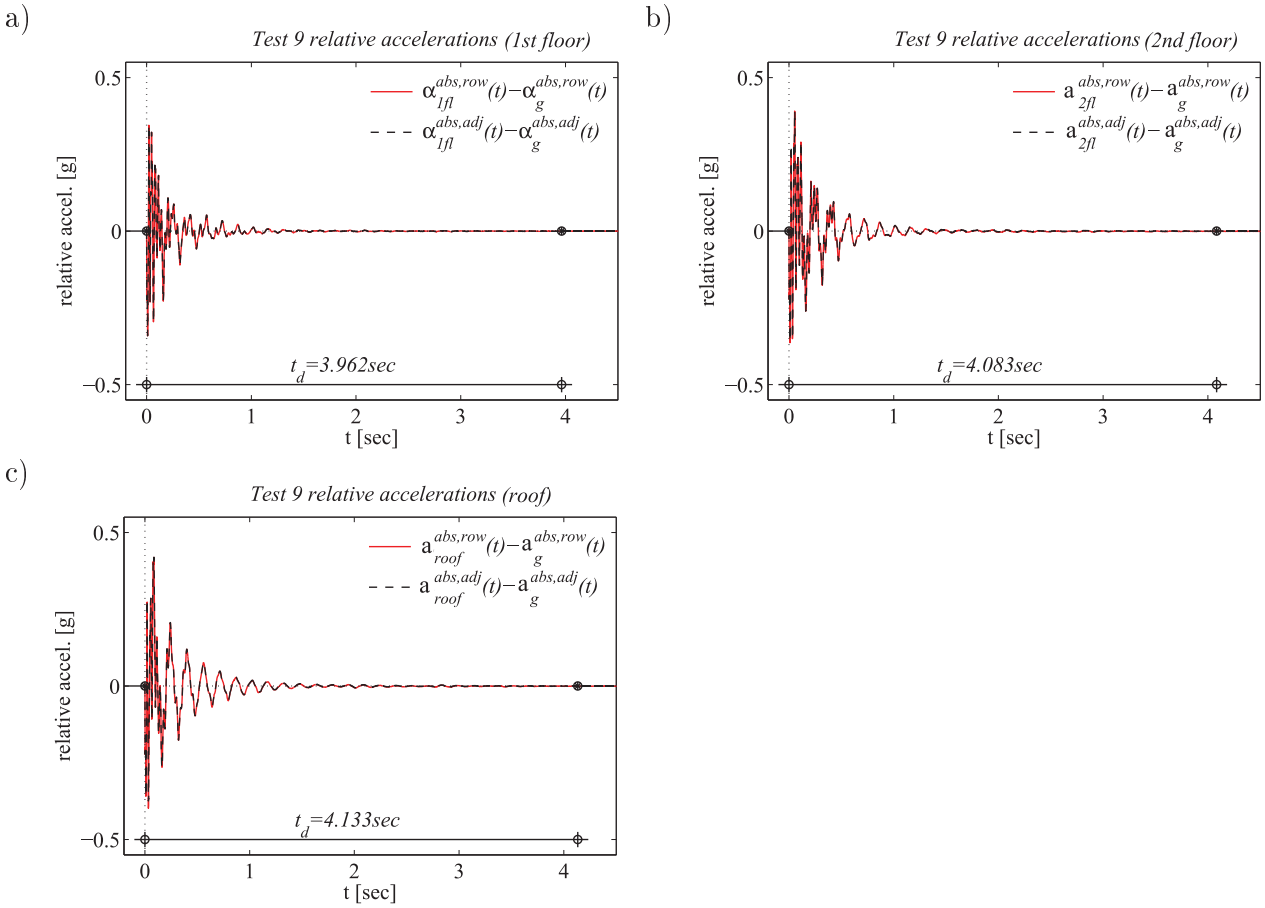

Figure 2.14: Relative accelerations at the Augusta superstructure under test 9 at first floor, second floor and roof; sub-plots a), b), c) respectively. The relative response is evaluated from the adjusted absolute response, see Figures 2.12, using Eq. 2.11. The raw signals are represented by red lines while the baseline fitted signals are shown by black lines. The times when motion starts and ceases are indicated by black markers. The motion duration is longer at the upper floors.

following the first mode. However classical modal analysis is not applicable in the case of isolated systems, since the damping matrix is non-classical. Non classical damping results to coupling of modes. The presence of a frequency other than the structural frequency is clear at the velocity and displacement traces shown in Figure 2.15. The zero reference velocity line seems to be distorted by a long period wave. This becomes more clear once the velocity is integrated to produce displacements. Two periods can be read from the displacement

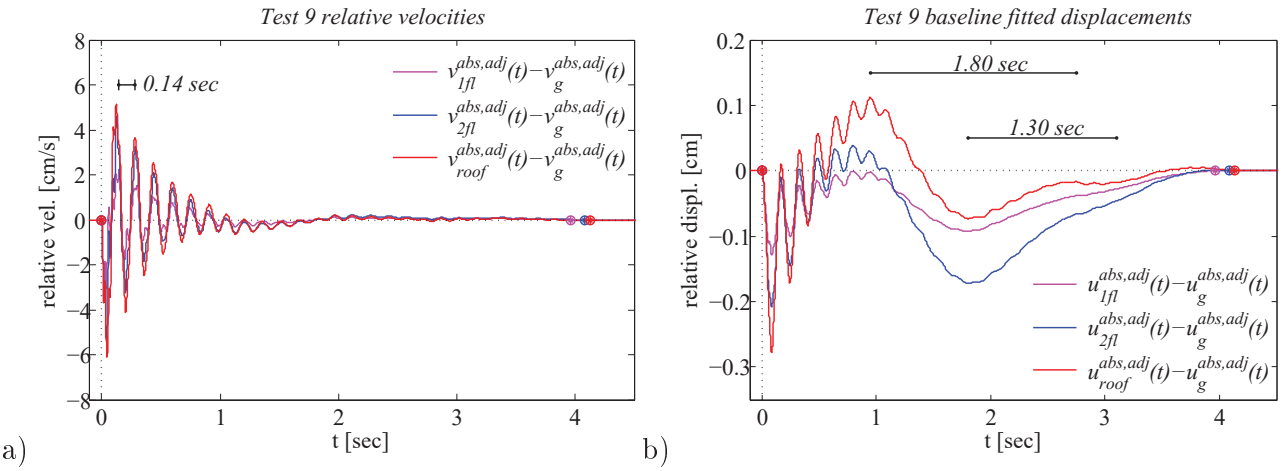

a) b)

Figure 2.15: Relative velocities and displacements at the Augusta superstructure under test 9; sub-plots a) and b) respectively. The relative response is evaluated from the adjusted absolute response, see Figures 2.13, using Eq. 2.11. The times when motion starts and ceases are indicated by markers. The relative motion starts at the same time at all floors, however it ends somewhat later at the upper floors.

Table 2.3: Peak relative superstructure response for the free vibration test 9 ($u_0 = 10.1cm$). The relative response is evaluated from the adjusted absolute response using Eq. 2.11. First column: component considered. Second column: peak relative acceleration response. Third column: peak relative velocity response. Fourth column: peak relative displacement response (within brackets the same displacement after application of a low cut filter with corner frequency $f_c = 0.30Hz$). Fifth column: motion duration.

Test 9: peak relative to the base response

floor	*acceleration*$[g]$	*velocity*$[cm/sec]$	*displacement*$[cm]$	$t_d[sec]$
first	0.345	3.384	0.129 (0.125)	3.962
second	0.391	5.348	0.208 (0.206)	4.083
third	0.420	6.075	0.278 (0.283)	4.133

diagram : a diminishing long period that can be attributed to the isolation system and a shorter period, observed easily also in the velocity trace, that can be attributed to the superstructure.

A proper simulation of the system response would require the evaluation of complex modes. The real motion deriving from the combination of one mode and its conjugate does

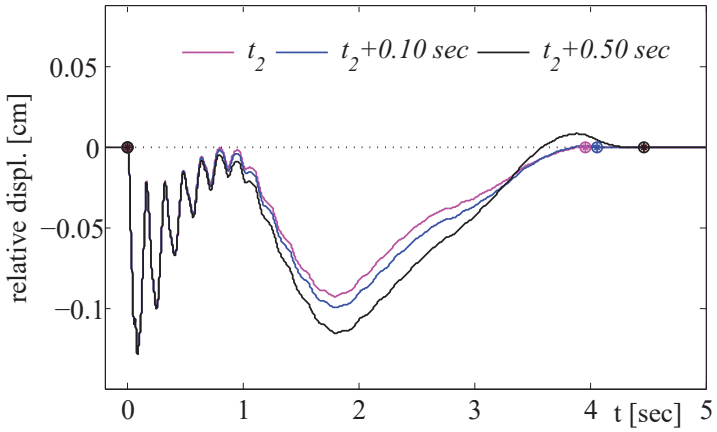

Figure 2.16: Investigation of the effect of motion duration on the first floor relative displacement under test 9. The start time of relative motion is equal to $t_1 = 0$. Three end times are considered: $t_2 = 3.962sec$ that is the end time of the absolute first floor acceleration motion, $t_2 + 0.1sec = 4.062sec$ and $t_2 + 0.5sec = 4.462sec$. The effect of the motion duration on the generated displacements becomes obvious after the $1sec$ of motion.

not preserve the shape in time. In fact, the relative floor displacements seem reach their maximum value at the same instant; however they cross zero at different times, see Figure 2.15 (b). Although the obtained relative response seems to be reasonable and justified by the theory of non classically damped systems, special concerns arise for the reliability of the obtained response, especially relative displacements. As it has been mentioned before, low amplitude records are suspectible for low signal to noise ratios. Moreover, low frequency noise is amplified with integration. For this reason, the need for further correction of the relative displacements is investigated.

Figure 2.16 shows the effect of time duration on the relative displacement of the first floor, which was evaluated as the difference between absolute first floor and ground floor displacements. Small changes in the time duration of the relative motion have drastic impact on the shape of the generated displacements after $1sec$ of motion. Figure 2.17 (b) shows the superstructure displacements after application of a low cut filter, with corner

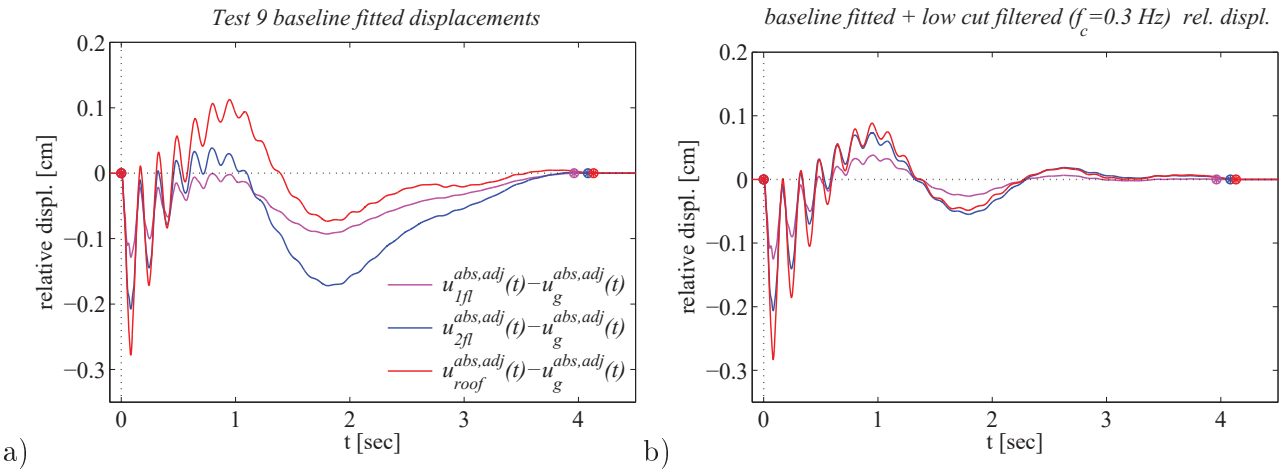

Figure 2.17: Investigation of the effect of low cut filtering on the relative displacements at the Augusta superstructure during test 9. (a) Relative displacements evaluated from the adjusted absolute response using Eq. 2.11. (b) Relative displacements of sub-plot (a) after application of a low cut filter. The corner frequency is chosen equal to $f_c = 0.30Hz$.

frequency of $f_c = 0.30Hz$. The filtering was performed in MATLAB using a digital filter with finite-duration impulse response (FIR) [55]. $f_c = 0.30Hz$ is a reasonable choice for the corner frequency since it is distant enough from the lowest frequency of interest; for the Augusta isolated building the fundamental frequency is greater than $0.50Hz(1.95sec)$. The fundamental frequency can be read from the FAS of the acceleration records (see Chapter 1, Figure 1.17). The filtered response seems more familiar since it resembles the response of classically damped systems responding in their linear range.

Filtering causes distortion of the signal versus the very end of motion [49]. The ringing of the filtered motion occurs because of the change of the signal from a non zero to a zero value at time t_d. The violation of the end conditions caused by filtering is adjusted by re-fitting the displacements according to the baseline scheme proposed herein. The practice of filtering a posteriori the relative displacements results to incompatible relative response data, i.e. double integration of the relative accelerations does no longer provide the desired relative displacements.

Unfortunately, the floor displacements were not measured during the tests; hence, one

Table 2.4: Start, end times and duration of the relative floor accelerations for free vibration test 9. First column: acceleration record considered. Second and third columns: Start and end times t_1 and t_2 of the main event, evaluated according to the procedure presented in section 2.3. Fourth column: duration of strong motion, $t_d = t_2 - t_1$. The relative motion duration as evaluated previously, on the basis of the fitted absolute response, is given within brackets. Fifth and sixth columns: thresholds ε_1 and ε_v used for the identification of times t_1 and t_2.

component	$t_1[sec]$	$t_2[sec]$	$t_d = t_2 - t_1[sec]$	$\varepsilon_1[\%]$	$\varepsilon_v[\%]$
first floor	1014.087	1018.150	4.063 (3.962)	2	0.60
second floor	1014.087	1018.170	4.083 (4.083)	2	1.20
roof	1014.087	1018.210	4.123 (4.133)	2	0.20

cannot conclude that the displacements of Figure 2.17 (a) are more reliable than the displacements of Figure 2.17 (b). However, the peak relative response at the time interval $[0, 1]sec$, where the motion is still relatively strong, is not influenced by filtering or the integration interval; implying that the peak relative response can be recovered with confidence.

2.6.2 Estimation of the relative superstructure response from the processing of the raw relative motion

In the previous paragraph the relative superstructure response was generated indirectly, from the adjusted absolute response, applying Eq. 2.11. Herein the relative response is evaluated directly, from the baseline fitting of the raw relative records. Table 2.4 provides information on the start and end times, t_1 and t_2, and the duration, t_d, of the relative acceleration records for test 9. The start times t_1 are estimated from the corresponding cumulative squared acceleration diagrams, see section 2.3. The motion starts when the time derivative of $CSA_n(t)$ becomes greater than the selected threshold ε_1, that is equal to 2% for all the signals considered. The end times t_2 are defined on the basis of the unprocessed relative velocities. The raw signals are integrated to provide the unprocessed velocities and straight lines are fitted in the interval $[1020, 1030]$, where the velocities show a clear linear

trend. The lines are extended to time t_1. The distance between each velocity curve and the corresponding linear velocity trend is calculated and normalized to the peak relative velocity. The motion is considered to have stopped when this distance, d_v, becomes smaller than a threshold ε_ν. The chosen values for ε_ν vary from $0.20 - 1.20\%$.

The results of Table 2.4 show that the relative motion starts simultaneously at time $t_1 = 1014.087sec$ at all floors. $t_1 = 1014.087sec$ is the time when the base starts moving, see Table 2.1. The fact that the relative motion results initiating at the same time at all floors can be attributed to the way the raw relative motion is evaluated. The raw relative signals are evaluated subtracting the ground floor record from the upper floor records, therefore the effect of the ground floor record is felt when evaluating t_1. The vibration stops at $t_2 = 1018.15sec$ at the first floor and somewhat later at the upper floors. As a result, the duration of strong motion is longer for the relative signals of the upper floors of the isolated building. The duration of the relative motion is given in the fourth column of Table 2.4. In the same column and within brackets, the duration of the relative motion as evaluated from the absolute motions, is provided. The two methods provide very similar motion durations t_d. One result cannot be preferred over the other since, as seen in the previous paragraphs, there is a lot of subjectivity in the selection of the thresholds and the determination of the end times of strong motion. Herein, the thresholds for the estimation of the end times were selected small enough to reassure conservative estimates of t_2.

The adjusted relative accelerations and velocities for the Augusta superstructure are shown in Figures 2.18, left plots and right plots respectively. Figures 2.18 demonstrate that the relative accelerations and velocities are identical, whichever way calculated. The baseline fitted relative response (dashed lines) is plotted together with the relative response evaluated from the fitted absolute response (continuous lines). The adjusted relative displacements are shown in Figures 2.19. Figures 2.19 show that the two methods lead to the same relative displacements in the beginning of motion $(0, 1)sec$; however after $1sec$ of motion they provide different results. While the differences are small for the displacements of the first and second floor, they are significant for the roof displacements. This is probably due to the different time

durations considered by the two methods and the accumulation of low frequency noise with numerical integration. Another interesting observation is that once the relative displacements are low cut filtered at $f_c = 0.30Hz$ they become essentially the same, see Figure 2.19. This result confirms the need for further fitting (filtering) of the displacements.

Figure 2.20 shows the inter-story drift histories for the Augusta free vibration test 9, as evaluated from the adjusted absolute response and the adjusted relative response; sub-plots a) and b) respectively. The peak drift values occur in the time range $(0, 1)sec$ and are the same, whichever the method of evaluation. As expected, the drifts are greater at the lower stories, that are generally subject to greater shear forces.

It should be noted that the maximum drift is 0.03%, substantially less than the 0.33% limit prescribed in the national specifications under the damage limit state [45]. The experiments were conducted on a finished structure; hence they were performed at low amplitudes to ensure that non-structural and structural components were not damaged during testing.

Tables 2.5 to 2.7 show the peak relative to the base response, as estimated from the processing of the raw relative signals. The corresponding peak response obtained from the processing of the absolute signals is also reported in brackets. It can be seen how the two methods used for the recovery of the relative response provide essentially the same peak floor accelerations, velocities, displacements and drifts. This results enforces the reliability of the method proposed for the processing of raw absolute and relative acceleration signals and the generation of meaningful velocities, displacements and drifts.

Table 2.5: Peak relative to the base superstructure response for the free vibration test 9 ($u_0 = 10.1cm$). The relative response is evaluated directly from the baseline fitting of the raw relative motion. The corresponding peak response evaluated from the fitted absolute response is given within brackets. First column: component considered. Second column: peak relative acceleration response. Third column: peak relative velocity response. Fourth column: motion duration.

	peak relative response		
floor	*acceleration*$[g]$	*velocity*$[cm/sec]$	$t_d[sec]$
first	0.345 (0.345)	3.402 (3.384)	4.063 (3.962)
second	0.391 (0.391)	5.396 (5.348)	4.083 (4.083)
third	0.420 (0.420)	6.287 (6.075)	4.123 (4.133)

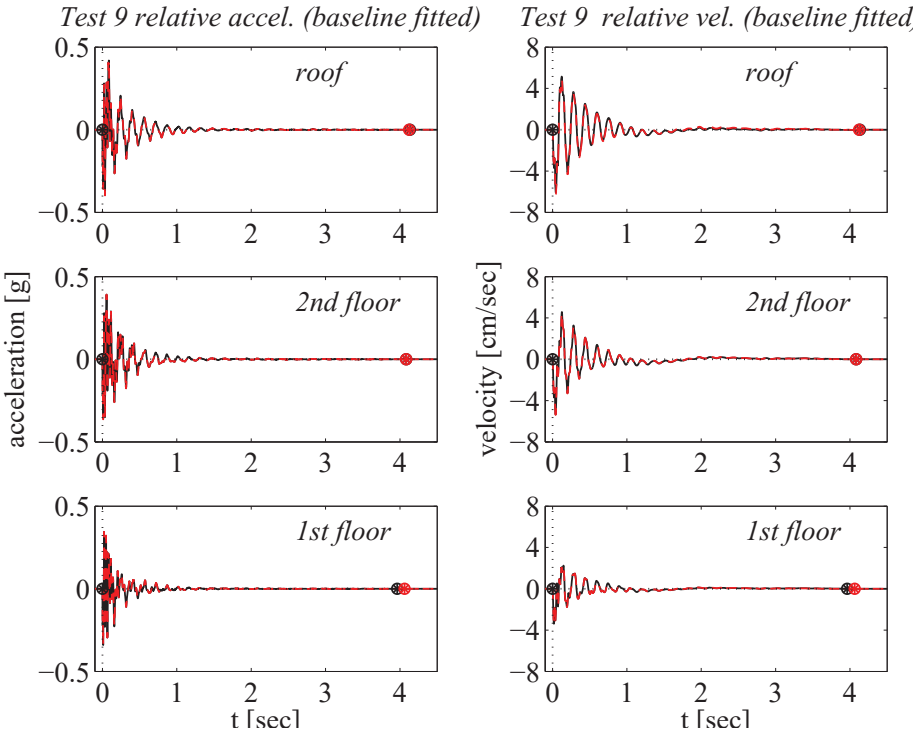

Figure 2.18: Relative floor accelerations and velocities for the Augusta free vibration test 9, as evaluated from the adjusted absolute response (continuous black lines) and the adjusted relative response (dashed red lines); left sub-plots and right sub-plots respectively. The relative response was fitted to zero at the beginning and end of motion, since the superstructure was expected to respond in the linear range under such a small excitation ($u_0 = 10.11cm$).

Table 2.6: Peak relative to the base displacements for the free vibration test 9 ($u_0 = 10.1cm$). The relative response is evaluated directly from the baseline fitting of the raw relative motion. The corresponding peak response evaluated from the fitted absolute response is given within brackets. First column: component considered. Second column: peak relative displacement response. Third column: peak relative displacement after application of a low cut filter with $f_c = 0.30Hz$.

	peak relative response	
floor	*displacement*[*cm*]	*filtered displacement*[*cm*]
first	0.130 (0.129)	0.126 (0.125)
second	0.211 (0.208)	0.207 (0.206)
third	0.290 (0.278)	0.281 (0.283)

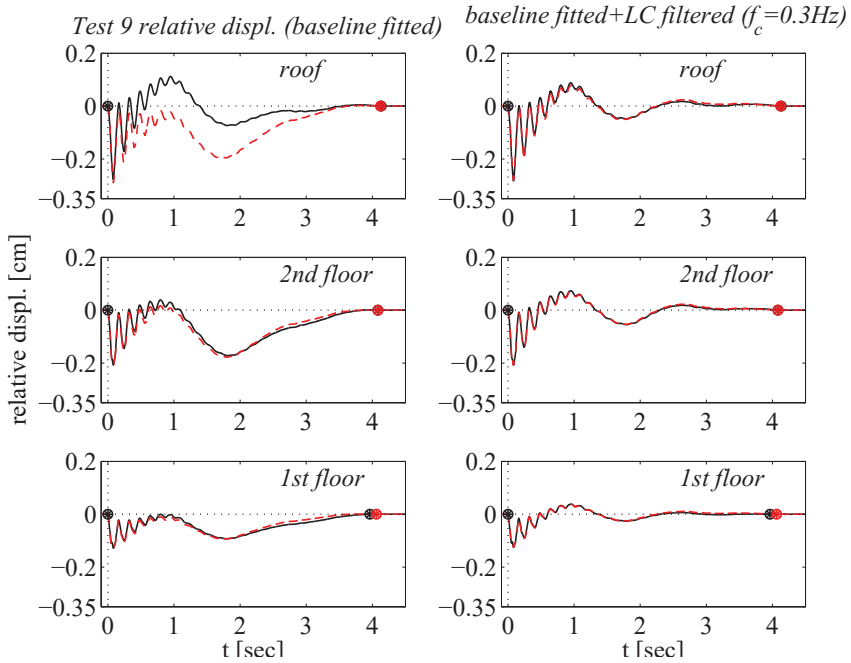

Figure 2.19: Relative floor displacement histories for the Augusta free vibration test 9, as evaluated from the adjusted absolute response (continuous black lines) and the adjusted relative response (dashed red lines); left sub-plots. The relative displacements were fitted to zero at the beginning and end of motion, since the superstructure was expected to respond in the linear range under such a small excitation ($u_0 = 10.11cm$). The right sub-plots represent the same displacements after implementation of a high pass filter with corner frequency $f_c = 0.30Hz$.

Table 2.7: Peak inter-story drifts for the free vibration test 9 ($u_0 = 10.1cm$). The corresponding peak drifts evaluated from the fitted absolute response are given within brackets. First column: component considered. Second column: peak inter-story drifts. Thirf column: peak inter-story drifts evaluated from the filtered relative displacements.

	peak relative response	
$floor$	$drift[10^{-3}]$	$filtered\,drift[\cdot 10^{-3}]$
$first$	0.306 (0.302)	0.295 (0.295)
$second$	0.260 (0.249)	0.255 (0.254)
$third$	0.242 (0.305)	0.226 (0.236)

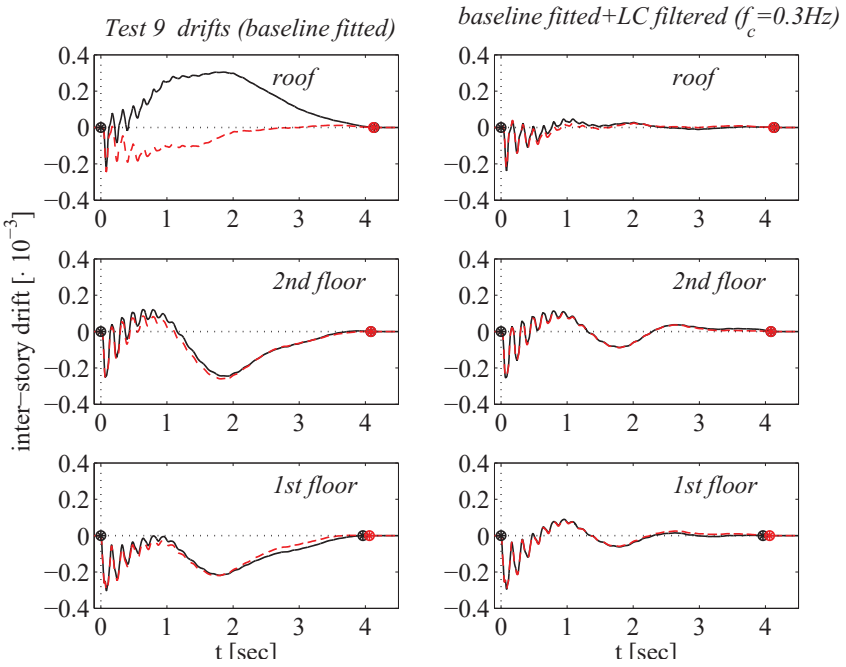

Figure 2.20: Inter-story drift histories for the Augusta free vibration test 9, as evaluated from the adjusted absolute response (continuous black lines) and the adjusted relative response (dashed red lines). The left sub-plots represent the drifts evaluated from the baseline fitted relative displacements, see Figure 2.19 left sub-plots, while the right sub-plots represent the drifts evaluated from the filtered relative displacements, see Figure 2.19 right sub-plots. The drifts are zero at the beginning and end of motion.

2.7 Signal processing for the full set of the available free vibration records

The baseline fitting scheme implemented in the previous paragraphs for the adjustment of the absolute and relative response observed in the Augusta building during test 9, is repeated for the adjustment of the full set of available records [5]. Due to space limitations, the baseline fitted response for the full set of dynamic tests (absolute and relative accelerations/velocities/displacements and inter-story drifts) and the parameters needed for the implementation of signal processing scheme (thresholds, intervals of strong motion, etc.) are not shown herein but instead in Appendix A.

Table 2.8 provides basic information on the generated, baseline fitted, displacements such as the initial and residual displacements u_0 and u_{res}, the duration of strong motion t_d (evaluated according to section 2.3) and the distance between experimental and generated displacement curves e^2 (evaluated according to Eq. 2.10). Figures 2.21 and 2.22 show the matching between measured and generated displacements.

Figures 2.23 show the peak absolute response of the Augusta building during tests 1-3-4-5-6-8-9-10, in terms of floor accelerations, velocities and displacements. Figures 2.24 show the peak relative displacement response and the peak inter-story drifts of the Augusta superstructure during the performed tests. The illustrated relative displacements, were first baseline fitted and then high passed filtered with a FIR filter of corner frequency that varied from $0.25Hz$ (test 1) to $0.30Hz$ (tests 3-4-5-6-8-9-10). The processing of the full set of raw relative motions showed that the filtering of the relative displacements is essential for the generation of meaningful responses, see Appendix A. Raw relative motions are of small amplitude and are suspectible of low signal-to-noise ratios; therefore there is the need for the removal of the low frequency noise even after the baseline adjustment, since the noise

[5] These would be the longitudinal records of the base, first, second and roof floor, namely the acceleration components obtained from the Augusta free vibration tests 1,3,4,5,6,8,9 and 10: components GFL-25X-TESTNUMBER, 1FL-25X-TESTNUMBER, 2FL-25X-TESTNUMBER, 3FL-X-TESTNUMBER

Table 2.8: Information on the processed ground floor displacements for all the dynamic tests performed on the Augusta building. First column: test number. Second and third columns: Initial and residual displacements u_0 and u_{res} . Fourth column: duration of strong motion, t_d, as evaluated according to section 2.3. Fifth column: distance between experimental and generated displacement curves, evaluated according to Eq. 2.10. The tests are presented in order of increasing initial displacement.

Dynamic test	$u_0[cm]$	$u_{res}[cm]$	$t_d[sec]$	$e^2[\%]$
1	5.8	1.5	2.205	0.04
3	6.8	0.6	2.867	0.04
4	6.8	1.3	2.880	0.10
10	10.0	1.8	3.961	0.03
9	10.1	1.7	3.913	0.06
8	10.3	0.8	4.035	0.09
5	10.9	1.7	3.228	0.05
6	11.7	1.9	4.023	0.01

can be amplified significantly at any stage of integration.

Observation of Figures 2.21 to 2.24 and Table 2.8 show that:

- The signal processing procedure proposed herein performs very satisfactorily for the whole set of experimental data, providing a very good match between predicted and measured displacements.
- The method can account for initial and end conditions, reassuring that the acceleration and velocity is zero at the beginning and end of motion. Moreover, it can recover permanent displacements, given that the latter have been measured.
- Although there is some subjectivity involved in the estimation of the times when the motion starts and ceases, the selection of reasonable time intervals for the strong motion provides meaningful results (velocities, displacements, drifts) that are in line with theoretical expectations.
- Tests with higher initial displacement have longer duration; more time is needed for the damping of stronger motions.

- Tests with higher energy input produce greater response, i.e. absolute and relative accelerations/velocities/ displacements and inter-story drifts.

- The absolute floor response, in terms of velocities and displacements, varies very little from floor to floor, implying almost a rigid superstructure response. In fact seismic isolation is a risk mitigation design technique that protects the structure from vibrations.

- The absolute floor accelerations are quite different; with the peak ground accelerations being always greater than the upper floor accelerations. The spikes observed in all the ground floor records could be attributed to a wave propagation phenomenon; as soon as the building is released the wave travels from the ground floor to the roof while attenuating with distance At the beginning of the test responds only the mass of the ground floor..

- Residual displacements vary from $0.60 - 1.9cm$. The magnitude of residual displacements is independent of the magnitude of the initial displacement. Tests with higher u_0 do not necessarily lead to higher residual displacements u_{res}.

- Tests 3 and 8 followed two unsuccessful release tests (tests 2 and 7) and there is evidence that the building was not recentered before repetition of the tests. This explains why tests 3 and 8 provide response which are not that similar to the responses obtained from tests of similar strain amplitude.

- The relative superstructure response is small but not negligible. The superstructure response in terms of relative to the base displacements resembles the first mode response of multi-storey buildings responding in their linear range. In fact, for such a small input the superstructure is expected to respond in the linear range. The relative displacements are higher at the top floors, while the story drifts are higher at the base floor (where the shear is more important).

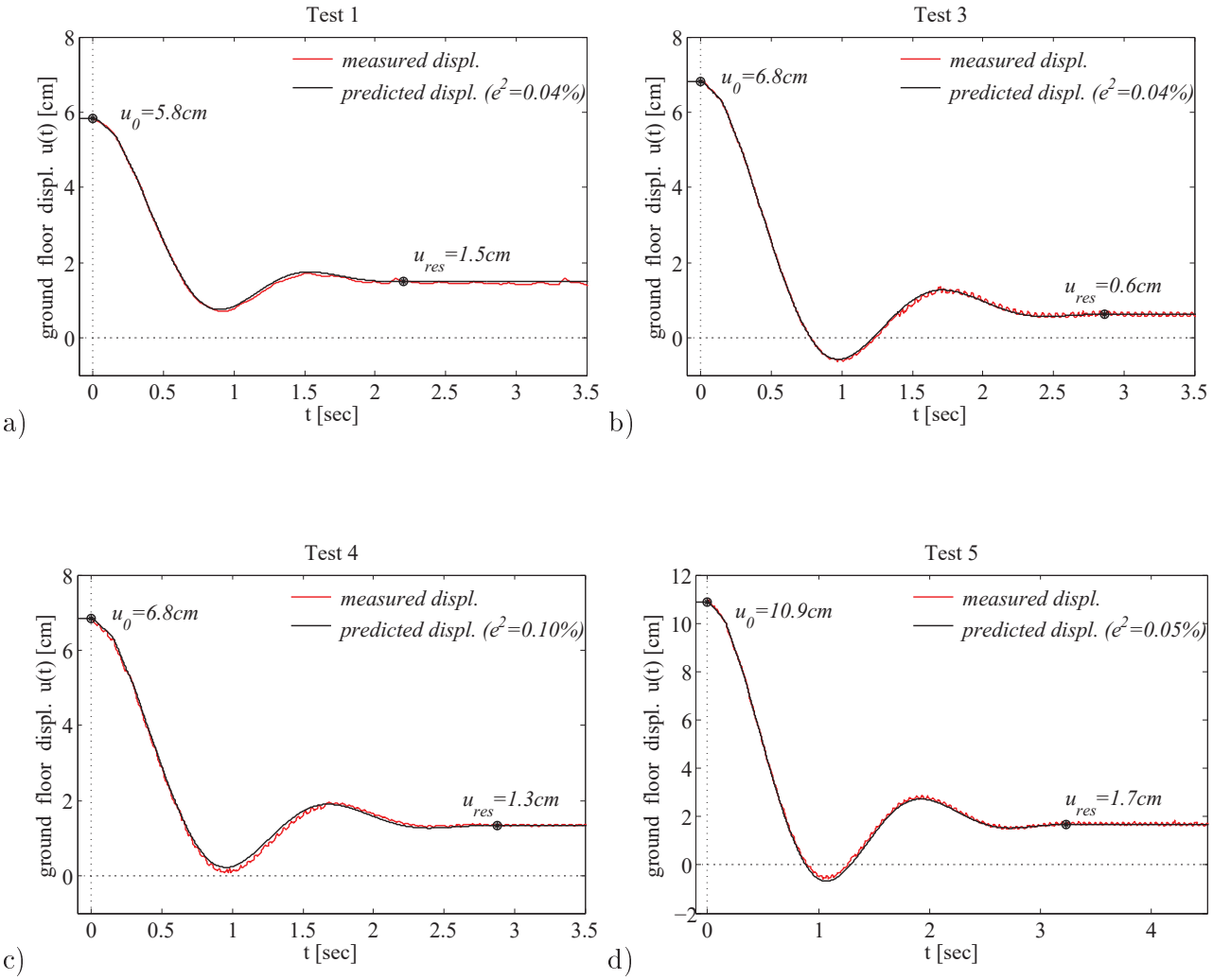

Figure 2.21: Comparison of measured and predicted displacements for the Augusta free vibration tests 1,3,4 and 5, sub-plots (a) to (d) respectively. All plots have the same scale to facilitate comparisons. The initial and residual displacements, u_0, u_{res}, are also provided in the figures. The distance between the two displacement traces, e^2, in the time range of the main event is given in the legend. e^2 is calculated from Eq. 2.10.

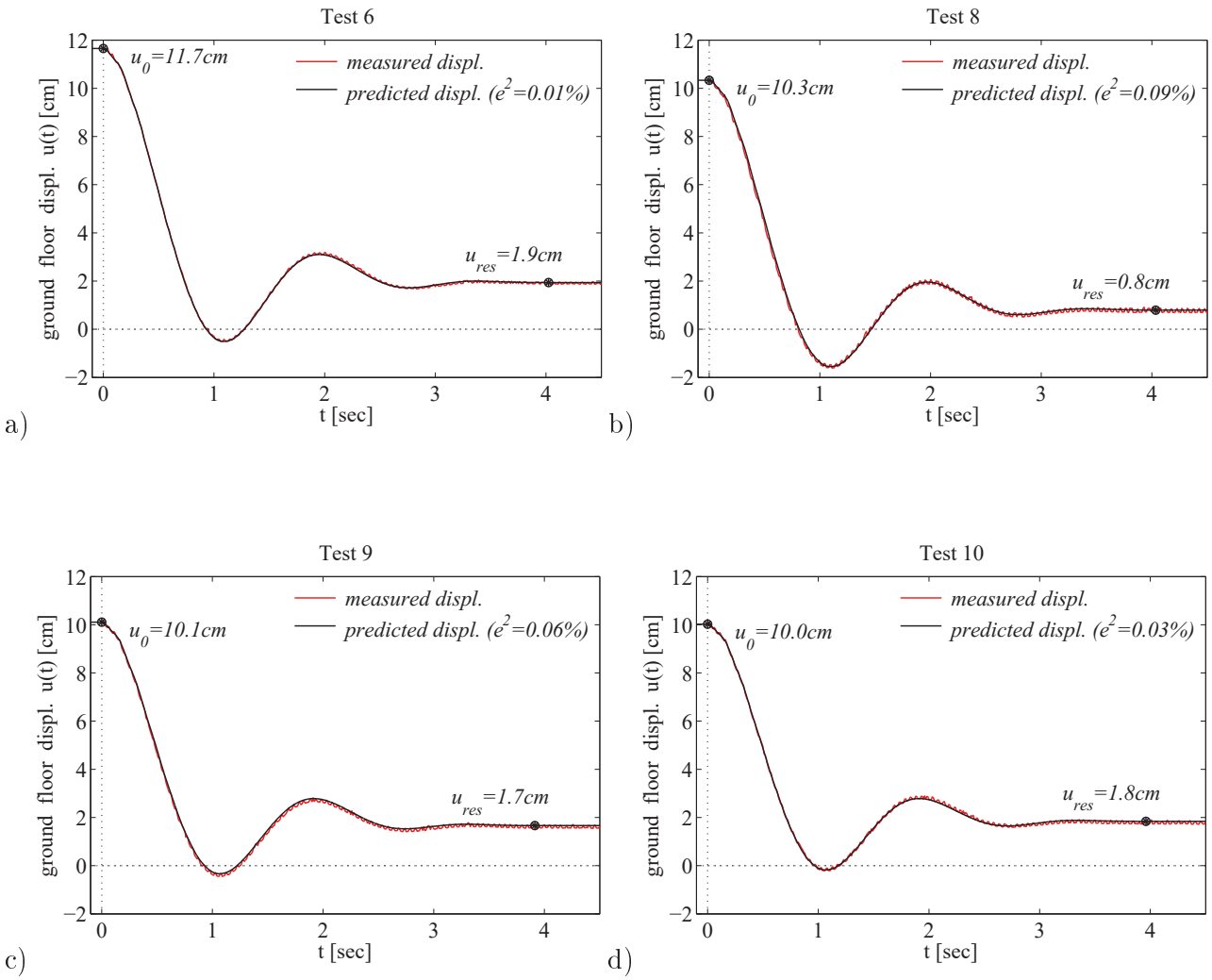

Figure 2.22: Comparison of measured and predicted displacements for the Augusta free vibration tests 6,8,9 and 10, sub-plots (a) to (d) respectively. All plots have the same scale to facilitate comparisons. The initial and residual displacements, u_0, u_{res}, are also provided in the figures. The distance between the two displacement traces, e^2, in the time range of the main event is given in the legend. e^2 is calculated from Eq. 2.10.

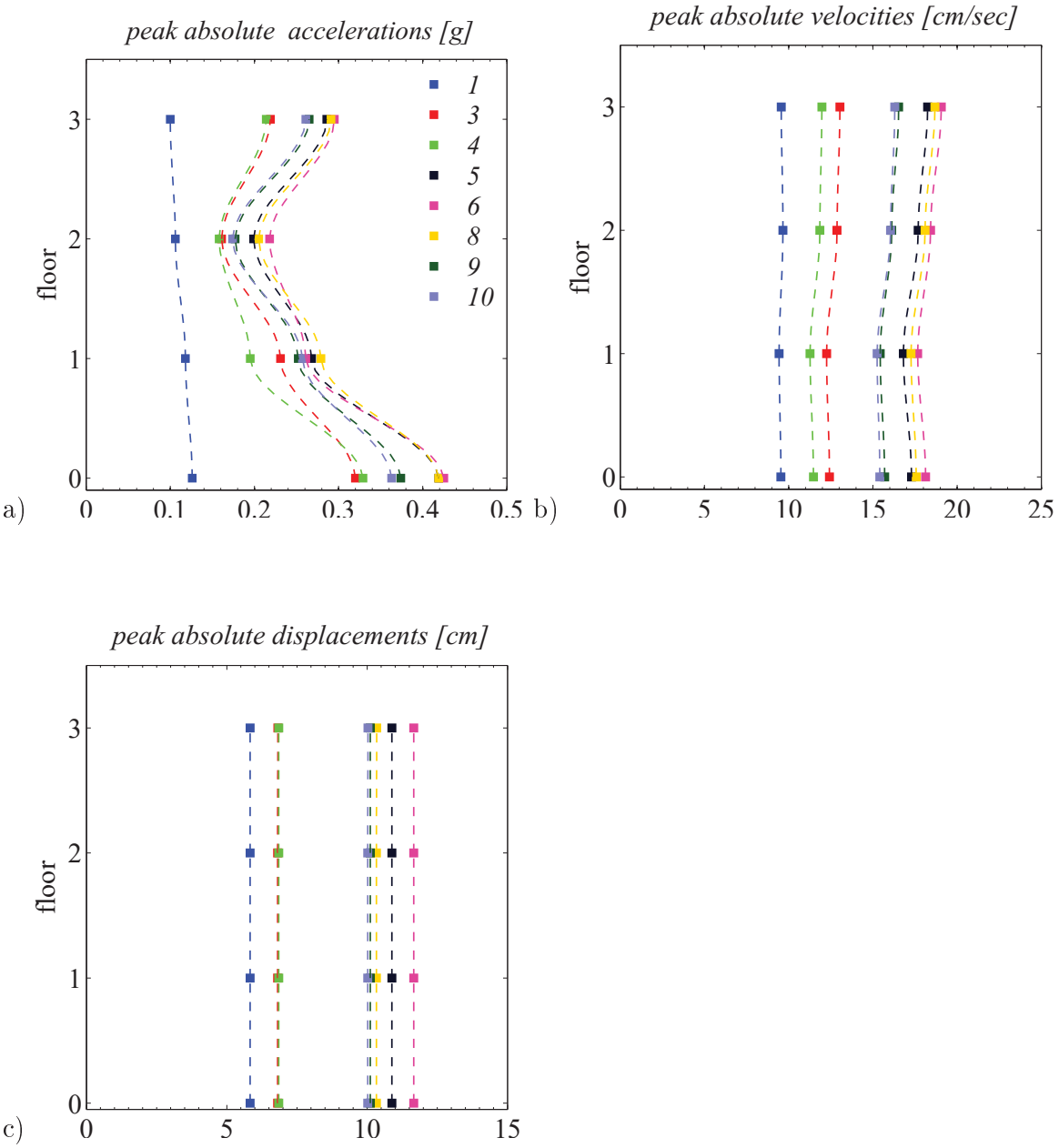

Figure 2.23: Peak absolute response of the Augusta building for tests 1,3,4,5,6,8,9 and 10, in terms of floor accelerations, velocities and displacements; sub-plots (a), (b) and (c) respectively.The initial displacements of the dynamic tests were (test, u_0):(1, 5.8cm), (3, 6.8cm),(4, 6.8cm),(5, 10.9cm),(6, 11.7cm),(8, 10.3cm),(9, 10.1cm),(10, 10cm).

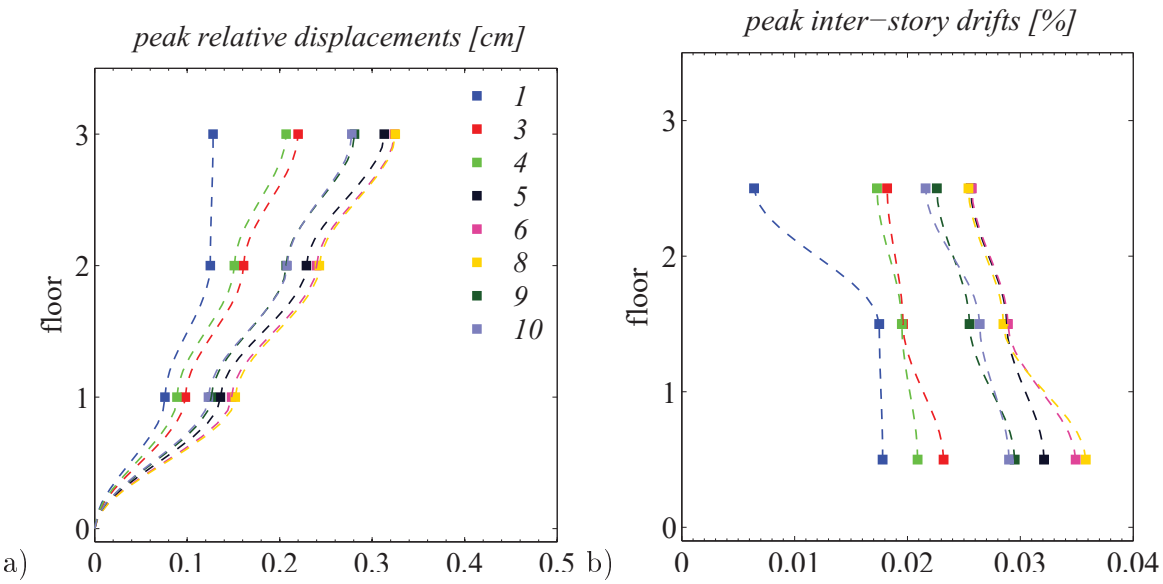

Figure 2.24: Peak relative displacement response and inter-story drifts of the Augusta building for tests 1,3,4,5,6,8,9 and 10; sub-plots (a) and (b) respectively. The initial displacements of the dynamic tests were (test,u_0):(1, 5.8cm), (3, 6.8cm),(4, 6.8cm),(5, 10.9cm),(6, 11.7cm),(8, 10.3cm),(9, 10.1cm),(10, 10cm).

2.8 Conclusions

A simple baseline fitting scheme is proposed herein for the processing of the strong motion data obtained from the Augusta free vibration tests. The method provides reliable results, without requiring significant computational effort. One main advantage of the method is the fact that it accounts for initial and end conditions. The method can recover permanent displacements, given that the latter have been measured. The baseline fitting procedure proposed makes use of polynomials of increasing order for the correction of the distorted acceleration, velocity and displacement baselines. The polynomial coefficients are determined directly from the boundary conditions; namely the initial and end accelerations, velocities and displacements. It is clear at this point that implementation of the method requires that the initial and residual displacements are available. The processing of the recorded data is performed in the time interval (t_1, t_2), where the motion is essential. The start time of the strong motion, t_1 , is evaluated on the basis of the cumulative squared acceleration diagram; t_1 is the time when CSA starts growing rapidly. The end time t_2 is selected as the time when the raw velocity trace starts to show a linear trend. The linear velocity trend is an indication of the presence of post-event noise; the noise causes a shift in the acceleration baseline which translates to a linear error in the velocity history. Although there is always subjectivity in the selection of the start and end times of motion, reasonable estimates of the strong motion duration lead to reasonable velocities and displacements.

The baseline scheme developed was applied for the processing of the absolute and relative acceleration signals obtained from the full Augusta data-set. The adjusted response included absolute and relative floor velocities, displacements and inter-story drifts. The generation of reasonable floor velocities, displacements and story drifts is of utmost importance, since this is structural information that is not measured during the experiments but is essential for the assessment of the building structural performance. The relative displacements and drifts were evaluated in two ways: (i) subtracting the adjusted ground floor response from the adjusted upper floor response and (ii) processing the raw relative motions. The implemen-

tation of methodologies (i) and (ii) provided identical relative accelerations and velocities. However, the two methods yielded different relative displacements. The differences were more pronounced in the second half period of motion, where the signal amplitude was significantly small and probably the noise was predominant. In fact, once high pass filtered, the displacements and drifts obtained from the two methods became identical, enforcing this way the reliability of the method.

Chapter 3

Structural identification from experimental data

This chapter summarizes recent developments in the system identification of base isolated structures using free vibration records. System identification is a very useful engineering practice that permits the assessment of the overall building state. For instance, in the special case of seismically isolated structures, it can serve for the detection of changes in the properties of the isolators and the superstructure. These changes could be due to manufacturing and installation imperfections, ageing, damage during earthquake etc. Earthquake response data, if available, can be also used for the dynamic identification of isolated structures [56].

Earlier work consisted in the identification of the Solarino isolation system using free vibration tests performed on one of the buildings in 2004 [41, 43, 57]. The identification was performed initially by means of the Least Squares Method [41] and subsequently using Evolution Strategies [43, 57]. The system response was generated using an analytical model developed for the problem at hand [41]. The bi-linear model was used for the description of the HDRB, while different friction models were considered for the description of the LFSB. Nevertheless, the complexity of the friction model was found to have no significant influence

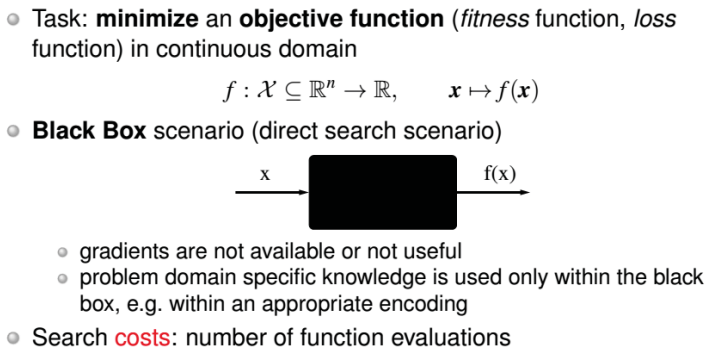

Figure 3.1: Black box optimization - problem statement (figure reproduced from [61]).

on the identification results [43]. However, an improvement of the HDRB model, the trilinear model, provided better identification results [43, 44]. A study on the performance of several Evolution Strategies on the 'toy problem', a basic identification problem specifically designed for HBIS, showed that the Covariance Matrix Adaptation - ES is the most effective for the problem at hand [43, 58].

3.1 Covariance Matrix Adaptation Evolution Strategy (CMA-ES)

The Covariance Matrix Adaptation - ES (CMA-ES) is a state-of-the evolutionary algorithm for difficult non-linear, non-convex optimization problems in continuous domain [42]. CMA-ES is highly competitive and should be implemented to unconstrained or bounded constraint optimization problems where derivative based methods, such as the quasi-Newton method, fail to provide solution [59]. The method was developed by Hansen in 1996 [60]; the problem statement is described in Figure 3.1.

Such as in any evolution strategy, in CMA-ES, new candidate solutions are sampled according to a multivariate normal distribution in the $\Re^n$. Pairwise dependencies between the variables in this distribution are represented by the covariance matrix. The candidate solutions (offspring) $\mathbf{x_i}$ are evaluated on the objective function $f : \Re^n \to \Re$ to be minimized.

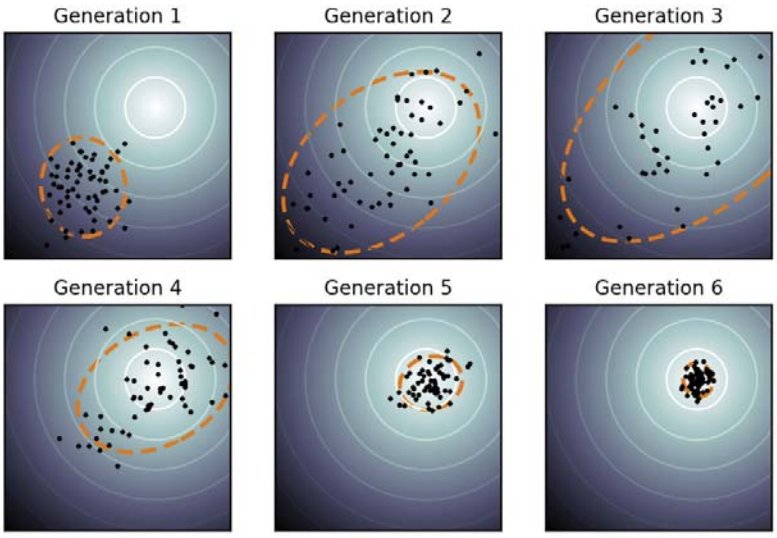

Figure 3.2: Illustrative application of the CMA-ES on a simple two-dimensional problem. The spherical optimization landscape is depicted with solid lines of equal f-values. The dots represent the offspring (population/candidate solutions) while the dotted lines represent the distribution of the population. Over the generations the distribution is evolved in order to provide better solutions. (The figure is reproduced from https://en.wikipedia.org/wiki/CMA-ES.)

A weighted combination of the μ best out of λ new candidate solutions is used to update the distribution parameters ((μ, λ) CMA-ES). Each iteration includes sampling of new solutions, re-ordering of the sampled solutions based on their fitness and update of the internal state variables based on the re-ordered samples. Over the generation sequence, individuals with better and better f-values are generated, see Figure 3.2. The five state variables are:

- $\mathbf{m} \in \Re^n$, the distribution mean and current favourite solution to the optimization problem,
- $\sigma \in \Re_+$, the step-size that controls the step length
- $\mathbf{C}$, a symmetric and positive definite $n \times n$ covariance matrix that determines the shape of the distribution ellipsoid
- $\mathbf{p}_\sigma, \mathbf{p}_\mathbf{c} \in \Re^n$, the evolution paths (i.e. the sequence of successive steps the strategy takes over a number of generations [42]).

The basic steps for the (μ, λ) CMA-ES algorithm are:

- Input: $\mathbf{m} \in \Re^n$, $\sigma \in \Re_+$, λ
- Initialize: $\mathbf{C} = \mathbf{I}, \mathbf{p_c} = \mathbf{0}, \mathbf{p}_\sigma = \mathbf{0}$.
  Set: $c_c \approx 4/n, c_\sigma \approx 4/n, c_1 \approx 2/n^2, c_\mu \approx \mu_w/n^2, c_1 + c_\mu \leq 1, d_\sigma \approx 1 + \sqrt{(\mu_w/n)}$, and $w_i = 1, ...\lambda$ such that $\mu_w = 1/\sum_{i=1}^{\mu} w_i^2 \approx 0.3\lambda$.
  w_i where $i = 1, ..\mu$ are recombination weights, $c_1, c_\mu, c_\sigma, c_c, c_\sigma$ are learning rates for the update of the covariance matrix and the step size and d_σ is a damping parameter used for step-size update.
- While the termination criteria are not met:
  - $\mathbf{x_i} = \mathbf{m} + \sigma \mathbf{y_i}, \mathbf{y_i} \sim \mathcal{N}_i(\mathbf{0}, \mathbf{C})$, for $i = 1, ..., \lambda$ (sampling)
  - $m \leftarrow \sum_{i=1}^{\mu} w_i x_{i:\lambda} = \mathbf{m} + \sigma \mathbf{y_w}$ where $\mathbf{y_w} = \sum_{i=1}^{\mu} w_i y_{i:\lambda}$ (update mean)
  - update the evolution paths $\mathbf{p_c}, \mathbf{p}_\sigma$[1]
  - $\mathbf{C} \leftarrow (1 - c_1 - c_\mu)\mathbf{C} + c_1 \mathbf{p_c} \mathbf{p_c^T} + c_\mu \sum_{i=1}^{\mu} w_i \mathbf{y_{i:\lambda}} \mathbf{y_{i:\lambda}^T}$ (update the covariance matrix)
  - $\sigma \leftarrow \sigma \times exp(\frac{\sigma_\sigma}{d_\sigma}(\frac{||\mathbf{p}_\sigma||}{E||\mathcal{N}(\mathbf{0},\mathbf{I})||} - 1))$ (update the step-size)

The search is terminated when:

- the maximum number of iterations, MaxIter, is reached (default MaxIter $= 10^3 * (N + 5)^2/\sqrt{(\lambda)}$), and/or
- the variable change is smaller than the tolerance TolX (default TolX $= 10^{-11} * max(\sigma(0))$), and/or
- the variable change is greater than the tolerance TolUpX (default TolUpX $= 10^3 * max(\sigma(0))$), and/or
- the function values change less than TolFun (default TolFun $= 10^{-12}$), and/or
- the function values are smaller than the tolerance TolHistFun (default TolHistFun $= 10^{-13}$), and/or

[1] the equations for the update of the evolution paths are not reported herein since they are rather cumbersome, but can be found in [42]

- the fitness stagnates for a long time.

As stated by Hansen in [59], the CMA-ES does not require a tedious parameter tuning for its application. The default strategy parameters are usually the optimal ones, since the algorithm is designed to perform well as it is. For the application of the CMA-ES the user should set an initial solution, an initial standard deviation (step-size) and possibly the termination criteria. Increasing the population size λ usually improves the global search capacity and the robustness of the method at the price of a reduced convergence speed [59, 42]. The authors suggest the users to perform independent Darts of the problem with increasing population size.

3.2 Laboratory data

Two series of acceptance tests were performed on the isolators used in the Augusta building, one for the rubber bearings and another for the sliding bearings. The tests were performed in the FIP S.p.a. laboratories, under the supervision of an accredited third party from the Construction Materials Testing Laboratory, University of Padova. The laboratory data are used herein for the identification of the static and dynamic properties of the rubber bearings under controlled conditions. The identified model parameters shall serve in the following identifications attempts for the establishment of a search domain where the system parameters are expected to be.

3.2.1 Evolution of the Italian seismic regulations

Before 2003, the Italian building code, established in 1974, was based on allowable stress design and left two thirds of the Italian territory without seismic provisions [62]. The 2002 $Mw5.7$ earthquake in Molise, Southern Italy, triggered the process for the revision of the existing regulations and the establishment of new seismic ones. The new provisions were inspired by Eurocode 8 and introduced new criteria for the seismic zonation, probabilistic definition of the ground motion, smoothed elastic and design response spectra, site amplification factors and design rules for the implementation of innovative technologies, such as base isolation, for the seismic design of new and existing structures [62]. The seismic provisions OPCM 3274 and successively the OPCM 3431, issued in 2003 and 2005 respectively, were the passage from the old generation to the new generation of seismic codes, i.e. from the working stress design to the performance based design of structures. The new code NTC08 was published in 2008 and became obligatory on July 2009. The Ministry of Infrastructures approved NTC14 in 14/11/14 but the regulations have not yet come into force. NTC14 is similar to the existing NTC08 and is in line with the European Norms. This latest Italian code will introduce simplification procedures for the design and will allow the reduction of seismic actions for existing structures.

3.2.2 Current testing protocol for isolation hardware

In 2009 the European Committee for Standardization (CEN) issued a draft of the Norm EN 15129 on anti-seismic devices. On August 1st, 2011, EN 15129 came officially into force in the European Union, replacing existing national specifications. The EN 15129 covers the design, manufacturing, testing and validation of the existing seismic hardware (rigid connection devices, displacement dependent devices, velocity dependent devices and isolators) [14]. The Norm is performance oriented, prescribing no failure and damage limitation requirements for the isolation devices under the Ultimate and Service Limit States respectively (ULS,SLS). EN 15129 prescribes a testing protocol for the manufacturers and accredited third parties. Manufacturers are responsible for the establishment and maintenance of a permanent factory production control to ensure that their products are in line with the EN 15129 performance specifications. The factory production control testing is equivalent to the qualification procedure testing prescribed in earlier Italian standards [45, 63]. The Notified Body is responsible for a peer review testing for the assessment of the performances of the anti-seismic device and approval of the factory production control testing, performed previously by the manufacturer. The peer testing is equivalent to the acceptance tests prescribed by the Italian Standards [45, 63]. There is an on going revision of EN 15129 expected to be completed by 2016 [64].

3.2.3 Earlier testing protocol for isolation hardare

On October 2009, FIP S.p.a. performed two series of acceptance tests on the isolators used in the Augusta building, one for the rubber bearings and another for the sliding bearings. The tests were performed in conformity with the national specifications OPCM 3431 [63]. The testing protocol prescribed by the Italian norm would be however in line with the later

[1]The tests were performed in the FIP S.p.a. laboratories, under the supervision of an accredited third party from the Construction Materials Testing Laboratory, University of Padova.

European norm EN 15129. A brief outline of the qualification and acceptance tests on rubber and friction isolators as required by OPCM 3431 is given below.

3.2.3.1 Rubber bearing testing according to OPCM 3431

The qualification tests should be performed at least on four bearings. Before testing two bearings should be exposed to artificial ageing (21 days under 70^oC). The qualification tests include:

1. Compression tests for the evaluation of the vertical stiffness K_v between 30% and 100% of the design vertical load.
2. Combined compression and shear tests (cyclic sinusoidal loading) for the evaluation of the static shear modulus G. G is evaluated from the third cycle data as following: $G = \frac{\tau(at\,0.58t_e)-\tau(at\,0.27t_e)}{(0.58t_e-0.27t_e)}$, where τ is the shear stress and t_e the total rubber thickness.
3. Combined compression and shear tests (cyclic sinusoidal loading) for the determination of the dynamic shear modulus G_{din} and equivalent damping ratio ξ at frequency $0.50Hz$. G_{din} is evaluated from the third cycle data as follows: $G_{din} = \frac{\tau}{\gamma} = \frac{F/A}{d/t_e}$ where F is the horizontal load acting on the bearing, A is the area of the bearing and $d = t_e$ the maximum displacement. G_{din} should lie in the range $0.35 - 1.40MPa$.
4. Combined compression and shear tests (cyclic sinusoidal loading) for the determination of the $G - \gamma$ relation at shear strain amplitudes $\gamma = 0.05 - 0.3 - 0.5 - 0.7 - 1.0 - 2$.
5. Creep tests.
6. Horizontal displacement capacity tests.
7. Repeated cyclic loading tests for the assessment of the stability of the shear properties.
8. Shear bond tests at shear strain $\gamma \geq 2.5$.

The acceptance tests on the isolation devices are performed with the same methodology used for the qualification tests. The acceptance tests must be performed on at least 20% of the devices and in any case on not less than 4 and not more than the total number of the devices to be used on site. The bearings are considered acceptable whenever they satisfy

the requirements specified below and the static shear modulus G does not differ more than $\pm 10\%$ from the value obtained from the qualification tests.

1. The external geometry must satisfy the prescriptions of the standards on rubber bearings.
2. For isolators taller than $100mm$ the height tolerance is $6mm$.
3. The static vertical stiffness should be evaluated between 30% and 100% of the vertical load.
4. The static shear modulus G, or alternatively, the dynamic shear modulus G_{din}, should be evaluated by the same methodology adopted for the qualification tests. The determination of the dynamic shear modulus G_{din} is preferred, since it provides information on the actual dynamic behaviour of the device.
5. The effectiveness of the steel-rubber adhesion should be assessed by the same methodology used for the qualification tests but adopting the value corresponding to the ULS design displacement d_2 for the strain γ.

Four elastomeric bearings used in the Augusta building were tested for the evaluation of the vertical stiffness and the static and dynamic lateral characteristics. The values of the vertical stiffness obtained were $(1167, 1316, 1566, 1299)kN/mm$, significantly higher than the required value $K_v > 800K_e = 800 \cdot 1.05 = 840kN/mm$. The bearings were subjected in combined compression and shear tests in couples (double shear test), see Figure 3.3. The cyclic tests were performed at a peak shear strain $\gamma = 1$. The static stress-strain curve for the first couple of isolators is shown in Figure 3.4 (a). The average static shear modulus of the couple of isolators tested was evaluated from the third cycle data as described above and resulted equal to 0.48MPa. This value corresponds to the tangent shear modulus; the manufacturer also calculated the secant shear modulus at $\gamma = 1$, this was equal to $0.65MPa$. The tangent shear modulus for the second couple of isolators tested was $0.51MPa$, while the secant shear modulus was $0.69MPa$. The bearings were also subjected to cyclic loading at a frequency of $0.5Hz$ for the evaluation of the dynamic shear modulus G_{din} at $\gamma = 1$. From

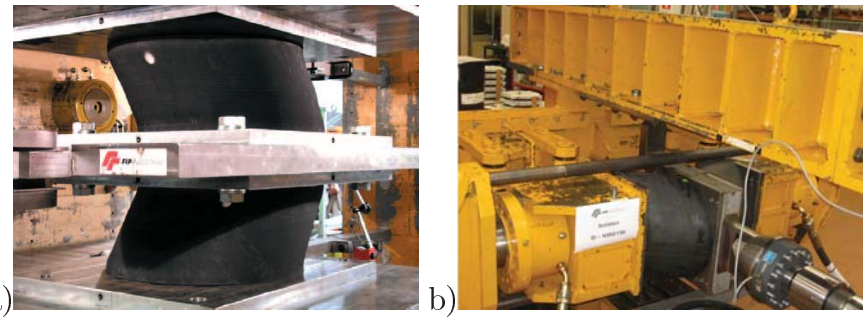

a) b)

Figure 3.3: Testing apparatus for double shear testing; photos (a) and (b). The figures are reproduced from the FIP product catalogue.

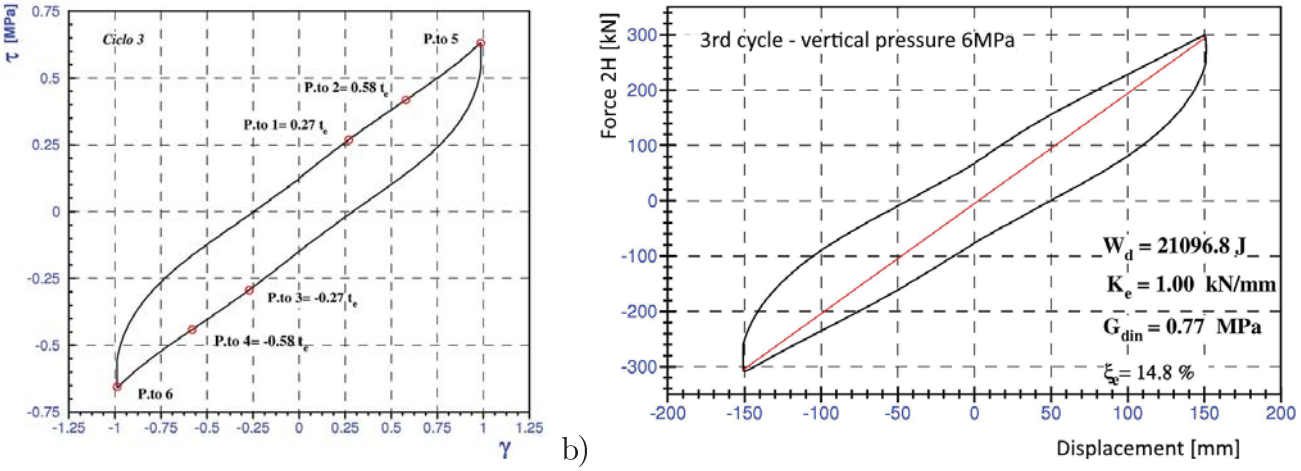

a) b)

Figure 3.4: Load-displacement curves obtained from the shear testing of two HDRBs at $d = 150mm (\gamma = 1)$. Sub-plot (a) corresponds to a static test while sub-plot (b) corresponds to a dynamic test at frequency $f = 0.50Hz$. The isolators were tested in parallel, hence the force measured was twice the force acting on each bearing. The figures are reproduced from the corresponding report on acceptance testing [65].

the load-displacement curve shown in Figure 3.4(b) the manufacturer evaluated the secant stiffness $K_e = 1.0kN/mm$ at $\gamma = 1$ and the energy dissipated in the cycle $W_d = 21,097J$. From the above values the dynamic shear modulus $G_{din} = 0.77MPa$ and the damping ratio $\xi_e = 14.8\%$ were derived. From the test performed on the second couple of isolators, not shown herein, the following parameters were evaluated:

$K_e = 1.05kN/mm$, $W_d = 22,588J$, $G_{din} = 0.81MPa$, $\xi_e = 15\%$.

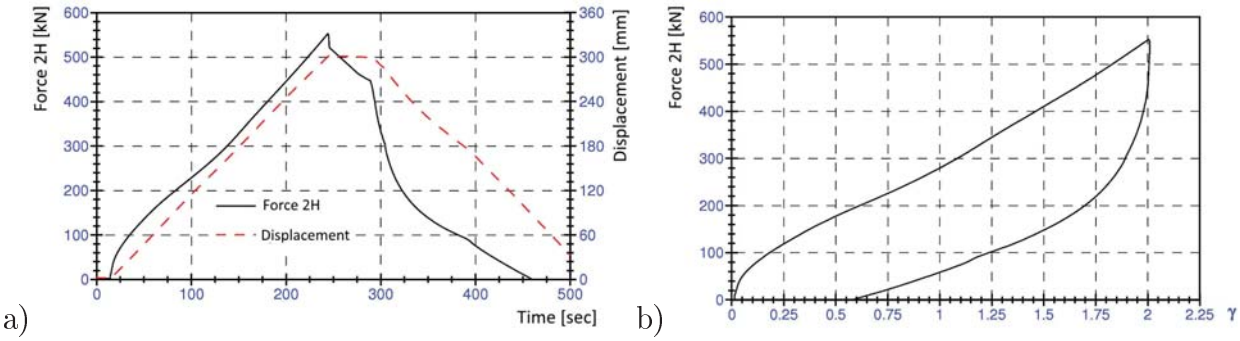

Figure 3.5: Load history and load-displacement curves for two HDRBs during adhesion test at displacement $d_2 = 300mm$; sub-plots (a) and (b). The two isolators were tested in parallel, hence the force measured was twice the force acting on each bearing. The figures are reproduced from manufacturer's report on acceptance testing[65].

The shear bond tests were performed in couples on all isolators, typical curves are shown in Figures 3.5.

3.2.3.2 Friction bearing testing according to OPCM 3431

Following the prescriptions of OPCM 3431, the qualification tests for friction bearings should be performed at least on two friction elements and include:

1. Combined compression-shear tests for the evaluation of the static coefficient of friction at three loads, V_{min}, V and V_{max}. V is the vertical load obtained in the seismic design situation. V_{min}, V_{max} are the minimum and maximum values of the vertical load V.
2. Combined compression-shear tests for the evaluation of the sliding coefficient of friction at V_{min}, V and V_{max}. The loading should be performed at three velocities (frequencies) equal to the design one and varied by $\pm 30\%$.
3. Repeated cyclic test for the assessment of the lateral displacement capacity of the friction slider at minimum displacement amplitude $d = 1.2d_2$ (the bearing should be able to perform at least 10 cycles with amplitude $d = 1.2d_2$).

The acceptance tests on the friction devices are performed with the same methodology used for the qualification tests. The acceptance tests must be performed at least on 20% of

the devices and in any case on not less than 4 and not more than the total number of the devices to be used on site. The devices are considered acceptable whenever they satisfy the requirements specified below.

1. The external geometry must satisfy the prescriptions of the standards on structural bearings.
2. The static coefficient of friction under constant pressure should be evaluated by the same procedure adopted in qualification tests.

One couple of each of the three types of sliding bearings used in the Augusta building was tested simultaneously for the evaluation of the friction coefficient. The tests were performed at a velocity of $4mm/min$ and at $0.5V_{max}$, $0.75V_{max}$ and V_{max}. The results for the predominant type of LFSB (VM 150/600/600) are shown in Figure 3.6. The start-up friction coefficient for the isolator considered varies from a maximum of 0.3% (under $0.5V_{max}$) to a minimum of 0.15% (under V_{max}). The sliding friction coefficient ranges from a maximum of 0.15% to a minimum 0.08%. Such exceptionally low values of the friction coefficient are due to the lubrication of the PTFE and, in the case of the sliding friction coefficient, to the very low testing velocity.

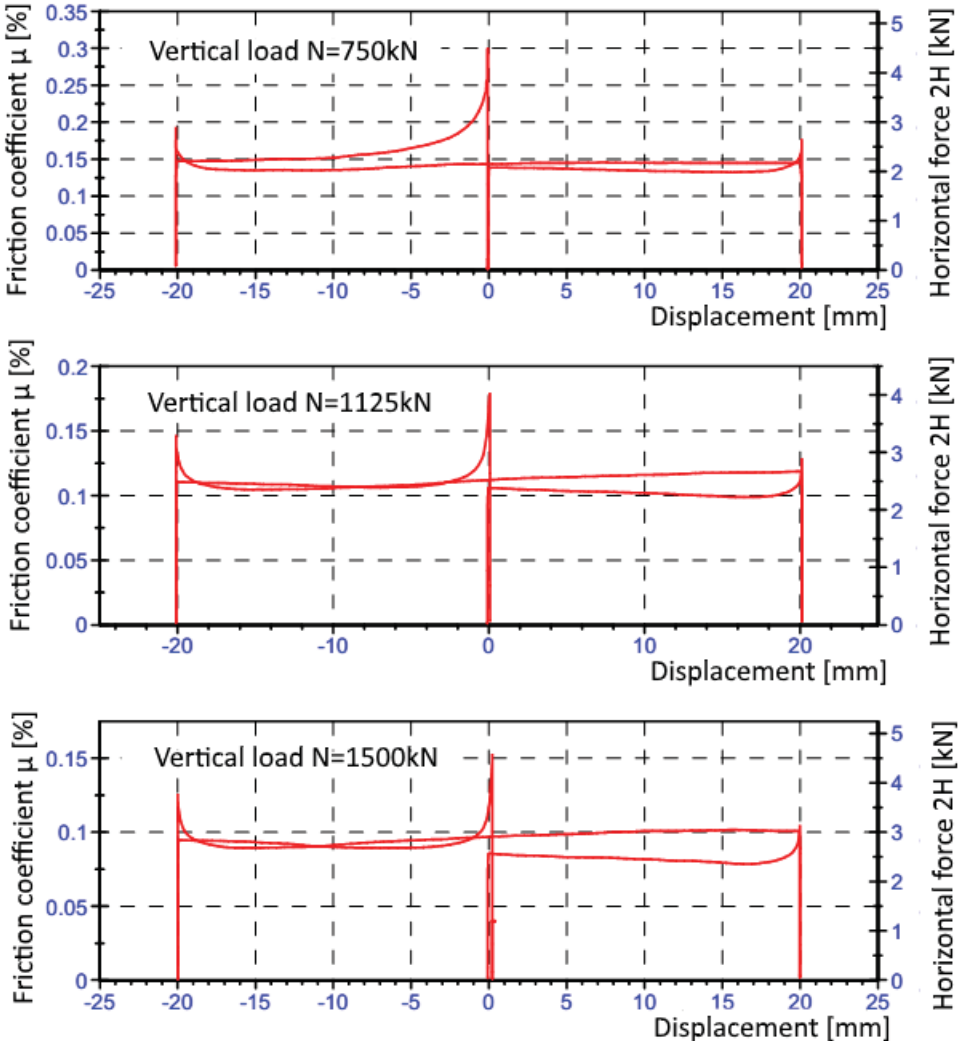

Figure 3.6: Friction coefficient for the sliding isolators VM 150/600/600 at load $0.5V_{max}$, $0.75V_{max}$ and V_{max}, where V_{max} is the maximum vertical load acting on the slider. The acceptance tests were performed at velocity $4mm/min$. The figure is reproduced from the manufacturer's report on acceptance testing [66].

3.3 Model parameter identification from laboratory data

The static and dynamic force displacement curves obtained from the acceptance tests performed on two couples of the Augusta elastomeric bearings and presented in the previous section shall be used herein for the identification of the rubber bearing model parameters.

3.3.1 Isolators models

A bi-linear model is adopted for the description of the HDRB constitutive behaviour; this model is used commonly in research and engineering practice for the description of the non-linearity of the rubber bearings [1]. Three parameters are needed for the definition of the bi-linear model: the elastic stiffness k_0, the post-elastic stiffness k_1 and the characteristic strength Q, Figure 3.7(a). For the description of the LFSB the Coulomb friction model is considered, 3.7(b). Although there are three types of LFSB present in the HBIS of Augusta, they are all assigned for simplicity the same coefficient of friction. Hence only one parameter defines the friction model, the coefficient of friction $\mu = F_{f0}/N$, where F_{f0} is the friction force and N is the axial load acting on the friction bearings.

The mechanical equivalents for the bi-linear and the Coulomb friction model are also shown in Figures 3.7. The bi-linear system is represented by two elastic springs, characterized by stiffnesses $k_e = k_0$ and $k_h = k_0 k_1/(k_0 - k_1)$, and a plastic slider characterized by the yielding force $F_y = Q + k_1 u_y$ (where u_y is the yield displacement). During the elastic phases the spring k_e is deforming, while the spring k_h stays still ($|F_p| < F_y = Q + k_1 u_y$). As soon as $|F_p| = F_y$ the system enters the yielding/ plastic/ post-elastic phase; during the plastic phase both springs deform and the overall stiffness of the system in series equals k_1. The Coulomb friction model can be interpreted as a plastic slider. While $|F_f| < F_{f0}$ the element remains blocked (stop phase); as soon as $|F_f| = F_{f0}$ the element starts moving (sliding phase). The friction force in the Coulomb model is a function of the friction coefficient and the sign of

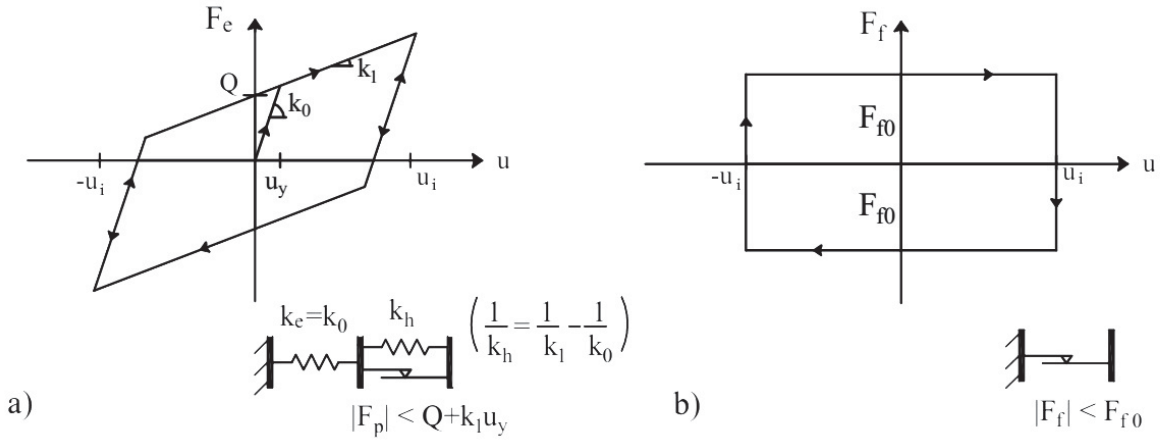

Figure 3.7: (a) and (b) Load - displacement constitutive model describing the non-linear behaviour of the HDRB and the LFSB.

the sliding velocity. The model is based on the assumption of constant friction coefficent; hence while it describes very well the friction force in the sliding phase of motion, it does not model properly the friction force during the stop phases. According to Constantinou et al. the stick-slip phenomenon can only occur when there is a natural variation in the friction force [6]. More elaborate models should be used for the proper modelling of the stick-slip motion, such as the Stribeck model [67]. For the problem at hand this is not a critical issue, since the friction bearings selected are not expected to contribute essentially to energy dissipation. The VM pot bearings series produced by FIP Industriale are characterized by low sliding coefficients of friction and are used primarily as structural bearings for the support of vertical loads.

The restoring force developed in the rubber bearings is given in Eqs 3.1(a) and (b) while the resisting force developed in the friction sliders is given in Eq. 3.1 (c).

$$F_e(u,\dot{u}) = k_0[u - u_i - u_y sign(\dot{u})] + k_1[u_i + u_y sign(\dot{u})] \quad (HDRB : elastic\ branch) \quad (3.1a)$$

$$F_e(u,\dot{u}) = k_0 u_y sign(\dot{u}) + k_1[u - u_y sign(\dot{u})] \quad (HDRB : plastic\ branch) \quad (3.1b)$$

$$F_f(sign(\dot{u})) = F_{f0} sign(\dot{u}) = (\mu N) sign(\dot{u}) \quad (LFSB) \quad (3.1c)$$

where $u_y = Q/(k_0 - k_1)$ is the yielding displacement and u_i is the initial displacement at the beginning of each elastic branch.

3.3.2 Lab data identification

The identification of the properties of the HDRB on the basis of the lab tests provided by the manufacturer is performed using the CMA-ES. The system parameter vector to be identified includes the properties (k_0, k_1, Q) of the bi-linear model describing the rubber bearings. For each set of candidate solutions the force-displacement curve is produced according to the constitutive laws of the the considered model $(F_e - u)_{sim}$, see Figure 3.7(a), and compared to the experimental curve $(F_e - u)_{exp}$. The fitness function to be minimized is defined below:

$$f = [(A - A^e)/A^e]^2 + \left[(I_{xx} - I^e_{xx})/I^e_{xx}\right]^2 + \left[(I_{yy} - I^e_{yy})/I^e_{yy}\right]^2 + \left[(I_{xy} - I^e_{xy})/I^e_{xy}\right]^2 \quad (3.2)$$

where $A^e, I^e_{xx}, I^e_{yy}, I^e_{xy}$ are the area and second moments of area of the experimental restoring force-displacement curve $(F_e - u)_{exp}$, and $A, I_{xx}, I_{yy}, I_{xy}$ are the corresponding quantities from the model $(F_e - u)_{sim}$.

The objective is to find a bi-linear model that dissipates equal energies with the bearing. The minimum value attained by Equation 3.2 provides an optimal set of parameters for each test. The identified mechanical properties of the Augusta HDRBs under static and dynamic conditions are given in Table 3.1. The identification results show that the properties of the HDRB under static conditions are significantly lower than the corresponding properties under dynamic conditions (65% for k_0, 17% for k_1 and 28% for Q).

The identified bi-linear models are shown against the experimental F-u curves in Figures 3.8 and 3.9. From observation of the figures it becomes clear that while the identification of the tangent stiffness k_1 and the characteristic strength Q is quite straight forward, the identification of the elastic stiffness k_0 is not so. In common practice, k_0 is selected by visual inspection in order to get an energy fit of the experimental loop [1].

Table 3.1: Mechanical properties of the rubber bearings identified from the third cycle force-displacement curves obtained from static and dynamic lab tests performed at $\gamma = 1$. The identification problem was solved using the CMA-ES. The CMA-ES was ran 10 times on each identification problem. The optimal solution is shown herein. First row: lab test id. Second row: number of identification runs that the solution was repeated over the total number of identification runs performed. Third row: identified elastic stiffness k_0. Fourth row: identified post-elastic stiffness k_1. Fifth row: identified characteristic strength Q. Fifth row: fitness function value (error) corresponding to the optimal solution.

	Static test 1 (7/10)	Static test 2 (9/10)	Dynamic test 1 (9/10)	Dynamic test 2 (9/10)
$k_0\,(kN/m)$	3509	3521	5413	6199
$k_1\,(kN/m)$	658	708	802	847
$Q\,(kN)$	27	28	37	40
$error$	$1.7E-06$	$1.3E-06$	$3.4E-06$	$3.2E-06$

3.3.2.1 Uniqueness of the optimal solution

The results of Table 3.1 show that the optimal solution is not unique; not all identification runs lead to the same solution. This fact implies that the CMA-ES provides a local rather than a global minimum of the objective function. Indeed, in most real applications the search for the global optimum is not feasible. Table 3.2 shows the identified mechanical properties of the rubber bearings obtained from the ten identification runs on the $F-u$ data available from the first static lab test. Runs 1,2,3 provide an unrealistic bi-linear system with negative stiffness and/or characteristic strength and are therefore disregarded. However these results show that even an unphysical system can be local minimum for the objective function. Figure 3.10 shows the comparison between the experimental and identified static $F-u$ loops relative to the first set of HDRB tested. Both the unphysical and physical systems, obtained by the identification runs 1,3 and 4-10 respectively (see Table 3.2), provide $F-u$ curves that match satisfactorily the experimental curve.

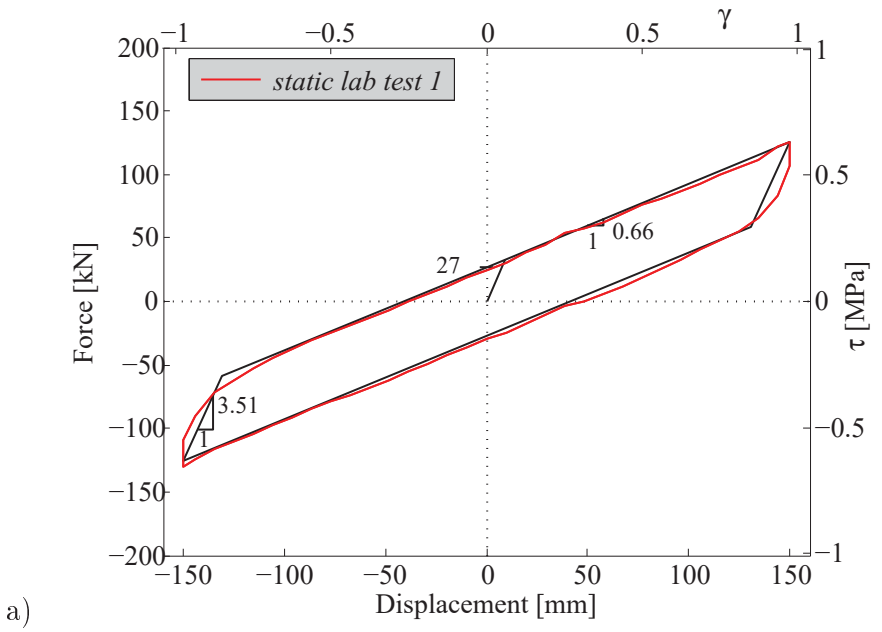

a)

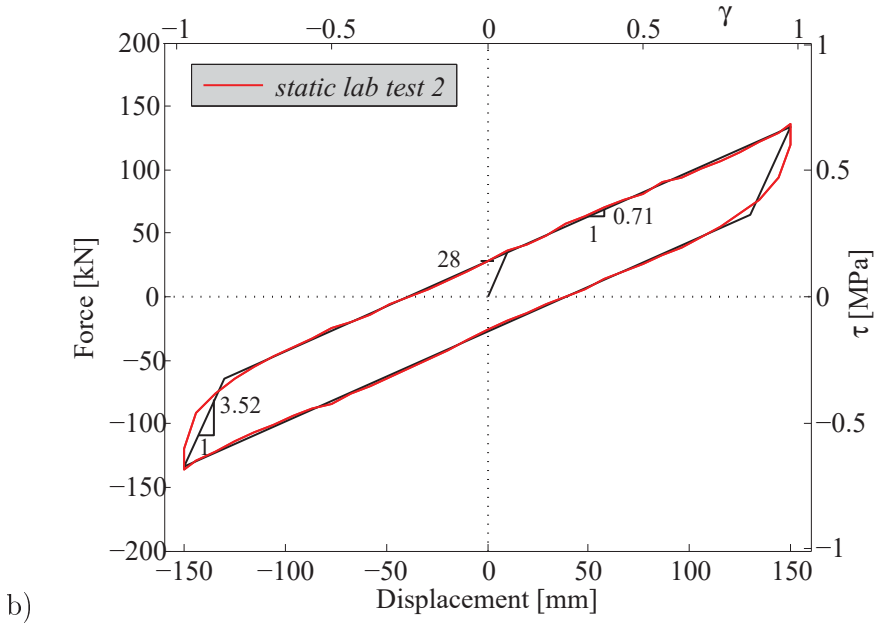

b)

Figure 3.8: Experimental and identified static force-displacement curves for the two sets of bearings tested, sub-plots (a) and (b). The experimental curves are shown in red while the identified bilinear curves are shown in black. The values of the identified characteristic strength (in kN) and the elastic and post-elastic stiffness (in kN/mm) are also shown.

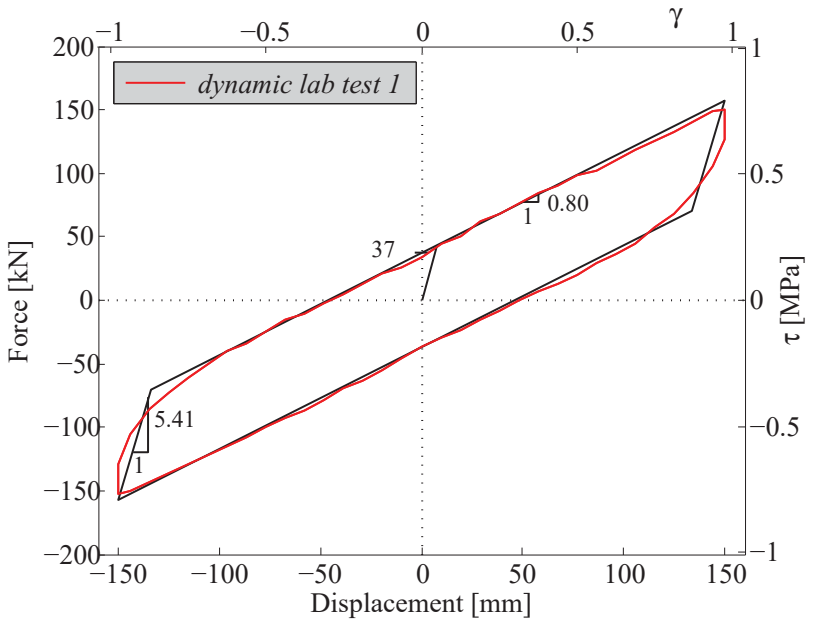

a)

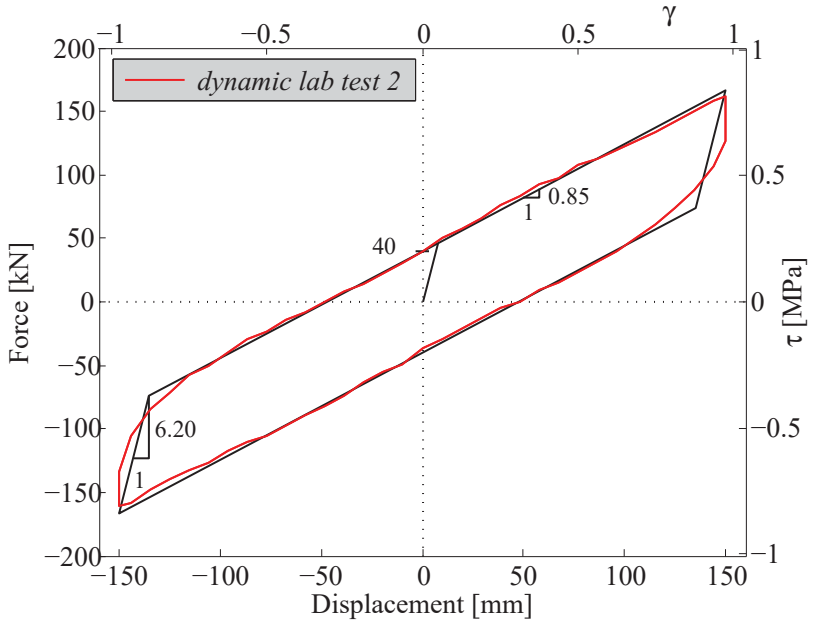

b)

Figure 3.9: Experimental and identified dynamic force-displacement curves for the two sets of bearings tested, sub-plots (a) and (b). The experimental curves are shown in red while the identified bilinear curves are shown in black. The values of the identified characteristic strength (in kN) and the elastic and post-elastic stiffness (in kN/mm) are also shown.

Table 3.2: Identified bilinear parameters for the first set of rubber bearings tested statically at $\gamma = 1$. The identification problem was solved 10 times using the CMA-ES. The parameters obtained from each identification run are shown herein. First row: identification run. Second row: identified elastic stiffness k_0. Third row: identified post-elastic stiffness k_1. Fourth row: identified characteristic strength Q. Fifth row: fitness function value (error) corresponding to the optimal solution.

Static test 1	Runs 1,3	Run 2	Runs 4 to 10
$k_0\,(kN/m)$	-2202	746	3509
$k_1\,(kN/m)$	694	-2108	658
$Q\,(kN)$	-27	400	27
$error$	$1.7E-06$	$1.7E-06$	$1.7E-06$

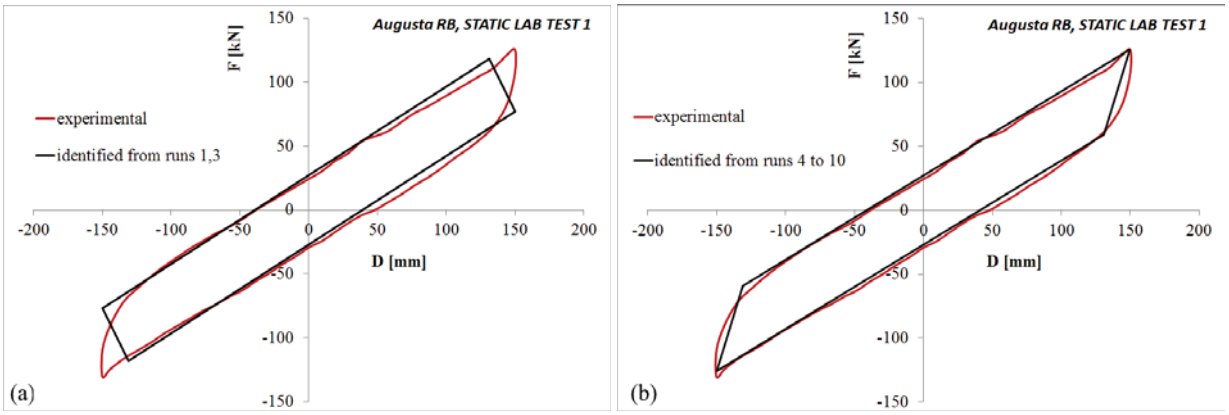

Figure 3.10: Experimental and identified $F-u$ curves, corresponding to the first set of HDRBs tested statically ($\gamma = 1$).The bilinear curves shown in sub-plots (a) and (b) were obtained from the identification runs 1,3 and 4-10 respectively.

3.4 Identification of the isolation system properties from the Augusta free vibration data

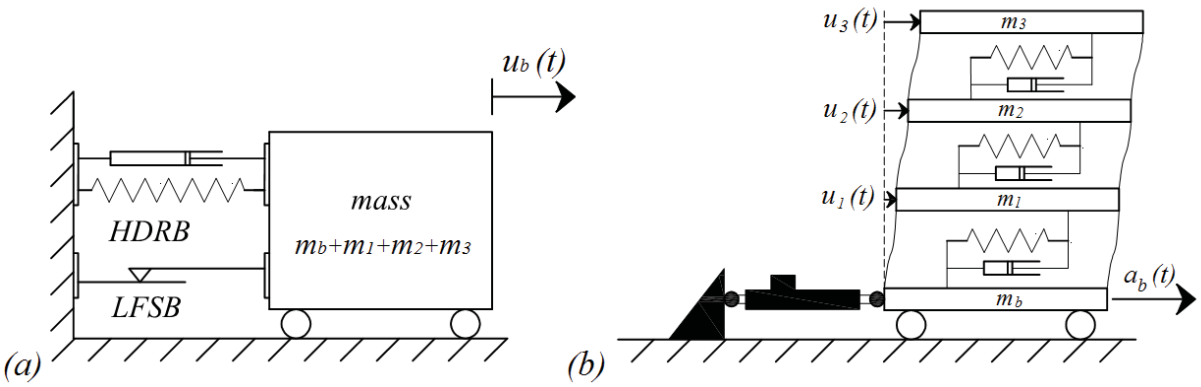

Figure 3.11: Rigid superstructure isolation model and fixed flexible superstructure model used in the two stage identification of the Augusta HBIS and the Augusta superstructure respectively; sub-plots (a) and (b).

The free vibration response obtained from the signal processing of the Augusta records, is used herein for the assessment of the properties of the isolated structure under dynamic excitation. The identification is performed in two stages. At the first stage the non-linear properties of the isolation system are identified; for this reason a simple one degree of freedom model is considered, see Figure 3.11(a). The flexibility of the superstructure is disregarded at this point. At the second stage the properties of the superstructure in the linear response range are identified. The superstructure response is simulated by means of a linear discrete model, fixed at the base. The superstructure is excited with the acceleration $a_b(t)$ developed at the non-linear isolation system, see Figure 3.11(b). The one way identification of the whole isolated structure using a more detailed model would provide probably better (more realistic) results. However this would lead to a considerable increase of the problem dimension and consequently of the computational effort involved. Considering the increased time required for the numerical response simulation of a more sophisticate candidate solution ($\sim 2min$), together with the increased number of offspring ($\lambda > 10$) and the considerable high number of

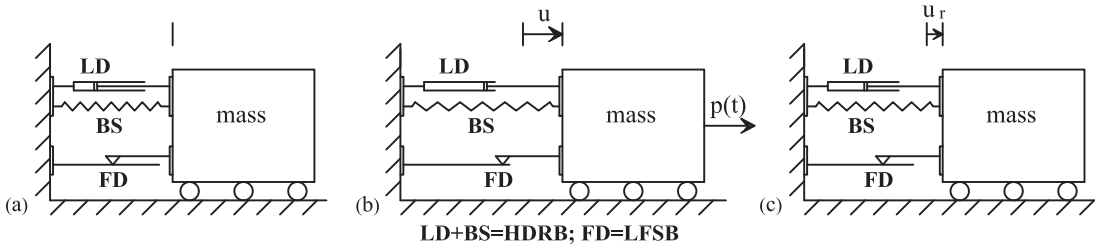

Figure 3.12: The physical model: (a) initial configuration, (b) deformed configuration during earthquake motion, and (c) rest configuration after the earthquake motion ceases.

iterations performed per run (~ 250), the waiting time for a single identification run results excessively long. In fact, identification attempts on HBIS characterized by a larger set of properties showed that the waiting times per run could result of the order of a working week [68]. These times are clearly unacceptable where limited computer resources are available.

The mechanical model considered for the identification of the Augusta HBIS is shown in Figure 3.12. The bi-linear spring and the viscous damper account for the HDRB, while the plastic slider accounts for friction in the LFSB. All HDRBs are of one class and hence are expected to have the same properties. The same coefficient of friction is assigned to all the LFSBs. Therefore, the system parameter vector to be identified consists in: the mass of the 'rigid' structure (m), the properties of the bi-linear spring (k_0, k_1, Q), the coefficient of friction of the sliders (μ) and the damping ratio relative to linear viscous damper (ζ). The equation of motion for the one degree of freedom model shown in Figure 3.12 is:

$$m\,\ddot{u}_b + c\,\dot{u}_b + F_e(u_b, \dot{u}_b) + F_f(sign(\dot{u}_b)) = p(t) \tag{3.3}$$

Eq. 3.3 shows how the external load $p(t)$ is balanced by the inertia force acting on the mass m, the resisting force in the linear viscous damper, the restoring force in the bi-linear spring F_e and the friction force in the slider F_f. In the case of free vibration $p(t) = 0$. The expressions for F_e and F_f have been already provided in Eqs 3.1. The restoring force in the bi-linear spring F_e takes different forms according to whether the system experiences an elastic phase of motion or a plastic one. The dynamic response of a hybrid base isolation system is thus governed by successive phases of elastic and yielding behaviour, each phase

described by a linear ordinary differential equation. In the case of free vibration a closed form solution can be provided in a sequential manner for each phase of motion . The analytic free vibration response solution can be extended to earthquake excitation, or forced vibration in general. Given the discrete nature of the sampled strong motion, the input excitation can be assumed to have a linear variation within the time step. Then, assuming that the properties of the system do not change within the time step, the analytic solution can be rearranged properly, see Eq. 3.4. A more detailed description of the solution algorithm can be found in [16].

$$u_b(t) = u_c(t) + u_{cp} + u_p(t) \tag{3.4}$$

where $u_b(t)$ is the displacement of the HBIS, $u_c(t)$ is the solution of the homogeneous equation, u_{cp} is a particular solution associated to plastic and friction terms and $u_p(t)$ is the particular solution associated to the linear load. The time t varies from $t(i)$ to $t(i) + \Delta t$, where Δt the duration of the $i - th$ step. The system may come to a rest any time that the static equilibrium is satisfied:

$$F_e(u_b = u_r, \dot{u}_b = 0) + F_f(\dot{u}_b = 0) = 0, \quad \text{where} \quad |F_f(\dot{u}_b = 0)| \leq F_{f0} \tag{3.5}$$

where u_r is the residual displacement, Fig. 3.12 (c).

3.4.1 Fitness function for the identification of the Augusta isolation system

The optimization problem for the identification of the Augusta HBIS is formulated as the minimization of the following functional:

$$f = \sum_{i=GFL}^{3FL} \frac{(u^i_{exp} - u_b)^T (u^i_{exp} - u_b)}{\left(u^i_{exp}\right)^T \left(u^i_{exp}\right)} + \sum_{i=GFL}^{3FL} \frac{(\dot{u}^i_{exp} - \dot{u}_b)^T (\dot{u}^i_{exp} - \dot{u}_b)}{\left(\dot{u}^i_{exp}\right)^T \left(\dot{u}^i_{exp}\right)} \tag{3.6}$$

where $u^i_{exp}, \dot{u}^i_{exp}$ is the experimental free vibration absolute displacement/velocity at the $i-th$ floor and $u_b, \dot{u}_b$ is the corresponding simulated response for the model shown in Figure 3.12. The experimental displacements and velocities at all floors are taken into account in the definition of the fitness function, since the identified rigid model should provide a response that matches the overall building response. The rigid superstructure response was simulated for each candidate solution $\boldsymbol{S} = [m, k_0, k_1, Q, \mu, \zeta]$ using the analytical algorithm described briefly above. The CMA-ES was ran 10 times on each set of free vibration data available. The population size λ was doubled in each restart of the algorithm. The remaining CMA-ES strategy parameters (maximum number of iterations and tolerance, see section 3.1) were set to their default value, which is also the optimal one according to the developers [59]. The identification was performed in a bounded search space to avoid the occurrence of non-physical solutions.

3.4.2 Identified HBIS models and discussion

The eight HBIS identified from the eight free vibration tests are shown in Table 3.3 together with the start point and the search space considered. The mass identified is the total mass of the building at test conditions. The HDRB properties obtained refer to a single bearing - all rubber bearings were assumed to have the same properties. The identified coefficient of friction μ should be multiplied by the vertical load N acting on the friction devices to provide the total friction force $F_{f0} = \mu N$ developed in the friction elements during sliding. N was estimated to be equal to $13,900kN$ under test conditions; this estimate was made considering vertical loads $750kN$, $900kN$, $25kN$ acting on the friction bearings VM 200/600/600 , VM 150/600/600 and VM 25/600/600 [2]. The initial guess for the system parameter vector $\boldsymbol{S}$ was made on the basis of the available data. The mass m was set equal to $2,000tons$, somewhat smaller than the building mass $m = 2,400tons$ provided from the structural designer for the finished building. The properties of the HDRB (k_0, k_1, Q) were set equal to the average of the

[2] $N = (4 * 750 + 12 * 900 + 4 * 25)kN = 13,900kN$

corresponding values obtained from the identification of the laboratory dynamic hysteresis loops, see Table 3.1. A conservative guess was made for the friction coefficient, assuming $\mu = 0.50\%$. The damping ratio for the linear viscous damper, which together with the bi-linear spring describes the HDRB, was set initially equal to a small value $\zeta = 1\%$. The search space for the (k_0, k_1, Q) was established on the basis of the corresponding static and dynamic properties identified from the available acceptance tests, see Table 3.1. The lower bounds for (k_0, k_1, Q) were obtained varying the static lab properties (k_0, k_1, Q) by approximately -30%, while the upper bounds are obtained varying the the corresponding dynamic lab properties by approximately $+20\%$. The lower bound for k_0 was further decreased to $2000kN/m$ since the first identification attempts showed a tendency of the elastic stiffness to take very low values. The search space for the building mass was set to $[1500, 2400]tons$. The bounds provided for the friction coefficient and the damping ratio were $[0, 4]\%$ and $[0, 5]\%$ respectively. The upper bound 4% for μ is also the upper limit prescribed by the Italian seismic code for friction devices [63]. Table 3.3 gives also the fitness function values (errors) corresponding to each identified (optimal) solution and the number of times the solution was repeated. The fitness function values were evaluated according to Eq. 3.6. Some basic statistics on the data obtained from the identification are provided in the last rows of Table 3.3 (mean, standard deviation and coefficient of variation of the identified model properties).

Observation of Table 3.3 shows how:

- All tests have been identified successfully leading to optimal solutions with very small errors ($< 10\%$). The validity of the findings is demonstrated by the fact that independent runs of the CMA-ES with increasing population size lead almost always to the same solution, see last column of Table 3.3.
- The optimal solution is not unique, corresponding to a local rather than a global minimum of the inverse problem. Hansen in [59] states that 'the objective of searching for a global optimum is neither feasible nor relevant in practice'. The repeatability of the optimal solution is a measure of the reliability of the output.

Table 3.3: Identified Augusta HBIS from the free vibration data of tests 1,3,4,5,6,8,9 and 10. First row: identified HBIS mechanical properties and error corresponding to the optimal solution. The number of times the solution was repeated over the total number or identification runs performed is given within brackets. Second row: start point of the identification run. Third and fourth rows: lower and upper bounds provided for the bounded search. Fifth to twelfth row: identified system parameter vector for tests 1 to 10. The tests are organized in terms of increasing strain amplitude. Thirteenth to fifteenth row: average, standard deviation and coefficient of variation of the identified properties.

	$m(tons)$	$k_0(kN/m)$	$k_1(kN/m)$	$Q(kN)$	$\mu(\%)$	$\zeta(\%)$	error	
start point	2000	5806	825	38.5	0.5	1		
lower bound	1500	2000	600	25	0	0		
upper bound	2400	7000	1000	50	5.0	5.0		
test 1 ($\gamma = 0.39$)	2226	3269	700	28.8	0.77	0	0.064	(2)
test 3 ($\gamma = 0.45$)	2326	2794	834	29.1	0.96	0	0.042	(6)
test 4 ($\gamma = 0.45$)	2282	2728	683	31.6	0.83	0	0.052	(8)
test 10 ($\gamma = 0.67$)	2400	2127	600	39.5	1.15	0	0.053	(10)
test 9 ($\gamma = 0.67$)	2400	2116	600	40.2	1.13	0	0.049	(10)
test 8 ($\gamma = 0.69$)	2373	2013	701	34.8	1.30	0	0.043	(3)
test 5 ($\gamma = 0.73$)	2387	2093	616	41.8	1.23	0	0.042	(9)
test 6 ($\gamma = 0.78$)	2400	2041	600	44.0	1.33	0	0.054	(10)
avg	2349	2398	667	36.2	1.09	0		
st.d.	66	470	82	5.9	0.21	0		
c.o.v. (%)	3	20	12	16	20	0		

- The mass of the rigid block was identified with values close to the upper bound $2,400 tons$, i.e. the mass value provided from the structural designer for the finished building. The building mass was the model property identified with the highest certainty (coefficient of variation equals 3%).
- The damping coefficient was identified with zero value in all identification runs performed, implying that there is no need for consideration of a pure viscous element - the hysteretic (bi-linear) model alone can describe satisfactorily the Augusta HBIS free vibration response at the low strain amplitude range.
- The properties of the HBIS change when different dynamic input (free vibration motion) is considered. This implies that (k_0, k_1, Q, μ) are strain dependent.
- Tests 3 and 4 were tests of equal energy input; however their identification leads to two

very different systems. The optimal solution obtained from test 4 seems to be more realistic in terms of post-yielding stiffness k_1, since it is in line with the values obtained from the remaining tests. Moreover the optimal solution provided by the identification of test 4 was repeated more times (8 out of 10) compared to the solution of test 3 that was repeated 6 times out of 10.

- The identification of test 8 yielded the same optimal solution only twice. This fact together with the fact that the identified properties for test 8 are significantly different in terms of post-yielding stiffness and coefficient of friction than those provided by tests 5,9 and 10 which were of similar energy input, raises doubts on the validity of the obtained solution. In fact, tests 3 and 8 followed the unsuccessful release tests 2 and 7, see for instance Figure 3.13. There is evidence that the structure was not recentered after the failed released tests. Moreover, it was documented that the residual displacement for test 8 was of the order of $12mm$. The records were not corrected to account for residual displacements; in fact the residual displacement reported in tests 3 and 8 are rather small compared to the ones documented for tests of similar amplitude, see Figures 1.12 and 1.13.

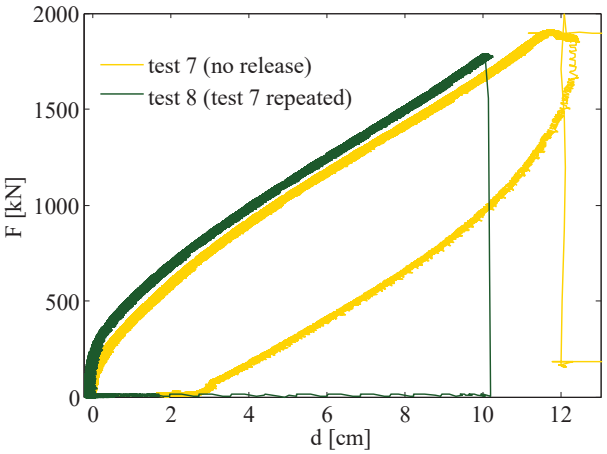

Figure 3.13: Force displacement curves for tests 7 and 8. There was no release under test 7. The test was repeated successfully afterwards (test 8). However the building was no re-centered before the test was repeated.

- Test 1 was the first of a series of release tests. The stiffening effect observed in Test 1 could be also due to Mullin's effect [69]. Mullins observed that rubber samples that softened over numerous cycles of stretching recovered their initial mechanical properties over time and noted that recovery of stiffness was accelerated and more complete at high temperatures. The remaining tests were performed within a short time, hence there is little change that the initial stiffness observed in Test 1 was recovered.
- The identified elastic stiffness varies from 2041 to $3269kN/m$. These values are approximately one third of the corresponding elastic stiffness under dynamic conditions and almost two thirds of the corresponding elastic stiffness under static conditions. It can be argued however that the lab tests were performed under controlled conditions and refer to a strain amplitude $\gamma = 1$, so a fair comparison is not straight-forward. Moreover, while k_1 is a property which can be selected straightforwardly Additionally, k_0 defines the stiffness under two separate modes of behaviour - the initial stiffness when the bearing is first loaded and the unloading stiffness after a displacement peak has been reached [1].
- k_1 varies from a maximum of $700kN/m$ for test 1 ($\gamma = 0.39$) to a minimum of $600KN/mm$ for tests 9,10 and 6 ($\gamma = 0.67 - 0.78$). [3]
- The characteristic strength Q varies from $28.8KN$ for test 1 ($\gamma = 0.39$) to $44.0kN$ for test 6 ($\gamma = 0.78$).
- Summarizing, k_0 and k_1 show a decreasing trend with increasing strain amplitude implying a reduction of the effective stiffness at higher displacements. Q instead tends to take greater values under higher amplitudes of motion. These results are typical of the cyclic behaviour of HDRB, see Figure 3.14. The hysteresis loops provided by the HDRB are not stable, the characteristic strength tends to increase at higher strain amplitudes, while the secant and tangent stiffnesses become softer [4]. The identified

[3] The results of test 3 provide even higher values for k_1, however for the reasons mentioned above, these results are unreliable.

[4] These observations are not valid however for $\gamma > 2.5 - 3$ where the rubber shows stiffening behavior

force-displacement loops for tests 1, 4, 5, 6 and 9 are shown in Figure 3.15.

- The identified friction coefficients vary from $0.77 - 1.33\%$ and are significantly higher than those established from the manufacturer on the basis of acceptance tests, see Figure 3.6. However there are three points to be raised: (i) the friction force-displacement curves provided by the manufacturer correspond to lab testing performed at very low velocities ($v = 4mm/min < 0.1mm/sec$ i.e. static conditions), while the velocities experienced during the experiments were significantly higher ($\sim 150mm/sec$). Several recent experimental studies have demonstrated the dependence of the sliding coefficient of friction on the velocity amplitude, air temperature, apparent pressure, lubrication and number of cycles [6, 21]. Dolce et al. performed more than 300 tests on un-lubricated and lubricated steel-PTFE interfaces. Their experimental findings on lubricated steel-PTFE interfaces, provided $\mu = 1 - 2.5\%$ for sliding velocities of the order of $150mm/sec$ and pressure $p = 9.38 - 21MPa$(Figure 10 in [21]). They also observed that the dependence of μ on velocity is smaller in lubricated interfaces than in the case of un-lubricated interfaces. (ii) The manufacturer at their relative product site states that the friction elements VM are structural elements characterized of low dissipation capacity, with sliding coefficient of friction of the order of 1%. [5]. (iii) The identification of another building isolated at the base by means of a similar HBIS from free vibration tests (Solarino building) yielded similar values for the friction coefficients, of the order of 1% [41].

[5] http://www.fipindustriale.it/index.php?area=106&menu=69&lingua=1

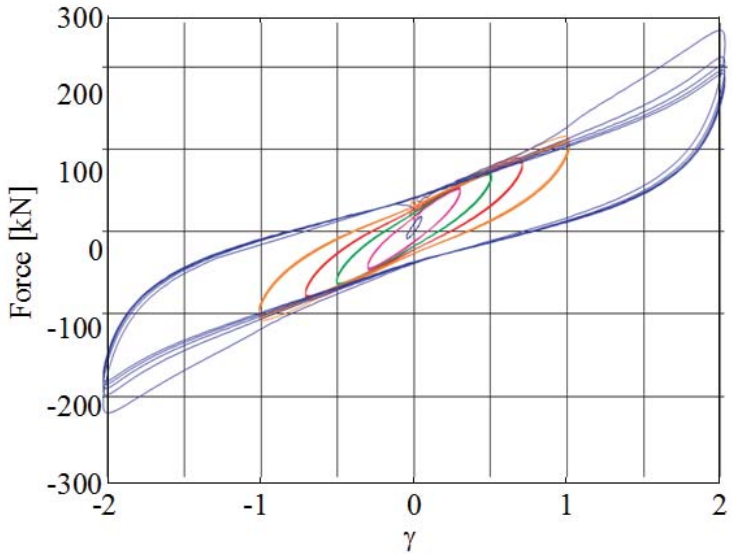

Figure 3.14: Typical hysteresis loops of HDRB at different strain amplitudes (the figure is reproduced from the manufacturer's catalogue).

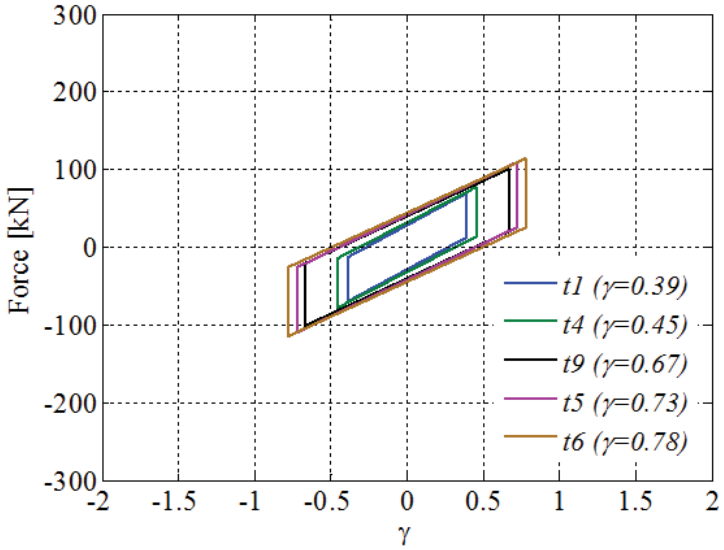

Figure 3.15: Hysteresis loops for the Augusta HDRB as obtained from the identification of tests 1,4,5,6 and 9.

3.4.3 Further discussion on the identified HBIS

The identified HBIS model properties can be used for the evaluation of the effective stiffness and period, k_{eff}, T_{eff}, the periods T_0, T_1 relative to the elastic and yielding phase, the frequencies f_{eff}, f_0, f_1, the yield displacement D_y, the energy dissipated per cycle by the rubber and sliding bearings W_D^{RB} and W_D^{SB} and the equivalent damping ratios ζ_{eq}, see expressions 3.7.(k_0, k_1, Q) refer to the single rubber bearing; for the evaluation of the isolation system periods, energies, damping ratios all 16 HDRBs used in the Augusta isolation system should be considered.

$$D_y = \frac{Q}{k_0 - k_1},\ k_{eff} = \frac{Q}{D} + k_1, \tag{3.7a}$$

$$T_{eff} = 2\pi\sqrt{\frac{m}{\sum_{i=1}^{16} k_{eff}}},\ T_0 = 2\pi\sqrt{\frac{m}{\sum_{i=1}^{16} k_0}},\ T_1 = 2\pi\sqrt{\frac{m}{\sum_{i=1}^{16} k_1}}, \tag{3.7b}$$

$$f_{eff} = \frac{1}{T_{eff}},\ f_0 = \frac{1}{T_0},\ f_1 = \frac{1}{T_1}, \tag{3.7c}$$

$$W_D^{SB} = \sum_{i=1}^{16} 4Q(D - D_y),\ W_D^{SB} = 4\mu N D, \tag{3.7d}$$

$$\zeta_{eq}^{RB} = \frac{W_D^{RB}}{\sum_{i=1}^{16} 2\pi k_{eff} D^2},\ \zeta_{eq}^{SB} = \frac{W_D^{SB}}{\sum_{i=1}^{16} 2\pi k_{eff} D^2}, \tag{3.7e}$$

$$\zeta_{eq} = \zeta_{eq}^{RB} + \zeta_{eq}^{SB} \tag{3.7f}$$

The properties estimated from Eqs 3.7 are shown in Table 3.4. The results of the table show how:

- The ratios k_0/k_1 tend to be essentially small varying between a minimum of 3.3 (test 6, $\gamma = 0.78$) to a maximum of 4.7 (test 1, $\gamma = 0.39$). The identification of the static and dynamic lab loops provided ratios k_0/k_1 that are significantly larger $(5 - 7)$. Naeim and Kelly in [1] provide ratios k_0/k_1 for typical HDRB equal to 3 and 6. In the light of the soft elastic stiffness k_0 identified by the Augusta tests, it was already discussed how

Table 3.4: Mechanical properties evaluated from the identified model parameters of the Augusta HBIS. First row: test number. Second row: strain amplitude. Third row: displacement amplitude. Fourth row: yield displacement. Fifth row: Elastic to post-elastic stiffness ratio. Sixth row: effective stifness of the HBIS. Seventh to ninth row: elastic, effective and post-elastic periods. Tenth to twelfth rows: elastic, effective and post-elastic frequencies. Thirteenth and fourteenth rows: energy dissipated per cycle by the rubber and friction devices. Fifteenth to seventeenth rows: equivalent damping ratios for the rubber, friction bearings and the overall HBIS. Eighteenth row: ratio of the equivalent damping ratios at γ and at $\gamma = 1$. Nineteenth row: ratio of the effective stiffness at γ and at $\gamma = 1$. The results of tests 3 and 8 are also presented, however they are probably unreliable, for the reasons mentioned above.

	test 1	*test 3*	*test 4*	*test 10*	*test 9*	*test 8*	*test 5*	*test 6*	
$\gamma = D/t_e$	0.39	0.45	0.45	0.67	0.67	0.69	0.73	0.78	
D	5.8	6.8	6.8	10	10.1	10.3	10.9	11.7	(cm)
D_y	1.1	1.5	1.5	2.6	2.7	2.7	2.8	0.0305	(cm)
k_0/k_1	4.7	3.3	4.0	3.5	3.5	2.9	3.4	3.4	(kN/m)
k_{eff}	1197	1262	1148	995	998	1040	1000	976	(kN/m)
T_0	1.30	1.43	1.44	1.67	1.67	1.44	1.68	1.70	(sec)
T_{eff}	2.14	2.13	2.21	2.44	2.44	2.37	2.43	2.5	(sec)
T_1	2.80	2.62	2.87	3.14	3.14	2.87	3.09	3.14	(sec)
f_0	0.77	0.70	0.70	0.60	0.60	0.59	0.60	0.59	(Hz)
f_{eff}	0.47	0.47	0.45	0.41	0.41	0.42	0.41	0.41	(Hz)
f_1	0.36	0.38	0.35	0.32	0.32	0.35	0.32	0.32	(Hz)
W_D^{RB}	86.2	99.0	106.3	187.4	191.7	170.5	215.8	243.4	$(kN \cdot m)$
W_D^{SB}	24.7	36.2	31.4	64.1	63.6	74.7	74.6	86.7	$(kN \cdot m)$
ζ_{eq}^{RB}	21.3	16.9	19.9	18.7	18.7	15.4	18.1	18.1	(%)
ζ_{eq}^{SB}	6.1	6.2	5.9	6.4	6.2	6.7	6.2	6.5	(%)
ζ_{eq}^{total}	27.4	23.0	25.8	25.1	24.9	22.1	24.3	24.6	(%)
$\zeta_{eq}(\gamma)/\zeta_{eq}(\gamma = 1)$	1.36	0.93	1.31	1.13	1.14	0.85	1.14	1.11	
$k_{eff}(\gamma)/k_{eff}(\gamma = 1)$	1.18	0.80	1.10	1.03	1.03	0.65	1.0	1.0	

the elastic stiffness is not a property with a clear physical interpretation, and therefore how k_0 and consequently the ratio k_0/k_1 are not easy to quantify.

- The effective stiffness k_{eff} varies from $900kN/m$ to $1197kN/m$, and tends to decrease with increasing displacement amplitude. This behavior is typical of HDRB. The isolation system should provide the necessary rigidity to prevent displacements and vibrations under frequently occurring loads such as wind and minor earthquakes, and

moreover the necessary flexibility to prevent the transmission of earthquake forces to the structure above a certain level [8].

- The effective period T_{eff} of the HBIS lies in the range $2.14 - 2.5sec$ and, as expected, tends to be longer under stronger motion. The effective period of the system is less than the period relative to the elastic phases, T_0, and smaller than the period relative to the yielding phases, T_1. Consequently $f_1 \leq f_{eff} \leq f_0$.
- The non-linear isolation system is not characterized by a single frequency; its bi-linear idealization shows how the system response is controlled by k_0 in the elastic phases and by k_1 in the yielding phases. The real period of the system will be somewhere in between (T_0, T_1). In fact, the fundamental period of the isolation system, as read from the displacement diagrams (Table 1.2, section 1.3) are within the range (T_0, T_1) and tend to be closer to the lower limit T_0. The identification of only one yielding branch and three elastic branches in the observed system response of test 9 might explain why T_0 dominates the system response, see Figure 3.21(a).
- The energy dissipated per cycle of motion, W_D increases with increasing amplitude, while the equivalent damping ratios are decreasing. This result is also confirmed in the literature [1]. The energy dissipated by the rubber bearings, W_D^{RB}, is in average three times greater than the energy dissipated in the LFSBs, W_D^{RB}. It should be highlighted however, that the main contribution of the sliders should be that of supporting a significant part of the weight of the superstructure and not dissipating energy. Given the identified building mass $m = 2,400tons$, the weight carried by the LFSB results equal to $N/W = 13,900/(2,400 * 9.807) \sim 60\%$ of the total weight of the building.
- A brief comment should be included herein on the dependence of the equivalent damping ratio ζ_{eq} on the ratio of the elastic and post-elastic stifnesses $\alpha = k_0/k_1$. Kelly and Naeim in [1] proved that ζ_{eq} and moreover its maximum value, depends directly on the ratio of the elastic and post-elastic stifnesses $\alpha = k_0/k_1$, see Eq. 3.8.

$$\zeta_{eq} = \frac{2\alpha}{\pi}\frac{y-1}{(y+a)y}, \quad where \quad y = \frac{D}{D_y} \geq 1, a = \frac{Q}{k_1 D_y} = \frac{k_0}{k_1} - 1 \tag{3.8a}$$

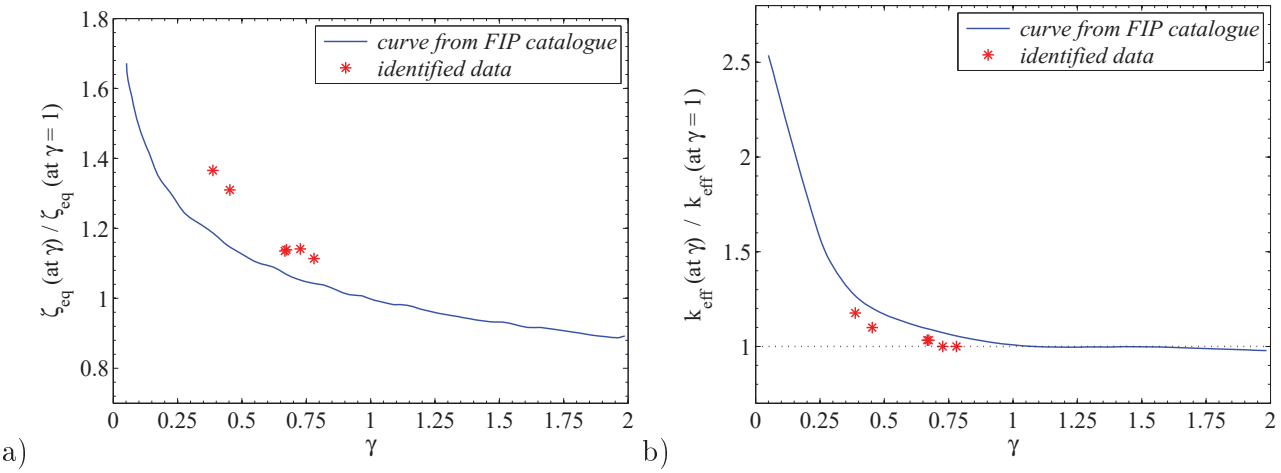

Figure 3.16: Identified $\zeta_{eq}(\gamma)/\zeta_{eq}(\gamma = 1)$ and $k_{eff}(\gamma)/k_{eff}(\gamma = 1)$ ratios for the HDRB used in the Augusta system (red points), sub-plots (a) and (b). In blue colour, typical $\zeta_{eq}(\gamma)/\zeta_{eq}(\gamma = 1)$ - γ and $k_{eff}(\gamma)/k_{eff}(\gamma = 1)$ - γ curves for the HDRB produced by FIP, as found in the manufacturer's catalogue.

$$\zeta_{max} = \frac{2\alpha}{\pi}[2(1+\alpha)^{\frac{1}{2}} + (2+\alpha)]^{-1}, \quad at \quad y = 1 + (1+\alpha)^{\frac{1}{2}} \tag{3.8b}$$

In fact the results of the table show that the smaller the k_0/k_1 ratio, the smaller the equivalent damping ratio.

- The last two rows of Table 3.4 provide the ratios of the identified equivalent damping ratio and effective stiffness at strain amplitude γ with respect to their corresponding value at $\gamma = 1$. $\zeta_{eq}(\gamma = 1) = 18.1\%$ and $k_{eff}(\gamma = 1) = 1590kN/m$, and are evaluated from the extrapolation of the corresponding identified data at $\gamma = 1$. Figures 3.16 show the identified $k_{eff}(\gamma)/k_{eff}(\gamma = 1) - \gamma, \zeta_{eq}(\gamma)/\zeta_{eq}(\gamma = 1) - \gamma$ relations in comparison to relative characteristic curves provided by the manufacturer in their catalogue. The corresponding ratios for tests 3 and 8 are not included in the graphs. The identified ratios $\zeta_{eff}(\gamma)/\zeta_{eff}(\gamma = 1)$ are always above the curve proposed by FIP, while the identified ratios $k_{eff}(\gamma)/k_{eff}(\gamma = 1)$ are always below the corresponding curve by FIP, indicating that the identified system is softer. The difference between suggested and identified ratios is maximum 13%. Unfortunately, there is no feedback on how

the curves were produced and to which elastomer they may refer, hence no further conclusions can be drawn on how the identified rubber bearing properties at different strain amplitudes compare to their expected values.

3.4.4 Matching of identified and experimental isolation system response for test 9 and energy equilibrium

The displacement response of the identified HBIS under test 9 is shown against the measured displacement in Figure 3.17. There is clearly a very good matching between experimental and identified displacements traces. This result demonstrates how the unidirectional system response of a symmetric isolation system can be successfully reproduced considering a simple one degree of freedom model. The ground floor and roof displacements of the identified rigid model are shown against the corresponding processed experimental displacements in Figures 3.18. The matching between identified and experimental traces is always good, however it appears that the identified system comes earlier to rest with a somewhat smaller residual displacement (1.59cm instead of 1.66cm). The time when the system comes to rest can be seen properly in the velocity and acceleration diagrams, see Figures 3.19 and 3.20. The identified system completes only one full cycle of motion due to energy dissipation by the friction damper and the bi-linear spring. Clearly, the observed floor accelerations are significantly different than the identified acceleration; the one degree of freedom rigid superstructure model cannot capture the effect of any mode higher than the fundamental isolation mode. However, the objective of the first stage identification was to find the non-linear properties of the isolation system. The properties of the superstructure in the linear response range are identified in the following.

The identified hysteretic loops for the rubber and friction devices are shown in Figure 3.21. Figure 3.21 (a) shows how the first branch of motion is characterized by an elastic and a yielding phase, while the last two branches of motion are purely elastic. In fact, slope discontinuities are visible in the acceleration history of the rigid model when there is a

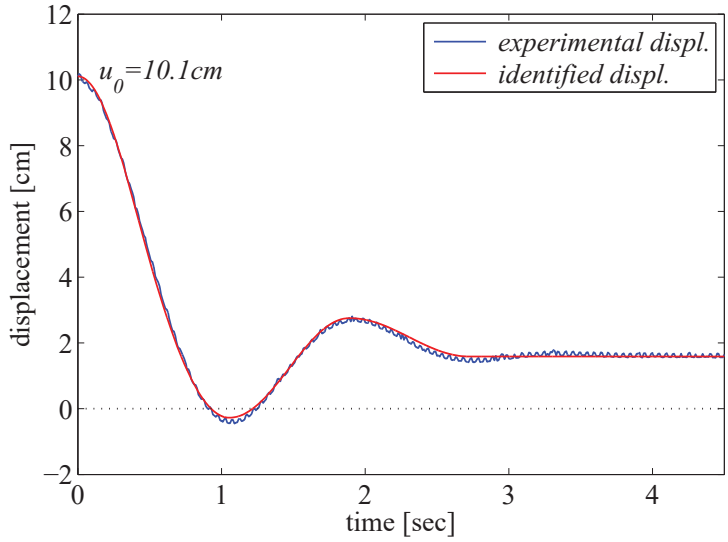

Figure 3.17: Comparison of experimental and identified deformation histories obtained from the identification of test 9.

transition from elastic to yielding phase. Slope discontinuities are also visible in the simulated velocity history every time that the velocity goes to zero and hence the friction force changes sign. These velocity slope discontinuities translate into jumps in the acceleration response history. The equation of motion 3.3 soon before and after the velocity drops to zero becomes:

$$m\,\ddot{u}_b^- + F_e + F_{f0} sign\dot{u}_b^- = 0 \; and \; m\,\ddot{u}_b^+ + F_e - F_{f0} sign\ddot{u}_b^- = 0 \tag{3.9}$$

Hence the acceleration jumps equals :

$$|\Delta\ddot{u}_b| = 2F_{f0}/m \tag{3.10}$$

For test 9 the acceleration jump noticed in the acceleration plots 3.20 would be $0.013g$. When the system comes to a rest the resisting force in the rubber bearings $F_e(u_r, 0) = -16 * 2.5 = -40kN$ is equilibrated by the force developed in the friction devices $F_f(u_b = u_r, \dot{u}_b = 0)$, with $|F_f(\dot{u}_b = 0)| < F_{f0} = \mu N = 157kN$.

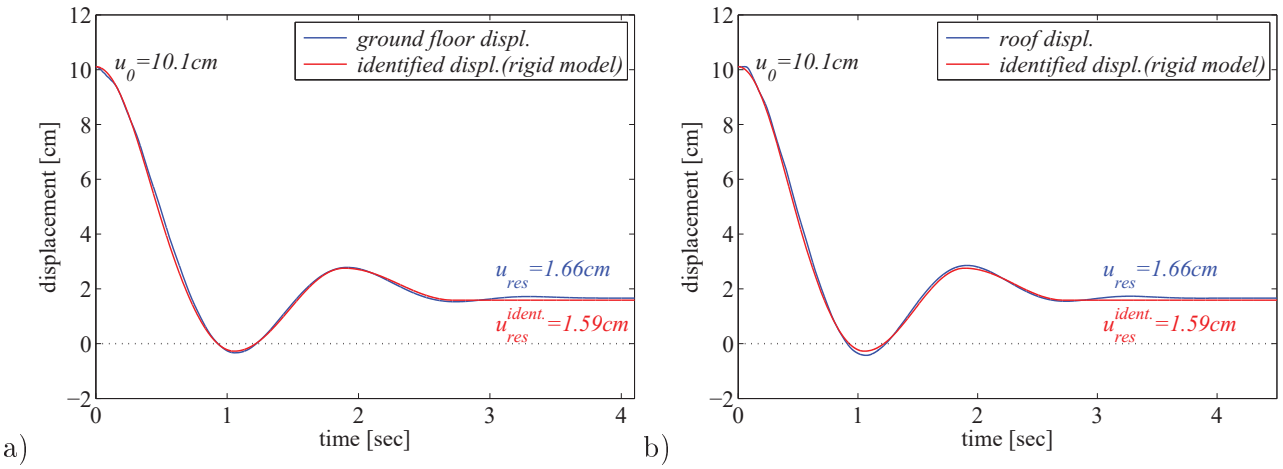

Figure 3.18: Comparison of experimental and identified displacement histories obtained from the identification of test 9. The identified HBIS displacement response is shown in red colour while the experimental ground floor and roof velocities are shown in blue colour; sub-plots (a) and (b).

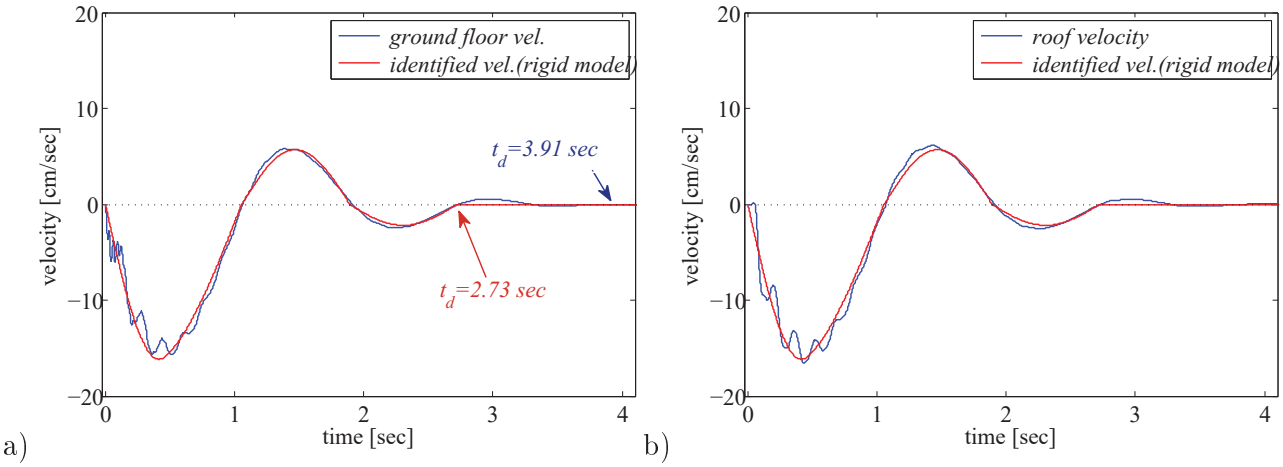

Figure 3.19: Comparison of experimental and identified velocity histories obtained from the identification of test 9. The identified HBIS velocity response is shown in red colour, while the experimental ground floor and roof velocities are shown in blue colour; sub-plots (a) and (b).

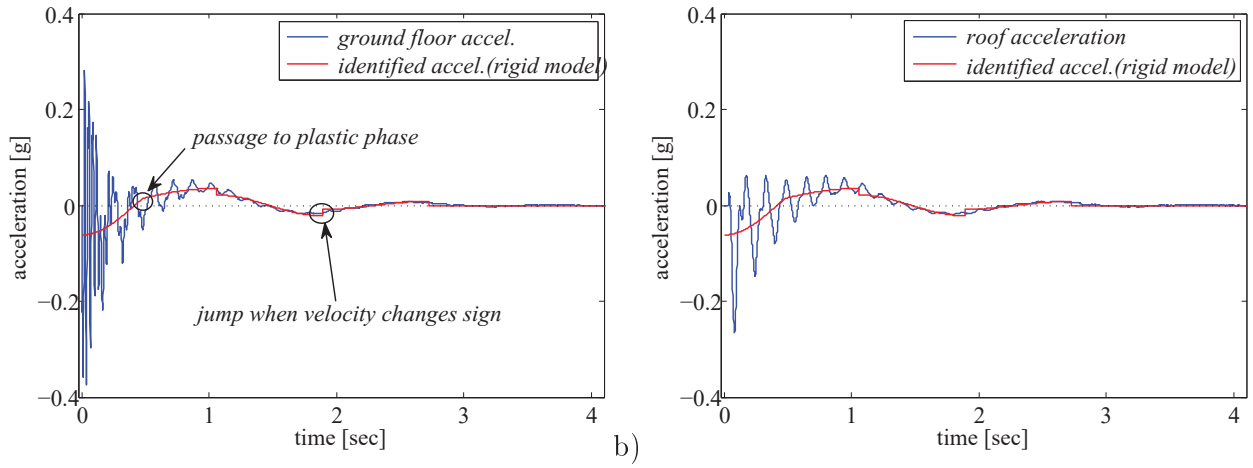

a) b)

Figure 3.20: Comparison of experimental and identified acceleration histories obtained from the identification of test 9. The identified HBIS acceleration response is shown in red colour, while the experimental ground floor and roof accelerations are shown in blue colour; sub-plots (a) and (b).

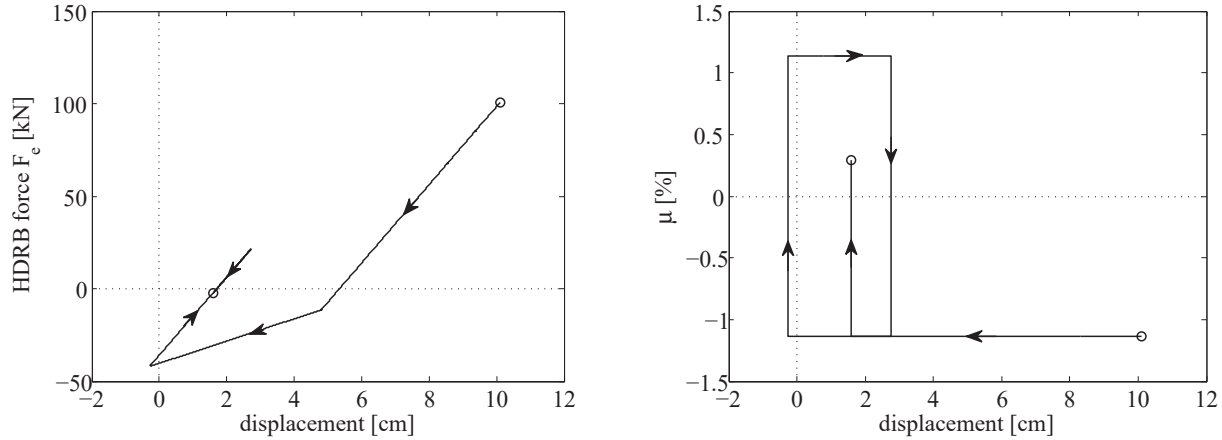

a) b)

Figure 3.21: Hysteretic loops for the identified bi-linear model (HDRB) and the identified Coulomb Friction model (LFSB) obtained from the identification of test 9; sub-plots (a) and (b).

To obtain the energy equilibrium, the equation of motion 3.3 is multiplied by an admissible displacement du_b and integrated in the time range $(0, t)$, see Eqs 3.11.

$$\int m\,\ddot{u}_b du_b + \int c\,\dot{u}_b du_b + \int F_e du_b + \int F_f du_b = \int p du_b \tag{3.11a}$$

$$\int_0^t m\,\ddot{u}_b \dot{u}_b d\tau + \int_0^t c\,\dot{u}_b \dot{u}_b d\tau + \int_0^t F_e \dot{u}_b d\tau + \int_0^t F_f \dot{u}_b d\tau = \int_0^t p \dot{u}_b d\tau \tag{3.11b}$$

After making use of integration by parts the dynamic equilibrium 3.11 can be re-written as:

$$E_K(t) + E_S(t) + E_{VD}(t) + E_{HDRB}(t) + E_{LFSB}(t) = E_S(0) + E_I t \tag{3.12a}$$

$$where \tag{3.12b}$$

$$E_K(t) = \frac{1}{2} m \dot{u}_b^2(t) \tag{3.12c}$$

$$E_S(t) = \frac{1}{2}\frac{F_e^2(u_b, \dot{u}_b)}{k_0} + \frac{1}{2}\frac{F_h^2(u_b, \dot{u}_b)}{k_h} \tag{3.12d}$$

$$E_{VD}(t) = \int_0^t c\,\dot{u}_b(\tau)^2 d\tau \tag{3.12e}$$

$$E_D^{RB}(t) = W_D^{RB}(t) + E_S(0) - E_S(t) \tag{3.12f}$$

$$W_D^{SB}(t) = \int_0^t F_e(u_b, \dot{u}_b)\dot{u}_b(\tau) d\tau \tag{3.12g}$$

$$E_D^{SB}(t) = \int_0^t F_f(sign(\dot{u}_b))\dot{u}_b(\tau) d\tau \tag{3.12h}$$

$$E_I(t) = \int_0^t p(\tau)\dot{u}_b(\tau) d\tau \tag{3.12i}$$

where $E_K(t)$ is the kinetic energy of the system, $E_S(t)$ is the stain energy stored in the elastic springs used for the description of the elastomeric bearings, see Figure 3.7(a).

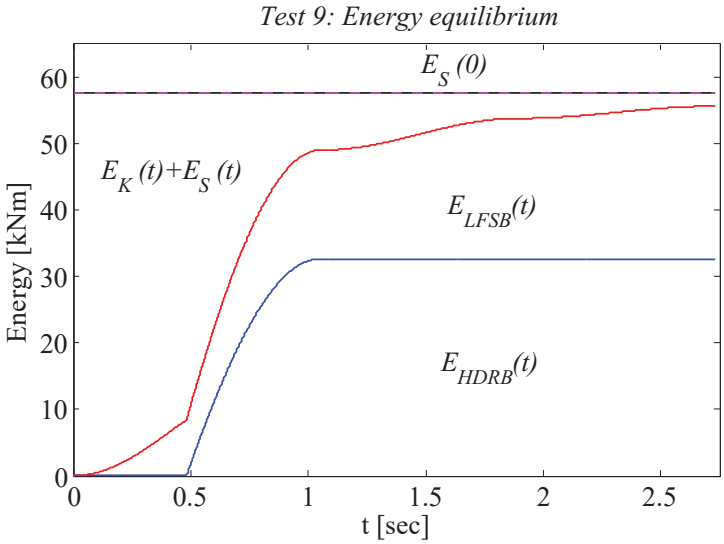

Figure 3.22: Energy dissipation in the identified Augusta HBIS.

$E_{VD}(t), E_D^{RB}(t), E_D^{SB}(t)$ are the energies dissipated in the linear viscous damper, the bi-linear spring and the friction slider respectively. $E_I(t)$ is the input energy; in the case of free vibration this equals zero. F_e, F_h are the restoring forces developed in the elastic springs of stiffness k_e, k_h used in the representation of the HDRB, see Figure 3.7(a). More information on the definition of $E_S(t), E_D^{RB}(t), E_D^{SB}(t)$ and the resisting forces F_e, F_h can be found in [56, 70].

Figure 3.22 shows the history of the kinetic, strain energy and the energy dissipated in the HBIS during the release test 9. The plot shows how the energy input initially to the system ($E_S(0)$), is transformed to kinetic ($E_K(t)$) and strain energy ($E_S(t)$) and energy dissipated by the rubber and friction bearings ($E_D^{RB}(t), E_D^{SB}(t)$). Since the viscous damping obtained from the identification of test 9 was zero, $E_{VD}(t) = 0$. The rubber bearings provide major contribution to energy dissipation through their non-linear behavior, see Figure 3.21(a). During elastic phases there is no energy dissipation in the HDRB, in fact elastic phases are translated to constant lines in the energy plot. The friction bearings are also involved in energy dissipation through their non-linear behavior, see Figure 3.21(b), although LFSB were identified by a small coefficient of friction $\mu \approx 1\%$. Increased dissipation in the sliders

could result to the excitation of higher modes through their stick-slip behaviour; this being an important disadvantage of sliding bearings [36].

3.4.5 Matching of identified and experimental isolation system response for tests 1,3,4,5,6,8 and 10

The response match in terms of HBIS displacement histories for the remaining tests identified can be seen in Figures 3.23 to 3.24. The identified one degree-of-freedom isolation systems provide displacement responses that match very satisfactorily the experimental ones. A trend observed in the identified responses is that of coming to rest earlier than what indicated by the experimental response, moreover with a smaller residual displacement than the observed one (of the order of 10% or less). A possible explanation could be the following. While the overall energy dissipated during the tests seems to be identified properly; a larger amount of hysteretic energy seems to be attributed to friction devices (higher μ, shortening of motion duration) and a smaller one to the rubber bearings (smoother stiffness, smaller residual displacements).

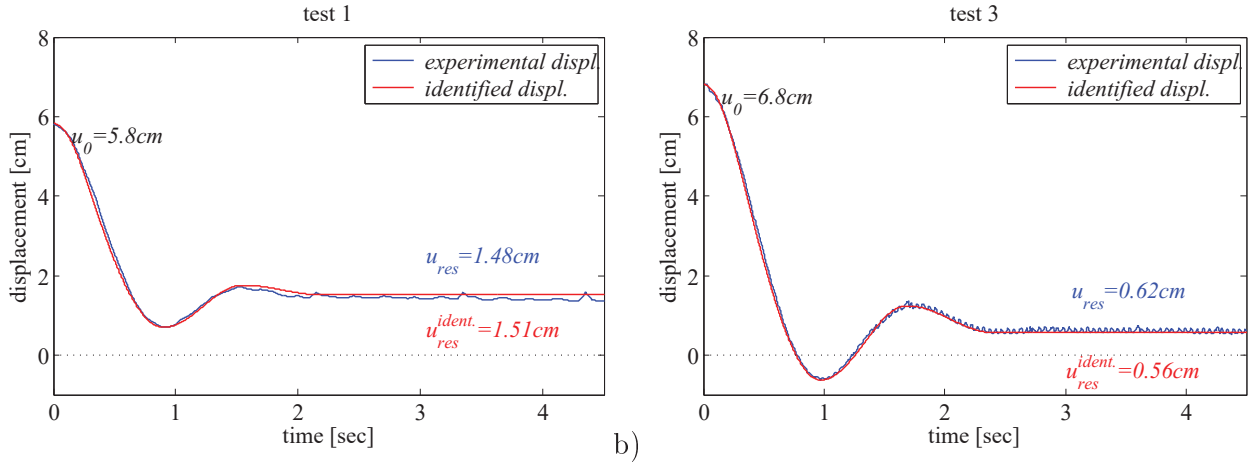

Figure 3.23: Comparison of experimental and identified HBIS displacements obtained from the identification of tests 1 and 3; sub-plots (a) and (b).

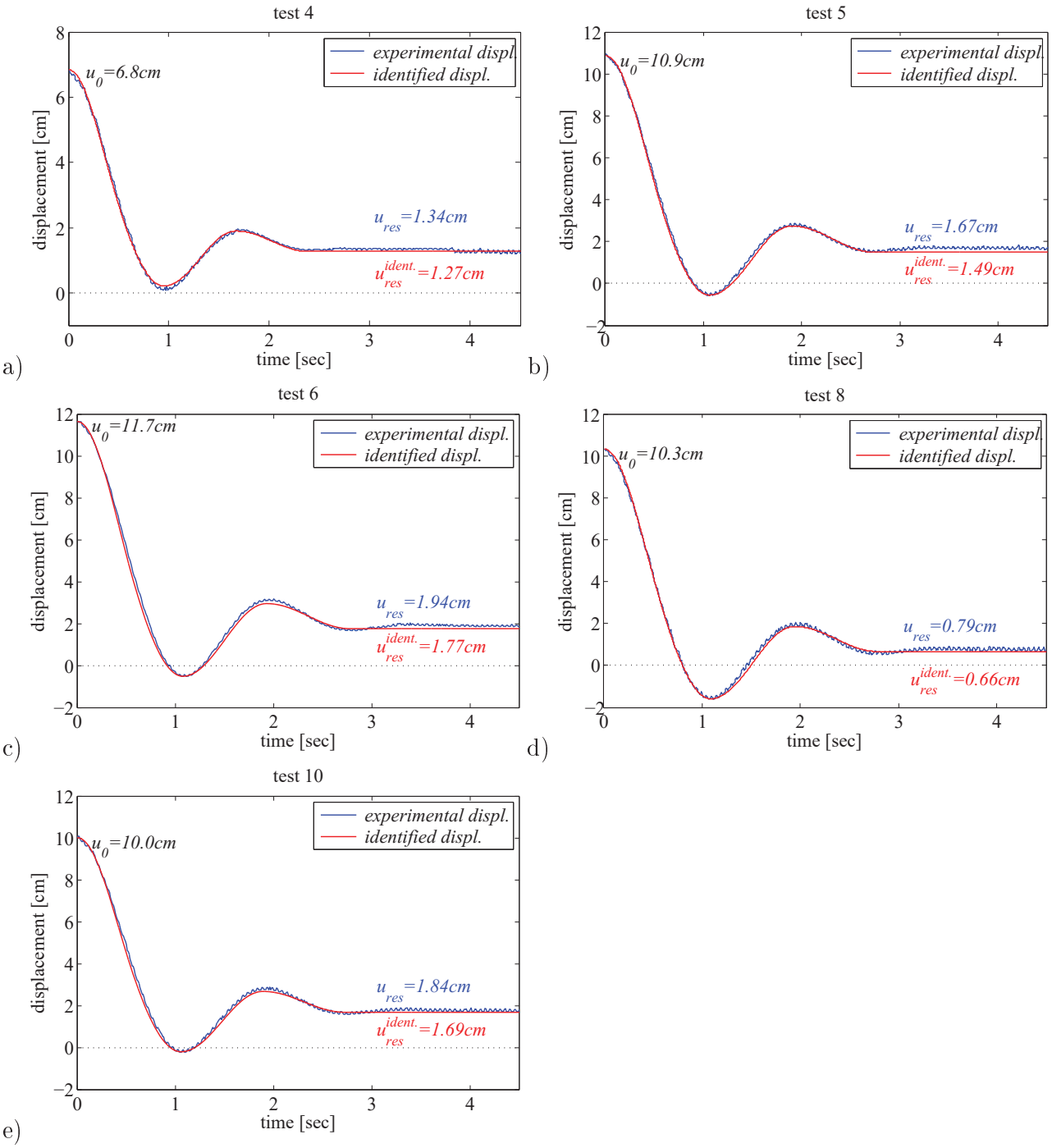

Figure 3.24: Comparison of experimental and identified HBIS displacements obtained from the identification of tests 4,6,8 and 10.

3.5 Identification of the flexible superstructure properties from the Augusta free vibration data

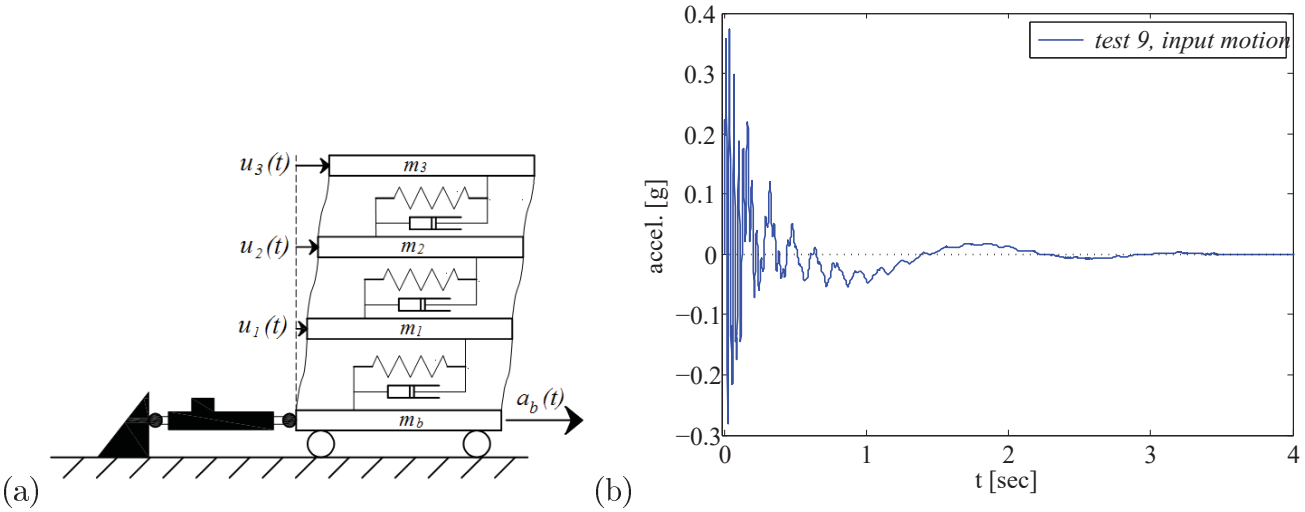

Figure 3.25: (a) Flexible superstructure model used for the identification of the Augusta building and (b) input motion $a_b(t) = \ddot{u}_b(t)$ for the fixed model under test 9.

The Augusta superstructure was designed to respond elastically at excitations that do not exceed the design level following the prescriptions of the Italian regulations [45, 63] [6]. Therefore, it is reasonable to assume that the superstructure responded within the linear-elastic range under the Augusta free vibration tests, since those were performed at very low amplitudes to ensure no damage to the finished building [33]. For the purposes of the identification, the superstructure is modeled as a viscously damped linear structural system fixed at the base, see Figure 3.25(a) . The non-linear contribution of the isolation system is considered indirectly, exciting the superstructure by the acceleration developed at the isolation system $\ddot{u}_b(t)$. $\ddot{u}_b(t)$ is the absolute acceleration recorded at the ground floor, just above the isolation system, during the experiments, see Figure 3.25(b).

[6] In terms of design spectrum, for reinforced concrete structures this implies a strength reduction factor $q = 1.5$.

The equation of motion for the linear superstructure model takes the following form:

$$\boldsymbol{M_{ss}}\,\ddot{\boldsymbol{u}}_{\boldsymbol{s}} + \boldsymbol{C_{ss}}\,\dot{\boldsymbol{u}}_{\boldsymbol{s}} + \boldsymbol{K_{ss}}\,\boldsymbol{u_s} = -\boldsymbol{M_s}\,\boldsymbol{\iota}\,\ddot{u}_b(t) \tag{3.13}$$

$$\boldsymbol{M_{ss}} = \begin{bmatrix} m_1 & & \\ & m_2 & \\ & & m_3 \end{bmatrix}, \quad \boldsymbol{C_{ss}} = \begin{bmatrix} c_{11} & c_{12} & c_{13} \\ c_{12} & c_{22} & c_{23} \\ c_{13} & c_{23} & c_{33} \end{bmatrix}, \quad \boldsymbol{K_{ss}} = \begin{bmatrix} k_{11} & k_{12} & k_{13} \\ k_{12} & k_{22} & k_{23} \\ k_{13} & k_{23} & k_{33} \end{bmatrix} \tag{3.14}$$

where $\boldsymbol{u_s}^T = [u_1, u_2, u_3]^T$ are the relative longitudinal displacements of the superstructure (relative with respect to the base, see Figure 3.25(a). $\boldsymbol{M_{ss}}, \boldsymbol{C_{ss}}, \boldsymbol{K_{ss}}$ are the mass, damping and stiffness matrices of the superstructure and $\boldsymbol{\iota}^T = [1, 1, 1]^T$ is the influence vector. $\boldsymbol{M_{ss}}$ is a diagonal matrix, with the lumped floor masses m_i $(i = 1, 2, 3)$ as diagonal entries, while $\boldsymbol{C_{ss}}$ and $\boldsymbol{K_{ss}}$ are full matrices, see Eq. 3.14.

Eq. 3.13 represents a coupled system of second order differential equations in which the independent variable is the time t and the dependent variables are the horizontal displacements $\boldsymbol{u}_s$. If the damping is classical, i.e. if the modes are orthogonal with respect to the system's damping matrix (other than orthogonal with respect to the mass and stiffness matrix), the equations of motion can be transformed to an uncoupled set of modal equations, Eq. 3.15(a), [2]. Each modal equation is solved for the modal coordinate $q_n(t)$ applying any known analytical or numerical method to determine the modal contributions to the response $\boldsymbol{u_{s,n}}(t) = \boldsymbol{\phi_n}\, q_n(t)$. The modal responses $\boldsymbol{u_{s,n}}(t)$ are then combined to obtain the total response $\boldsymbol{u_s}(t)$, Eq 3.15(b).

$$\ddot{q}_n(t) + 2\,\zeta_n\,\omega_n\,\dot{q}_n(t) + \omega_n^2\,q_n(t) = -\Gamma_n\,\ddot{u}_b(t) \quad (n = 1, 2, 3) \tag{3.15a}$$

$$\boldsymbol{u_s}(t) = \sum_{n=1}^{3} \boldsymbol{\phi}_n\, q_n(t) \tag{3.15b}$$

where $\boldsymbol{\phi}_n$ is the $n-th$ mode of the undamped system and ω_n, ζ_n the corresponding modal frequency and damping ratio.

3.5.1 System parameter vector for the linear superstructure model

Eqs 3.15 imply that the model parameters required for the description of the superstructure response are the following 18:

- 3 modal participation factors $\Gamma_1,\ \Gamma_2,\ \Gamma_3$;
- 3 modal periods $T_1,\ T_2,\ T_3$;
- 3 modal damping ratios $\zeta_1,\ \zeta_2,\ \zeta_3$;
- 3 first mode components $\phi_{11},\ \phi_{21},\ \phi_{31}$;
- 3 second mode components $\phi_{12},\ \phi_{22},\ \phi_{32}$;
- 3 third mode components $\phi_{13},\ \phi_{23},\ \phi_{33}$.

However the essential model parameters required for the simulation of the system response can be reduced to the following 12:

- 3 floor masses $m_1,\ m_2,\ m_3$;
- 3 modal periods $T_1,\ T_2,\ T_3$;
- 3 modal damping ratios $\zeta_1,\ \zeta_2,\ \zeta_3$;
- 3 first mode components $\phi_{11},\ \phi_{21},\ \phi_{31}$.

In the reduced system parameter vector, the modal participation factors have been replaced by the floor masses, which physically are more meaningful and easily quantifiable [7]. Given the mass distribution and the mode shapes the modal participation factors can be evaluated from the following expression:

$$\Gamma_n = \frac{L_n}{M_n} = \frac{\boldsymbol{\phi_n^T M_s \iota}}{\boldsymbol{\phi_n^T M_s \phi_n}} \tag{3.16}$$

The reduced system parameter vector includes only the first mode shape $\boldsymbol{\phi_1^T} = [\phi_{11},\ \phi_{21},\ \phi_{31}]^T$. excluding the two higher modes $\boldsymbol{\phi_2^T} = [\phi_{12},\ \phi_{22},\ \phi_{32}]^T$ and $\boldsymbol{\phi_3^T} = [\phi_{13},\ \phi_{23},\ \phi_{33}]^T$. In fact,

[7] An interesting commentary on Γ_n can be found in [2]:'Γ_n is usually referred to as a modal participation factor, implying that it is a measure of the degree to which the $n-th$ mode participates in the response. This terminology is misleading, however, because Γ_n is not independent of how the mode is normalized, nor a measure of the modal contribution to a response quantity '.

if $\boldsymbol{\phi_1}$ is known, $\boldsymbol{\phi_2}$ and $\boldsymbol{\phi_3}$ can be found solving the following constrained non-linear minimization problem:

$$\text{Minimize: } f_{min} = \boldsymbol{\phi_1^T M_{ss} \phi_2} + \boldsymbol{\phi_2^T M_{ss} \phi_3} + \boldsymbol{\phi_3^T M_{ss} \phi_1} \tag{3.17a}$$

$$\text{subject to: } c_1 = \phi_{12}\,\phi_{32} \leq 0, \quad c_2 = \phi_{13}\,\phi_{23} \leq 0, \quad c_3 = \phi_{23}\,\phi_{33} \leq 0 \tag{3.17b}$$

$$\text{and: } c_{eq,1} = \boldsymbol{\phi_2^T M_{ss} \phi_2} = 1, \quad c_{eq,2} = \boldsymbol{\phi_3^T M_s \phi_3} = 1 \tag{3.17c}$$

The solution to the minimization problem described in Eqs 3.17 provides a set of mode vectors which are orthonormal with respect to the mass matrix ($\boldsymbol{\phi_i^T M_{ss} \phi_j} = \delta_{ij}$, where $i, j = 1, 2, 3$). The inequality constraints, Eq. 3.17 (b), control the mode shape; for the typical 3 degree-of-freedom uni-dimensional system considered herein, the first mode has no nodes (all components have the same sign), the second mode has one node (one component is of different sign) and the third mode has two nodes (two components are of different sign).

The constrained optimization problem is solved in MATLAB using the *fmincon* function. The algorithm does not suffer from accuracy and stability issues. Extension of the algorithm to higher dimension problems would require the establishment of more inequality constrains, to ensure that the solution is reliable and unique. However this implies that the signs of the modal components, i.e. essentially the node positions, are known.

3.5.2 Fitness function for the identification of the Augusta superstructure model

The optimization problem for the identification of the Augusta superstructure was formulated as the minimization of the following fitness function:

$$f = \frac{\sum_{i=1}^{3} \int (\dot{u}_{exp}^{rel,i} - \dot{u}^{rel,i})^T (\dot{u}_{exp}^{rel,i} - \dot{u}^{rel,i})\, dt}{\sum_{i=1}^{3} \int \dot{u}_{exp}^{rel,i^T} \dot{u}_{exp}^{rel,i}\, dt} + \frac{\sum_{i=1}^{3} \int (\ddot{u}_{exp}^{rel,i} - \ddot{u}^{rel,i})^T (\ddot{u}_{exp}^{rel,i} - \ddot{u}^{rel,i})\, dt}{\sum_{i=1}^{3} \int \ddot{u}_{exp}^{rel,i^T} \ddot{u}_{exp}^{rel,i}\, dt} \tag{3.18}$$

where $\dot{u}^{rel,i}_{exp}, \ddot{u}^{rel,i}_{exp}$ are the relative to the base i-floor velocity and acceleration histories obtained from the processing of the Augusta free vibration records. $\dot{u}^{rel,i}, \ddot{u}^{rel,i}$ are the corresponding simulated relative velocity and acceleration histories. The relative superstructure response was generated for each candidate system parameter vector $\boldsymbol{S} = [m_1, m_2, m_3, T_1, T_2, T_3, \zeta_1, \zeta_2, \zeta_3, \phi_{11}, \phi_{21}, \phi_{31}]$ implementing classical modal superposition, Eqs 3.15. The optimal solution is the solution providing floor velocities and accelerations which match the observed ones. The reason why the relative displacements were not included in the fitness function Eq. 3.18 is some uncertainty on the reliability of the processed relative displacements, an issue discussed in detail in Chapter 2 (Signal Processing). Another relevant point that should be mentioned is that only the response in the first two seconds of motion was considered in the evaluation of the fitness function. The observed relative free vibration response is damped significantly after $2sec$, thus little and probably meaningless information can be retrieved from the last segment of motion.

The CMA-ES was ran 10 times on the free vibration data of tests 4,5,9 and 10. Test 1 was a test of a very small amplitude and hence was not considered herein. Tests 3 and 8 provided doubtful results in the identification of the HBIS and thus were not included in the superstructure system identification [8]. The population size was doubled in every restart of the algorithm, while all remaining CMA-ES parameters were set to their default value. The identification was performed in a bounded search space to ensure the occurrence of feasible solutions. The start point and the search space considered are given in Table 3.5. An extra parameter was added to the identification problem, i.e. the total superstructure mass m_s. The algorithm was restrained to look for solutions for which $m_s = m_1 + m_2 + m_3$. This was done by adding the penalty term $(m_s - m_1 - m_2 - m_3)^2/m_s^2$ to the fitness function f, Eq. 3.18.

[8] Tests 3 and 8 followed the unsuccessful release tests 2 and 7; the building was not recentered upon repetition of 7, and probably was not recentered after upon repetition of test 2.

Table 3.5: Start point and search space considered in the identification of the Augusta superstructure model. First column: model parameters. Second column: initial point for the identification. Third column: lower bound properties. Fourth column: upper bound properties. The periods are expressed in *sec*, the corresponding frequency value in Hz is given within brackets.

	start value	*lower bound*	*upper bound*
m_1 $(tons)$	571	400	1390
m_2 $(tons)$	571	400	1390
m_3 $(tons)$	248	175	1390
m_s $(tons)$	1390	1180	1600
T_1 (sec)	0.15 (6.6 Hz)	0.10 (10 Hz)	1 (1 Hz)
T_2 (sec)	0.07 (13 Hz)	0.05 (20 Hz)	1 (1 Hz)
T_3 (sec)	0.05 (20 Hz)	0.02 (50 Hz)	1 (1 Hz)
ζ_1 (%)	1	0	10
ζ_2 (%)	1	0	10
ζ_3 (%)	1	0	10
$\boldsymbol{\phi_1}$	$\begin{pmatrix}0.014\\0.028\\0.042\end{pmatrix}$	$\begin{pmatrix}0\\0\\0\end{pmatrix}$	$\begin{pmatrix}1\\1\\1\end{pmatrix}$

3.5.3 Identified Augusta superstructure models

The initial guess for the total mass was $m_s = 1,390 tons$, i.e. the superstructure mass for the finished building as estimated by the structural designer. This mass was distributed to the floors according to their areas, resulting to $m_1 = m_2 = 571 tons$ for the two bottom floors and $m_3 = 248 tons$ for the appendix. The structural periods were estimated to $0.15 sec, 0.07 sec, 0.05 sec$ ($6.6 Hz, 13 Hz, 20 Hz$ in terms of frequencies); values corresponding to the Fourier Amplitude Spectra peaks of the recorded accelerations, see Figures 1.17. The modal damping ratio was taken 1% for all modes. The first mode shape was assumed to be linearly increasing with height and was approximated to $\boldsymbol{\phi_1}^T = [0.014, 0.028, 1]^T$ (the initial guess for $\boldsymbol{\phi_1}$ was normalized so that the first modal mass takes unit value). The lower bounds for the floor masses were $400 tons$ for the first and second floor masses and $175 tons$ for the roof mass. The corresponding upper bound was $1,390 tons$ for all m_i. The superstructure mass m_s was allowed to vary $\pm 15\%$ with respect to the design estimate $1,390 tons$. The lower

bounds for T_1, T_2, T_3 were $0.1, 0.05, 0.02sec$ $(10, 20, 50Hz)$ respectively. The upper bound was $1sec$ $(1Hz)$ for all modal periods. Finally, the search space for the modal damping ratios was $[0, 10]\%$, while the search space for first modal components ϕ_{i1} was $[0, 1]$.

The superstructure model parameters obtained from the identification of tests 4,5,6,9 and 10 are provided in Table 3.6. The mode shapes corresponding for the identified system are shown in Figure 3.26. $\boldsymbol{\phi_1}$ was obtained from the identification, while $\boldsymbol{\phi_2}, \boldsymbol{\phi_3}$ where evaluated a posteriori from the solution of the minimization problem shown in Eq. 3.17. The identified system vector reported herein corresponds to the optimal solution provided by the CMA-ES. As in the case of the identified HBIS, the solution provided by the CMA-ES is not unique; the identification of different tests results to somewhat different systems. Moreover, independent identification runs on the same set of data provide often different system parameter vectors. The solution reported herein is the optimal solution, i.e. the one which corresponds to a local minimum of the fitness function Eq. 3.18 and shows increased repeatability.

Observation of Table 3.6 and Figure 3.26 show that:

- The superstructure mass m_s, the two first modal periods T_1, T_2 and the second modal damping ratio ζ_2 are the identified properties with the lowest scatter. On the contrary, the first and third damping ratios ζ_1 and ζ_3 are the identified properties with the largest scatter $(> 20\%)$.

- The identified superstructure mass seems to be somewhat larger than the one estimated by the structural designer, approximately $7 - 15\%$.

- Tests 5, 6, 9 and 10, which are tests of similar amplitude, yield the same modal periods (frequencies); with one exception however. $T_3 = 0.03sec$ $(f_3 = 33Hz)$ for test 10 and $T_3 = 0.06sec$ $(f_3 = 18Hz)$ for the remaining tests. This is a very interesting output; the Fourier Amplitude Spectra of the recorded accelerations, shown in Figures 1.17, imply that there are essentially 4 structural frequencies. The model adapted herein is a 3DOF model unable to catch more than three modal frequencies. Test 4, being a

Table 3.6: Identified Augusta superstructure models. First column: model properties. Second to sixth column: optimal solutions (system parameter vectors) obtained from the identification of tests 4,5,6,9 and 10. Herein, the modal shape ordinates are normalized so that $\phi_{31} = 1$ The tests are organized in terms of increasing amplitude (peak base floor acceleration-PBA). Seventh to ninth column: statistics on the obtained properties (mean, standard deviation and coefficient of variation). The fitness value (error) corresponding to the optimal solution is given in the last row of the table. The number of times the solution was repeated over the total number of identification runs are given in the last row within brackets.

	test 4	*test 10*	*test 9*	*test 5*	*test 6*	*avg*	*stdev*	*cov*(%)
$PBA(g)$	0.329	0.363	0.374	0.419	0.425			
$m_1\ (tons)$	710	400	667	690	784	650	146.5	23
$m_2\ (tons)$	544	840	536	466	446	567	158.7	28
$m_3\ (tons)$	282	248	254	291	363	288	45.6	16
$m_s\ (tons)$	1544	1488	1459	1453	1594	1508	60.1	4
$T_1\ (sec)$	0.26	0.27	0.27	0.27	0.27	0.27	0.00	1
$T_2\ (sec)$	0.08	0.09	0.09	0.09	0.09	0.09	0.00	2
$T_3\ (sec)$	0.05	0.03	0.06	0.06	0.06	0.05	0.01	22
$f_1\ (Hz)$	3.9	3.7	3.7	3.8	3.7	3.77	0.05	1
$f_2\ (Hz)$	12.1	11.7	11.6	11.6	11.4	11.70	0.28	2
$f_3\ (Hz)$	18.8	33.2	18.1	18.1	18.0	21.23	6.70	32
$\zeta_1\ (\%)$	1.1	1.8	3.2	4.2	2.5	0.03	0.01	46
$\zeta_2\ (\%)$	6.0	5.4	6.3	6.4	5.4	0.06	0.00	8
$\zeta_3\ (\%)$	1.8	4.0	2.5	2.7	2.4	0.03	0.01	30
$\boldsymbol{\phi}_1$	$\begin{pmatrix}0.446\\0.471\\1.0\end{pmatrix}$	$\begin{pmatrix}0.471\\0.724\\1.0\end{pmatrix}$	$\begin{pmatrix}0.452\\0.812\\1.0\end{pmatrix}$	$\begin{pmatrix}0.456\\0.817\\1.0\end{pmatrix}$	$\begin{pmatrix}0.467\\0.821\\1.0\end{pmatrix}$	$\begin{pmatrix}0.456\\0.798\\1.0\end{pmatrix}$	$\begin{pmatrix}0.01\\0.04\\0\end{pmatrix}$	$\begin{pmatrix}2\\5\\0\end{pmatrix}$
error	$0.077^{(2/10)}$	$0.081^{(3/10)}$	$0.067^{(4/10)}$	$0.063^{(6/10)}$	$0.063^{(8/10)}$			

test of lower amplitude, resulted to somewhat smaller modal periods with respect to tests 5,6, and 9.

- The first mode shapes identified from tests 4,5,6 and 9 are essentially the same, see also Figure 3.27. Small variations are found in the second mode shapes of the identified systems. These differences become larger in the third mode shapes. Once more test 10 is the test providing different results. The differences in the obtained mode shapes can be attributed to the different mass distributions obtained from the identification of the single tests, see Table 3.7. All tests but test 10 indicate a decrease of the mass

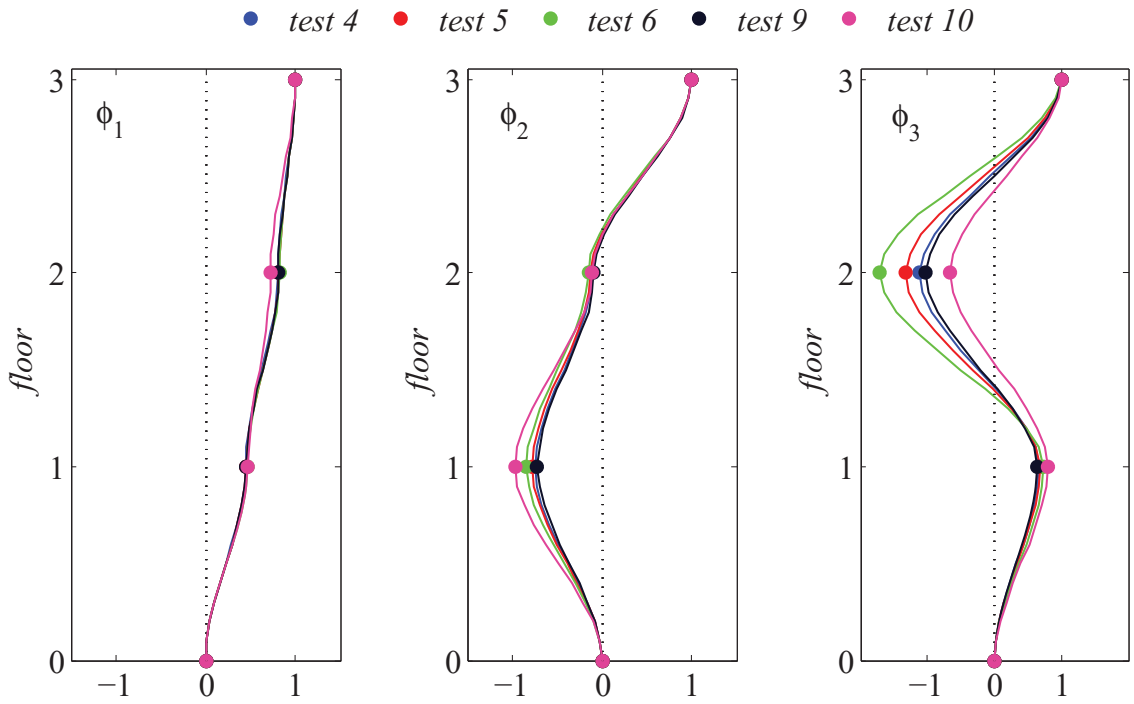

Figure 3.26: Vibration mode shapes of the Augusta superstructure obtained from the identification of tests 4,5,6,9 and 10.

Table 3.7: Identified floor mass ratios m_i/m_s, where m_i $(i = 1, 2, 3)$ is the identified lumped mass at floor-i and m_s the identified superstructure mass. The tests are ordered in terms of increasing Peak Base floor Acceleration (PBA).

	test 4	*test 10*	*test 9*	*test 5*	*test 6*
$PBA(g)$	0.329	0.363	0.374	0.419	0.425
m_1/m_s	0.46	0.27	0.46	0.47	0.49
m_2/m_s	0.35	0.56	0.37	0.32	0.28
m_3/m_s	0.18	0.17	0.17	0.20	0.23
$(m_1+m_2+m_3)/m_s$	1.00	1.00	1.00	1.00	1.00

with the superstructure height : $m_1 \approx 0.45m_s, m_2 \approx 0.35m_s, m_3 \approx 0.20m_s$. The roof lies at the top of the building and occupies a significant smaller area than any other floor hence it is reasonable to be identified with the lowest mass, see building exterior photo 1.1 . The second floor has the same area as the first one, however there is a terrace on this floor, and there dead and live load is reduced.

- The first and third modal damping ratios are identified with an average value of 3% for all tests considered. This is a common value used in the design of RC structures at the working stress levels [2]. Most building codes make reference to a 5% damping ratio in the code-specified earthquake forces and design spectrum. Test 4, being a test of smaller energy input, provides first and third modal damping ratios of the order of 1%, implying a decreasing energy dissipation capacity with decreasing amplitude.

- The identification of all tests provided high damping ratios for the second mode, of the order of 6%. This output is discussed in greater detail in section 3.5.5.

All tests considered were identified successfully, providing systems whose response matches very closely the observed one - in fact the error for the optimal solutions was much less than 10%. Figures 3.27 to 3.30 show the matching between experimental and identified relative response (first floor and roof velocities, accelerations, displacements and drifts) for test 9. The matching is very satisfactory in terms of relative velocities and accelerations, however it is less satisfactory in terms of displacements and drifts. The identified displacements resemble very well the experimental ones in the initiation of motion, when the peak response occurs, but the traces become somewhat different ever after. The distance between experimental and identified displacements becomes more evident when the drifts are evaluated. Two possibilities can be considered at this point (i) either the identified model is not able to simulate properly the system displacement response and/or (ii) the relative displacements recovered by the processing of the relative accelerations contain some error (noise). Probably there is truth in both points raised. The implementation of a unidirectional, viscously damped linear system for the simulation of the superstructure might be limiting. Moreover, the processing of low amplitude motions, which tend to suffer from low SNR, could lead to unreliable displacement estimates, see Chapter 2 on Signal Processing.

Figure 3.31 (a) shows the time variations of the kinetic, strain and viscously damped energies for the identified system under test 9. The sum of $E_k(t)$, $E_S(t)$ and $E_D(t)$ equals

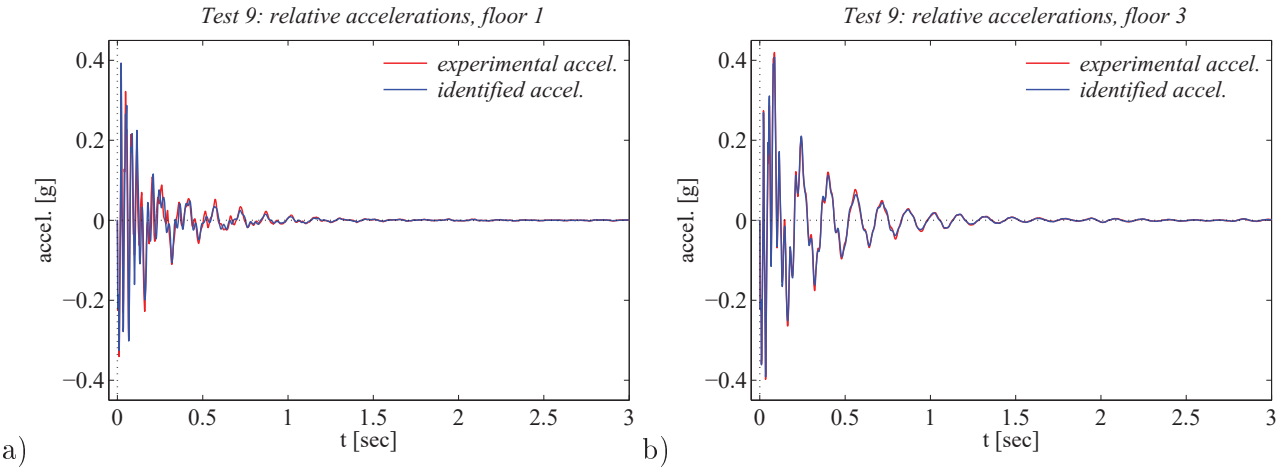

a) b)

Figure 3.27: Comparison of identified and experimental relative accelerations under test 9: (a) first floor and (b) roof responses.

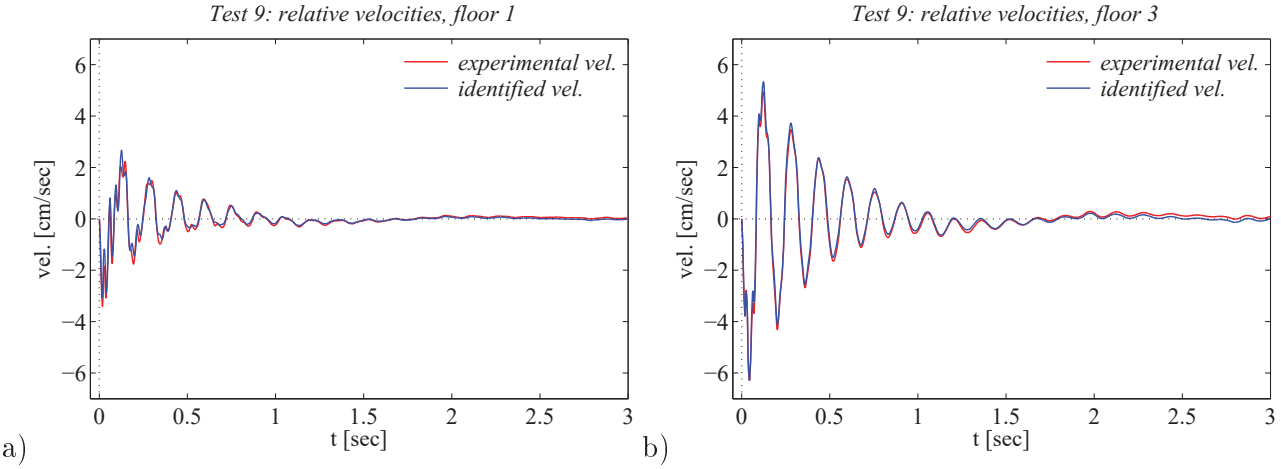

a) b)

Figure 3.28: Comparison of identified and experimental relative velocities under test 9: (a) first floor and (b) roof responses.

the energy input in the system $E_I(t)$, see Eq. 3.19.

$$E_K(t) + E_S(t) + E_D(t) = E_I(t), \tag{3.19a}$$

$$E_K(t) = \frac{1}{2}\dot{\boldsymbol{u}}_{\boldsymbol{s}}(t)^T \boldsymbol{M}_{\boldsymbol{ss}}\dot{\boldsymbol{u}}_{\boldsymbol{s}}(t), \quad E_S(t) = \frac{1}{2}\boldsymbol{u}_{\boldsymbol{s}}(t)^T \boldsymbol{K}_{\boldsymbol{ss}}\boldsymbol{u}_{\boldsymbol{s}}(t), \tag{3.19b}$$

$$E_D(t) = \int_0^t \dot{\boldsymbol{u}}_{\boldsymbol{s}}(\tau)^T \boldsymbol{C}_{\boldsymbol{ss}}\dot{\boldsymbol{u}}_{\boldsymbol{s}}(\tau)d\tau, \quad E_I(t) = -\int_0^t \dot{\boldsymbol{u}}_{\boldsymbol{s}}(\tau)^T \boldsymbol{M}_{\boldsymbol{s}\iota}\ddot{\boldsymbol{u}}_{\boldsymbol{b}}(\tau)d\tau \tag{3.19c}$$

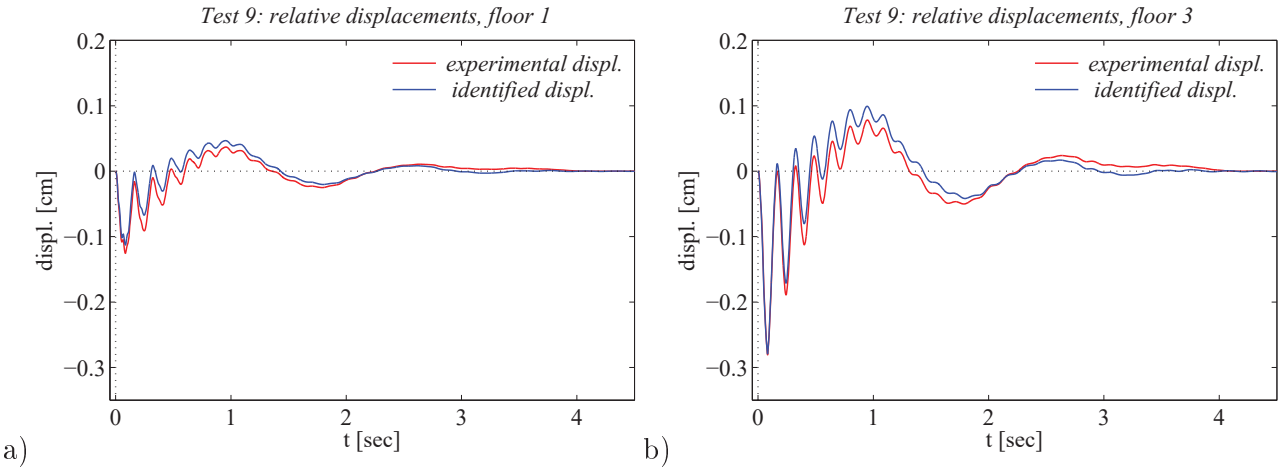

a) b)

Figure 3.29: Comparison of identified and experimental relative displacements under test 9: (a) first floor and (b) roof responses.

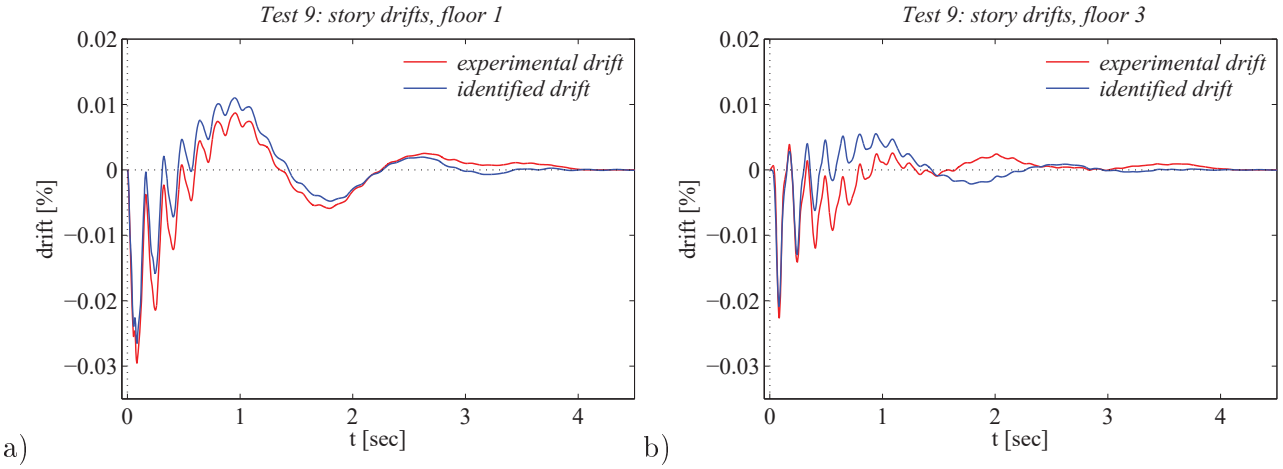

a) b)

Figure 3.30: Comparison of identified and experimental drifts under test 9: (a) first floor and (b) roof responses.

Figure 3.31 (b) shows the modal energy histories, defined in Eq. 3.20. The concept of modal energies provides an energy perspective to the evaluation of the dominant modes. Modal energy criteria find application in structural control problems. Pang et al. in [71] propose a modal energy control algorithm for the reduction of the response of a structure to strong motion. Figure 3.31 (b) clearly shows how that the energy input is predominant in the first structural mode. The energy contribution of the second mode is by no means

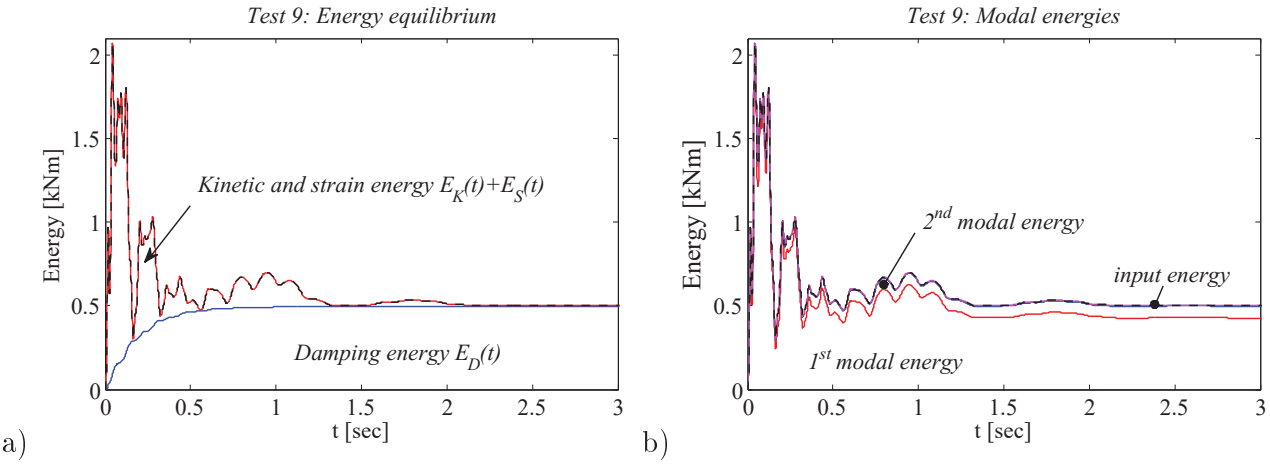

Figure 3.31: (a) Time variation of energy dissipated by viscous damping and of kinetic plus strain energy for the identified system under test 9. (b) Time variation of the input energy and the corresponding modal energies.

negligible. The energy input to the third mode is trivial, implying small participation of the highest mode to the system response.

$$E_n(t) = -\int_0^t \boldsymbol{\phi_n^T \dot{u}_s(\tau)^T M_{ss} \iota} \ddot{u}_b(\tau) d\tau, \quad \sum_{n=1}^{3} E_n(t) = E_I(t) \tag{3.20}$$

3.5.4 Stiffness and damping matrices

The stiffness and damping coefficients k_{ij} and c_{ij} where not among the identified system parameters, nevertheless they can be easily evaluated in a post-processing level of the obtained properties. The damping matrix can be constructed from the identified damping ratios ζ_n by superposition of modal damping matrices, according to Eq. 3.21. The damping matrix provided by this expression is classical, i.e. the modes are orthogonal with respect to $\boldsymbol{C_{ss}}$. This is a necessary condition for the decoupling of the system equations of motion 3.13 and the application of classical modal superposition method. As mentioned by Chopra [2] : 'Classical damping is an appropriate idealization if similar damping mechanisms are distributed throughout the structure (e.g., a multistory building with a similar structural system and structural materials over its height).' Of course, for the reduced, fixed base superstructure

model subjected to moderate to low ground motion this is a reasonable assumption. The assumption of classical damping is debatable for the study of the overall base isolated structure, even if the structure itself has classical damping. This is because in the common DOFs there is contribution from both subsystems; contribution of the isolation system, which is characterized by increased hysteretic capacity and the superstructure.

$$\boldsymbol{C_{ss}} = \boldsymbol{M_{ss}}(\sum_{1}^{3} \frac{2\zeta_n \omega_n}{M_n} \boldsymbol{\phi_n} \boldsymbol{\phi_n^T}) \boldsymbol{M_{ss}} \tag{3.21}$$

where $M_n = 1$ is the n^{th} modal mass

The stiffness matrix can be evaluated from Eq. 3.23. For this expression to be valid, the modes should be normalized so that the modal masses take unit values.

$$\boldsymbol{K}_{modal} = \boldsymbol{I}\boldsymbol{\Omega}_s^2 \rightarrow \boldsymbol{\Phi}_s^T \boldsymbol{K_{ss}} \boldsymbol{\Phi_s} = \boldsymbol{\Omega}_s^2 \rightarrow \boldsymbol{K_{ss}} = (\boldsymbol{\Phi}_s^T)^{-1} \boldsymbol{\Omega}_s^2 (\boldsymbol{\Phi_s})^{-1} \tag{3.22}$$

where $\boldsymbol{K}_{modal}$ is the modal stiffness matrix and $\boldsymbol{\Omega}_s^2$ a diagonal matrix with entries the modal frequencies.Eq. 3.22 can be re-written as:

$$\boldsymbol{K_{ss}} = \boldsymbol{M_{ss}} \left(\sum_{n=1}^{3} \frac{\omega_n^2}{M_n} \boldsymbol{\phi_n} \, \boldsymbol{\phi_n}^{\boldsymbol{T}} \right) \boldsymbol{M_{ss}} \tag{3.23}$$

Substituting in Eqs 3.21, 3.23 the superstructure properties identified by test 9, we obtain the following stiffness and damping matrices:

$$\boldsymbol{C_{ss}} = \begin{bmatrix} 4.65 & -0.62 & -1.14 \\ -0.62 & 2.02 & -0.70 \\ -1.14 & -0.70 & 1.47 \end{bmatrix} (*10^3 kNs/m), \quad \boldsymbol{K_{ss}} = \begin{bmatrix} 4.22 & -2.45 & 0.25 \\ -2.45 & 3.73 & -1.68 \\ 0.25 & -1.68 & 1.39 \end{bmatrix} (*10^6 kN/m) \tag{3.24}$$

3.5.5 Discussion

An intriguing result obtained from the identification of the Augusta superstructure was the high second modal damping ratio, $\zeta_2 \approx 6\%$. Figures 3.32 show the peak relative superstructure response in terms of relative to the base displacements, velocities and accelerations, as

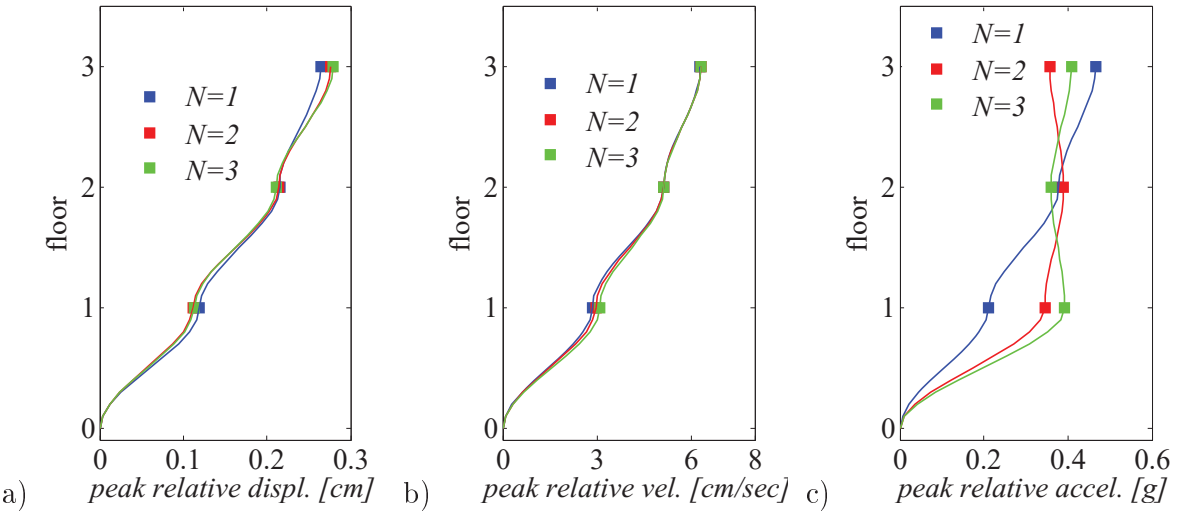

Figure 3.32: Peak relative displacement, velocity and acceleration; sub-plots (a), (b) and (c). The peak response is approximated considering N=1,2 or 3 modes. When all modes are considered (N=3) the response is the exact one.

identified from the data of test 9. The peak response is built considering $N = 1, 2, 3$ modes. When $N = 3$ all modes are considered and the response is the exact one [9]. Observation of the figures shows that the first mode response can fit the exact peak floor displacement and velocity responses with error less than 10%. However, at least 2 modes should be considered for a good approximation of the acceleration responses, i.e. of the inertia forces (shear forces). The contribution of the higher modes seems to be more prominent for the first floor acceleration.

Figure 3.33 shows the time variation of three modal accelerations at the first floor of the fixed base building model. The first floor acceleration is shown for completeness at the last sub-plot. Observation of the figure reveals that the second modal acceleration is important for building up the peak acceleration response within the first instants of motion, however its contribution to the system response becomes trivial in the following time span.

Exciting higher frequencies serves for increased energy dissipation, since the energy is dissipated faster at higher frequencies. Consider for instance a SDOF oscillator characterized

[9] Exact because a linear, classically damped model is assumed herein.

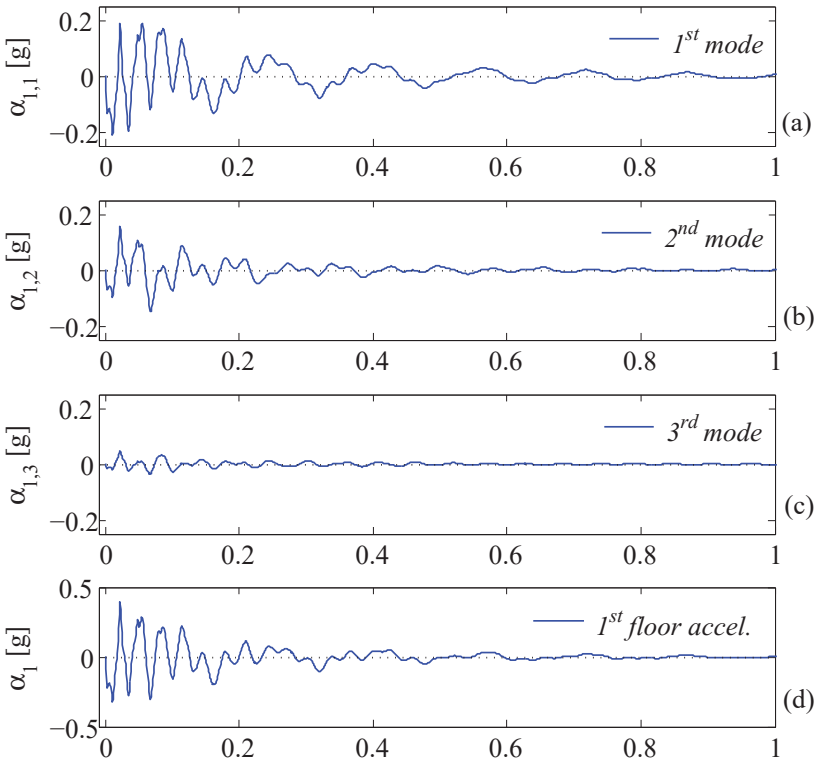

Figure 3.33: Modal contributions to the first floor relative acceleration for test 9: sub-plots (a), (b) and (c). The first floor acceleration, obtained from modal superposition is shown in sub-plot (d).

by natural frequency ω and damping ratio ζ. The displacement, velocity and acceleration response $u(t)$ of the oscillator to an impulsive load which translates to an initial velocity v_0 is:

$$u(t) = \frac{v_0}{\omega_D} exp(-\zeta\omega t) sin\omega_D t \tag{3.25a}$$

$$\dot{u}(t) = \frac{v_0}{\sqrt{(1-\zeta^2)}} exp(-\zeta\omega t) cos(\omega_D t - \theta) \tag{3.25b}$$

$$\ddot{u}(t) = \omega_D v_0 exp(-\zeta\omega t) sin(\omega_D t - 2\theta) \tag{3.25c}$$

where $\omega_D = \omega\sqrt{1-\zeta^2}$ is the damped frequency and $\theta = arctan(\zeta/\sqrt{1-\zeta^2})$ the phase angle.

Figure 3.34 shows the time variation of the energy (per unit mass) dissipated by three

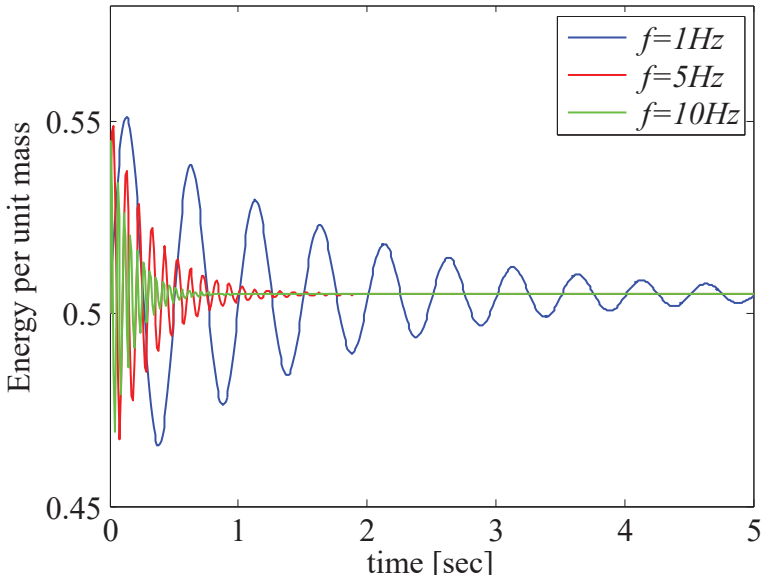

Figure 3.34: Energy dissipation under impulse load ($v_0 = 1m/sec$) in single-degree-of-freedom oscillators characterized by frequencies $f = 1, 5, 10Hz$ and damping ratio $\zeta = 5\%$.

SDOF oscillators subjected to $v_0 = 1m/sec$ and characterized by frequencies $\omega = 2\pi, 10\pi, 20\pi rad/sec$ (or $1, 5, 10Hz$) and damping ratio $\zeta = 5\%$. Figure 3.34 confirms that the rate of energy dissipation is greater at higher frequencies. Although not examined in this simple application, it is well known that an increased damping ratio may reduce the system response and accelerate the decay of this response [2, 8].

Summarizing, the relative acceleration response observed during the Augusta experiments implies high rates of energy dissipation upon initiation of motion. A model which can capture this behaviour is a multi-degree-of-freedom model with an increased damping capacity at higher frequencies.

The observed structural behaviour, i.e. large acceleration/energy amplitudes upon initiation of motion that decay very fast in time or in simple words excitation of higher modes, occurs because of the way the test was performed. A proper set-up of the free vibration test would require that a uniform displacement (force) is applied to the building before the building was released and set into free vibration motion, see Figure 3.35 (a). This test

configuration is by no means feasible for the excitation of multi-story structures. For this reason, in the Augusta tests the structure was pushed to the desired amplitude level by applying a concentrated load above the isolation plane, see Figure 3.35 (a). The sudden release of the load resulted to an impulse load induced at the system. The impulse load, characterized by a broadband frequency content excited all modes, causing vibrations to the superstructure. The non-linearity of the isolation system contributed also to the excitation of higher modes. In fact, the tendency of the pot bearings to evoke higher modes in the system response through their stick-slip behavior is one of their major drawbacks as seismic protection systems [36].

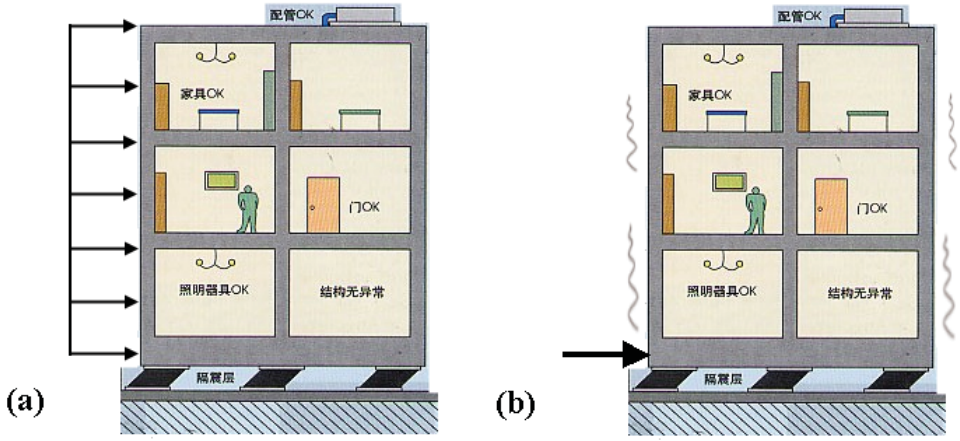

Figure 3.35: (a) Ideal and (b) actual release test configuration.

A last observation is made on the identified frequency content of the superstructure response. The Fourier Amplitude Spectra (FAS) of the experimental and identified first floor accelerations for test 9 together with the the Fourier Amplitude Spectrum of the input motion are shown in Figure 3.36. The FAS of the experimental superstructure response has four peaks at frequencies $6.5, 13.2, 18.9, 31.7Hz$. Instead the FAS of the identified acceleration response has three peaks at frequencies $6.5, 13.2, 31.7Hz$. These frequencies are almost double the identified modal frequencies for test 9 $(3.7, 11.6, 18.1Hz)$.

The peak Fourier amplitudes of the identified superstructure response occur at frequencies

other than the identified modal frequencies. This is because herein, the fixed base model was subjected to the ground floor displacement $\ddot{u}_b(t)$. As consequence, the modal components of the response were characterized by both the frequency content of the excitation and the superstructure (i.e. the identified modal frequencies). Take for instance Figures 3.33, more than one frequency can be read in each modal acceleration response. The FAS of the input motion $\ddot{u}_b(t)$ is also shown in Figure 3.36; in fact the peaks of the identified superstructure response and the input motion occur at the same frequencies.

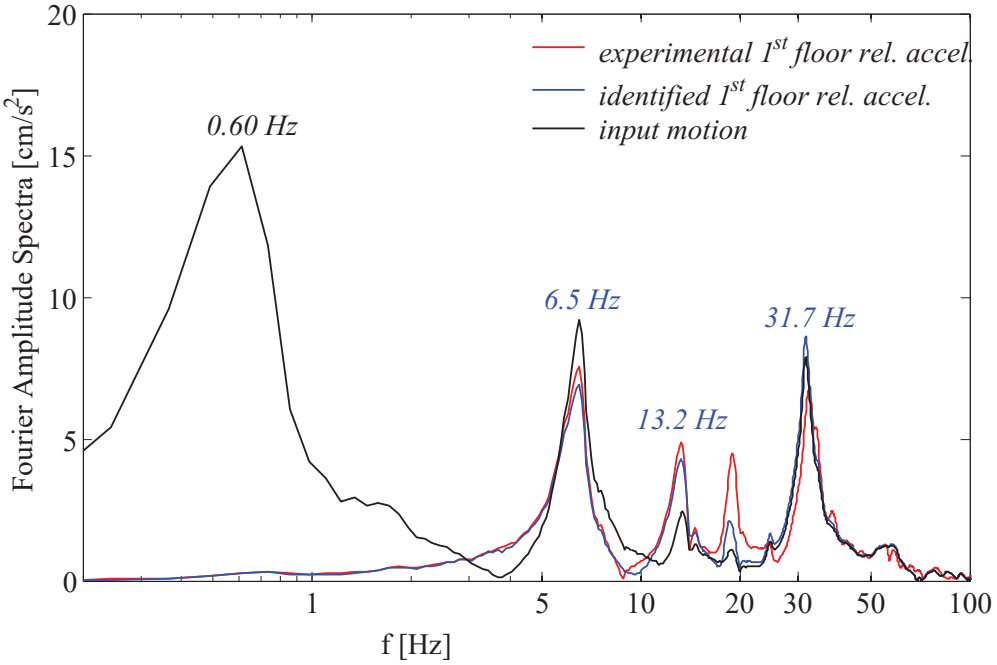

Figure 3.36: Comparison of the Fourier Amplitude Spectra (FAS) of the experimental and identified first floor relative accelerations under test 9 (red and blue lines respectively). The FAS of the ground floor acceleration, used as input motion for the excitation of the fixed base superstructure model is shown in black. The peaks of the FAS are found at frequencies $6.5, 13.2, 31.7 Hz$; the identified modal frequencies of the superstructure were $3.7, 11.6, 18.1 Hz$.

3.5.6 Matching of identified and experimental superstructure response for tests 4,5,6 and 10

The comparison between identified and observed peak response for tests 4, 5, 6 and 10 is provided in the following figures for completeness. The matching is very satisfactory in all cases. The identified systems tend to underestimate the peak floor response, the error in the peak response is no great than 15%. The real system is definitely more complicated than visualized herein and probably more flexible and/or less damped.

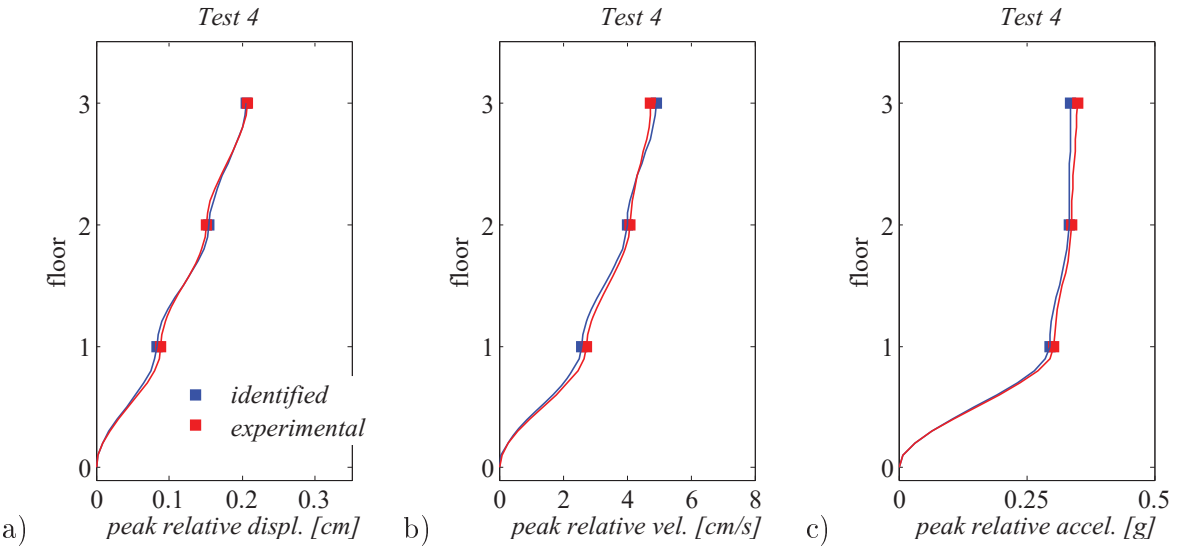

a) b) c)

Figure 3.37: Comparison between identified and experimental peak relative displacement, velocity and acceleration for test 4; sub-plots (a), (b) and (c).

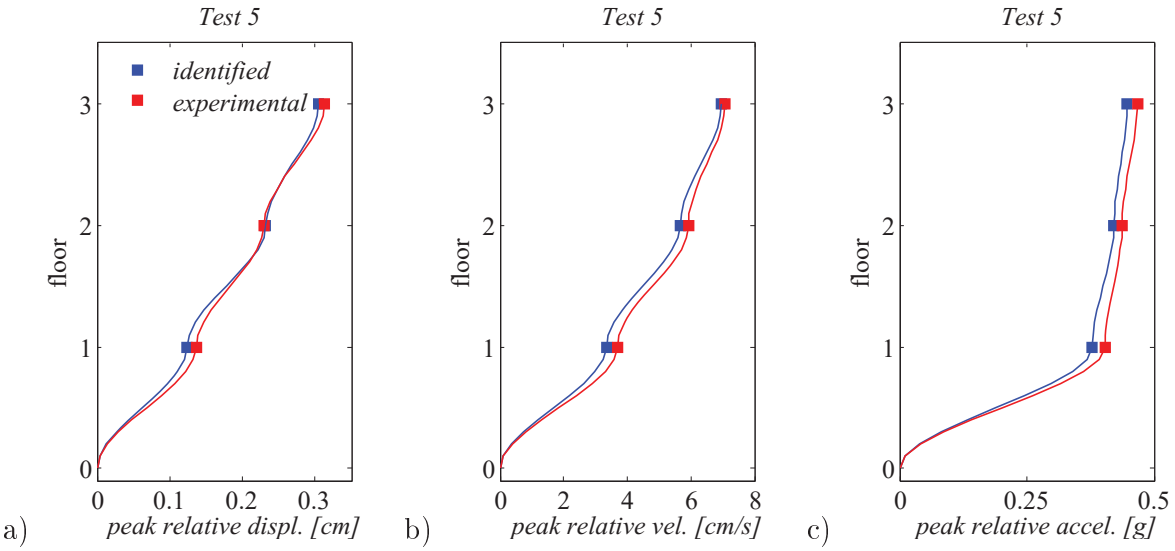

Figure 3.38: Comparison between identified and experimental peak relative displacement, velocity and acceleration for test 5; sub-plots (a), (b) and (c).

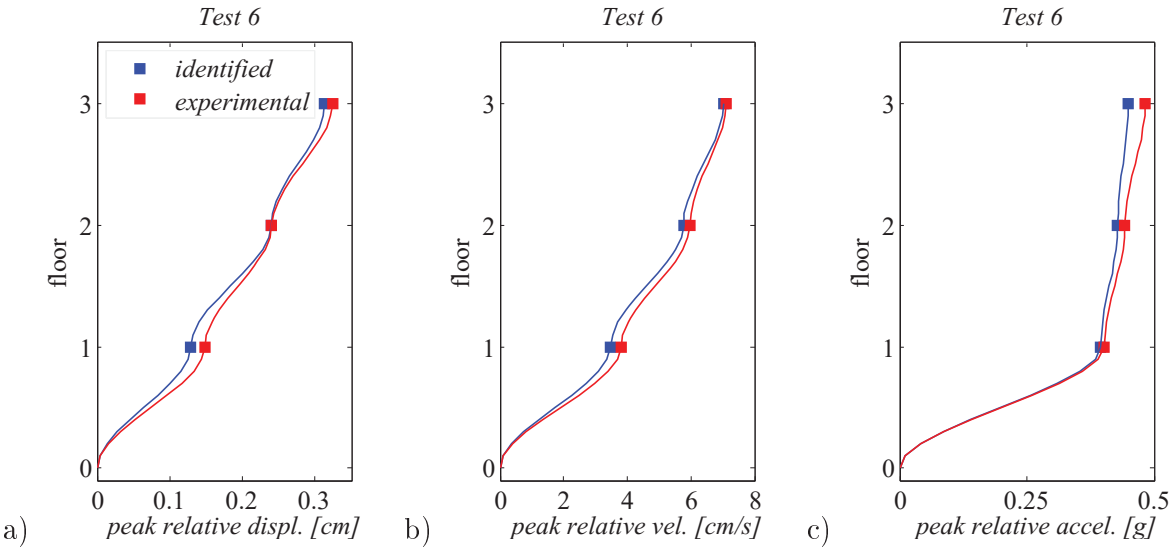

Figure 3.39: Comparison between identified and experimental peak relative displacement, velocity and acceleration for test 6; sub-plots (a), (b) and (c).

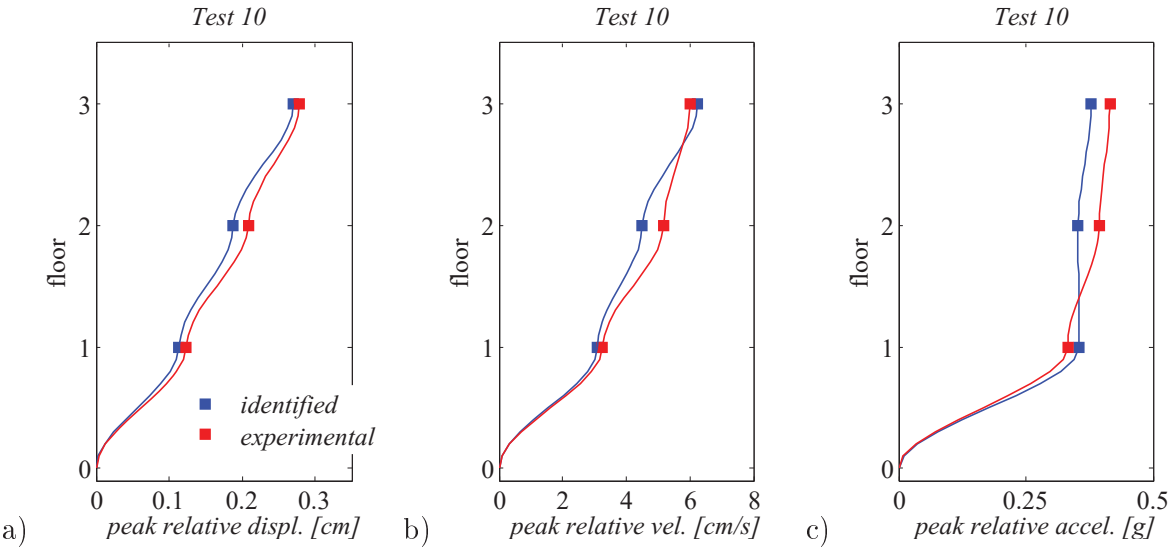

a) b) c)

Figure 3.40: Comparison between identified and experimental peak relative displacement, velocity and acceleration for test 10; sub-plots (a), (b) and (c).

3.6 Conclusions

A two stage implementation of the CMA-ES was made herein for the identification of the isolation system and superstructure properties of the Augusta building. The free vibration data recorded during the Augusta release tests were used in the identification. The HBIS and the superstructure models obtained from the identification reproduce satisfactorily the observed experimental response. In the following section the identified model parameters will serve as input data for the response simulation of the isolated building by means of a more sophisticated model, which accounts for both the non-linearity of the isolation system and the flexibility of the superstructure.

Chapter 4

Constrained optimization procedure for the 1-D strong motion response simulation of hybrid base isolated buildings

This chapter presents a constrained non-linear optimization algorithm for the 1-D response simulation of hybrid base isolated structures subject to strong motion. The constrained optimization procedure (COP) was first developed for the 1-D dynamic response simulation of non-linear hybrid base isolation systems [72]. The performance of the algorithm was tested on the one-degree-of-freedom model, for which analytical solutions are available. Once the robustness and accuracy of the algorithm was verified, the numerical solution was extended to account for bi-directional excitation and multi-degree-of-freedom systems. The theoretical bases of the algorithm lie on earlier research work by Reinhorn and Sivaselvan on the generalized Lagrangian formulation for the structural collapse simulation of large-scale structural systems [70, 73]. Reinhorn and Sivaselvan observed that dynamic models of structural systems, whose constituent material and component constitutive behaviors can be derived

from stored energy functions and dissipation potentials, can be represented using a mixed Lagrangian formalism (MLF). In the MLF, the action integral is defined on the basis of the Generalized Standard Material Framework (stored energy and dissipation functions) and the governing equations are derived as the Euler-Lagrange equations of a generalized Hamilton's principle [73]. The evolution of the structural state in time is provided by a weak formulation. For non-conservative systems, such as elastic-plastic systems, only the weak form is applicable. In fact, Hamilton's variational principle relies on a Lagrangian formulation of a system which accounts for conservative dynamics but cannot describe generic non-conservative interactions [74] . After the governing equations are recovered and discretized in time, the time step response is addressed as a convex optimization problem.

4.1 Multi-degree-of-freedom model for hybrid base isolated buildings under 1-D excitation

The constrained non-linear optimization algorithm was developed for the response simulation of hybrid base isolated systems under 1-D excitation. The structural model accounts for the non-linearity of the isolation system and the flexibility of the linear superstructure, see Figure 4.1. The basic assumptions considered in modelling the system are:

- A plane model describing the behaviour of the isolated building along the longitudinal direction X is considered.
- The ground floor slab that connects all the isolation elements is assumed to be rigid, hence one degree of freedom is associated to the base, the translational displacement u_b.
- Each floor i has one degree of freedom u_s^i.
- The bi-linear and Coulomb models are used for the description of the non-linear behavior of the rubber and sliding bearings, see Figure 4.1(c).

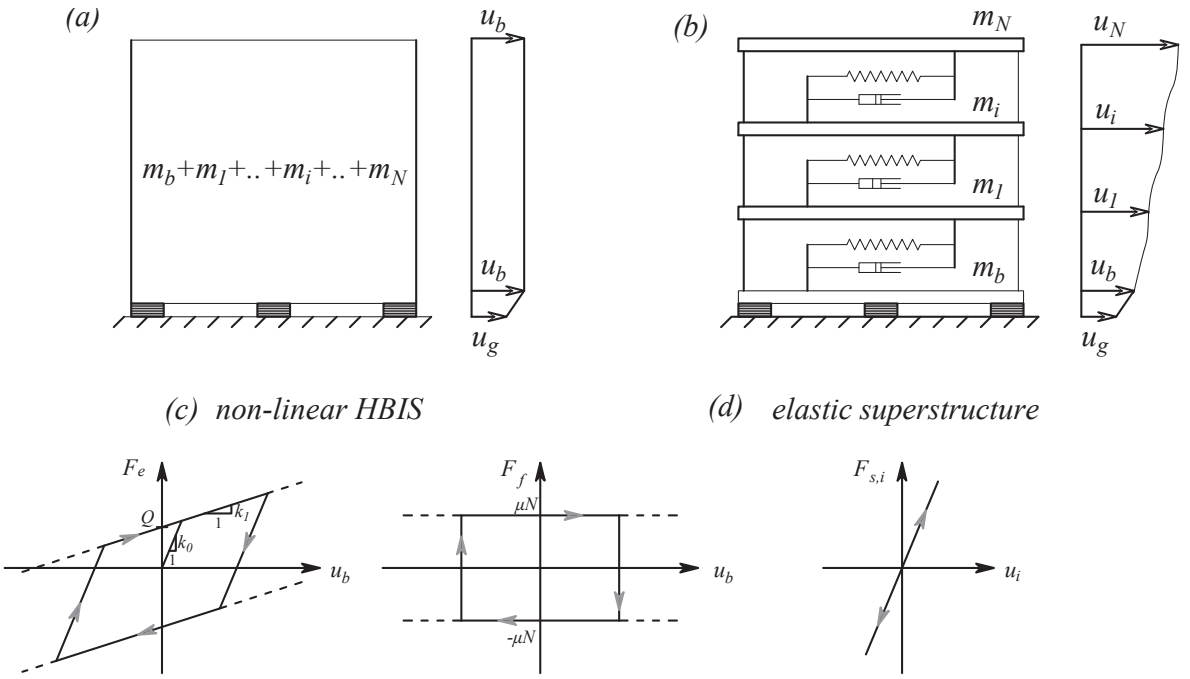

Figure 4.1: Structural models for the response simulation of base isolated buildings to 1D excitation. (a) Rigid superstructure model accounting only for the non-linearity of the isolation system, see sub-plot (c). (b) Updated model describing the non-linear behaviour of the isolation system, see sub-plot (c), and the linear behaviour of the superstructure, see sub-plot (d).

- A linear model is considered for the description of the superstructure, since this should remain in the elastic range under the design earthquake, Figure 4.1(d).
- Bi- or tri-directional excitation, 3-D modeling of the isolated structure, the hardening of the HDRB and the non-linearity of the superstructure for motions beyond the design level earthquake are significant aspects of the assessment practice but are not examined herein. The constrained non-linear optimization algorithm procedure developed serves for the validation of the identified model used in the free vibration simulation of the Augusta building. Extensions of the procedure for bi-directional effects can be found in [75, 76].

4.2 Governing equations of motion

The dynamic equilibrium for the base isolated system illustrated in Figure 4.1(b) is:

$$\boldsymbol{M}\,\dot{\boldsymbol{\nu}}(t) + \boldsymbol{C}\,\boldsymbol{\nu}(t) + \boldsymbol{K}\,\boldsymbol{u}(t) + \boldsymbol{B}\,\boldsymbol{F}(u_b(t), \dot{u}_b(t)) = \boldsymbol{P}(t) \tag{4.1}$$

or

$$\begin{bmatrix} m_b & \mathbf{0} \\ \mathbf{0} & \boldsymbol{M_{ss}} \end{bmatrix} \begin{pmatrix} \dot{\nu}_b \\ \dot{\boldsymbol{\nu}}_{\boldsymbol{s}} \end{pmatrix} + \begin{bmatrix} C_{bb} & \boldsymbol{C_{bs}} \\ \boldsymbol{C_{sb}} & \boldsymbol{C_{ss}} \end{bmatrix} \begin{pmatrix} \nu_b \\ \boldsymbol{\nu}_{\boldsymbol{s}} \end{pmatrix} + \begin{bmatrix} K_{bb} & \boldsymbol{K_{bs}} \\ \boldsymbol{K_{sb}} & \boldsymbol{K_{ss}} \end{bmatrix} \begin{pmatrix} u_b \\ \boldsymbol{u}_{\boldsymbol{s}} \end{pmatrix} + \begin{pmatrix} F_b \\ \mathbf{0} \end{pmatrix} = \begin{pmatrix} P_b \\ \boldsymbol{P}_s \end{pmatrix} \tag{4.2a}$$

where

$$\boldsymbol{B}\,\boldsymbol{F} = [\boldsymbol{B_e}, \mathbf{0}, \boldsymbol{B_f}] \begin{pmatrix} F_e \\ F_h \\ F_f \end{pmatrix} = \begin{bmatrix} 1 & 0 & 1 \\ \mathbf{0}^{N\times 1} & \mathbf{0}^{N\times 1} & \mathbf{0}^{N\times 1} \end{bmatrix} \begin{pmatrix} F_e \\ F_h \\ F_f \end{pmatrix} = \begin{pmatrix} F_e + F_f \\ \mathbf{0}^{N\times 1} \end{pmatrix} = \begin{pmatrix} F_b \\ \mathbf{0}^{N\times 1} \end{pmatrix} \tag{4.2b}$$

u_b and ν_b are the displacement and velocity at the isolation level (ground floor), while $\boldsymbol{u_s}$ and $\boldsymbol{\nu_s}$ are the vectors of the upper floor displacements and velocities, see Figure 4.1(b). u_b and $\boldsymbol{u_s}$ are relative to the ground. F_e and F_h are the resisting forces provided by the elastic springs k_e and k_h used in the representation of the rubber bearings. F_f is the friction force provided by the friction sliders. The transformation matrix $\boldsymbol{B}$, or equivalently the transformation matrices $\boldsymbol{B_e}, \boldsymbol{B_f}$, map the resisting forces $\boldsymbol{F}$ developed in the isolation system to the resultant forces $(F_b, \mathbf{0}^{1XN})^T$ acting at the considered degrees-of-freedom $(u_b, \boldsymbol{u_s}^T)^T$. More specifically, the non-linear forces developed at the HBIS are felt at the isolation level, yet not at the superstructure. m_b is the mass at the base floor, just above the isolation level. The damping and stiffness properties of the isolation system are denoted with the sub-script "bb". In reality, these contain also the stiffness coming from the substructure, see section 4.2.1. $\boldsymbol{M_{ss}}, \boldsymbol{C_{ss}}, \boldsymbol{K_{ss}}$ are the superstructure mass, damping and stiffness matrices associated to the N degrees of freedom of the superstructure. $\boldsymbol{P}$ is the vector of the external forces applied along the considered degrees of freedom u_b and $\boldsymbol{u_s}$. Interaction between

superstructure and isolation system is considered through the coupling terms taking the sub-script "bs" (or "sb"). As it is shown in the following section, section 4.2.1, the coupling terms derive only from the superstructure, since the response of the isolation system depends only on the degree of freedom of the isolation system.

4.2.1 Assembly of the global matrices

$\boldsymbol{M, C, K}$ are the global mass, damping and stiffness matrices associated to the absolute degrees of freedom shown in Figure 4.1(b). $\boldsymbol{M, C, K}$ can be easily assembled from the local mass, damping and stiffness properties of the isolation (m_b, c_b, k_b) and the superstructure $\boldsymbol{M_{ss}, C_{ss}, K_{ss}}$, see Eq. 4.3. Herein the contribution of the rubber bearings to energy dissipation is considered through the non-linear forces F_b, hence the equivalent stiffness k_b will be zero.

$$\boldsymbol{M_{ss}} = \begin{bmatrix} m_1 & & & \\ & m_i & & \\ & & .. & \\ & & & m_N \end{bmatrix}, \quad \boldsymbol{K}_{ss} = \begin{bmatrix} k_{11} & k_{1i} & ... & k_{1N} \\ & k_{ii} & .. & k_{iN} \\ & & .. & .. \\ (sym) & & & k_{NN} \end{bmatrix}, \quad \boldsymbol{C}_{ss} = \begin{bmatrix} c_{11} & c_{1i} & ... & c_{1N} \\ & c_{ii} & .. & c_{iN} \\ & & .. & .. \\ (sym) & & & c_{NN} \end{bmatrix} \tag{4.3}$$

The transformation matrices $\boldsymbol{T_b, T_s}$ transform the base isolation and superstructure displacements from the local coordinate system where the stiffness k_b (or $\boldsymbol{K_{ss}}$) is known to the global coordinate system where the stiffness matrix $\boldsymbol{K}$ is unknown, see Eqs 4.4.

$$u_b = \boldsymbol{T_b}\, \boldsymbol{u} = (1 \quad \boldsymbol{0}_{1\times N}) \begin{pmatrix} u_b \\ \boldsymbol{u}_s \end{pmatrix} = u_b \tag{4.4a}$$

$$\boldsymbol{u_{s,rel}} = \boldsymbol{T_s}\, \boldsymbol{u} = (-\boldsymbol{1}_{N\times 1}\ \boldsymbol{I}_{N\times N}) \begin{pmatrix} u_b \\ \boldsymbol{u}_s \end{pmatrix} = \boldsymbol{u_s} - \boldsymbol{1}u_b \tag{4.4b}$$

where $\boldsymbol{u_{s,rel}}$ are the relative to the base displacements of the superstructure associated to the superstructure mass, stiffness and damping matrices.

The relation between the local and the global stiffness matrices can be easily found, recalling that the work performed by the internal forces should be the same, either evaluated in the local or the global coordinate system:

$$\delta W_{int} = \delta \boldsymbol{u}^T \boldsymbol{K}\, \boldsymbol{u} = \delta u_b^T\, k_b u_b + \delta \boldsymbol{u_{s,rel}^T}\, \boldsymbol{K_{ss}} \boldsymbol{u_{s,rel}} \tag{4.5a}$$

$$\delta \boldsymbol{u}^T \boldsymbol{K}\, \boldsymbol{u} = \delta (\boldsymbol{T}_b\, \boldsymbol{u})^T k_b\, (\boldsymbol{T}_b\, \boldsymbol{u}) + \delta (\boldsymbol{T_s}\, \boldsymbol{u})^T \boldsymbol{K_{ss}}\, (\boldsymbol{T_s}\, \boldsymbol{u}) \tag{4.5b}$$

$$\delta \boldsymbol{u}^T \boldsymbol{K}\, \boldsymbol{u} = \delta \boldsymbol{u}^{\,T} \left(\boldsymbol{T_b^T} k_b \boldsymbol{T_b} + \boldsymbol{T_s^T} \boldsymbol{K_{ss}} \boldsymbol{T_s} \right) \boldsymbol{u} \tag{4.5c}$$

Eq. 4.5(c) holds for any admissible displacement $\boldsymbol{u}$ or virtual displacement $\delta \boldsymbol{u}$, hence the global stiffness matrix equals:

$$\boldsymbol{K} = \boldsymbol{T_b^T} k_b \boldsymbol{T}_b + \boldsymbol{T_s^T} \boldsymbol{K_{ss}} \boldsymbol{T_s} \tag{4.6}$$

Substitution of the the expressions 4.4 for the transformation matrices $\boldsymbol{T_b}, \boldsymbol{T_s}$ into Eq. 4.6 results to the following global stiffness matrix $\boldsymbol{K}$:

$$\boldsymbol{K} = \begin{bmatrix} K_{bb} & \boldsymbol{K_{bs}} \\ \boldsymbol{K_{bs}} & \boldsymbol{K_{ss}} \end{bmatrix} = \begin{pmatrix} 1 \\ \boldsymbol{0^T} \end{pmatrix} k_b \begin{pmatrix} 1 & \boldsymbol{0} \end{pmatrix} + \begin{pmatrix} \boldsymbol{-1^T} \\ \boldsymbol{I} \end{pmatrix} \boldsymbol{K_{ss}} \begin{pmatrix} \boldsymbol{-1} & \boldsymbol{I} \end{pmatrix} \tag{4.7a}$$

$$\boldsymbol{K} = \begin{bmatrix} K_{bb} & \boldsymbol{K_{bs}} \\ \boldsymbol{K_{bs}} & \boldsymbol{K_{ss}} \end{bmatrix} = \begin{bmatrix} k_b + \boldsymbol{1^T K_{ss} 1} & \boldsymbol{-1^T K_{ss}} \\ \boldsymbol{-K_{ss} 1} & \boldsymbol{K_{ss}} \end{bmatrix} \tag{4.7b}$$

The global damping matrix can be evaluated accordingly:

$$\boldsymbol{C} = \boldsymbol{T_b}^T c_b\, \boldsymbol{T_b} + \boldsymbol{T_s}^T \boldsymbol{C_{ss}}\, \boldsymbol{T_s} = \begin{bmatrix} c_b + \boldsymbol{1^T C_{ss} 1} & \boldsymbol{-1^T C_{ss}} \\ \boldsymbol{-C_{ss} 1} & \boldsymbol{C_{ss}} \end{bmatrix} = \begin{bmatrix} C_{bb} & \boldsymbol{C_{bs}} \\ \boldsymbol{C_{bs}} & \boldsymbol{C_{ss}} \end{bmatrix} \tag{4.8}$$

$\boldsymbol{K}, \boldsymbol{C}$ are symmetric, semi-positive definite matrices; $\boldsymbol{K}, \boldsymbol{C}$ have one eigenvalue equal to zero, this is due to the fact that they describe the rigid body motion. $\boldsymbol{M}$ is diagonal, with entries the ground floor mass m_b (just above the isolation system) and the floor masses m_i $(i = 1, ..i, N)$.

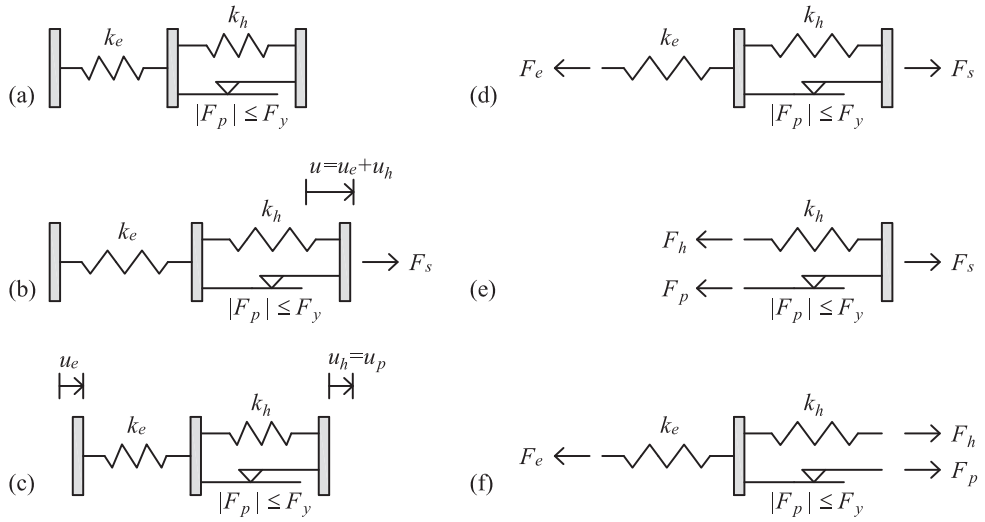

Figure 4.2: Mechanical model for HDRB isolators: (a) undeformed model; (b) deformed model under force F_s; (c) undeformed model after rigid body translation; (d)-(f) equilibrium conditions.

4.2.2 Equilibrium equations for the isolation system

As seen in the previous chapter, the non-linear behavior of each HDRB is modelled using two elastic springs characterized by stiffness $k_e^i = k_0^i$ and $k_h^i = \frac{k_0 k_1}{k_0 - k_1}$ respectively, and a plastic slider with yield force F_y^i. The two springs work in series, therefore the restoring force provided by the $i-th$ HDRB equals the restoring force F_e^i provided by the elastic spring k_e^i or equivalently the sum of the restraining forces provided by the spring k_h^i and the plastic slider, i.e. ${F_h}^i + {F_p}^i$, see Figure 4.2. Thus, the equilibrium equation for the rubber bearings becomes:

$$F_e = F_h + F_p \tag{4.9}$$

F_e, F_p, F_h are the resultants of the corresponding forces F_e^i, F_p^i, F_h^i developed at the single HDRBs, i.e. $F_e = \sum_{i=1}^{NR} F_e^i, F_p = \sum_{i=1}^{NR} F_p^i, F_h = \sum_{i=1}^{NR} F_h^i$, where NR is the number of the HDRB used in the isolation system. Similarly $k_e = \sum_{i=1}^{NR} k_e^i, k_h = \sum_{i=1}^{NR} k_h^i$ are the stiffnesses provided by the NR rubber bearings. In the considered case study, all isolators are of the same class, hence provide the same resisting forces.

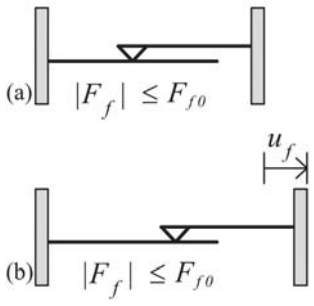

Figure 4.3: Friction slider in neutral position and in displaced position, sub-plots (a) and (b).

4.2.3 Compatibility equations, elastic constitutive equations and flow rules

The compatibility equations 4.10 relate the velocities at the elastic springs ($\nu_e = \dot{u}_e, \nu_h = \dot{u}_h$), the velocities at the plastic and friction sliders ($\nu_p = \dot{u}_p, \nu_f = \dot{u}_f$) to the velocities at the considered degrees of freedom ($\boldsymbol{\nu} = \dot{\boldsymbol{u}}$), see Figures 4.2 and 4.3.

$$\nu_e + \nu_p = \boldsymbol{B_e}^T \boldsymbol{\nu} \tag{4.10a}$$

$$\nu_h = \nu_p \tag{4.10b}$$

$$\nu_f = \boldsymbol{B_f}^T \boldsymbol{\nu} \tag{4.10c}$$

where $\boldsymbol{B_e}^T \boldsymbol{\nu} = \boldsymbol{B_f}^T \boldsymbol{\nu} = \nu_b$, ν_b being the velocity at the isolation system.

The constitutive equations 4.11 associate the velocities ν_e, ν_h to the rates of the corresponding elastic forces F_e, F_h:

$$\nu_e = A_e \dot{F}_e \tag{4.11a}$$

$$\nu_h = A_h \dot{F}_h \tag{4.11b}$$

where $A_e = \frac{1}{k_e}$ and $A_h = \frac{1}{k_h}$.

The plastic and sliding velocities ν_p, ν_f, related to the yielding and friction forces F_p, F_f,

can be defined through the dissipation function $\varphi(F_p, F_f)$:

$$\nu_p = \frac{\partial \varphi(F_p, F_f)}{\partial F_p}, \quad \nu_f = \frac{\partial \varphi(F_p, F_f)}{\partial F_f} \tag{4.12a}$$

$$\varphi(F_p, F_f) = \varphi_p(F_p) + \varphi_f(F_f) \tag{4.12b}$$

$$\varphi_p(F_p) = U_E, \ \varphi_f(F_f) = U_C \tag{4.12c}$$

U_E and U_C are the indicator functions of the polyhedral sets defining the feasible domains for the plastic force F_p and the friction force F_f [72, 73].

$$E = \{F_p : |F_p| \leq F_y\} \tag{4.13a}$$

$$C = \{F_f : |F_f| \leq F_{f0}\} \tag{4.13b}$$

4.2.4 Rearranged compatibility equations

The compatibility equations 4.10 can be rewritten in the following form:

$$\begin{bmatrix} A_e & 0 & 0 \\ 0 & A_h & 0 \\ 0 & 0 & 0 \end{bmatrix} \begin{pmatrix} \dot{F}_e \\ \dot{F}_h \\ \dot{F}_f \end{pmatrix} + \begin{pmatrix} \nu_p \\ -\nu_p \\ \nu_f \end{pmatrix} = \begin{pmatrix} \boldsymbol{B_e^T} \\ \boldsymbol{0^T} \\ \boldsymbol{B_f^T} \end{pmatrix} \boldsymbol{\nu} \tag{4.14}$$

$$\text{or } \boldsymbol{A}\,\ddot{\boldsymbol{J}} + \frac{\partial \varphi}{\partial \dot{\boldsymbol{J}}} = \boldsymbol{B}^T \boldsymbol{\nu} \tag{4.15}$$

$$\text{where } \dot{\boldsymbol{J}}^T = \boldsymbol{F}^T = (F_e, F_h, F_f) \tag{4.16}$$

Eq. 4.15 shows how the sum of the elastic and the plastic strain rates $\boldsymbol{A}\,\ddot{\boldsymbol{J}}$ and $\frac{\partial \varphi}{\partial \dot{\boldsymbol{J}}}$ respectively, equals the total strain rate $\boldsymbol{B}^T \boldsymbol{\nu}$.

4.3 Lagrangian formalism

For convenience, the dynamic equilibrium 4.1 and the compatibility equations 4.15 are repeated herein:

$$\boldsymbol{M}\,\ddot{\boldsymbol{u}} + \boldsymbol{C}\,\dot{\boldsymbol{u}} + \boldsymbol{K}\,\boldsymbol{u} + \boldsymbol{B}\,\dot{\boldsymbol{J}} - \boldsymbol{P} = \boldsymbol{0} \tag{4.17a}$$

$$\boldsymbol{A}\,\ddot{\boldsymbol{J}} + \frac{\partial \varphi}{\partial \dot{\boldsymbol{J}}} - \boldsymbol{B}^T\,\dot{\boldsymbol{u}} = \boldsymbol{0} \tag{4.17b}$$

where $\boldsymbol{A}, \boldsymbol{B}, \dot{\boldsymbol{J}}, \boldsymbol{\varphi}$ where defined in Eqs 4.12, 4.14 and 4.16.

Pre-multiplying Eq. 4.17(a) by a kinematically admissible virtual displacement $\delta\boldsymbol{u}$ satisfying compatibility, and Eq. 4.17(b) by an admissible virtual impulse $\delta\boldsymbol{J}$ satisfying equilibrium, we obtain:

$$\delta\boldsymbol{u}^T\,\boldsymbol{M}\,\ddot{\boldsymbol{u}} + \delta\boldsymbol{u}^T\,\boldsymbol{C}\,\dot{\boldsymbol{u}} + \delta\boldsymbol{u}^T\,\boldsymbol{K}\,\boldsymbol{u} + \delta\boldsymbol{u}^T\,\boldsymbol{B}\,\dot{\boldsymbol{J}} - \delta\boldsymbol{u}^T\,\boldsymbol{P} = 0 \tag{4.18a}$$

$$\delta\boldsymbol{J}^T\,\boldsymbol{A}\,\ddot{\boldsymbol{J}} + \delta\boldsymbol{J}^T\,\frac{\partial \varphi}{\partial \dot{\boldsymbol{J}}} - \delta\boldsymbol{J}^T\,\boldsymbol{B}^T\,\dot{\boldsymbol{u}} = 0 \tag{4.18b}$$

The variation of the action integral for the entire structure is obtained after adding Eqs 4.18(a) and (b), integrating over the time interval $(0, t)$ and making use of integration by parts:

$$\delta\mathcal{I} = -\,\delta \int_0^t \left(\frac{1}{2}\dot{\boldsymbol{u}}^{\boldsymbol{T}}\,\boldsymbol{M}\,\dot{\boldsymbol{u}} - \frac{1}{2}\boldsymbol{u}^{\boldsymbol{T}}\,\boldsymbol{K}\,\boldsymbol{u} + \frac{1}{2}\dot{\boldsymbol{J}}^{\boldsymbol{T}}\,\boldsymbol{A}\,\dot{\boldsymbol{J}} + \boldsymbol{J}^{\boldsymbol{T}}\,\boldsymbol{B}^{\boldsymbol{T}}\,\dot{\boldsymbol{u}} \right) d\tau \tag{4.19a}$$

$$+ \int_0^t (\delta\boldsymbol{u}^T\,\boldsymbol{C}\,\dot{\boldsymbol{u}})\,d\tau + \int_0^t \left(\delta\boldsymbol{J}^T\,\frac{\partial \varphi(\dot{\boldsymbol{u}}, \dot{\boldsymbol{J}})}{\partial \dot{\boldsymbol{J}}} \right) d\tau - \int_0^t (\delta\boldsymbol{u}^T\,\boldsymbol{P})\,d\tau = 0 \tag{4.19b}$$

The variation of the action integral, Eq. 4.19, can be rewritten as:

$$\delta\mathcal{I} = -\delta \int_0^t \mathcal{L}(\boldsymbol{u}, \boldsymbol{J}, \dot{\boldsymbol{u}}, \dot{\boldsymbol{J}})\, d\tau + \int_0^t \left(\delta \boldsymbol{u}^T \frac{\partial \bar{\varphi}(\dot{\boldsymbol{u}}, \dot{\boldsymbol{J}})}{\partial \dot{\boldsymbol{u}}} \right) d\tau + \int_0^t \left(\delta \boldsymbol{J}^T \frac{\partial \bar{\varphi}(\dot{\boldsymbol{u}}, \dot{\boldsymbol{J}})}{\partial \dot{\boldsymbol{J}}} \right) d\tau - \int_0^t \delta \boldsymbol{u}^T \boldsymbol{P}\, d\tau = 0 \tag{4.20}$$

with the Lagrangian $\mathcal{L}$ and the dissipation function $\bar{\varphi}$ given by

$$\mathcal{L}(\boldsymbol{u}, \boldsymbol{J}, \dot{\boldsymbol{u}}, \dot{\boldsymbol{J}}) = \frac{1}{2} \dot{\boldsymbol{u}}^{\boldsymbol{T}} \boldsymbol{M}\, \dot{\boldsymbol{u}} - \frac{1}{2} \boldsymbol{u}^{\boldsymbol{T}} \boldsymbol{K}\, \boldsymbol{u} + \frac{1}{2} \dot{\boldsymbol{J}}^{\boldsymbol{T}} \boldsymbol{A}\, \dot{\boldsymbol{J}} + \boldsymbol{J}^{\boldsymbol{T}} \boldsymbol{B}^{\boldsymbol{T}}\, \dot{\boldsymbol{u}} \tag{4.21a}$$

$$\bar{\varphi}(\dot{\boldsymbol{u}}, \dot{\boldsymbol{J}}) = \frac{1}{2} \dot{\boldsymbol{u}}^{\boldsymbol{T}} \boldsymbol{C}\, \dot{\boldsymbol{u}} + \varphi(\dot{\boldsymbol{J}}) \tag{4.21b}$$

In the definition of the generalized Lagrangian we recognize the kinetic energy of the system, $E_K = \frac{1}{2} \dot{\boldsymbol{u}}^{\boldsymbol{T}} \boldsymbol{M}\, \dot{\boldsymbol{u}}$, the strain energy of the superstructure, $E_S^S = \frac{1}{2} \boldsymbol{u}^{\boldsymbol{T}} \boldsymbol{K}\, \boldsymbol{u}$ and the elastic strain energy in the isolation system, $E_S^{RB} = \frac{1}{2} \dot{\boldsymbol{J}}^{\boldsymbol{T}} \boldsymbol{A}\, \dot{\boldsymbol{J}} = \frac{1}{2k_0} {F_e}^2 + \frac{1}{2k_h} {F_h}^2$. The work term $W_b = \boldsymbol{J}^{\boldsymbol{T}} \boldsymbol{B}^{\boldsymbol{T}}\, \dot{\boldsymbol{u}} = \int F_b\, dt\, \dot{u}_b = F_b\, du$ is related to the impulse of the forces in the isolation system. It follows that $E_S^{RB} + W_b$ is the opposite of the energy dissipated in the isolation system.

Conversely, the Lagrangian and dissipation functions shown in Eqs 4.21 can be used in the Euler - Lagrange equations to recover the governing equations of motion 4.17.

$$\frac{d}{dt} \left(\frac{\partial \mathcal{L}}{\partial \dot{\boldsymbol{u}}} \right) - \frac{\partial \mathcal{L}}{\partial \boldsymbol{u}} + \frac{\partial \bar{\varphi}}{\partial \dot{\boldsymbol{u}}} = \boldsymbol{P} \tag{4.22a}$$

$$\frac{d}{dt} \left(\frac{\partial \mathcal{L}}{\partial \dot{\boldsymbol{J}}} \right) - \frac{\partial \mathcal{L}}{\partial \boldsymbol{J}} + \frac{\partial \bar{\varphi}}{\partial \dot{\boldsymbol{J}}} = \boldsymbol{0} \tag{4.22b}$$

Table 4.1: Time discretization formulae.

u	v	$\dot{v}$	F	$\dot{F}$
$u^i + \frac{h}{4}(\nu^{i+1} + \nu^i)$	$\frac{1}{2}(\nu^{i+1} + \nu^i)$	$\frac{1}{h}(\nu^{i+1} - \nu^i)$	$\frac{1}{2}(F^{i+1} + F^i)$	$\frac{1}{h}(F^{i+1} - F^i)$

4.4 Discretization of governing equations of motion

Implementation of classical modal analysis, or complex modal analysis in the case of non-classical damping, is not applicable for the decoupling of the equations of motion 4.17, due to the presence of the non-linear forces $\boldsymbol{B}\,\boldsymbol{F}$. There is therefore the need for implementation of a direct integration scheme, for example Newmark's method [2]. In traditional non-linear numerical methods, the displacement method is combined with an incremental iterative scheme to provide the non-linear structural response; the system displacements are thus the primary unknowns. The Mixed Lagrangian Approach followed herein, allows the restatement of the structural response problem as a constrained optimization-based problem, where the primary unknowns are the dissipative forces and/or the irreversible strain rates. For the formulation of the time step optimization problem, the governing equations of motions are discretized in time and rearranged accordingly to provide the relationship between the primary unknowns F_p, F_f (or equivalently the velocities ν_p, ν_f) and the remaining system parameters, i.e. displacements, velocities and accelerations. Central differences and the mid-point rule are used for the time discretization of the governing equations, see Table 4.1. Throughout this chapter the time step shall be denoted by $h = t(i+1) - t(i)$.

4.4.1 Discretization of equations of motion

Discretization of the equations of motion 4.1 leads to the following equation:

$$\boldsymbol{M}\frac{\boldsymbol{\nu}^{i+1}-\boldsymbol{\nu}^{i}}{h}+\boldsymbol{C}\frac{\boldsymbol{\nu}^{i+1}+\boldsymbol{\nu}^{i}}{2}+\boldsymbol{K}\left(\boldsymbol{u}^{i}+\frac{h}{4}(\boldsymbol{\nu}^{i+1}+\boldsymbol{\nu}^{i})\right)+\boldsymbol{B}\frac{\boldsymbol{F}^{i+1}+\boldsymbol{F}^{i}}{2}=\frac{\boldsymbol{P}^{i+1}+\boldsymbol{P}^{i}}{2} \quad (4.23)$$

Eq. 4.23 can be solved for the vector velocities $\boldsymbol{\nu}^{i+1}$:

$$\boldsymbol{\nu}^{i+1}=\bar{\boldsymbol{\nu}}^{i}-\frac{h}{2}\bar{\boldsymbol{M}}^{-1}\left(\boldsymbol{B_e}\,F_e^{i+1}+\boldsymbol{B_f}\,F_f^{i+1}\right) \quad (4.24a)$$

$$where \quad \bar{\boldsymbol{\nu}}^{i}=\bar{\boldsymbol{M}}^{-1}\left(\bar{\bar{\boldsymbol{M}}}\boldsymbol{\nu}^{i}-h\boldsymbol{K}\,\boldsymbol{u}^{i}+\frac{h}{2}(\boldsymbol{P^{i+1}}+\boldsymbol{P}^{i}-\boldsymbol{B}\,\boldsymbol{F}^{i})\right) \quad (4.24b)$$

$$\bar{\boldsymbol{M}}=\boldsymbol{M}+\frac{h}{2}\boldsymbol{C}+\frac{h^2}{4}\boldsymbol{K},\ \bar{\bar{\boldsymbol{M}}}=\boldsymbol{M}-\frac{h}{2}\boldsymbol{C}-\frac{h^2}{4}\boldsymbol{K} \quad (4.24c)$$

In Eq. 4.24 (a) the product $\boldsymbol{B}\,\boldsymbol{F}$ was replaced by the sum $[\boldsymbol{B_e},0,\boldsymbol{B_f}][F_e,F_h,F_f]^T=\boldsymbol{B_e}\,F_e+\boldsymbol{B_f}\,F_f$.

4.4.2 Discretization of the compatibility equations

The compatibility equations 4.14 can be discretized in the form given below:

$$A_e\frac{{F_e}^{i+1}-{F_e}^{i}}{h}+\frac{{\nu_p}^{i+1}+{\nu_p}^{i}}{2}={\boldsymbol{B_e}}^{T}\,\frac{\boldsymbol{\nu}^{i+1}+\boldsymbol{\nu}^{i}}{2} \quad (4.25a)$$

$$A_h\frac{{F_h}^{i+1}-{F_h}^{i}}{h}-\frac{{\nu_p}^{i+1}+{\nu_p}^{i}}{2}=0 \quad (4.25b)$$

$$\frac{{\nu_f}^{i+1}+{\nu_f}^{i}}{2}={\boldsymbol{B_f}}^{T}\,\frac{\boldsymbol{\nu}^{i+1}+\boldsymbol{\nu}^{i}}{2} \quad (4.25c)$$

Using Eq. 4.9 into Eq. 4.25(b) and solving for ${F_e}^{i+1}$ we obtain:

$${F_e}^{i+1}={F_p}^{i+1}+\frac{h}{2}{A_h}^{-1}\,{\nu_p}^{i+1}-{\bar{F}_p}^{i} \quad (4.26a)$$

$$where \quad \bar{F}_p{}^i = F_p{}^i - F_e{}^i - \frac{h}{2} A_h{}^{-1}\, \nu_p{}^i \tag{4.26b}$$

4.4.3 Discrete governing equations

The expression for the velocities ν^{i+1}, Eq. 4.24(a), is used in the discretized compatibility Eqs 4.25(a) and (c) and the latter are solved for the plastic strain rates ν_p^{i+1}, ν_f^{i+1}, providing:

$$\begin{pmatrix} \nu_p^{i+1} \\ \nu_f^{i+1} \end{pmatrix} = \begin{pmatrix} \bar{\nu}_e^i \\ \bar{\nu}_f^i \end{pmatrix} - \begin{bmatrix} \bar{A}_{ee} & \bar{A}_{ef} \\ \bar{A}_{fe} & \bar{A}_{ff} \end{bmatrix} \begin{pmatrix} F_e{}^{i+1} \\ F_f{}^{i+1} \end{pmatrix} \tag{4.27a}$$

where

$$\begin{pmatrix} \bar{\nu}_e^i \\ \bar{\nu}_f^i \end{pmatrix} = \begin{pmatrix} \bar{\bar{\nu}}_e{}^i \\ \bar{\bar{\nu}}_f{}^i \end{pmatrix} + \begin{bmatrix} \bar{\bar{A}}_{ee} & \bar{\bar{A}}_{ef} \\ \bar{\bar{A}}_{fe} & \bar{\bar{A}}_{ff} \end{bmatrix} \begin{pmatrix} F_e{}^i \\ F_f{}^i \end{pmatrix} \tag{4.27b}$$

$$\bar{\bar{\nu}}_e{}^i = (\boldsymbol{B_e^T} + \boldsymbol{B_e^T}\bar{\boldsymbol{M}}^{-1}\bar{\bar{\boldsymbol{M}}})\,\nu^i - \nu_p{}^i + \frac{h}{2}\boldsymbol{B_e}^T\,\bar{\boldsymbol{M}}^{-1}(\boldsymbol{P}^{i+1} + \boldsymbol{P}^i - 2\boldsymbol{K}\,\boldsymbol{u}^i) \tag{4.27c}$$

$$\bar{\bar{\nu}}_f{}^i = (\boldsymbol{B_f^T} + \boldsymbol{B_f^T}\bar{\boldsymbol{M}}^{-1}\bar{\bar{\boldsymbol{M}}})\,\nu^i - \nu_f{}^i + \frac{h}{2}\boldsymbol{B_f}^T\,\bar{\boldsymbol{M}}^{-1}(\boldsymbol{P}^{i+1} + \boldsymbol{P}^i - 2\boldsymbol{K}\,\boldsymbol{u}^i) \tag{4.27d}$$

$$\bar{A}_{ee} = \frac{2}{h}A_e + \frac{h}{2}\boldsymbol{B_e^T}\,\bar{\boldsymbol{M}}^{-1}\,\boldsymbol{B_e}, \quad \bar{A}_{ef} = \bar{A}_{fe} = \frac{h}{2}\boldsymbol{B_e^T}\,\bar{\boldsymbol{M}}^{-1}\,\boldsymbol{B_f}, \quad \bar{A}_{ff} = \frac{h}{2}\boldsymbol{B_f^T}\,\bar{\boldsymbol{M}}^{-1}\,\boldsymbol{B_f} \tag{4.27e}$$

$$\bar{\bar{A}}_{ee} = \frac{2}{h}A_e - \frac{h}{2}\boldsymbol{B_e^T}\,\bar{\boldsymbol{M}}^{-1}\,\boldsymbol{B_e}, \quad \bar{\bar{A}}_{ef} = \bar{\bar{A}}_{fe} = -\bar{A}_{ef}, \quad \bar{\bar{A}}_{ff} = -\bar{A}_{ff} \tag{4.27f}$$

4.4.4 Dual forces and velocities

The forces and velocities related by Eq. 4.27 are not dual in a power sense. While the friction velocities ν_f are combined with the corresponding friction forces F_f, the plastic strain rates ν_p are combined with the elastic forces F_e. Nevertheless, if the expression 4.26 for ${F_e}^{i+1}$ is replaced in Eq. 4.27(a), after trivial manipulations those can be re-written as:

$$\begin{pmatrix} \nu_p^{i+1} \\ \nu_f^{i+1} \end{pmatrix} = \begin{pmatrix} \tilde{\nu}_p^i \\ \tilde{\nu}_f^i \end{pmatrix} - \begin{bmatrix} D_{pp} & D_{pf} \\ D_{fp} & D_{ff} \end{bmatrix} \begin{pmatrix} {F_p}^{i+1} \\ {F_f}^{i+1} \end{pmatrix} \tag{4.28}$$

$$or \;\; \hat{\boldsymbol{\nu}}^{i+1} = \tilde{\boldsymbol{\nu}}^i - \boldsymbol{D}\,\hat{\boldsymbol{F}}^{i+1} \tag{4.29}$$

$$where \;\; D_{pp} = \left(\bar{A}_{ee}^{-1} + \frac{h}{2} {A_h}^{-1} \right)^{-1}, \; D_{pf} = D_{pp}\,\bar{A}_{ee}^{-1}\,\bar{A}_{ef} = D_{fp} \tag{4.30a}$$

$$D_{ff} = D_{fp}\,\bar{A}_{ee}^{-1}\,\bar{A}_{ef} - \bar{A}_{fe}\,\bar{A}_{ee}^{-1}\,\bar{A}_{ef} + \bar{A}_{ff} \tag{4.30b}$$

$$\tilde{\nu}_p^i = D_{pp}\,\bar{A}_{ee}^{-1}\,\bar{\nu}_e^i + D_{pp}\,\bar{F}_p^i, \quad \tilde{\nu}_f^i = \bar{\nu}_f^i - \frac{h}{2}\bar{A}_{fe}\,{A_h}^{-1}\,D_{pp}\,\bar{A}_{ee}^{-1}\,\bar{\nu}_e^i + D_{fp}\,\bar{F}_p^i \tag{4.30c}$$

The expressions for $\bar{\nu}_e^i, \bar{\nu}_f^i, \bar{A}_{ee}, \bar{A}_{ef}, \bar{A}_{fe}, \bar{A}_{ff}$ are provided in Eqs 4.27 (b) to (f).

4.5 Time step solution

The solution to Eq. 4.29 can be addressed as a constrained optimization problem [72]. Eq. 4.29 sets the stationary conditions for the following functional:

$$\begin{aligned} &Minimize \; \Phi(\hat{\boldsymbol{F}}^{i+1}) = \tfrac{1}{2}(\hat{\boldsymbol{F}}^{i+1})^T \boldsymbol{D}(\hat{\boldsymbol{F}}^{i+1}) - \hat{\boldsymbol{F}}^{i+1}\tilde{\boldsymbol{\nu}}^i \\ &subject\ to\ the\ non\ linear\ constraints \;\; |\boldsymbol{F}| - \boldsymbol{U} \leq 0 \end{aligned} \tag{4.31}$$

The optimization problem 4.31 may be formulated in terms of velocities, making use of the force-velocity relationship 4.29 :

$$\begin{aligned} &Minimize\ \Psi(\hat{\boldsymbol{\nu}}^{i+1}) = \tfrac{1}{2}(\hat{\boldsymbol{\nu}}^{i+1} - \tilde{\boldsymbol{\nu}}^{i})^T \boldsymbol{D}^{-1}(\hat{\boldsymbol{\nu}}^{i+1} - \tilde{\boldsymbol{\nu}}^{i}) - (\hat{\boldsymbol{\nu}}^{i+1} - \tilde{\boldsymbol{\nu}}^{i})^T \boldsymbol{D}^{-1}\tilde{\boldsymbol{\nu}}^{i} \\ &subject\ to\ the\ non\ linear\ constraints\ \ |\boldsymbol{F}| - \boldsymbol{U} \leq 0 \end{aligned} \tag{4.32}$$

Once the force vector $\hat{\boldsymbol{F}}^{i+1}$ is obtained by solving the optimization problem 4.31, the velocity vector $\boldsymbol{\nu}^{i+1}$ is obtained from Eq. 4.29. Similarly, once the velocity vector $\boldsymbol{\nu}^{i+1}$ is obtained by solving the optimization problem 4.32 the corresponding forces are obtained by inverting Eq. 4.29. Table 4.2 shows how to evaluate the remaining response parameters at the end of the time step, given the velocities $\boldsymbol{\nu}^{i+1}$ and the forces $\hat{\boldsymbol{F}}^{i+1}$.

General methods for the solution of constrained optimization problems can be found in classical textbooks on optimization [77, 78, 79]. In their work on numerical collapse simulation of large-scale structural systems, Sivaselvan et al. used an augmented Lagrangian approach coupled with Newton's method [70, 73]. Herein the Matlab function *fmincon* is used for the solution of the optimization problem.

Note: The demonstration of the positive definiteness of the matrix $\boldsymbol{D}$ *was straight-forward in the case of the one-degree-of-freedom system [72]; however it becomes rather cumbersome in the multi-degree-of-freedom case. In the numerical applications of the algorithm performed on the identified isolated structure, the matrix* $\boldsymbol{D}$ *was found to be positive definite; therefore the functional* Φ *(or* Ψ*) was convex and admitted a global minimization.*

Table 4.2: Evaluation of kinematic and mechanical unknowns at the end of each time-step.

Velocities	$\boldsymbol{\nu}^{i+1} = \bar{\boldsymbol{\nu}}^{i} - \frac{h}{2}\bar{\boldsymbol{M}}^{-1}\left(\boldsymbol{B_e}\, {F_e}^{i+1+\boldsymbol{B_f}\,{F_f}^{i+1}}\right)$ (Eq. 4.24)
	${\nu_h}^{i+1} = {\nu_p}^{i+1}$
	${\nu_e}^{i+1} = \boldsymbol{B_e^T}\,\boldsymbol{\nu}^{i+1} - {\nu_h}^{i+1}$
Displacements	$\boldsymbol{u}^{i+1} = \boldsymbol{u}^{i} + \frac{h}{2}(\boldsymbol{\nu}^{i+1} + \boldsymbol{\nu}^{i})$
	${u_h}^{i+1} = {u_p}^{i+1} = {u_p}^{i} + \frac{h}{2}({\nu_p}^{i+1} + {\nu_p}^{i})$
	${u_e}^{i+1} = \boldsymbol{B_e^T}\,\boldsymbol{u}^{i+1} - {u_h}^{i+1}$
Forces	${F_h}^{i+1} = A_e\ {u_h}^{i+1}$
	${F_e}^{i+1} = {F_h}^{i+1} + {F_p}^{i+1}$
Accelerations	$\dot{\boldsymbol{\nu}}^{i+1} = 0$, if $\boldsymbol{\nu}^{i+1} = 0$ and $\lvert{F_f}^{i+1}\rvert < F_{f0}$
	$\dot{\boldsymbol{\nu}}^{i+1} = \boldsymbol{M^{-1}}\left[\boldsymbol{P}^{i+1} - \boldsymbol{C}\,\boldsymbol{\nu}^{i+1} - \boldsymbol{K}\,\boldsymbol{u}^{i+1} - \boldsymbol{B}\,\boldsymbol{F}^{i+1}\right]$ otherwise

4.6 Energy equilibrium

The equation of motion 4.17(a) is pre-multiplied by a kinematically admissible virtual displacement $\delta \boldsymbol{u}$ satisfying compatibility, see Eq. 4.18(a), and then integrated over the time range $(0, t)$:

$$\int_0^t \dot{\boldsymbol{u}}^T \boldsymbol{M}\, \ddot{\boldsymbol{u}}\, d\tau + \int_0^t \dot{\boldsymbol{u}}^T \boldsymbol{C}\, \dot{\boldsymbol{u}}\, d\tau + \int_0^t \dot{\boldsymbol{u}}^T \boldsymbol{K}\, \boldsymbol{u}\, d\tau + \int_0^t \dot{\boldsymbol{u}}^T \boldsymbol{B}\, \boldsymbol{F}\, d\tau = \int_0^t \dot{\boldsymbol{u}}^T \boldsymbol{P}\, d\tau \tag{4.33}$$

Eq. 4.33 can be rewritten as:

$$E_K(t) + E_{VD}(t) + E_S^S(t) - E_S^S(0) + W_b(t) = E_P(t) \tag{4.34a}$$

$$\textit{where } E_K(t) = \int_0^t \dot{\boldsymbol{u}}^T \boldsymbol{M}\, \ddot{\boldsymbol{u}}\; d\tau = \frac{1}{2} \dot{\boldsymbol{u}}(t)^T \boldsymbol{M}\, \dot{\boldsymbol{u}}(t) \tag{4.34b}$$

$$E_{VD}(t) = \int_0^t \dot{\boldsymbol{u}}^T \boldsymbol{C}\, \dot{\boldsymbol{u}}\, d\tau \tag{4.34c}$$

$$E_S(t) - E_S(0) = \int_0^t \dot{\boldsymbol{u}}^T \boldsymbol{K}\, \boldsymbol{u}\, d\tau = \frac{1}{2} \boldsymbol{u}(t)^T \boldsymbol{K}\, \boldsymbol{u}(t) - \frac{1}{2} \boldsymbol{u}(0)^T \boldsymbol{K}\, \boldsymbol{u}(0) \tag{4.34d}$$

$$W_b(t) = \int_0^t \dot{\boldsymbol{u}}^T \boldsymbol{B}\, \boldsymbol{F}\, d\tau \tag{4.34e}$$

$$E_P(t) = \int_0^t \dot{\boldsymbol{u}}^T \boldsymbol{P}\, d\tau \tag{4.34f}$$

$E_K(t)$ is the kinetic energy, $E_S^S(t)$the strain energy stored in the linear superstructure and $E_{VD}(t)$ the energy dissipated by linear viscous damping during motion. $E_P(t)$ is the energy input to the system by the strong motion. The term $W_b(t)$ represents the work of the non-linear forces developed in the isolation system and is further developed making use

of the equilibrium, compatibility and constitutive equations 4.9, 4.10 and 4.11:

$$\begin{aligned}
W_b(t) &= \int_0^t [F_e\nu_e + F_e\nu_p + F_f\nu_f]d\tau \\
W_b(t) &= \int_0^t (F_e\nu_e + F_h\nu_h)\, d\tau + \int_0^t F_p\nu_p d\tau + \int_0^t F_f\nu_f d\tau \\
W_b(t) &= \int_0^t \left(F_e A_e\dot{F}_e + F_h A_h\dot{F}_h\right) d\tau + \int_0^t F_p\nu_p d\tau + \int_0^t F_f\nu_f d\tau \\
W_b(t) &= \tfrac{1}{2}A_e\, F_e(t)^2 + \tfrac{1}{2}A_h\, F_h(t)^2 - \tfrac{1}{2}A_e\, F_e(0)^2 - \tfrac{1}{2}A_h\, F_h(0)^2 + \int_0^t F_p\nu_p d\tau + \int_0^t F_f\nu_f d\tau
\end{aligned} \tag{4.35}$$

Eq. 4.35 can be rewritten as following:

$$W_b(t) = E_S^{RB}(t) - E_S^{RB}(0) + E_D^{RB}(t) + E_D^{SB}(t) \tag{4.36a}$$

$$where \quad E_S^{RB}(t) = \frac{1}{2}\frac{F_e(t)^2}{k_e} + \frac{F_h(t)^2}{k_h} \tag{4.36b}$$

$$E_D^{RB}(t) = \int_0^t F_p(\tau)\nu_p(\tau)d\tau, E_D^{SB}(t) = \int_0^t F_f(\tau)\nu_f(\tau)d\tau \tag{4.36c}$$

In the expression 4.36 for the work of the resisting forces of the isolation system $W_b(t)$ we recognize the strain energy $E_S^{RB}(t)$, which is the energy stored in the elastic springs k_0, k_h used in the mechanical representation of the elastomeric bearings and the energy dissipated by the rubber and sliding bearings, $E_D^{RB}(t)$ and $E_D^{SB}(t)$ respectively.

Summarizing, the energy equilibrium for the structural system considered herein becomes:

$$E_K(t) + E_{VD}(t) + E_S(t) + E_D^{RB}(t) + E_D^{SB}(t) = E_I(t) \tag{4.37a}$$

$$where\ E_S(t) = E_S^S(t) + E_S^{RB}(t),\ E_I(t) = E_P(t) + E_S(0) \tag{4.37b}$$

The equilibrium equation 4.37 shows how the kinetic and stain energy stored in the linear superstructure and the elastic springs of the bi-linear HBIS, $E_K(t), E_S(t)$, together with the energy dissipated by damping and non-linear resisting forces in the rubber and friction bearings, $E_{VD}(t), E_D^{RB}(t), E_D^{SB}(t)$, balances the energy input to the system $E_I(t)$.

4.7 Numerical application 1: free vibration response simulation of the Augusta isolated building

The constrained optimization procedure, described in section 4.5, is applied for the free vibration response simulation of the isolated Augusta building under test 9 ($u_0 = 10.1cm$).

4.7.1 Input properties

The input properties for the four-degree-of-freedom model are the ones obtained from the individual identifications of the HBIS and the superstructure under test 9, see Table 4.3.

The damping and stiffness matrices of the superstructure are constructed by superposition of the corresponding modal matrices $\tilde{\boldsymbol{C}}, \tilde{\boldsymbol{K}}$, see Eqs 4.38. $\tilde{\boldsymbol{C}}, \tilde{\boldsymbol{K}}$ are diagonal matrices with entries $\tilde{C}_{nn} = 2\zeta_n \omega_n M_n$, $\tilde{K}_{nn} = \omega_n^2 M_n$, where M_n is the modal mass.

$$\boldsymbol{C_{ss}} = \left(\boldsymbol{\Phi^T}\right)^{-1} \tilde{\boldsymbol{C}}\, \boldsymbol{\Phi^{-1}} = \boldsymbol{M_{ss}} \left(\sum_{n=1}^{3} \frac{2\zeta_n \omega_n}{M_n} \boldsymbol{\phi_n}\, \boldsymbol{\phi_n}^{\boldsymbol{T}} \right) \boldsymbol{M_{ss}} \tag{4.38a}$$

$$\boldsymbol{K_{ss}} = \left(\boldsymbol{\Phi^T}\right)^{-1} \tilde{\boldsymbol{K}}\, \boldsymbol{\Phi^{-1}} = \boldsymbol{M_{ss}} \left(\sum_{n=1}^{3} \frac{\omega_n^2}{M_n} \boldsymbol{\phi_n}\, \boldsymbol{\phi_n}^{\boldsymbol{T}} \right) \boldsymbol{M_{ss}} \tag{4.38b}$$

The superstructure mass given in Table 4.3 is 10% greater than the one obtained by the identification of the superstructure for test 9 ($m_s = 1602.5tons$ against $m_s = 1456.8tons$). The need for calibration of the superstructure mass derives from the following fact. For any positive real number λ, the system $(\lambda \boldsymbol{M_{ss}}, \lambda \boldsymbol{K_{ss}})$ has the same frequencies and modes of vibration of the system $(\boldsymbol{M_{ss}}, \boldsymbol{K_{ss}})$, see Eqs 4.39. However, for one λ the superstructure system will lead to the observed response when combined with the isolation system (m_b, k_0, k_1) and input in the four-degree-of-freedom isolated building model. Figures 4.4 show the comparison of the observed and simulated response, in terms of the relative roof velocity (relative with respect to the base), before and after calibration of the superstructure mass m_s. As

Table 4.3: Input model properties for the response simulation of the Augusta building under test 9. The input isolation system properties are the total mass m, the bi-linear model parameters for the individual HDRB, k_0, k_1, Q and the friction coefficient for the friction sliders μ. The yielding force F_p and the friction forces F_{f0} for the single isolators are also provided (three values are given for F_{f0} since there are three types of sliders, assigned for simplicity the same μ, but experiencing different axial loads). The input superstructure system properties are the superstructure mass matrix $\boldsymbol{M_{ss}}$, the modal frequencies f_n, damping ratios ζ_n and modes $\boldsymbol{\phi_n}$.

isolation system properties

$m\,(tons)$	$k_0\,(kN/m)$	$k_1\,(kN/m)$	$Q\,(kN)$	$\mu(\%)$	$F_y(kN)$	$F_{f0}(kN)$
2400	2116	600	40.2	1.13	56.15	[7.93,10.29,0.28]

superstructure properties

$\boldsymbol{M_{ss}}(tons)$	$[f_1, f_2, f_3](Hz)$	$[\zeta_1, \zeta_2, \zeta_3](\%)$	$[\boldsymbol{\phi_1}, \boldsymbol{\phi_2}, \boldsymbol{\phi_3}]$
$1602.5\begin{pmatrix} 0.46 & 0 & 0 \\ 0 & 0.37 & 0 \\ 0 & 0 & 0.17 \end{pmatrix}$	[4.1,12.8,19.9]	[3.52,6.97,2.80]	$\begin{pmatrix} 0.452 & -0.713 & 0.638 \\ 0.812 & -0.090 & -1.026 \\ 1.0 & 1.0 & 1.0 \end{pmatrix}$

seen in the first sub-plot, the non-calibrated model has different frequency characteristics than the actual system.

$$\lambda \left(\boldsymbol{K_{ss}} - \boldsymbol{\Omega_s^2 M_{ss}} \right) \boldsymbol{\Phi} = \boldsymbol{0} \tag{4.39a}$$

$$\ddot{q}_n(t) + 2\,\zeta_n\,\omega_n\,\dot{q}_n(t) + \omega_n^2\,q_n(t) = -\Gamma_n\,\ddot{u}_b(t), \boldsymbol{u_s}(t) = \sum_{n=1}^{3} \boldsymbol{\phi}_n\,q_n(t) \tag{4.39b}$$

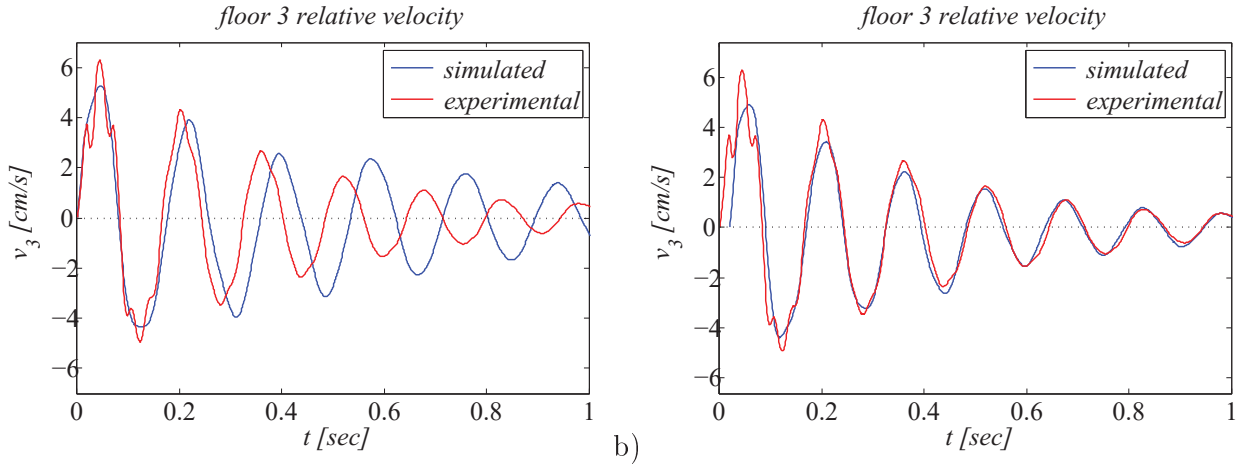

Figure 4.4: Comparison between simulated and experimental relative velocity response (floor 3, test 9) before and after calibration of the superstructure mass; sub-plots (a) and (b).

The global mass, damping and stiffness matrices are built on the basis of the identified properties of the isolation system and the superstructure, see Eqs 4.40.

$$\boldsymbol{M} = \begin{bmatrix} 797.5 & 0 & 0 & 0 \\ 0 & 733.3 & 0 & 0 \\ 0 & 0 & 589.5 & 0 \\ 0 & 0 & 0 & 279.6 \end{bmatrix} (tons),$$

$$\boldsymbol{C} = \begin{bmatrix} 4.25 & -3.84 & -0.92 & 0.50 \\ -3.84 & 6.19 & -0.83 & -1.52 \\ -0.92 & -0.83 & 2.69 & -0.94 \\ 0.50 & -1.52 & -0.94 & 1.96 \end{bmatrix} (*10^3 kNsec/m), \tag{4.40}$$

$$\boldsymbol{K} = \begin{bmatrix} 2.10 & -2.69 & 0.54 & 0.05 \\ -2.69 & 5.63 & -3.27 & 0.33 \\ 0.54 & -3.27 & 4.96 & -2.23 \\ 0.05 & 0.35 & -2.23 & 1.85 \end{bmatrix} (*10^6 kN/m)$$

4.7.2 Test 9 free vibration response simulation

For the response simulation of test 9 an initial displacement $u(0) = 10.1cm$ is given at all degrees-of-freedom together with a load $P(t)$ at the base. The load $P(t)$ is added for a more realistic simulation of the unloading phase of the test.

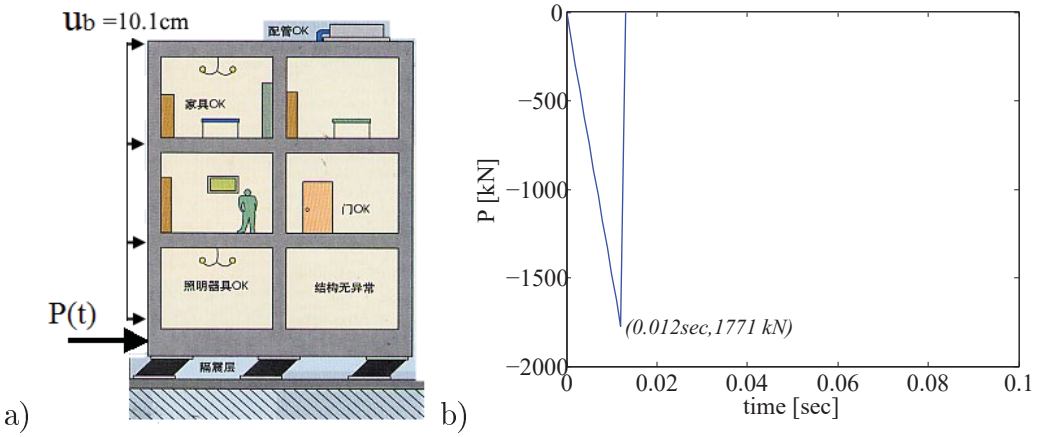

Figure 4.5: Sub-plots (a) and (b). Initial displacement ($\boldsymbol{u}(0) = 10.1cm$) and load conditions used in the free vibration response simulation of the Augusta isolated building under test 9.

Figures 4.6 to 4.8 show the matching between experimental, identified and simulated responses for test 9, in terms of floor accelerations, velocities and displacements. All responses are relative to the ground. The experimental response includes the measured floor accelerations and the corresponding velocities and displacements obtained after the processing of the acceleration signals, see Chapter 2 on signal processing. The identified absolute response is evaluated from the superposition of the responses of the identified HBIS (rigid superstructure model) and the identified fixed base superstructure model, shown in Figures 3.18 to 3.20 (section 3.4.2) and Figures 3.27 to 3.29 (section 3.5.3) respectively. The simulated free vibration response is the response evaluated using the identified HBIS and superstructure properties, Table 4.3, and the four-degree-of-freedom isolated model, see Figure 4.1. The simulated and identified response show a very good matching with the observed response. The considered models tend to underestimate the residual displacement and the duration of strong motion (at the base floor). Observation of the absolute responses obtained from

the simulation of the whole isolation structure, show how the algorithm can account for the fact that while the base stops moving at $t = 2.73sec$, the upper floors continue to vibrate until the motion is damped out. The four-degree-of freedom model, having 4 frequencies, can describe very well the high frequency characteristics of the acceleration responses of the lower floors. However, it seems that the model does not damp sufficiently the response after the first half cycle of motion.

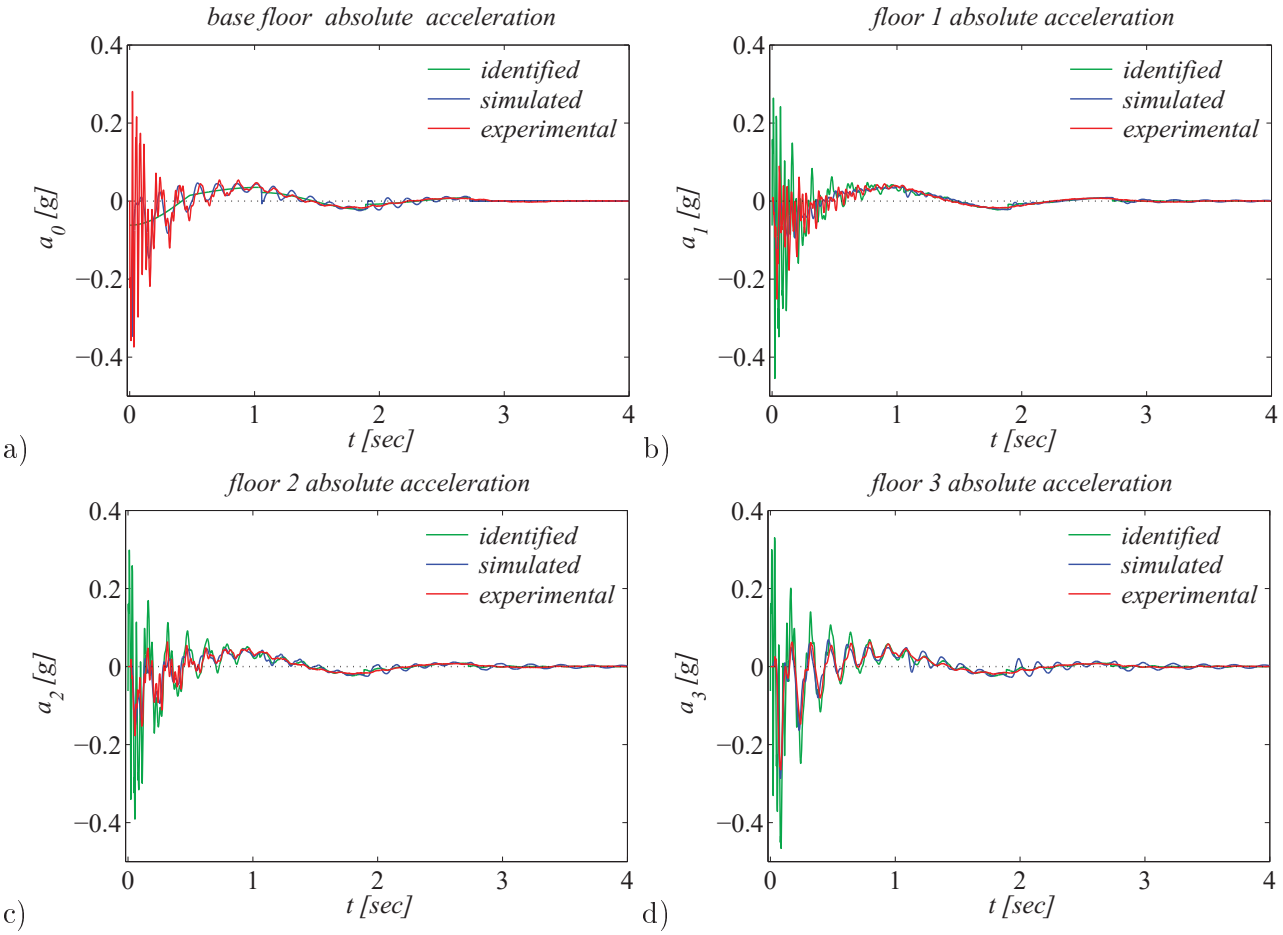

Figure 4.6: Comparison of experimental, identified and simulated absolute base floor, first floor, second floor and roof accelerations of the Augusta building under test 9.

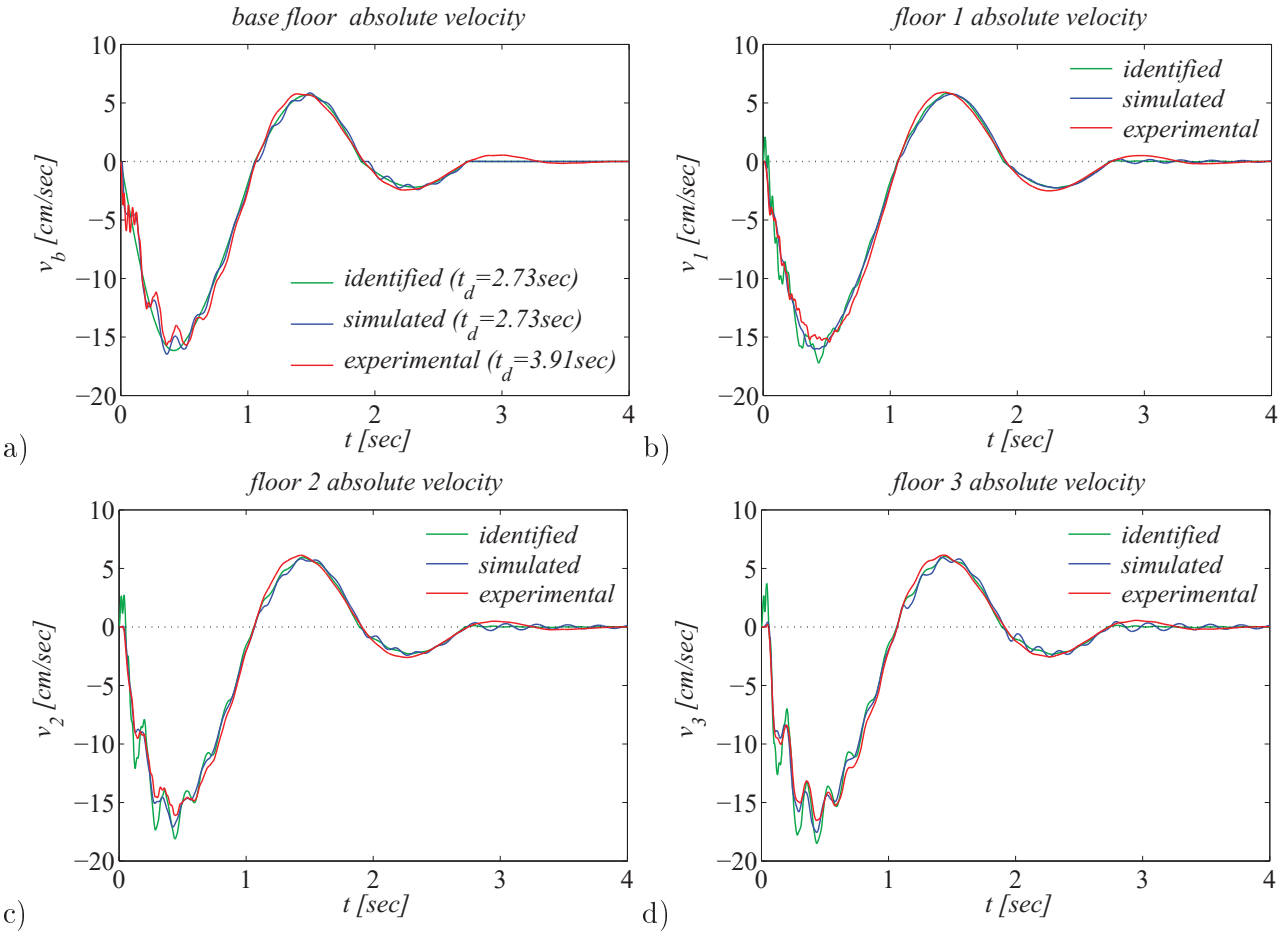

Figure 4.7: Comparison of experimental, identified and simulated absolute base floor, first floor, second floor and roof velocities of the Augusta building under test 9.

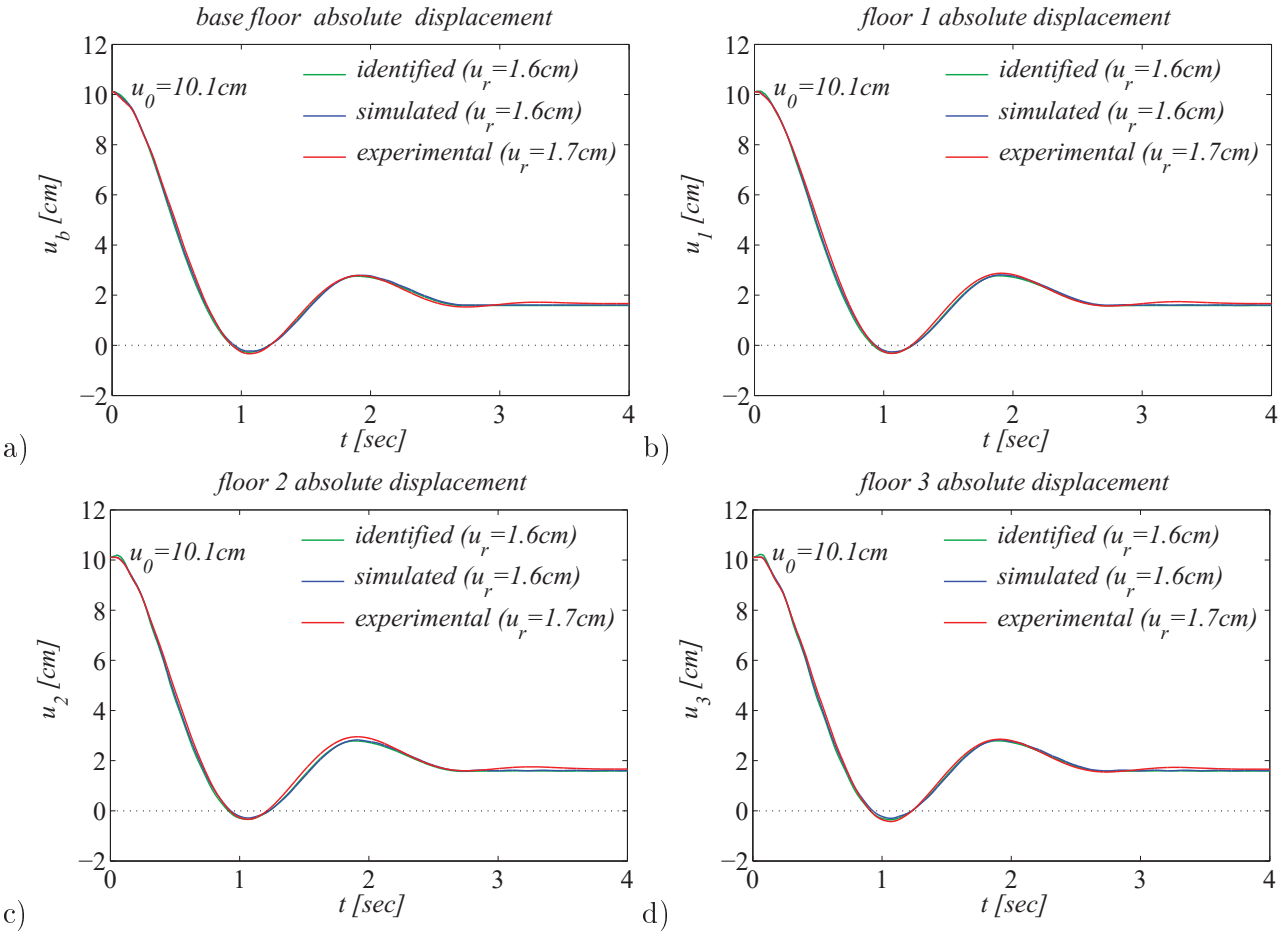

Figure 4.8: Comparison of experimental, identified and simulated absolute base floor, first floor, second floor and roof displacements of the Augusta building under test 9.

Figures 4.9 to 4.11 show the matching between experimental, identified and simulated relative to the base floor responses for test 9. The relative identified response is evaluated using the identified fixed superstructure model, see Figures 3.27 to 3.29 (section 3.5.3). Both the fixed and the isolated base models, reproduce very well the observed response, especially in terms of relative floor velocities and accelerations. The isolated building model provides relatively high responses at times $t \approx 1sec$ and $t \approx 2sec$, when the velocity changes sign. This occurs because of the relatively high friction forces developed in the isolation system; the change of sign in the velocity, causes a jump at the Coulomb friction force, which translates to a jump in the acceleration and a pulse in the relative velocity history. The four-degree-of-freedom model tends to underestimate the peak relative response, which occurs at the beginning of the motion. So does the identified fixed superstructure model. This is probably due to the limitation of the models to account for 3 structural freqeuncies only. The relative simulated response is damped more slowly than what observed in the experiments.

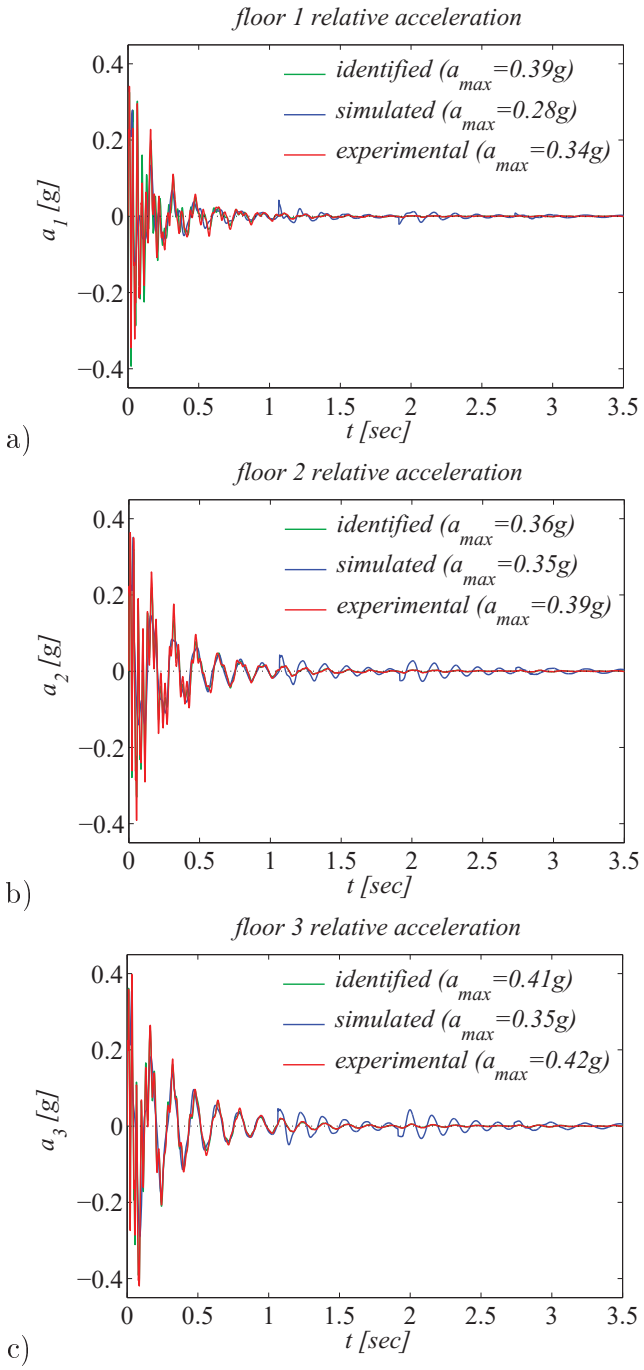

Figure 4.9: Comparison of experimental, identified and simulated relative to the base first floor, second floor and roof accelerations of the Augusta building under test 9.

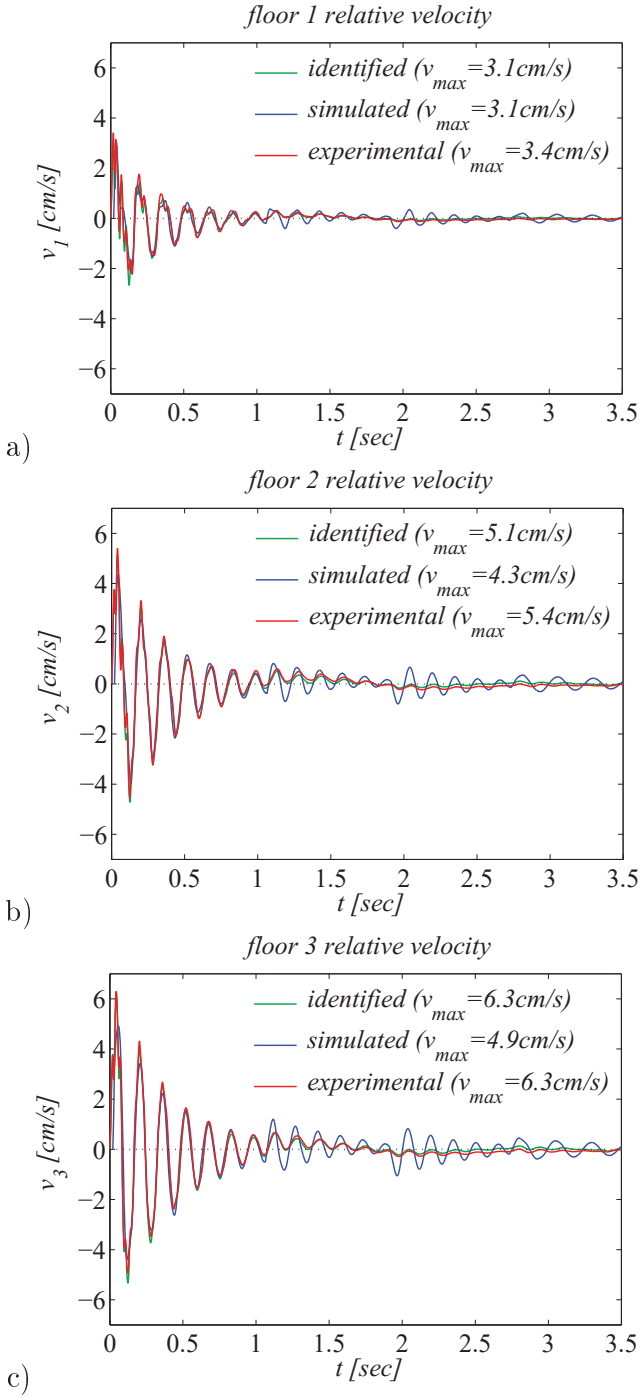

Figure 4.10: Comparison of experimental, identified and simulated relative to the base first floor, second floor and roof velocities of the Augusta building under test 9.

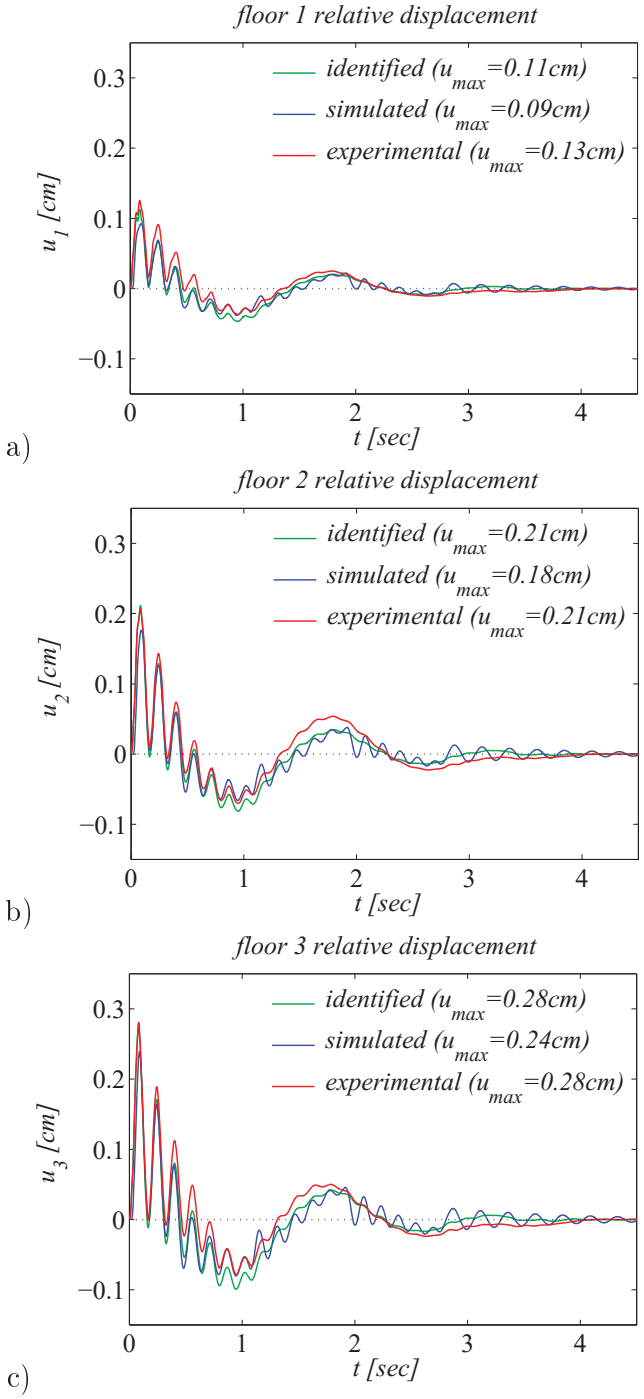

Figure 4.11: Comparison of experimental, identified and simulated relative to the base first floor, second floor and roof displacements of the Augusta building under test 9.

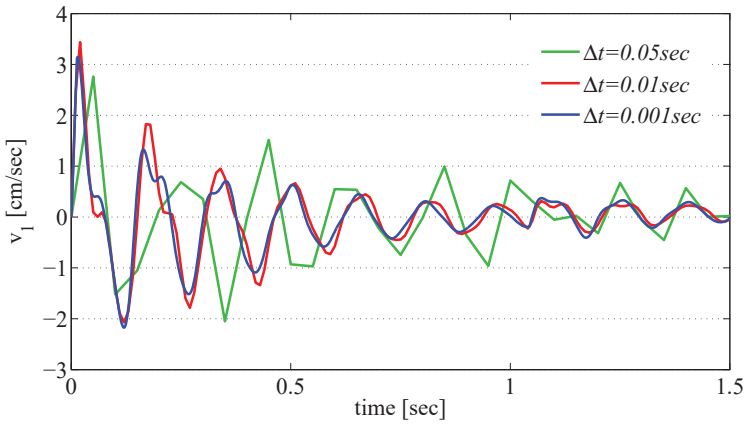

Figure 4.12: Effect of the selection of the time step on the performance of the constrained optimization algorithm. The figure shows the comparison of free vibration response under test 9, in terms of the first floor relative to the base velocity, considering increasing time steps $\Delta t = 0.001sec, 0.01sec, 0.05sec$.

Before closing this section a brief comment is included on the stability and accuracy of the numerical results. As shown in Figure 4.12, the selection of a relatively small time step is essential for the precise description of the input load and the corresponding response. However, even for larger time steps the constrained optimization procedure converges to a solution, without suffering stability issues. In the free vibration simulations shown in this section the time step was equal to $h = 0.001sec$.

4.8 Numerical application 2: earthquake response simulation of the Augusta isolated building

4.8.1 Input ground motions

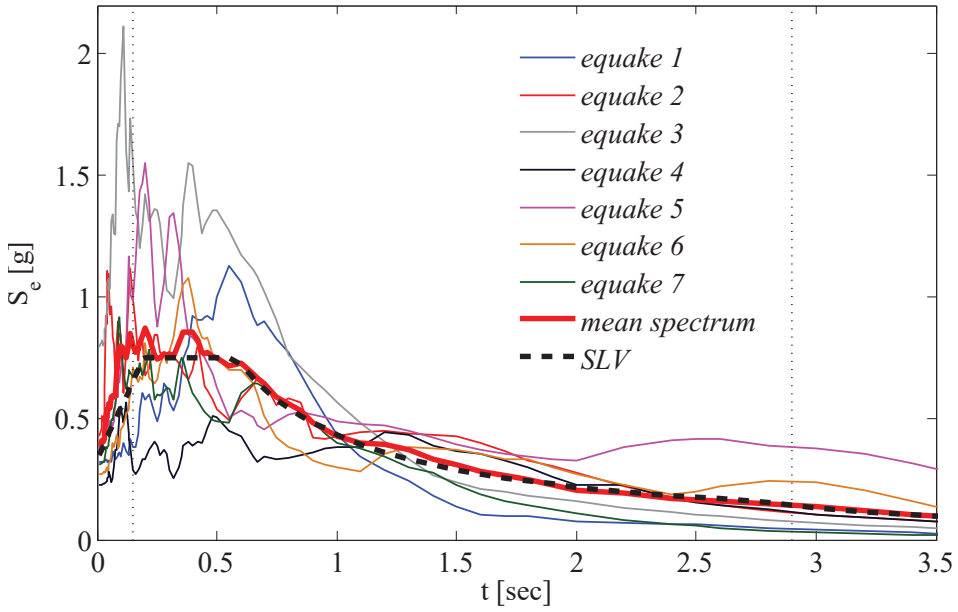

Figure 4.13: Set of ground motions compatible with the NTC08 life safety limit state spectrum (probability of exceedance $P = 10\%$). Vertical lines are drawn at periods $T = 0.15sec$ and $T = 1.2 * T_{is} = 2.90sec$; NTC08 requires that the mean spectrum of the selected ground motions does not fall more than 10% below the design spectrum in the period range $T = 0.15 - 2.90sec$. More information on the selected events is provided in Table 4.4.

The structure was subjected to a set of 7 motions, compatible with the NTC08 design spectrum at the life safety limit state (SLV: probability of exceedance $P = 10\%, a_g = 0.289g$, return period $T_R = 712yrs$[33]), see Figure 4.13 and Table 4.4. The Italian Standards require that the average spectrum of the selected set of motions does not fall more than 10% below the design spectrum in the period range $T = 0.15sec$ to $T = 1.2 * T_{is}$, where T_{is} is the effective

Table 4.4: Characteristics of the selected SLV spectrum compatible motions. Second column: event id. Third column: station and component. Fourth column: moment magnitude. Fifth and sixth columns: depth and epicentral distance.

No	Earthquake	Station[component]	Mw	$D(km)$	$R(km)$
1	Montenegro 1979	BUD [EW]	6.2	5	8.3
2	L' Aquila 2009	AQK[NS]	6.1	8.3	1.8
3	L' Aquila 2009	AQV [EW]	6.1	8.3	4.9
4	Irpinia 1980	BGI [EW]	6.9	8.3	21.9
5	Irpinia 1980	STURNO [EW]	6.9	15	33.3
6	Irpinia 1980	STURNO [NS]	6.9	15	33.3
7	Friuli 1976	GMN[EW]	6.0	11.3	4

period of the isolation system. Herein $T_{is} = 2.44sec$, as obtained from the identification of the HBIS model for test 9.

The spectrum compatible motions were obtained using the REXELite application within ITACA[1], which allows to search combinations of seven 1- or 2-components strong motion records, compatible in average with a specified code spectrum [80].

The input motions include the 1979 Montenegro, the 1976 Friuli, the 1980 Irpinia and the 2009 L' Aquila mainshocks, see Table 4.4. An earlier study on the earthquake response simulation of isolated systems showed that the registrations at the Bagnoli, Sturno (Irpinia 1980) and AQK stations (L'Aquila 2009) have near fault characteristics, thus inducing high displacement demands at systems responding to their long period range [16]. The selected scaled motions are shown in Figure 4.14.

[1]ITACA (ITalian ACcelerometric Archive): http://itaca.mi.ingv.it/ItacaNet/CadmoDriver?_action_do_menu=1&_page=REX_rexel_homepage&_rock=INVALID&_state=find&_tabber=5&_token=NULLNULLNULLNULL

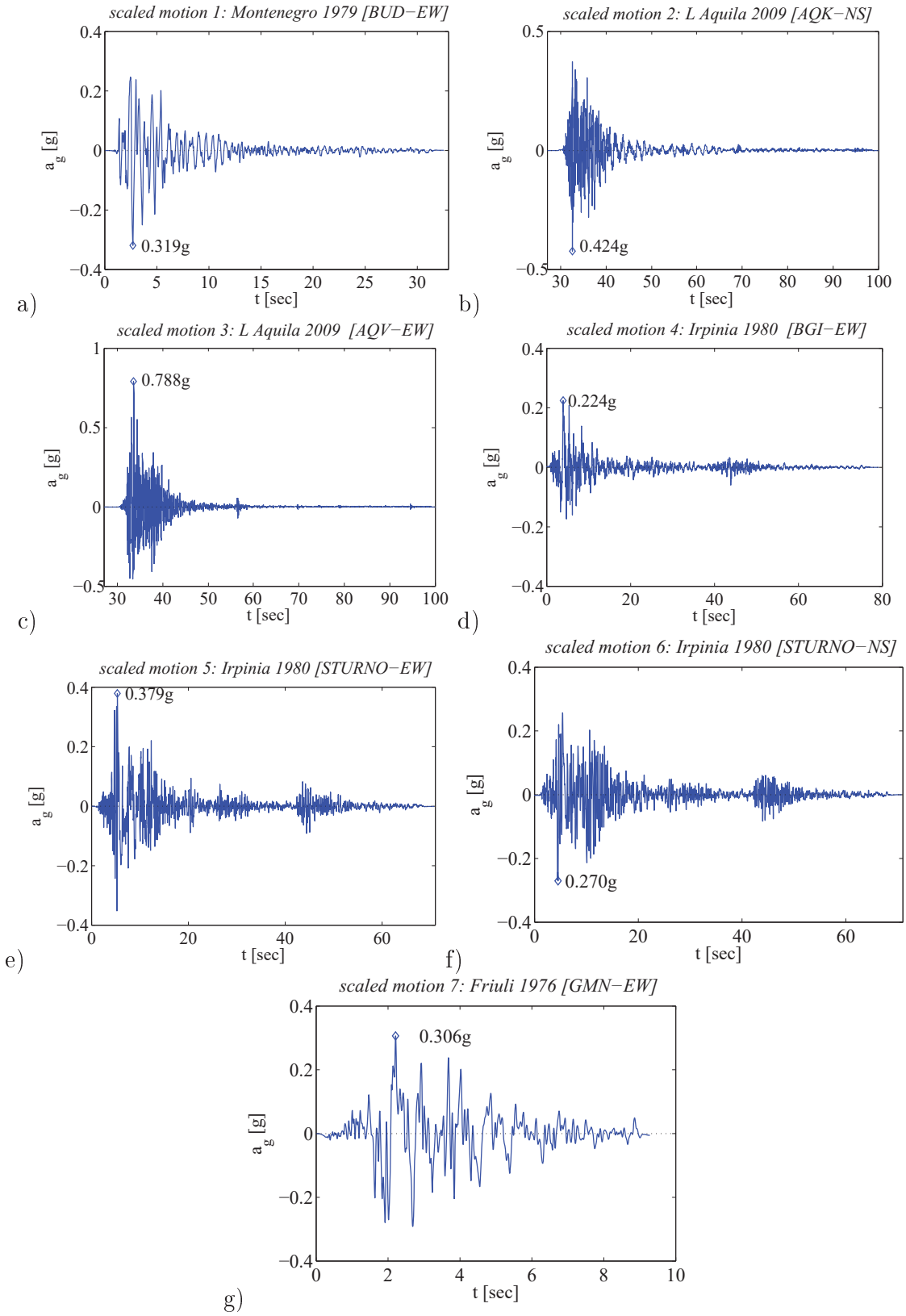

Figure 4.14: Set of 7 ground motions compatible with the NTC08 design spectrum at the life safety limit state.

4.8.2 Isolated structure response to strong motion 4

The system response under one of the selected spectrum compatible motions (event 4, scaled Iprinia 1980-BGI) is shown in this section. Figure 4.15 shows the acceleration histories at the base and the upper floors of the Augusta building together with the input motion for event 4. Figure 4.16 shows the corresponding floor displacements (relative to the ground). The inter-story drift histories for the strong motion 4 are shown in Figure 4.17. The obtained response demonstrates the effectiveness of the base isolation. The introduction of the flexible bearings 'isolates' the building from the shaking ground; the energy input in the system by the earthquake is dissipated essentially in the non-linear isolation system. The bearings accommodate the largest part of the displacement demand induced by the motion, while the superstructure responds essentially as a rigid body (similar floor acceleration and displacement histories and very small inter-story drifts, see Figures 4.15 to 4.16). The maximum shear strain demand on the rubber bearings is $\gamma_{max} = 21.51/15 = 1.43$. The non-linearity of the isolation system results to a residual displacement at the end of the motion, however this is very small of the order of $0.50cm$.

Figures 4.18 show the resisting forces developed in the isolation system during the ground motion considered. The F-u hysteresis loops are shown only for one rubber bearing, since they are all of one class. The F-u loop for the sliding elements are shown only for sliders of type 2, which are the ones experiencing larger vertical loads ($V = 900kN$). Figure 4.18(c) shows the time intervals when the elastomer undergoes yielding. Yielding (or plastic) phases occur in the first ten seconds of motion, when the motion is stronger.

Finally, figure 4.19 shows the evolution of the kinetic and strain energies together with the energy dissipated in the isolation system during motion 4. $E_K, E_S, E_D^{RB}, E_D^{SB}, E_I$ were evaluated according to section 4.6. The dissipation of the energy input by the ground motion is made in the rubber and friction sliders, while the contribution of damping to energy dissipation is negligible.

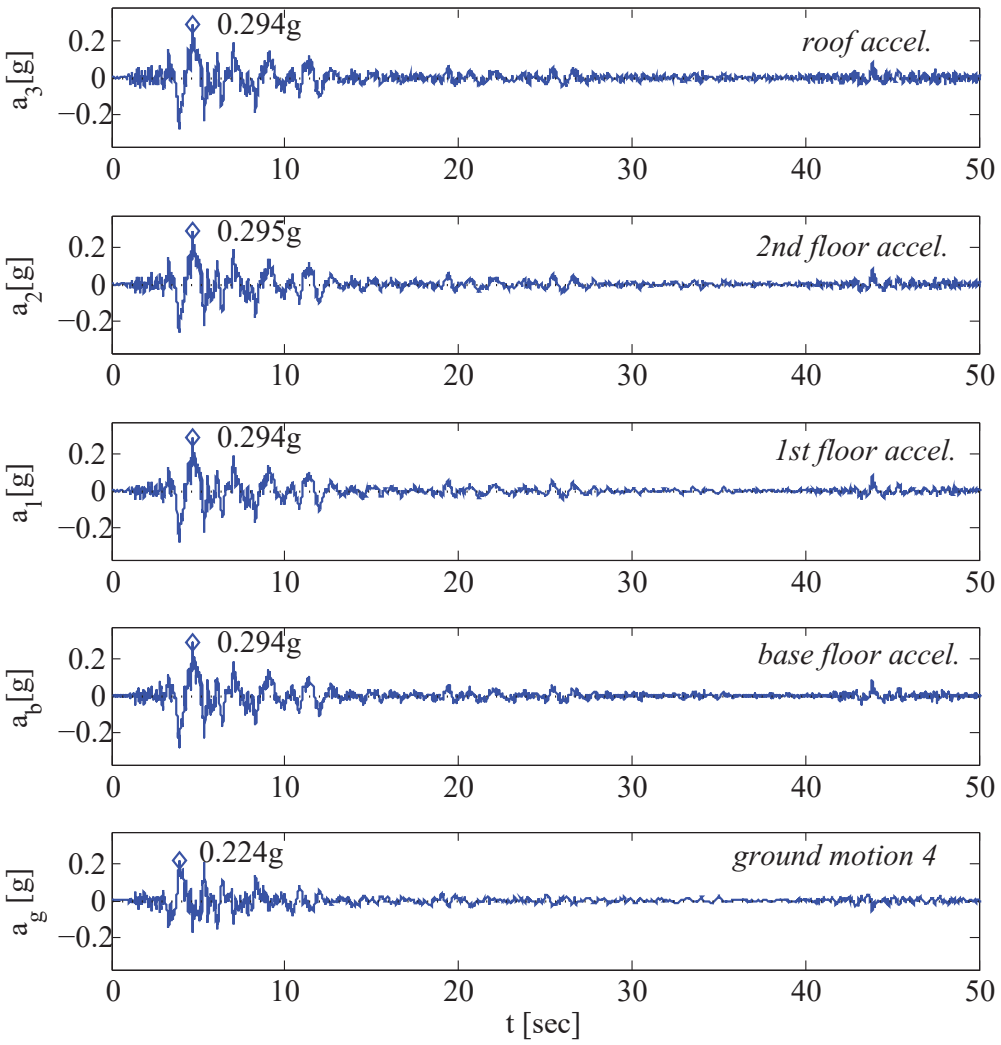

Figure 4.15: Acceleration histories at the ground, the base floor and the upper floors of the Augusta building during motion 4 (Irpinia 1980-BGI, scaled).

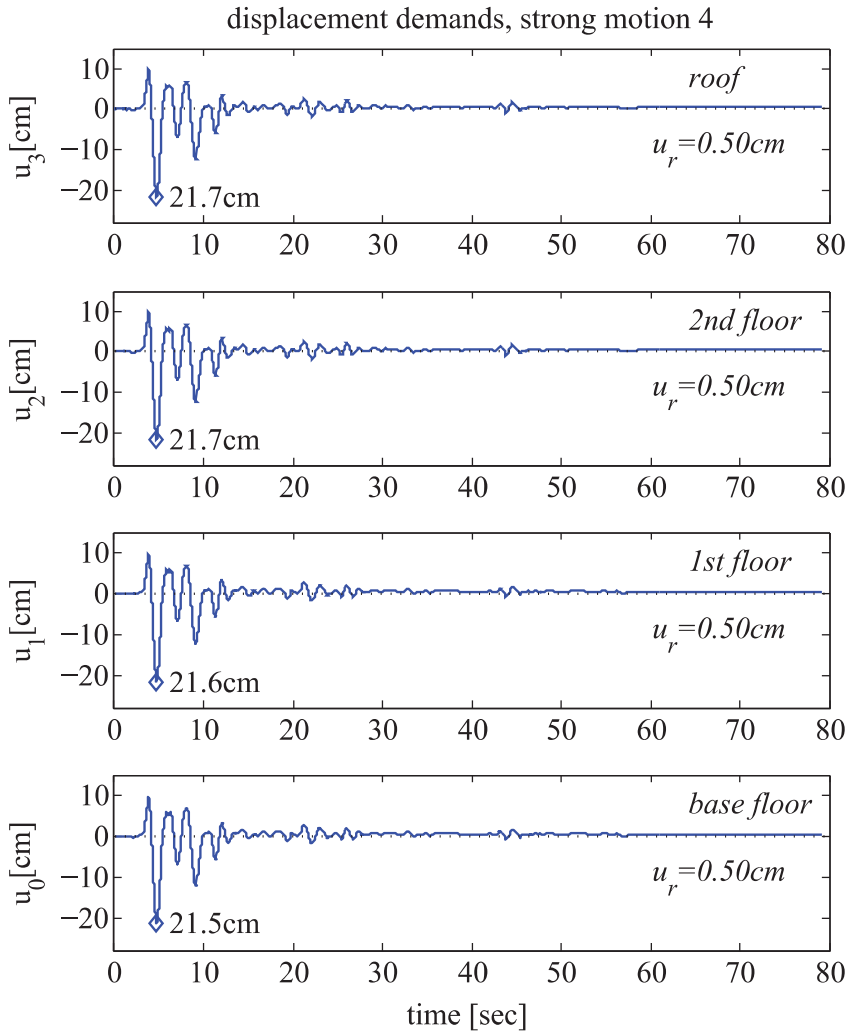

Figure 4.16: Displacement histories at the base and the upper floors of the Augusta building during strong motion 4 (Irpinia 1980-BGI, scaled). The maximum shear strain demand on the rubber bearings is $\gamma_{max} = 21.51/15 = 1.43$.

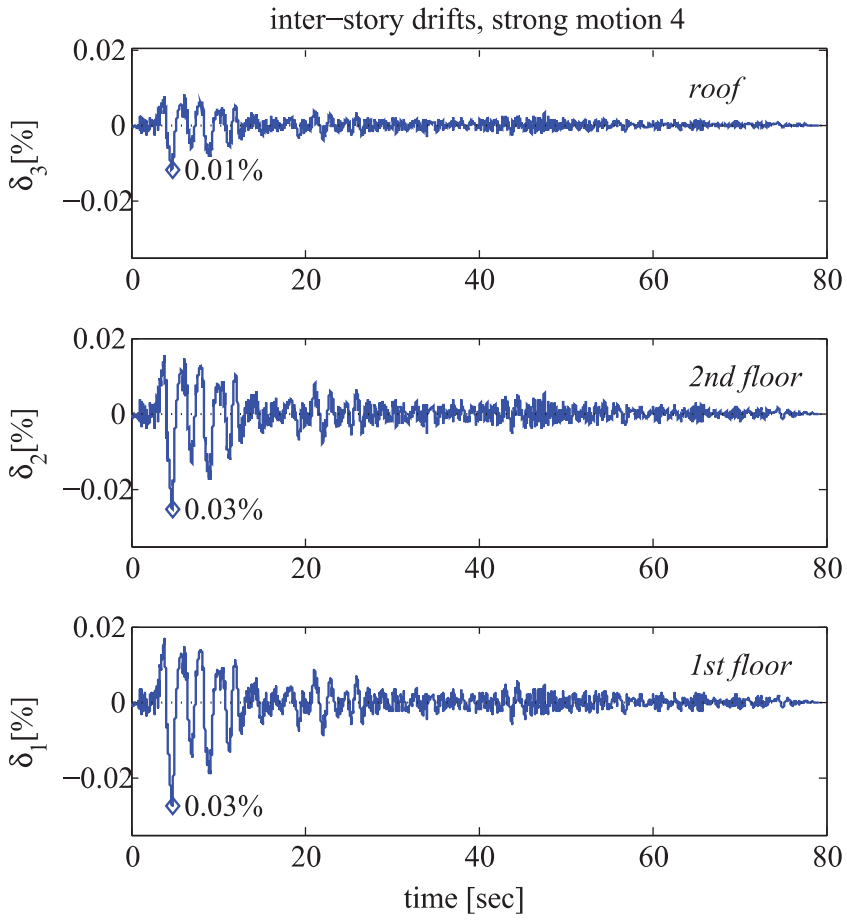

Figure 4.17: Inter-story drift histories at the Augusta superstructure during strong motion 4 (Irpinia 1980-BGI, scaled). The obtained drifts are significantly smaller than the NTC08 limit $\delta = 2/3 * 0.5\% = 0.33\%$ for SLS.

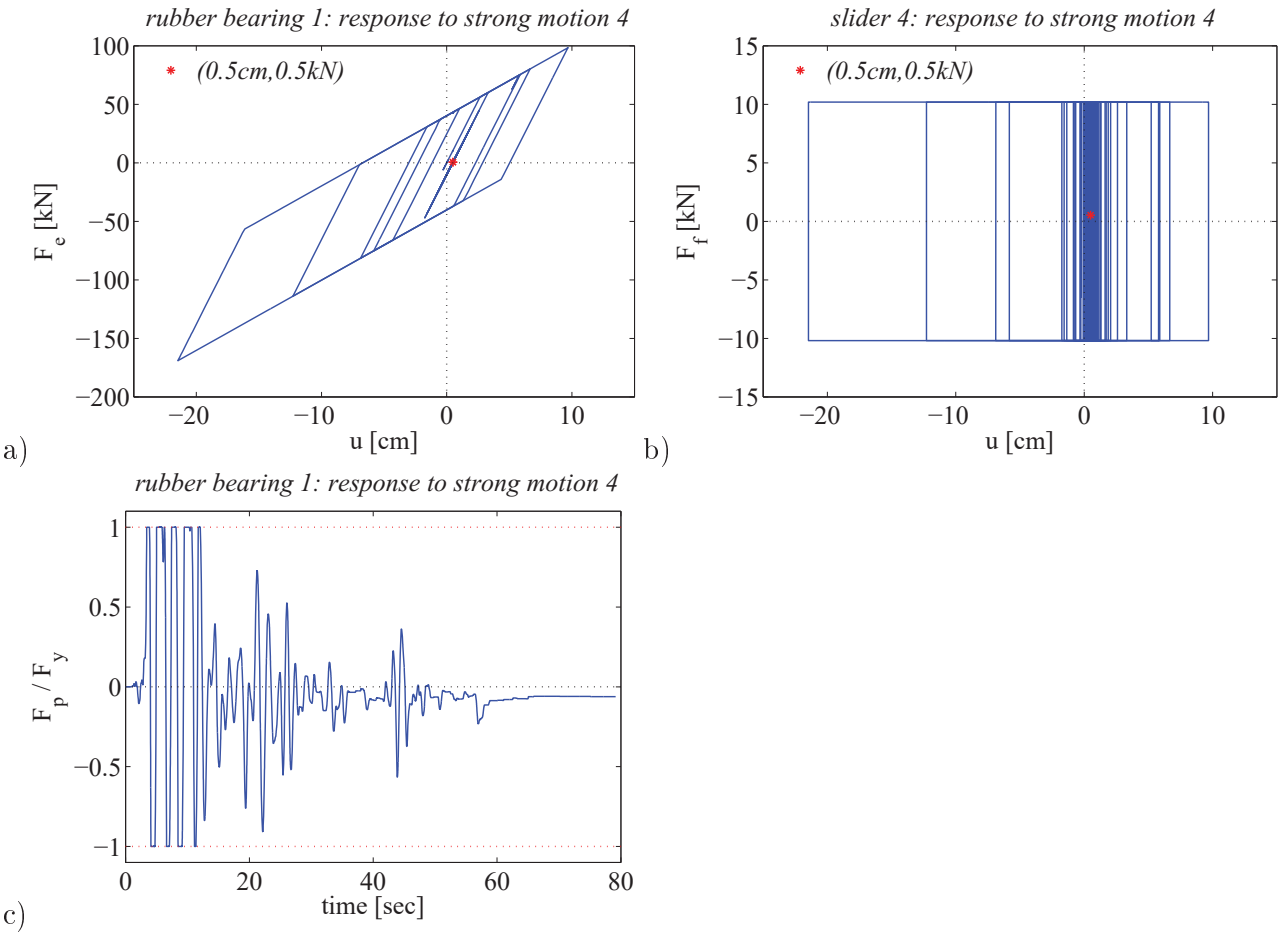

Figure 4.18: (a), (b) Force-displacement loops for one rubber bearing (no 1, see Figure 1.4) and one friction slider (no 4, see Figure 1.4) during earthquake 4 (Irpinia 1980-BGI, scaled). (c) Time intervals of yielding for the elastomers.

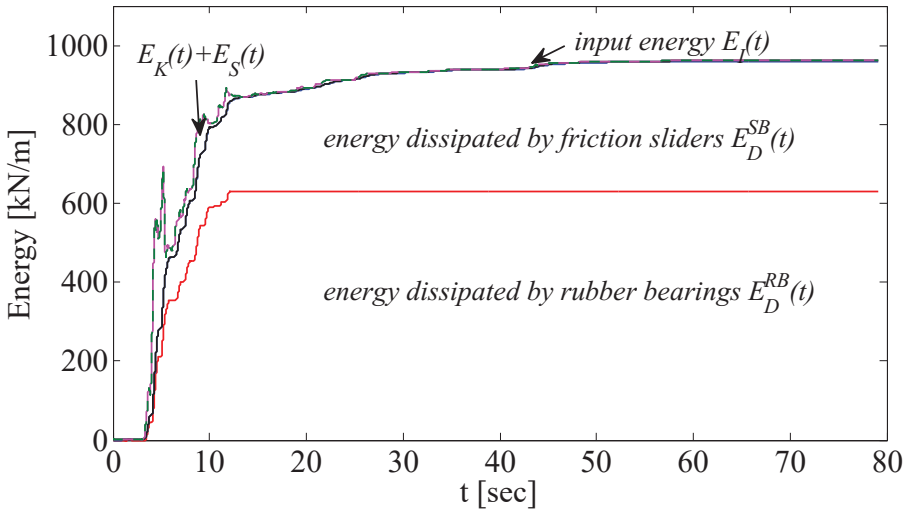

Figure 4.19: Evolution of the kinetic and strain energies together with the energy dissipated in the isolation system during motion 4.

4.8.3 Peak response to the selected ground motions

Figures 4.20 show the peak acceleration, displacement and inter-story drift demands imposed to the structure by the seven SLV spectrum compatible strong motions. The average response is also provided. The seven motions are characterized by different intensity and frequency content, thus leading to very different demands. In particular, motion 5, i.e. the scaled Irpinia 1980, station Sturno, component EW record, calls for the maximum displacement demand for the isolation system ($u_b \approx 66cm$). This occurs because the fundamental period of the isolated structure lies in the long period range, where the dominant components of the motion are found, see Figure 4.13. A previous study by Oliveto et al. showed that the Sturno-EW record has near fault characteristics, resulting to excessive demands for long period systems [16]. The average peak displacement demand, induced by the SLV spectrum compatible motions is only slightly smaller than the displacement demand prescribed by the Italian Standards [33, 45]:

$$d_{SLV}(T_{is} = 2.44sec, \zeta = 18.7\%) = 24.5cm \tag{4.41}$$

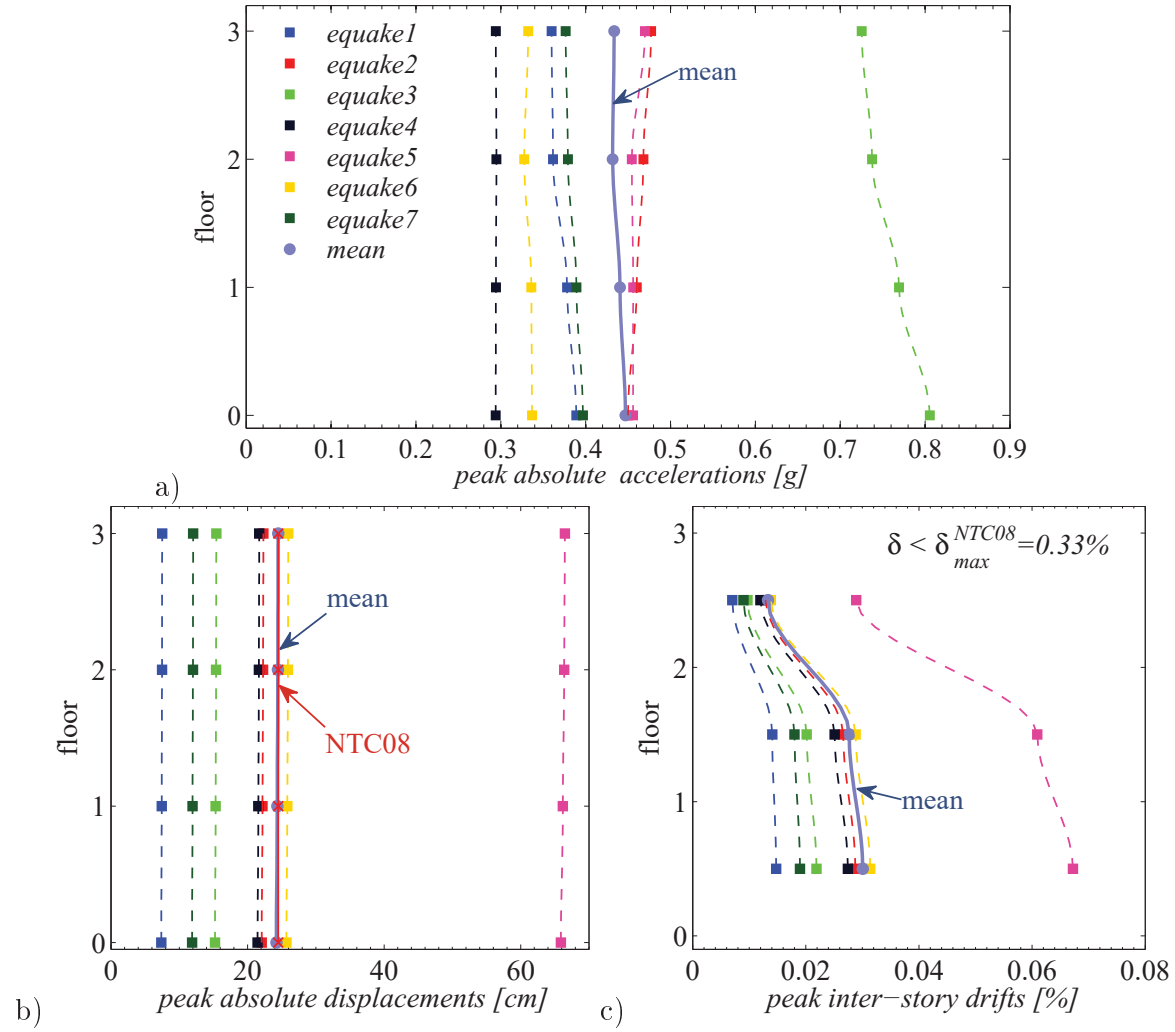

Figure 4.20: Acceleration, displacement and drifts demands for the SLV spectrum compatible motions; sub-plots (a), (b) and (c). The displacement demand as evaluated from the NTC08 is also shown in sub-plot (b).

where $T_{is} = 2.44sec$ and $\zeta = 18.7\%$ are the identified effective period and damping of the isolation system obtained from the identification of test 9, see Table 3.4 in section 3.4.3.

The maximum inter-story drifts for the seven motions considered, are very small with respect to the limits imposed by the NTC08 for the serviceability limit states ($\delta_{max}^{NTC08} = 2/3 \cdot 0.005 = 0.33\%$).

The 1D earthquake response simulation of the building is mainly illustrative and has the

purpose of demonstrating the effectiveness of the algorithm proposed to provide meaningful results. In reality, the properties of the rubber bearings under earthquake excitation will not be the quasi-static properties obtained from the identification of the Augusta tests, but the corresponding dynamic lab properties (which are essentially higher). Moreover, for strong motions like the one recorded at Sturno, the hardening behaviour of the rubber shall be activated. The hardening of the rubber at extreme load conditions cannot be captured with the bilinear model considered herein.

Within this section, very few information was provided on the corresponding equivalent lateral force procedure prescribed by the Italian Standards. For the interested reader, more information on the NTC08 design procedures for the isolation system design at the ultimate limit states, using linear static analysis can be found in [33].

4.9 Conclusions

This chapter presented an energy based constrained optimization procedure for the one dimensional dynamic response simulation of hybrid base isolated systems with flexible superstructure responding in the linear range. The method provides the time step system response to any dynamic load, as the solution of a minimization problem, where the function to be minimized describes the dissipation power, i.e. the rate of the work of the non-conservative forces developed in the isolation system. Implementation of the algorithm for the free vibration response simulation of the Augusta building, using the identified properties for the isolation system and the superstructure provided very good results, which matched satisfactorily the experimental ones. That leads to the conclusion that the identified isolated building properties, obtained from the two stage identification of the non-linear HBIS and the linear superstructure are physically meaningful and serve as a reliable input for the more realistic modelling of the structure.

Chapter 5

Conclusions

This dissertation investigates the behaviour of an isolated building in Augusta, Italy, under a series of full scale push and sudden release tests, performed on the building upon completion (March 2013). The isolation system consisted of 16 high damping rubber bearings and 20 low friction sliding bearings. Eight release tests were performed on the building, with displacement amplitudes that varied from 5.8 to 11.7cm - in terms of shear strain amplitude in the rubber that translates to $\gamma = 0.39 - 0.78$. The tests were characterized by a long quasi-static loading phase, and a short dynamic phase where the building was left to oscillate. The static phase was at least 100 times longer than the dynamic one. The test records included the displacements at the isolation level and the floor accelerations. The recorded transverse displacements were negligible, implying that the unidirectional excitation did not cause appreciable rotation. The longitudinal free vibration records where significant but short, indicating that the system came to rest soon (within the second cycle of motion). This was due to the low initial amplitude and the presence of friction. The obtained acceleration records were processed by means of a baseline fitting scheme developed for the problem at hand. Once adjusted, the floor response was used in the identification of the isolation system and superstructure properties. The identified parameters were then used for the simulation of the overall system response. A constrained optimization procedure was developed for the

time step solution of the non-linear differential equations.

5.1 Baseline fitting using increasing order polynomials (Chapter 2)

A simple baseline fitting scheme was proposed herein for the removal of the low frequency noise from the Augusta records. The method does not require significant computational effort and accounts for boundary conditions, provided that those are known. The polynomial coefficients used in the baseline fitting are determined from the boundary conditions; namely the initial and end accelerations, velocities and displacements. The deterministic definition of the polynomial coefficients and the recovery of permanent displacements enforces the reliability of the method and makes it an attractive alternative to high pass filtering, which instead requires proficient users and includes a lot of subjectivity in the filter parameter selection. The baseline scheme developed was applied for the processing of the absolute and relative acceleration signals obtained from the full Augusta data-set and provided the adjusted response in terms of absolute and relative floor accelerations, velocities, displacements and inter-story drifts. The predicted ground floor displacements matched very satisfactorily the observed ones. There was some uncertainty in the reliability of the predicted relative displacements and drifts versus the end of motion, however such uncertainty cannot be avoided since the signal-to-noise ratio tends to be significantly low for small amplitude motions.

5.2 Dynamic identification of the non-linear isolation system and the linear superstructure (Chapter 3)

The dynamic identification of the system was performed in the time domain using the Covariance Matrix Adaptation Evolution Strategy, a stochastic algorithm used in difficult, non-linear optimization where commonly used gradient methods fail to provide a minimum.

The excessive computational times related to the increased problem dimensionality did not allow the identification of the overall isolated system parameters. Instead, the identification was performed at two stages, for the separate identifications of the isolation system and the superstructure. The objective function was defined as the distance between simulated and experimental response. In the identification of the isolation system, the rubber bearings were modelled using a bilinear system, while the friction sliders were modelled using the Coulomb model. The dynamic identification of the isolation system and the superstructure reveiled that:

- The solution to the minimization problem is not unique and corresponds to a local rather than a global minimum of the optimization. The optimal solution is the one which is physically meaningful and shows increased repeatability.

- The optimal solution varies from test to test, implying that the rubber and friction properties depend on the motion amplitude.

- The elastic and post-elastic stiffnesses, k_0, k_1 and consequently the effective stiffness k_{eff} of the rubber decrease with increasing displacement amplitude indicating period elongation under stronger motions. The characteristic strength Q tends to increase with increasing γ, while the equivalent viscous damping ζ_{eq} tends to decrease with γ. The softening of the rubber at higher strain amplitudes is well documented in the literature. This observation is not valid for extreme loading, where rubber hardening occurs.

- The identified rubber properties lie significantly below the corresponding dynamic lab properties and are in average lower than the static lab ones. A direct comparison of identified and lab properties is not applicable since the lab tests correspond to a higher strain amplitude ($\gamma = 0.39 - 0.79$ against $\gamma = 1$). The identified softened stiffnesses lead to the conclusion that the bearings could not recover their dynamic properties after experiencing a very long static phase (loading history dependence of the rubber).

- The sliding coefficient of friction obtained from the identification is in average 1% and shows increasing trend with increasing velocity amplitude. While the value obtained is consistent with the suggestions of the manufacturer for μ, when multiplied by the axial load acting on the isolators and integrated over the displacement domain results to significant energy dissipation. The friction force identified for the first cycle of motion (where the velocity is large) is too probably too large for the successive cycles.

- The simplicity of the bi-linear and Coulomb model is not considered to have affected significantly the results. The bi-linear model describes with sufficient accuracy the hysteretic behaviour of the rubber at moderate strain range. Moreover it allows for the analytical solution of the equation of motion. The use of strain-adaptive models for the rubber and more detailed friction models [20, 6] would be rather recommended when considering strong motion, where the system exhibits several cycles of motion and there is significant redistribution of axial load, heating and stick-slip motion.

- The identification of the superstructure provided the floor mass distribution and the modal properties of the considered three-degree-of-freedom viscously damped linear model (modal frequencies, damping ratios, modes of vibration). All tests, but one, provided very similar results, showing that the inherent properties of the superstructure do not depend on the input excitation (in the linear range). There was evidence that the second mode provided significant contribution to the flexible superstructure response. Higher frequencies can be detected in any acceleration record obtained from the Augusta tests. The excitation of higher frequencies is related more to the type of induced excitation and less to the non-linearity of the isolation system. When the building was released, an impulsive force acted at the base. This force was transmitted to the superstructure, however it attenuated with distance and time.

5.3 1D dynamic response simulation of the hybrid base isolated building (Chapter 4)

The identified properties of the system were input in a synthesized model of the isolated structure which was used in the response simulation of the experiments. The matching between simulated and experimental response was very satisfactory, both in terms of absolute and relative response. The coupled non-linear equations of motion were solved using a constrained optimization procedure developed for the 1D dynamic response simulation of isolated buildings. In the numerical algorithm proposed, the function to be minimized was defined on the basis of the energy dissipated in the isolation system, while the optimization constraints corresponded to the feasible domains of the non-conservative forces developed in the isolation system.

5.4 Limitations and needs for further investigation

The push and sudden release tests used to provide dynamic data for the identification of the mechanical properties of base isolated buildings, such as the Solarino buildings in 2004 and the Augusta building in 2013, have advantages and disadvantages over laboratory tests conducted on single isolators or on scaled down models of substructures. The main advantage is that the overall behavior of the actual building and of its complete isolation system is tested. Also the way the tests are performed enables the excitation of high frequencies in the superstructure which may be useful in the identification of the properties of the superstructures besides those of the isolation system. The main disadvantage is that, unless a strong power unit is available, the initial displacement can be applied only in a quasi-static fashion. The long duration of the pushing phase, because of creep in the elastomers, determines a softening of the load-displacement curve as compared to the one that would be obtained by applying the displacement at a much higher speed as that corresponding to the fundamental period of the system. These stiffness properties are retained in the following

dynamic phase of free vibration with the result that the identified properties of the isolation system are closer to those obtained by quasi-static laboratory tests on single isolators than by dynamic tests. The obvious recommendation for the repetition of full-scale push and release tests of the type of the Solarino and Augusta ones is to increase the velocity of application of the initial displacement to a level where creep of the elastomer is negligible.

Another lesson learned from the tests performed on the Augusta building is that the floor slab just above the isolation system should be stiff enough to be considered as axially rigid. In this way all isolators would undergo the same displacement and high frequency motions within the slab would be avoided. These motions could determine also complex interactions between perimeter elastomeric isolators and internal sliding isolators.

A limitation of the results of the present work derives from the amplitude of the applied displacements. This was constrained by the need not to cause damage to the non-structural elements of the building and by the limited power available for the application of the initial displacement. Identification of the properties of the isolation system with the same model at larger amplitudes of imposed displacements would have provided different results.

Elastomeric bearings exhibit different properties at small, intermediate and large shear strains; the model used in the present work is more appropriate for shear strains not much larger than 1. When, as is the case with large earthquakes, the expected strains are expected in the full range from small to large, say from 0 up to 2 or more, more complete models than the bi-linear one would be required. However, given an improved model, the identification procedure introduced herein could still be applied.

In modelling the sliding bearings the simple Coulomb friction model was used, although in the literature more sophisticated models exist that allow for the change of the friction coefficient with velocity and possibly pressure and temperature. In the present study the simple model was used in consideration that the effect of friction from the low-friction sliding bearings was expected to be small.

Bibliography

[1] Farzad N and Kelly J. *Design of Seismic Isolated structures. From Theory to Practice*. John Wiley & Sons, 1999.

[2] Chopra A. *Dynamics of Structures. Theory and Applications to Earthquake Engineering*. 4th edition. Pearson Prentice Hall, New Jersey, 2012.

[3] Constantinou M C et al. *LRFD-Based analysis and design procedures for bridge bearings and seismic isolators*. Tech. rep. MCEER-11-0004. Multidisciplinary Center for Earthquake Engineering Research, State University of New York at Buffalo, USA, 2011.

[4] Oliveto G and Marletta M. "Seismic retrofitting of reinforced concrete buildings using traditional and innovative techniques". In: *ISET Journal of Earthquake Technology* 42.2-3 (2005). Paper Number No.454, pp. 21–46.

[5] Constantinou M C. *CIE 625 : Aseismic Base Isolation*. Class notes. State University of New York at Buffalo. 2015.

[6] Constantinou M C et al. *Performance of Seismic Isolation Hardware under Service and Seismic Loading*. Tech. rep. MCEER-07-0012. Multidisciplinary Center for Earthquake Engineering Research, State University of New York at Buffalo, USA, 2007.

[7] Warn G and Ryan K. "A Review of Seismic Isolation for Buildings: Historical Development and Research Needs". In: *Buildings* 2.3 (2012), pp. 300–325.

[8] Villaverde R. *Fundamental Concepts of Earthquake Engineering*. Boca Raton, FL: CRC Press, 2009.

[9] Kani N. "Current state of seismic-isolation design". In: *Journal of Disaster Research* 4.3 (2009). Special Issue on 'Japan's Advanced Technology for Building Seismic Protection', pp. 175–181.

[10] Nagarajaiah S and Xiaohong S. "Response of base-isolated USC hospital building in Northridge earthquake". In: *Journal of Structural Engineering* 126.10 (2000), pp. 1177–1186.

[11] Nishiyama I et al. "Building damage by the 2011 Tohoku Japan earthquake and coping activities by Nilim and Bri collaborated with the administration". In: *Proceedings of the International Symposium on Engineering Lessons Learned from the 2011 Great East Japan Earthquake, March 1-4, 2012, Tokyo, Japan*. 2011, pp. 504–515.

[12] Hijikata K et al. "Behavior of a base-isolated building at Fukushima Dai-Ichi nuclear power plant during the Great East Japan earthquake". In: *International Symposium on Engineering Lessons Learned from the 2011 Great East Japan Earthquake*. Japan Association for Earthquake Engineering. Mar. 2012, pp. 1542–1551.

[13] EERI. *Special Earthquake Report: Learning from earthquakes. Performance of engineered structures in the Mw 9.0 Tohoku, Japan, Earthquake of March 11, 2011*. Jan. 2012.

[14] EN 15129. *Antiseismic Devices. Brussels: Comité Européen de Normalisation (CEN)*. 2009.

[15] Becker T. "Advanced modeling of the performance of structures supported on Triple Friction Pendulum bearings". PhD thesis. University of California, Berkeley, 2011.

[16] Oliveto G, Athanasiou A, and Oliveto N D. "Analytical earthquake response of 1D hybrid base isolation systems". In: *Soil Dynamics and Earthquake Engineering* 43 (2012), pp. 1–15.

[17] Bouc R. "Forced vibration of mechanical systems with hysteresis". In: *Proceedings of the Fourth Conference on Nonlinear Oscillation. Prague, Czechoslovakia*. 1967, p. 315.

[18] Wen Y. "Method for random vibration of hysteretic systems". In: *Journal of the Engineering Mechanics Division* 102.2 (1976), pp. 249–263.

[19] Nagarajaiah S, Reinhorn A, and Constantinou M C. "Nonlinear dynamic analysis of 3-D base isolated structures". In: *Journal of Structural Engineering* 117 (1991), pp. 2035–2054.

[20] Kikuchi M and Aiken I D. "An analytical hysteresis model for elastomeric seismic isolation bearings". In: *Earthquake engineering & Structural Dynamics* 26.2 (1997), pp. 215–231.

[21] Dolce M, Cardone D, and Croatto F. "Frictional behavior of Steel-PTFE Interfaces for Seismic Isolation". In: *Bulletin of Earthquake Engineering* 3.1 (2005), pp. 75–99.

[22] Mokha A and Lee P. "Wings of isolation". In: *Modern Steel Construction* (1999).

[23] Fenz D M and Constantinou M C. "Behaviour of the double concave Friction Pendulum bearing". In: *Earthquake Engineering & Structural Dynamics* 35.11 (2006), pp. 1403–1424.

[24] Fenz D M and Constantinou M C. "Spherical sliding isolation bearings with adaptive behavior: theory". In: *Earthquake Engineering & Structural Dynamics* 37.2 (2008), pp. 163–183.

[25] Morgan T and Mahin S. "Achieving reliable seismic performance enhancement using multi-stage friction pendulum isolators". In: *Earthquake Engineering & Structural Dynamics* 39.13 (2010). Special EESD issue on seismic protection techniques, pp. 1443–1461.

[26] Zayas V. "Seismic design for a resilient and sustainable society". In: *8CUEE, 8th International Conference on Urban Earthquake Engineering*. Center for Urban Earthquake Engineering, Tokyo Institute of Technology. Mar. 2011, pp. 1217–1225.

[27] Fenz D M and Constantinou M C. "Spherical sliding isolation bearings with adaptive behavior: experimental verification". In: *Earthquake Engineering & Structural Dynamics* 37.2 (2008), pp. 185–205.

[28] Becker T and Mahin S. "Experimental and analytical study of the bi-directional behavior of the Triple Friction Pendulum isolator". In: *Earthquake Engineering & Structural Dynamics* 41.3 (2012), pp. 355–373.

[29] Sarkisian M and Lee P. "Enhanced seismic performance of the new San Bernardino Justice Center". In: *Proceedings 2011 SEAOC convention*. 2011.

[30] Kelly J and Konstantinidis D. *Mechanics of Rubber Bearings for Seismic and Vibration Isolation*. John Wiley & Sons, 2011.

[31] Nakai M et al. "Iconic architectural forms enabled by base-isolation". In: *Journal of Disaster Research* 4.3 (2009). Special Issue on 'Japan's Advanced Technology for Building Seismic Protection', pp. 182–191.

[32] Oliveto G et al. "Preliminary results from full-scale free vibration tests on a four story reinforced concrete building after seismic rehabilitation by base isolation". In: *JSSI 10th Anniversary Symposium on Performance of Response Controlled Buildings, Yokohama, Japan*. Nov. 2004, pp. 126–135.

[33] Oliveto G, Athanasiou A, and Granata M. "Blind simulation of full scale free vibration tests on a three story base isolated building". In: *10CUEE, 10th International Conference on Urban Earthquake Engineering*. Center for Urban Earthquake Engineering, Tokyo Institute of Technology. Mar. 2013, pp. 1303–1316.

[34] Ryan K, Coria C, and Dao N. *Large scale earthquake simulation of a hybrid lead rubber isolation system designed with consideration of nuclear seismicity*. NUREG/CR-7196. Prepared for: Office of Nuclear Regulatory Research U.S. Nuclear Regulatory Commission. 2013.

[35] Kelly J M and Beucke K E. "A friction damped base isolation system with fail-safe characteristics". In: *Earthquake Engineering & Structural Dynamics* 11.1 (1983), pp. 33–56.

[36] Saif H, Lee D, and Retamal E. *Viscous damping for base isolated structures*. Technical paper archives, Taylor Devices.

[37] Beck J and Jennings P. "Structural identification using linear models and earthquake records". In: *Earthquake Engineering & Structural Dynamics* 8.2 (1980), pp. 145–160.

[38] Stewart J, Conte J, and Aiken I. "Observed behavior of seismically isolated buildings". In: *Journal of Structural Engineering* 125.9 (1999), pp. 955–964.

[39] Nagarajaiah S. "System identification of base-isolated USC hospital building from recorded response". In: *17th International Modal Analysis Conference*. 1999, pp. 159–165.

[40] Oliveto N D, Scalia G, and Oliveto G. "Dynamic identification of structural systems with viscous and friction damping". In: *Journal of Sound and Vibration* 318 (2008), pp. 911–926.

[41] Oliveto N D, Scalia G, and Oliveto G. "Time domain identification of hybrid base isolation systems using free vibration tests". In: *Earthquake Engineering & Structural Dynamics* 39 (2010), pp. 1015–1038.

[42] Hansen N. *The CMA Evolution Strategy: A Tutorial*. Available online at http://www.lri.fr/~hansen/cmatutorial.pdf.

[43] Athanasiou A et al. "Dynamical modeling and parameter identification of seismic osolation systems by evolution strategies". In: vol. 465. Studies in Computational Intelligence. Revised and Selected Papers of the International Joint Conference, IJCCI 2011, Paris, France, October 24-26, 2011. Springer Berlin Heidelberg, 2013, pp. 101–118.

[44] Markou A, Athanasiou A, and Oliveto G. "Recent Advances in Dynamic Identification and Response Simulation of Hybrid Base Isolation Systems". In: *15th World Conference on Earthquake Engineering. 15WCEE, Lisbon, Portugal*. Sept. 2012.

[45] *NTC08 Norme Tecniche per le Costruzioni*. 2008.

[46] *EN1998: Eurocode 8: Design of Structures for Earthquake Resistance*. European Committee for Standardization (CEN), 2005.

[47] Oliveto G and Markou A. "The dynamics of a pushing and quick release device for dynamic testing of seismic isolated buildings". In: *Second European Conference on Earthquake Engineering and Seismology. 2ECEES, Istanbul, Turkey*. Aug. 2014.

[48] Wikipedia. *Signal processing — Wikipedia, The Free Encyclopedia*. [Online; accessed 14-September-2015]. 2015. URL: https://en.wikipedia.org/w/index.php?title=Signal_processing%5C&oldid=679265871.

[49] Douglas J and Boore D. "High-frequency filtering of strong-motion records". In: *Bulletin of Earthquake Engineering* 9 (2011), pp. 395–409.

[50] Chiu H C. "Stable baseline correction of digital strong-motion data". In: *Bulletin of the Seismological Society of America* 87.4 (1997), pp. 932–944.

[51] Boore D and Bommer J. "Processing of strong-motion accelerograms: Needs, options and consequences". In: *Soil Dynamics and Earthquake Engineering* 25 (2005), pp. 93–115.

[52] Trifunac M and Lee V. *Routine computer processing of strong-motion accelerograms*. Tech. rep. EERL 73-03. Pasadena, California: Earthquake Engineering Research Laboratory, Oct. 1973.

[53] Boore D. *Fundamentals of Seismology and Seismic Hazard Assessment. Measures of strong motion and processing of data*. ROSE School, 2013: Engineering Seismology Class Lecture. 2013.

[54] Trifunac M and Brady A. "A study on the duration of strong earthquake ground motion". In: *Bulletin of the Seismological Society of America* 65.3 (1975), pp. 581–626.

[55] MATLAB, R2013a. *The MathWorks Inc.* 2013.

[56] Oliveto G et al. "A preliminary study on the identification of seismic isolation systems from earthquake records". In: *10CUEE, 10th International Conference on Urban Earthquake Engineering*. Center for Urban Earthquake Engineering, Tokyo Institute of Technology. Mar. 2013, pp. 1415–1424.

[57] Athanasiou A and Oliveto G. "Modelling hybrid base isolation systems for free vibration simulations". In: *8CUEE. 8th International Conference on Urban Earthquake Engineering*. Center for Urban Earthquake Engineering, Tokyo Institute of Technology. Mar. 2011, pp. 1293–1302.

[58] Athanasiou A et al. "Evolutionary algorithms for the identification of structural systems in earthquake engineering". In: *ECTA 2011. International Conference on Evolutionary Computation Theory and Applications, Paris, France*. Oct. 2011, pp. 52–62.

[59] Hansen N. *The CMA Evolution Strategy*. https://www.lri.fr/~hansen/cmaesintro.html. Mar. 2014.

[60] Hansen N and Ostermeier A. "Adapting arbitrary normal mutation distributions in evolution strategies: The covariance matrix adaptation". In: *Proceedings of the 1996 IEEE International Conference on Evolutionary Computation*. 1996, pp. 312–317.

[61] Auger A and Hansen N. *Tutorial CMA-ES - Evolution Strategies and Covariance Matrix Adaptation*. GECCO' 13, tutorial slides. July 2013.

[62] Montaldo V et al. "Seismic hazard data for the new Italian building code based on European standard". In: *100th Anniversary Earthquake Conference: Commemorating the 1906 San Francisco Earthquake*. 2006.

[63] OPCM 3431. *Norme Techniche per il Progetto, la Valutazione e l'Adequamento Sismico degli Edifici*. Sezione 10: Edifici con Isolamento Sismico. 2005.

[64] Medeot R. "Application and revision of the European Norm EN 15129 on anti-seismic devices". In: *Second European Conference on Earthquake Engineering and Seismology. 2ECEES, Istanbul, Turkey*. Aug. 2014.

[65] FIP Industriale. *Verbale di prova di accetazione su isolatori sismici in elastomero armato SI-N 500/150*. Tech. rep. VP 44/09. Laboratorio Prove e Collaudi della FIP Industriale.

[66] FIP Industriale. *Verbale di prova di accetazione su appoggi VM 25/600/600 , VM 150/600/600 e VM 200/600/600*. Tech. rep. VP 48/09. Laboratorio Prove e Collaudi della FIP Industriale.

[67] Andersson S, Söderberg A, and Björklund S. "Friction models for sliding dry, boundary and mixed lubricated contacts". In: *Tribology International* 40 (2007), pp. 580–587.

[68] Athanasiou A et al. "Problems in the identification of base isolation systems from earthquake records". In: *GECCO '13 Companion: Proceedings of the 15th annual conference companion on Genetic and evolutionary computation*. New York, USA: ACM, July 2013, pp. 1651–1654.

[69] Mullins L. "Softening of rubber by deformation." In: *Rubber Chemistry and Technology* 42.1 (1969), pp. 339–362.

[70] Sivaselvan M V and Reinhorn A M. "Lagrangian approach to structural collapse simulation". In: *Journal of Engineering Mechanics* 132.8 (2006), pp. 795–805.

[71] Pang M, Lou T, and Zhao M. "On modal energy in civil structural control". In: *Journal of Zhejiang University SCIENCE A* 9.7 (2008), pp. 878–887.

[72] Oliveto G, Oliveto N D, and Athanasiou A. "Constrained optimization for 1-D dynamic and earthquake response analysis of hybrid base-isolation systems". In: *Soil Dynamics and Earthquake Engineering* 67 (2014), pp. 44–53.

[73] Sivaselvan M V et al. "Numerical collapse simulation of large-scale structural systems using an optimization-based algorithm". In: *Earthquake Engineering & Structural Dynamics* 38.5 (2009), pp. 655–677.

[74] Galley C R. "Classical mechanics of non-conservative systems". In: *Physical Review Letters* 110.17 (2013).

[75] Oliveto N D, Oliveto G, and Athanasiou A. "Mixed Lagrangian Formulation for Dynamic and Earthquake Response of 2D Hybrid Base Isolation Systems". In: *9th International Conference on Urban Earthquake Engineering/ 4th Asia Conference on Earthquake Engineering*. Center for Urban Earthquake Engineering, Tokyo Institute of Technology. Mar. 2012, pp. 1373–1382.

[76] Oliveto G and Athanasiou A. "Mixed Lagrangian Formulation for the dynamic response of base isolated buildings to earthquake excitation". In: *XXI CONGRESSO AIMETA, Torino*. Sept. 2013.

[77] Ravindran A, Ragsdell K, and Reklaitis G. *Engineering Optimization: Methods and Applications*. John Wiley & Sons, Hoboken, New Jersey, 2006.

[78] Nocedal J and Wright S. *Numerical Optimization*. 2nd. Springer, New York, 2006.

[79] Boyd S and Vandenberghe L. *Convex Optimization*. Cambridge University Press, UK, New York, 2004.

[80] Iervolino I, Galasso C, and Cosenza E. "REXEL computer aided record selection for code-based seismic structural analysis". In: *Bulletin of Earthquake Engineering* 8.2 (2009), pp. 339–362.

Appendix A

Signal processing of the Augusta records

The processed motion data for the full set of the Augusta tests are shown herein. The baseline fitting scheme is implemented for the adjustment of the longitudinal records of the base, first, second and roof floor, namely the acceleration components obtained from the Augusta free vibration tests 1,3,4,5,6,8,9 and 10 : components GFL-25X-01, 1FL-25X-01, 2FL-25X-01, 3FL-X-01, GFL-25X-03, 1FL-25X-03, 2FL-25X-03, 3FL-X-03, GFL-25X-04, 1FL-25X-04, 2FL-25X-04, 3FL-X-04, GFL-25X-05, 1FL-25X-05, 2FL-25X-05, 3FL-X-05, GFL-25X-06, 1FL-25X-06, 2FL-25X-06, 3FL-X-06, GFL-25X-08, 1FL-25X-08, 2FL-25X-08, 3FL-X-08, GFL-25X-09, 1FL-25X-09, 2FL-25X-09, 3FL-X-09, GFL-25X-10, 1FL-25X-10, 2FL-25X-10, 3FL-X-10.

The Appendix is organized as follows:

- Section A.1 provides information on the start times t_1, end times t_2 and motion durations t_d for the absolute and relative records obtained from the free vibration Augusta tests, see Tables A.1 to A.3. The thresholds ε_1 and ε_v and the time interval used for the identification of the linear velocity trend, which are needed for the estimation of times t_1 and t_2 are given in Tables A.1 and A.3.

- Section A.2 provides the peak free vibration response in terms of absolute floor accelerations, velocities and displacements, see Tables A.6 and A.7.

- Section A.3 provides the peak relative superstructure response in terms of absolute floor accelerations, velocities and displacements, see Tables A.6 to A.7.

- Sections A.4 to A.10 show the plots of the baseline fitted absolute response, the baseline fitted relative response evaluated indirectly from the adjusted absolute response and the baseline fitted relative response evaluated directly from the processing of the row relative signals for tests 1, 3, 4, 5, 6, 8 and 10. The results for test 9 can be found in the main text and are not repeated herein. The absolute response presented in the above mentioned sections includes absolute floor accelerations, velocities and displacements. The relative response consists in relative floor accelerations, velocities, displacements and inter-story drifts.

A.1 Motion duration - tables

Table A.1: Duration of strong motion for tests 1, 3 and 4. First column: start time of absolute motion t_1^{abs}. Second column: end time of absolute motion t_2^{abs}. Third column: duration of absolute motion $t_d^{abs} = t_2^{abs} - t_1^{abs}$. Fourth column: start time of absolute motion t_1^{rel}. Fifth column: end time of absolute motion t_2^{rel}. Sixth column: duration of relative motion $t_d^{rel} = t_2^{rel} - t_1^{rel}$ (within brackets the relative motion duration as evaluated from the absolute motion start and end times, i.e. $t_d^{rel} = t_2^{abs} - t_1^{abs,groundfloor}$).

$Test\,1$ ($u_0 = 5.83cm$)	$t_1^{abs}[sec]$	$t_2^{abs}[sec]$	$t_d^{abs}[sec]$	$t_1^{rel}[sec]$	$t_2^{rel}[sec]$	$t_d^{rel}[sec]$
ground floor record	415.075	417.280	2.205			
first floor record	415.081	417.290	2.209	415.075	417.200	2.125 (2.215)
second floor record	415.099	417.300	2.201	415.075	417.210	2.135 (2.225)
roof record	415.103	417.310	2.207	415.075	417.220	2.145 (2.235)

$Test\,3$ ($u_0 = 6.81cm$)	$t_1^{abs}[sec]$	$t_2^{abs}[sec]$	$t_d^{abs}[sec]$	$t_1^{rel}[sec]$	$t_2^{rel}[sec]$	$t_d^{rel}[sec]$
ground floor record	470.133	473.000	2.867			
first floor record	470.138	473.010	2.872	470.133	473.060	2.927 (2.877)
second floor record	470.145	473.020	2.875	470.133	473.060	2.927 (2.887)
roof record	470.164	473.050	2.886	470.133	473.070	2.937 (2.917)

$Test\,4$ ($u_0 = 6.83cm$)	$t_1^{abs}[sec]$	$t_2^{abs}[sec]$	$t_d^{abs}[sec]$	$t_1^{rel}[sec]$	$t_2^{rel}[sec]$	$t_d^{rel}[sec]$
ground floor record	463.620	466.500	2.880			
first floor record	463.624	466.530	2.906	463.620	466.560	2.940 (2.910)
second floor record	463.632	466.560	2.928	463.620	466.590	2.970 (2.940)
roof record	463.651	466.580	2.929	463.620	466.600	2.980 (2.960)

Table A.2: Duration of strong motion for tests 5, 6 and 8. First column: start time of absolute motion t_1^{abs}. Second column: end time of absolute motion t_2^{abs}. Third column: duration of absolute motion $t_d^{abs} = t_2^{abs} - t_1^{abs}$. Fourth column: start time of absolute motion t_1^{rel}. Fifth column: end time of absolute motion t_2^{rel}. Sixth column: duration of relative motion $t_d^{rel} = t_2^{rel} - t_1^{rel}$ (within brackets the relative motion duration as evaluated from the absolute motion start and end times, i.e. $t_d^{rel} = t_2^{abs} - t_1^{abs,groundfloor}$).

$Test\,5$ $(u_0 = 10.88cm)$	$t_1^{abs}[sec]$	$t_2^{abs}[sec]$	$t_d^{abs}[sec]$	$t_1^{rel}[sec]$	$t_2^{rel}[sec]$	$t_d^{rel}[sec]$
ground floor record	1067.992	1071.220	3.228			
first floor record	1067.997	1071.228	3.231	1067.992	1071.955	3.963 (3.236)
second floor record	1068.004	1071.233	3.229	1067.992	1071.956	3.964 (3.241)
roof record	1068.024	1071.234	3.210	1067.992	1071.957	3.965 (3.242)

$Test\,6$ $(u_0 = 11.66cm)$	$t_1^{abs}[sec]$	$t_2^{abs}[sec]$	$t_d^{abs}[sec]$	$t_1^{rel}[sec]$	$t_2^{rel}[sec]$	$t_d^{rel}[sec]$
ground floor record	1215.377	1219.400	4.023			
first floor record	1215.383	1219.430	4.047	1215.377	1219.430	4.053 (4.053)
second floor record	1215.389	1219.440	4.051	1215.377	1219.440	4.063 (4.063)
roof record	1215.409	1219.460	4.051	1215.377	1219.440	4.063 (4.083)

$Test\,8$ $(u_0 = 10.33cm)$	$t_1^{abs}[sec]$	$t_2^{abs}[sec]$	$t_d^{abs}[sec]$	$t_1^{rel}[sec]$	$t_2^{rel}[sec]$	$t_d^{rel}[sec]$
ground floor record	385.165	389.200	4.035			
first floor record	385.171	389.240	4.069	385.165	389.220	4.055 (4.075)
second floor record	385.177	389.250	4.073	385.165	389.240	4.075 (4.085)
roof record	385.200	389.260	4.060	385.165	389.320	4.155 (4.095)

Table A.3: Duration of strong motion for tests 9 and 10. First column: start time of absolute motion t_1^{abs}. Second column: end time of absolute motion t_2^{abs}. Third column: duration of absolute motion $t_d^{abs} = t_2^{abs} - t_1^{abs}$. Fourth column: start time of absolute motion t_1^{rel}. Fifth column: end time of absolute motion t_2^{rel}. Sixth column: duration of relative motion $t_d^{rel} = t_2^{rel} - t_1^{rel}$ (within brackets the relative motion duration as evaluated from the absolute motion start and end times, i.e. $t_d^{rel} = t_2^{abs} - t_1^{abs,groundfloor}$).

$Test\,9$ $(u_0 = 10.11cm)$	$t_1^{abs}[sec]$	$t_2^{abs}[sec]$	$t_d^{abs}[sec]$	$t_1^{rel}[sec]$	$t_2^{rel}[sec]$	$t_d^{rel}[sec]$
ground floor record	1014.087	1018.000	3.913			
first floor record	1014.092	1018.049	3.957	1014.087	1018.150	4.063 (3.962)
second floor record	1014.109	1018.170	4.061	1014.087	1018.170	4.083 (4.083)
roof record	1014.122	1018.220	4.098	1014.087	1018.210	4.123 (4.133)

$Test\,10$ $(u_0 = 10.02cm)$	$t_1^{abs}[sec]$	$t_2^{abs}[sec]$	$t_d^{abs}[sec]$	$t_1^{rel}[sec]$	$t_2^{rel}[sec]$	$t_d^{rel}[sec]$
ground floor record	1052.849	1056.810	3.961			
first floor record	1052.855	1056.820	3.965	1052.849	1056.920	4.071 (3.971)
second floor record	1052.862	1056.840	3.978	1052.850	1056.920	4.070 (3.991)
roof record	1052.878	1056.920	4.042	1052.849	1056.940	4.091 (4.071)

Table A.4: Intervals of time where there is a clear linear trend in the row absolute and/or relative velocity trace. A straight line is drawn in this interval and extended until time t_1.

Test 1:	$[420, 430]sec$	*Test 6:*	$[1225, 1235]sec$
Test 3:	$[480, 490]sec$	*Test 8:*	$[395, 405]sec$
Test 4:	$[470, 480]sec$	*Test 9:*	$[1020, 1030]sec$
Test 5:	$[1075, 1085]sec$	*Test 10:*	$[1060, 1070]sec$

Table A.5: Thresholds ε_1 and ε_v used for the determination of start and times times of strong absolute and relative motion (sub-scripts $'abs'$ and $'rel'$ respectively).

	Test 1 : thresholds in %				*Test 3 : thresholds in %*				*Test 4 : thresholds in %*			
floor	ε_1^{abs}	ε_v^{abs}	ε_1^{rel}	ε_v^{rel}	ε_1^{abs}	ε_v^{abs}	ε_1^{rel}	ε_v^{rel}	ε_1^{abs}	ε_v^{abs}	ε_1^{rel}	ε_v^{rel}
ground	1.00	0.90			1.00	0.30			2.00	0.10		
first	0.10	1.00	1.00	1.00	8.00	0.30	8.00	1.00	2.00	0.10	2.00	0.40
second	1.00	1.00	1.00	0.90	8.00	0.30	8.00	1.00	10.00	0.10	2.00	0.40
roof	1.00	1.10	1.00	1.00	8.00	0.30	8.00	0.40	10.00	0.10	2.00	0.40

	Test 5 : thresholds in %				*Test 6 : thresholds in %*				*Test 8 : thresholds in %*			
floor	ε_1^{abs}	ε_v^{abs}	ε_1^{rel}	ε_v^{rel}	ε_1^{abs}	ε_v^{abs}	ε_1^{rel}	ε_v^{rel}	ε_1^{abs}	ε_v^{abs}	ε_1^{rel}	ε_v^{rel}
ground	2.00	1.00			2.00	0.28			2.00	0.20		
first	2.00	1.00	2.00	0.28	2.00	0.25	2.00	0.10	2.00	0.30	2.00	0.40
second	2.00	1.00	2.00	0.16	2.00	0.26	2.00	0.01	2.00	0.45	2.00	0.80
roof	5.00	1.00	2.00	0.28	5.00	0.26	2.00	0.01	8.00	0.15	2.00	0.20

	Test 9 : thresholds in %				*Test 10 : thresholds in %*			
floor	ε_1^{abs}	ε_v^{abs}	ε_1^{rel}	ε_v^{rel}	ε_1^{abs}	ε_v^{abs}	ε_1^{rel}	ε_v^{rel}
ground	1.00	0.10			2.00	1.50		
first	2.00	0.10	2.00	0.60	2.00	1.70	2.00	0.80
second	10.00	0.20	2.00	1.20	2.00	1.65	2.00	0.70
roof	12.00	0.20	2.00	0.20	2.00	1.50	2.00	0.25

A.2 Peak absolute free vibration response - tables

Table A.6: Peak free vibration response of the Augusta building in terms of absolute floor acceleration, velocity and displacement during tests 1, 3, 4, 5 and 8.

	Test 1 : Peak absolute response			*Test 3 : Peak absolute response*		
	accel.$[g]$	*vel.*$[cm/sec]$	*displ.*$[cm]$	*accel.*$[g]$	*vel.*$[cm/sec]$	*displ.*$[cm]$
ground floor	0.126	9.54	5.83	0.320	12.42	6.81
first floor	0.118	9.43	5.83	0.231	12.25	6.81
second floor	0.106	9.66	5.83	0.161	12.87	6.81
roof	0.100	9.56	5.83	0.219	13.04	6.82

	Test 4 : Peak absolute response			*Test 5 : Peak absolute response*		
	accel.$[g]$	*vel.*$[cm/sec]$	*displ.*$[cm]$	*accel.*$[g]$	*vel.*$[cm/sec]$	*displ.*$[cm]$
ground floor	0.329	11.47	6.85	0.419	17.29	10.88
first floor	0.195	11.27	6.85	0.268	16.81	10.88
second floor	0.158	11.85	6.85	0.199	17.69	10.88
roof	0.214	11.97	6.85	0.286	18.25	10.88

	Test 6 : Peak absolute response			*Test 8 : Peak absolute response*		
	accel.$[g]$	*vel.*$[cm/sec]$	*displ.*$[cm]$	*accel.*$[g]$	*vel.*$[cm/sec]$	*displ.*$[cm]$
ground floor	0.425	18.13	11.66	0.419	17.57	10.33
first floor	0.261	17.66	11.66	0.279	17.26	10.33
second floor	0.218	18.42	11.66	0.205	18.10	10.33
roof	0.295	19.06	11.66	0.291	18.68	10.34

Table A.7: Peak free vibration response of the Augusta building in terms of absolute floor acceleration, velocity and displacement during tests 9 and 10.

	Test 9 : Peak absolute response			*Test 10 : Peak absolute response*		
	accel.$[g]$	*vel.*$[cm/sec]$	*displ.*$[cm]$	*accel.*$[g]$	*vel.*$[cm/sec]$	*displ.*$[cm]$
ground floor	0.374	15.70	10.11	0.363	15.41	10.02
first floor	0.252	15.43	10.11	0.257	15.25	10.02
second floor	0.177	16.12	10.11	0.174	16.05	10.02
roof	0.265	16.53	10.11	0.261	16.30	10.03

A.3 Peak relative superstructure response - tables

Table A.8: Peak relative to the base response for tests 1, 3 and 4. The relative response is evaluated directly from the baseline fitting of the row relative motion. The corresponding peak response evaluated from the fitted absolute response is given within brackets. First column: component considered. Second column: peak relative floor accelerations. Third column: peak relative floor velocities. Fourth column: peak relative floor displacements. Fifth column: peak relative floor displacements after application of a low cut filter with $f_c = 0.25Hz$ (test1) and $f_c = 0.30Hz$ (tests 3 and 4). Sixth column: peak inter-story drifts. Seventh column: peak inter-story drifts evaluated from filtered displacements.

Test 1 : Peak relative to the base response

floor	*acceleration* [g]	*velocity* [cm/sec]	*displacement* [cm]	*filtered displ.* [cm]	*drift* [10^{-3}]	*filtered drift* [10^{-3}]
first	0.120 (0.120)	1.680 (1.679)	0.072 (0.072)	0.076 (0.076)	0.169 (0.169)	0.178 (0.179)
second	0.173 (0.173)	3.009 (2.989)	0.125 (0.138)	0.132 (0.132)	0.187 (0.213)	0.175 (0.174)
third	0.167 (0.167)	3.055 (3.057)	0.128 (0.128)	0.132 (0.133)	0.118 (0.139)	0.064 (0.073)

Test 3 : Peak relative to the base response

floor	*acceleration* [g]	*velocity* [cm/sec]	*displacement* [cm]	*filtered displ.* [cm]	*drift* [10^{-3}]	*filtered drift* [10^{-3}]
first	0.297 (0.297)	2.701 (2.686)	0.103 (0.110)	0.098 (0.098)	0.242 (0.260)	0.232 (0.231)
second	0.336 (0.336)	4.234 (4.217)	0.153 (0.152)	0.161 (0.161)	0.195 (0.195)	0.196 (0.197)
third	0.370 (0.370)	5.056 (4.961)	0.215 (0.210)	0.220 (0.221)	0.191 (0.180)	0.182 (0.185)

Test 4 : Peak relative to the base response

floor	*acceleration* [g]	*velocity* [cm/sec]	*displacement* [cm]	*filtered displ.* [cm]	*drift* [10^{-3}]	*filtered drift* [10^{-3}]
first	0.304 (0.304)	2.739 (2.742)	0.086 (0.086)	0.089 (0.089)	0.202 (0.202)	0.209 (0.209)
second	0.338 (0.336)	4.100 (4.086)	0.144 (0.143)	0.151 (0.151)	0.185 (0.195)	0.195 (0.194)
third	0.349 (0.349)	4.753 (4.651)	0.203 (0.198)	0.207 (0.207)	0.182 (0.169)	0.173 (0.175)

Table A.9: Peak relative to the base response for tests 5, 6 and 8. The relative response is evaluated directly from the baseline fitting of the row relative motion. The corresponding peak response evaluated from the fitted absolute response is given within brackets. First column: component considered. Second column: peak relative floor accelerations. Third column: peak relative floor velocities. Fourth column: peak relative floor displacements. Fifth column: peak relative floor displacements after application of a low cut filter with $f_c = 0.30Hz$. Sixth column: peak inter-story drifts. Seventh column: peak inter-story drifts evaluated from filtered displacements.

Test 5 : Peak relative to the base response

floor	*acceleration* [g]	*velocity* [cm/sec]	*displacement* [cm]	*filtered displ.* [cm]	*drift* [10^{-3}]	*filtered drift* [10^{-3}]
first	0.403 (0.403)	3.688 (3.674)	0.144 (0.143)	0.136 (0.138)	0.339 (0.336)	0.321 (0.324)
second	0.437 (0.419)	5.920 (5.898)	0.231 (0.230)	0.229 (0.231)	0.273 (0.272)	0.288 (0.289)
third	0.467 (0.467)	7.077 (6.970)	0.319 (0.313)	0.313 (0.316)	0.269 (0.256)	0.256 (0.261)

Test 6 : Peak relative to the base response

floor	*acceleration* [g]	*velocity* [cm/sec]	*displacement* [cm]	*filtered displ.* [cm]	*drift* [10^{-3}]	*filtered drift* [10^{-3}]
first	0.402 (0.402)	3.806 (3.790)	0.140 (0.138)	0.148 (0.148)	0.329 (0.326)	0.349 (0.349)
second	0.443 (0.432)	5.965 (5.947)	0.231 (0.230)	0.240 (0.241)	0.288 (0.288)	0.289 (0.290)
third	0.483 (0.483)	7.104 (7.008)	0.322 (0.317)	0.324 (0.326)	0.281 (0.268)	0.257 (0.262)

Test 8 : Peak relative to the base response

floor	*acceleration* [g]	*velocity* [cm/sec]	*displacement* [cm]	*filtered displ.* [cm]	*drift* [10^{-3}]	*filtered drift* [10^{-3}]
first	0.358 (0.358)	3.703 (3.695)	0.206 (0.213)	0.152 (0.152)	0.484 (0.501)	0.358 (0.358)
second	0.403 (0.403)	5.891 (5.886)	0.228 (0.227)	0.243 (0.243)	0.283 (0.284)	0.285 (0.285)
third	0.485 (0.485)	6.840 (6.706)	0.316 (0.309)	0.325 (0.328)	0.272 (0.251)	0.254 (0.262)

Table A.10: Peak relative to the base response for tests 9 and 10. The relative response is evaluated directly from the baseline fitting of the row relative motion. The corresponding peak response evaluated from the fitted absolute response is given within brackets. First column: component considered. Second column: peak relative floor accelerations. Third column: peak relative floor velocities. Fourth column: peak relative floor displacements. Fifth column: peak relative floor displacements after application of a low cut filter with $f_c = 0.30Hz$. Sixth column: peak inter-story drifts. Seventh column: peak inter-story drifts evaluated from filtered displacements.

Test 9 : Peak relative to the base response

floor	*acceleration* [g]	*velocity* [cm/sec]	*displacement* [cm]	*filtered displ.* [cm]	*drift* [10^{-3}]	*filtered drift* [10^{-3}]
first	0.345 (0.345)	3.402 (3.384)	0.130 (0.129)	0.126 (0.125)	0.306 (0.302)	0.295 (0.295)
second	0.391 (0.391)	5.396 (5.348)	0.211 (0.208)	0.207 (0.206)	0.260 (0.249)	0.255 (0.254)
third	0.420 (0.420)	6.287 (6.075)	0.290 (0.278)	0.281 (0.283)	0.242 (0.305)	0.226 (0.236)

Test 10 : Peak relative to the base response

floor	*acceleration* [g]	*velocity* [cm/sec]	*displacement* [cm]	*filtered displ.* [cm]	*drift* [10^{-3}]	*filtered drift* [10^{-3}]
first	0.332 (0.332)	3.252 (3.250)	0.116 (0.116)	0.123 (0.123)	0.273 (0.273)	0.290 (0.291)
second	0.394 (0.394)	5.172 (5.180)	0.194 (0.195)	0.208 (0.208)	0.271 (0.252)	0.264 (0.264)
third	0.415 (0.415)	6.002 (5.951)	0.272 (0.269)	0.278 (0.279)	0.349 (0.230)	0.216 (0.218)

A.4 TEST 1-graphs

A.4.1 Baseline fitted absolute free vibration response

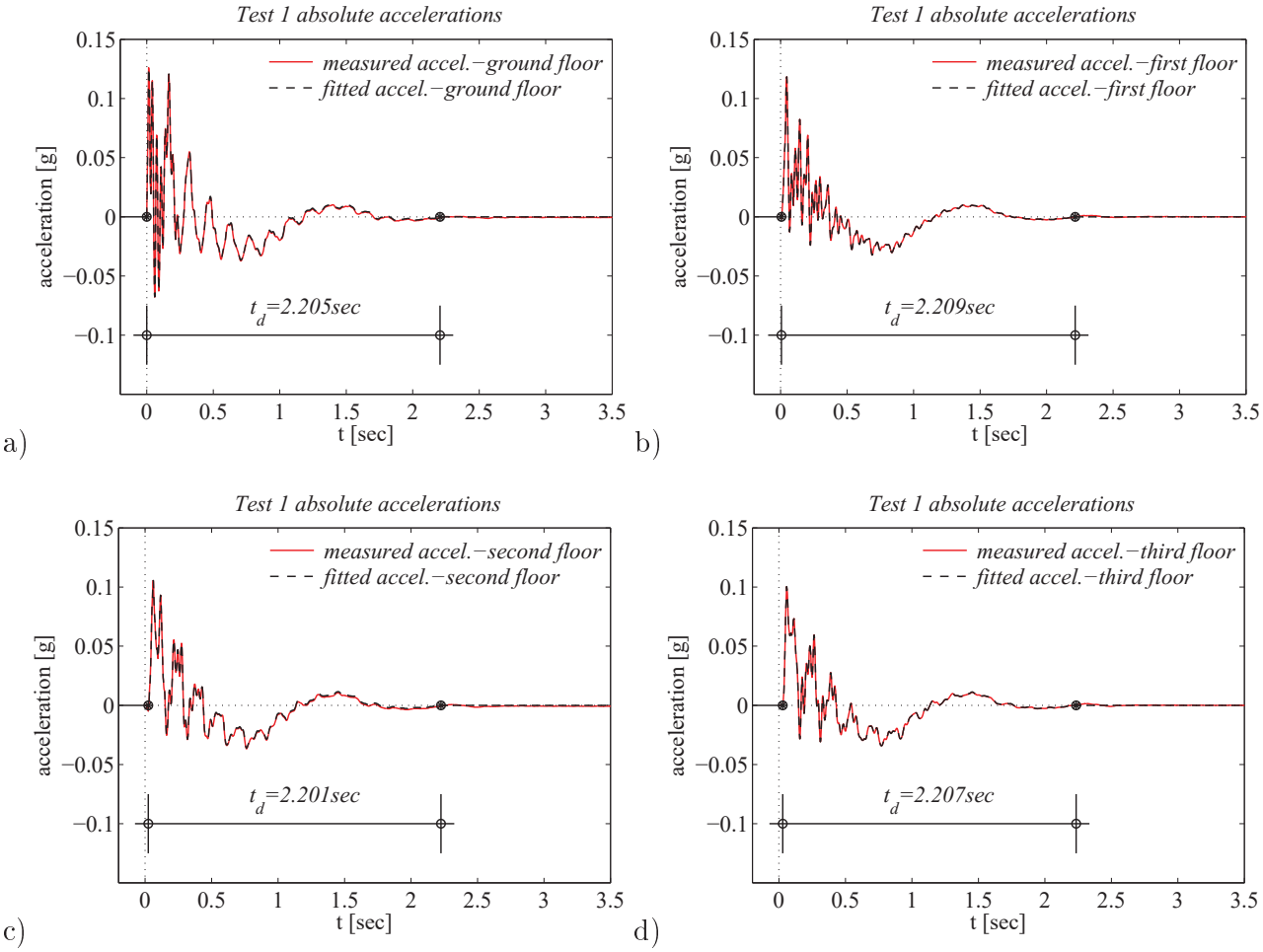

Figure A.1: Absolute acceleration response of the Augusta building during test 1: ground floor, first floor, second floor and roof response; sub-plots a), b), c), d) respectively. The row signals are represented by red lines while the baseline fitted signals are shown by black lines. The times when motion starts and ceases are indicated by black markers. The duration of strong motion is given.

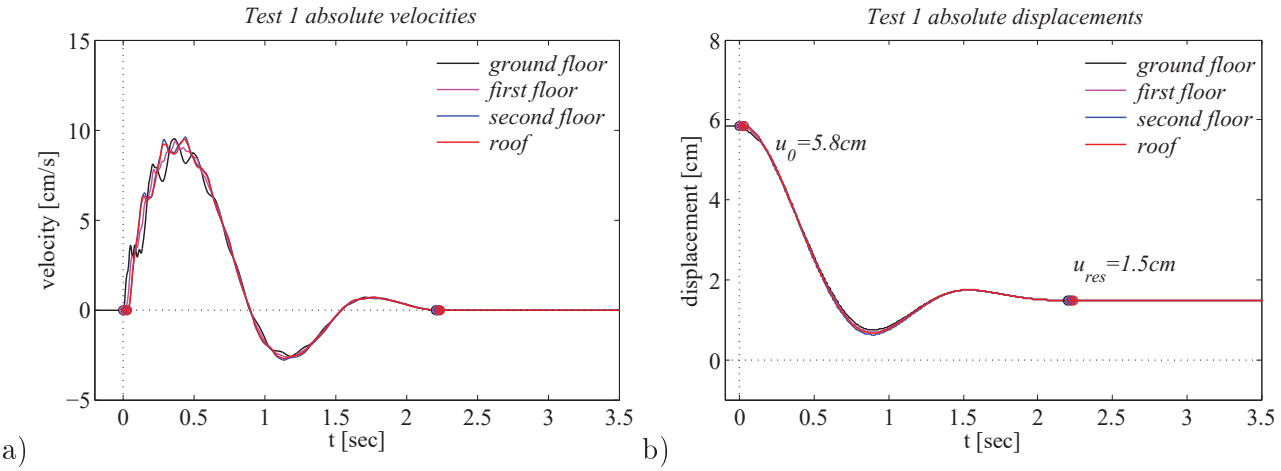

a) b)

Figure A.2: Adjusted absolute velocities and displacements at the ground floor, first floor, second floor and roof of the Augusta building during test 1; sub-plots a) and b) respectively. The times when motion starts and ceases are indicated by markers. The motion starts and ends somewhat later at the upper floors.

A.4.2 Test 1: Relative superstructure response evaluated from the processed absolute response

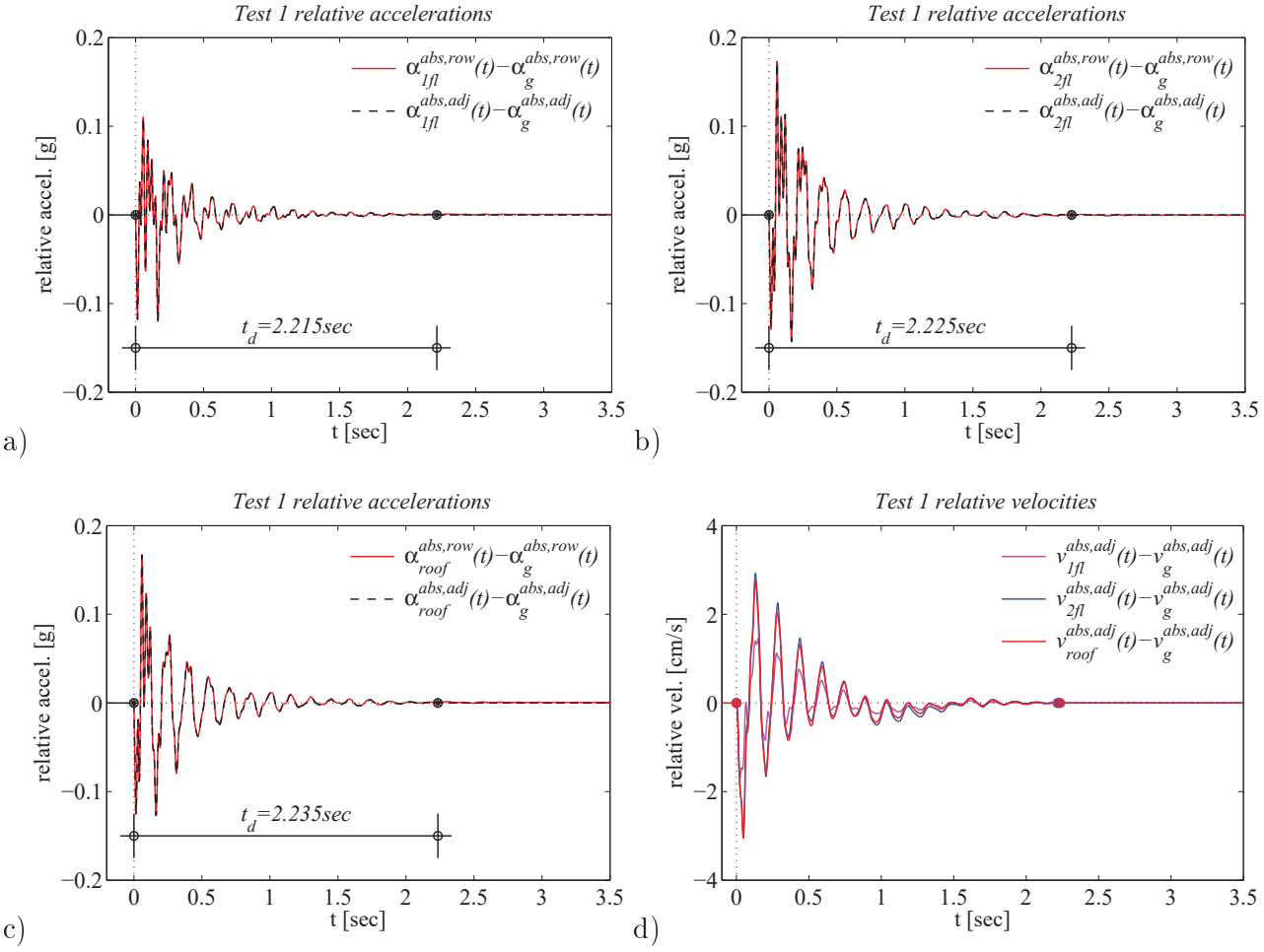

Figure A.3: Relative acceleration response at the Augusta superstructure under test 1 at first floor, second floor and roof; sub-plots a), b), c) respectively. The row signals are represented by red lines while the baseline fitted signals are shown by black lines. Sub-plot d) shows the relative floor velocities. The times when motion starts and ceases are indicated by markers. *('abs': absolute response, 'row': unprocessed response, 'adj': adjusted response, '1fl, 2fl, roof': first floor, second floor and roof response)*

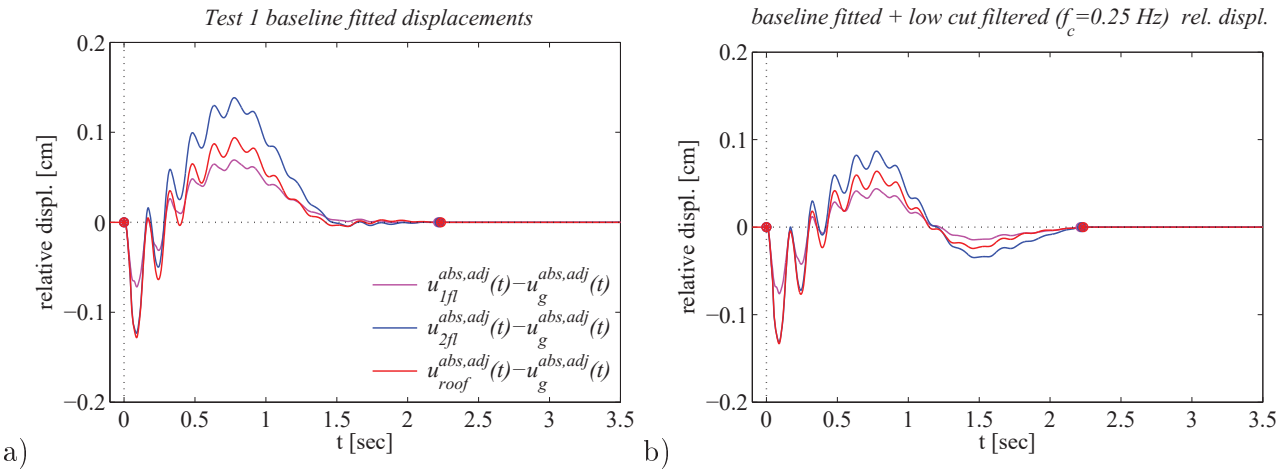

Figure A.4: Relative displacements at the Augusta superstructure during test 1; sub-plot a). Sub-plot b) shows the relative floor displacements of sub-plot a) after application of a low cut filter with corner frequency equal to $f_c = 0.25Hz$. The times when motion starts and ceases are indicated by markers. *('abs': absolute response, 'row': unprocessed response, 'adj': adjusted response, '1fl, 2fl, roof': first floor, second floor and roof response)*

A.4.3 Test 1: Relative superstructure response evaluated from the baseline fitting of the row relative motion

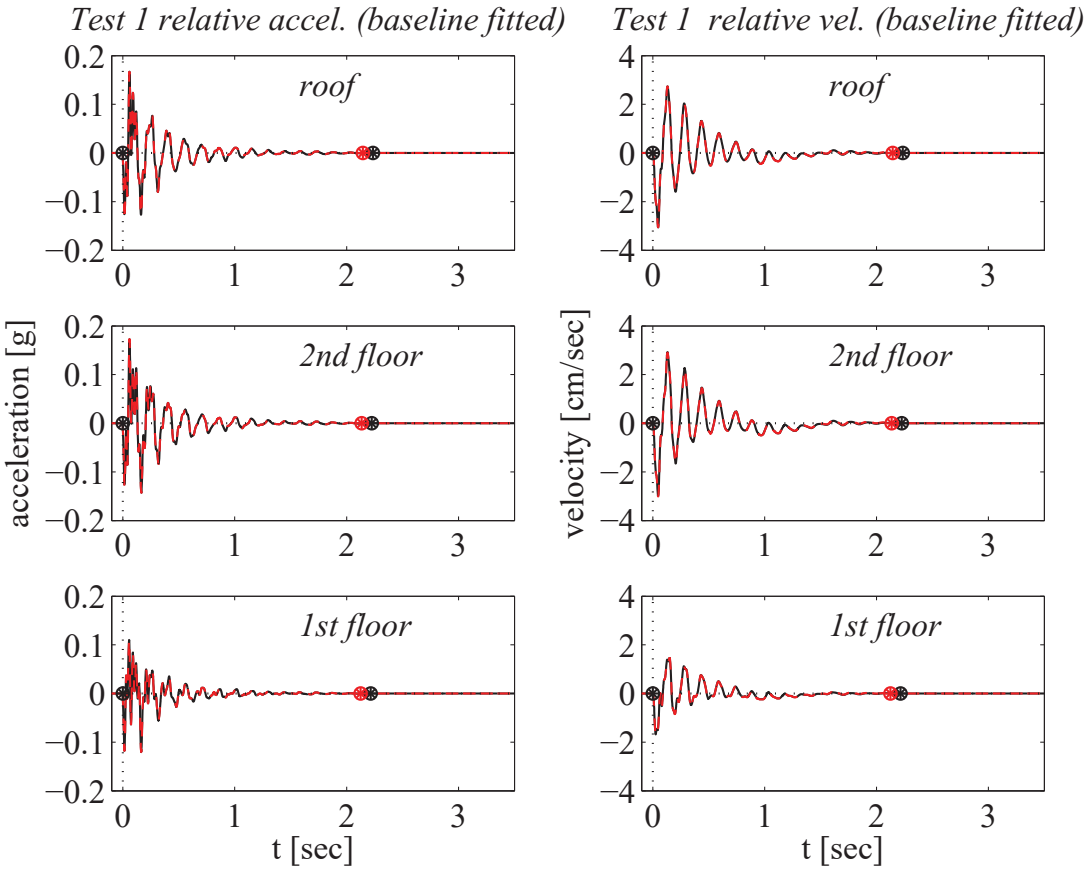

Figure A.5: Relative floor accelerations and velocities for the Augusta free vibration test 1, as evaluated from the adjusted absolute response (continuous black lines) and the adjusted relative response (dashed red lines); left sub-plots and right sub-plots respectively. The relative response is zero at the beginning and end of motion, since the superstructure is expected to respond in the linear range under such a small excitation. The times when motion starts and ceases are indicated by markers.

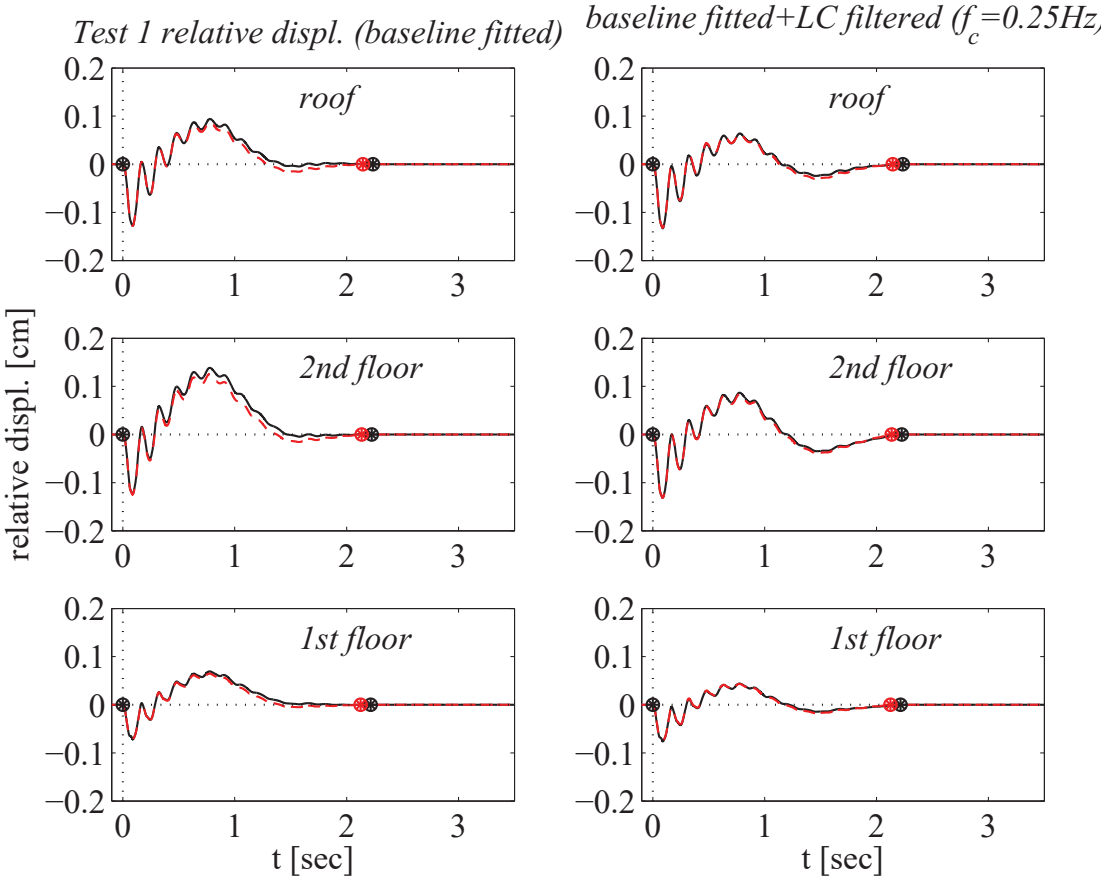

Figure A.6: Relative floor displacement histories for the Augusta free vibration test 1, as evaluated from the adjusted absolute response (continuous black lines) and the adjusted relative response (dashed red lines); left sub-plots. The relative displacements are zero at the beginning and end of motion, since the superstructure is expected to respond in the linear range under such a small excitation. The right sub-plots represent the same displacements after implementation of a low cut filter with corner frequency $f_c = 0.25Hz$. After filtering, the relative displacement responses obtained by the two procedures become essentially the same. The times when motion starts and ceases are indicated by markers.

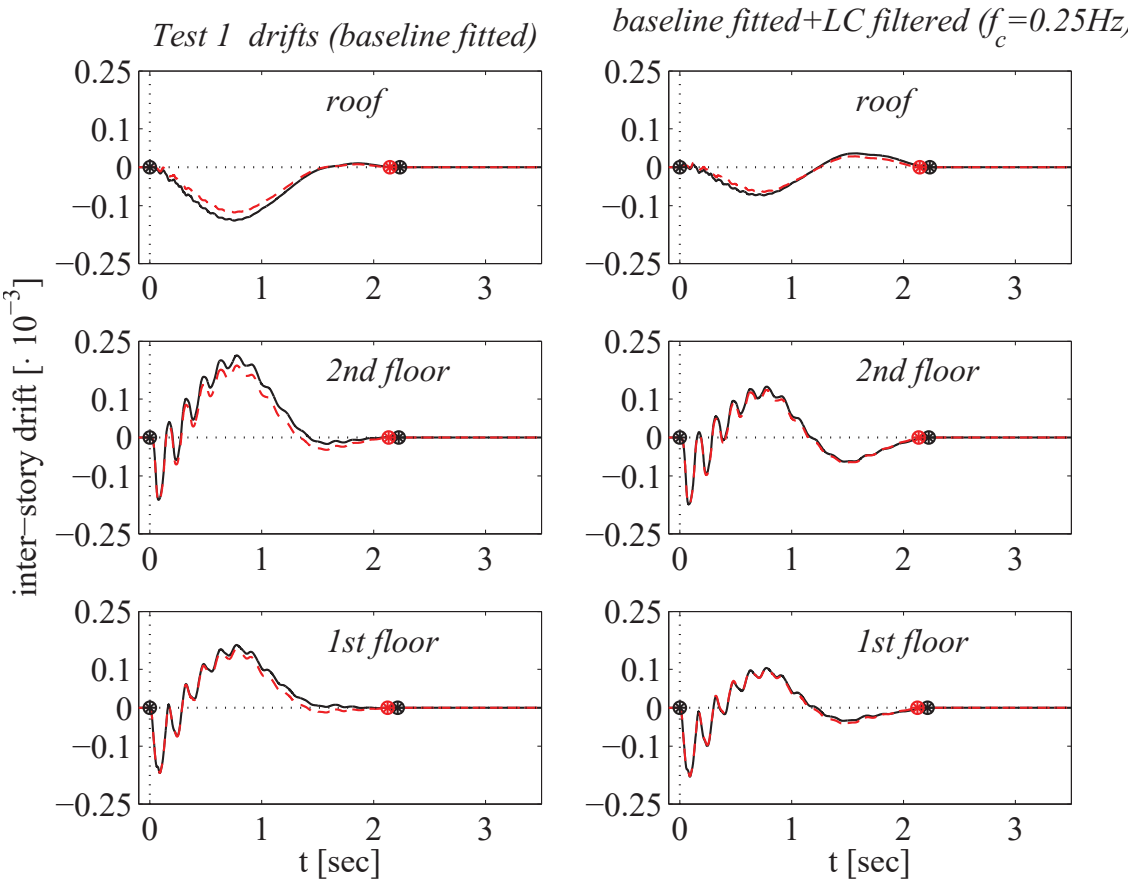

Figure A.7: Inter-story drift histories for the Augusta free vibration test 1, as evaluated from the adjusted absolute response (continuous black lines) and the adjusted relative response (dashed red lines); left sub-plots. The drifts are zero at the beginning and end of motion, since the superstructure is expected to respond in the linear range under such a small excitation. The right sub-plots represent the drifts evaluated from the corresponding filtered displacements. After filtering, the drifts obtained by the two procedures become essentially the same. The times when motion starts and ceases are indicated by markers.

A.5 TEST 3-graphs

A.5.1 Baseline fitted absolute free vibration response

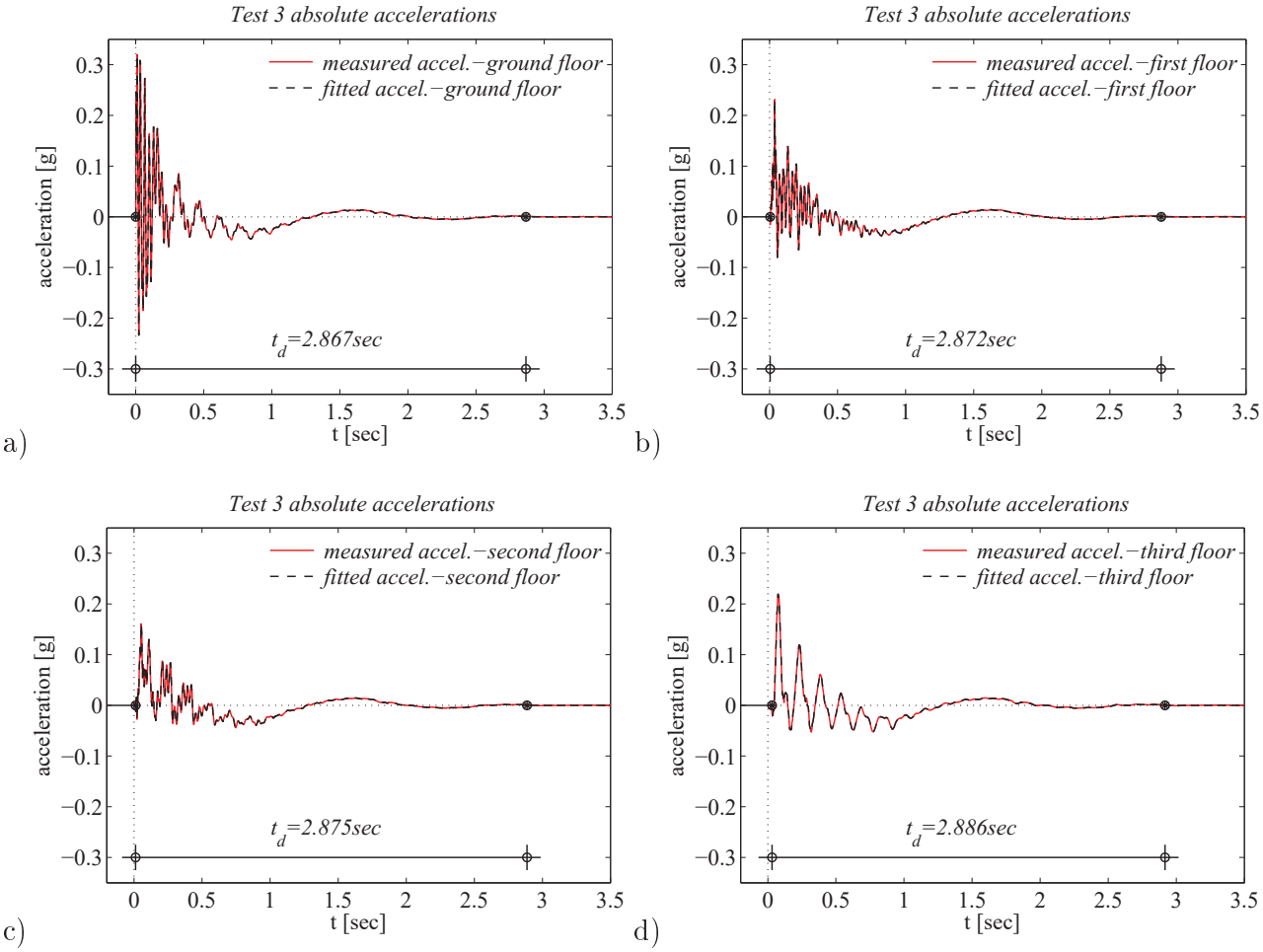

Figure A.8: Absolute acceleration response of the Augusta building during test 6: ground floor, first floor, second floor and roof response; sub-plots a), b), c), d) respectively. The row signals are represented by red lines while the baseline fitted signals are shown by black lines. The times when motion starts and ceases are indicated by black markers. The duration of strong motion is given.

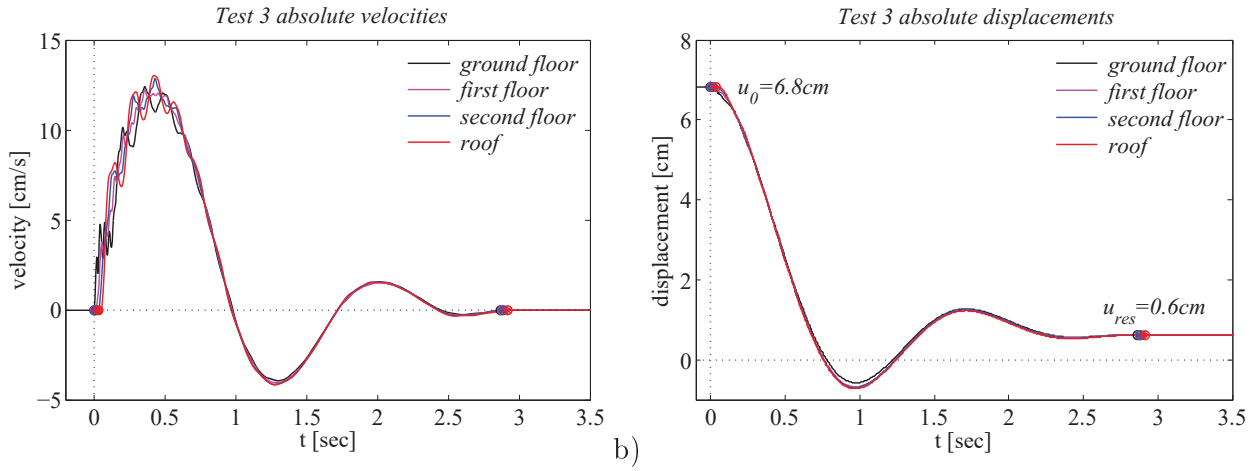

a) b)

Figure A.9: Adjusted absolute velocities and displacements at the ground floor, first floor, second floor and roof of the Augusta building during test 6; sub-plots a) and b) respectively. The times when motion starts and ceases are indicated by markers. The motion starts and ends somewhat later at the upper floors.

A.5.2 Test 3: Relative superstructure response evaluated from the processed absolute response

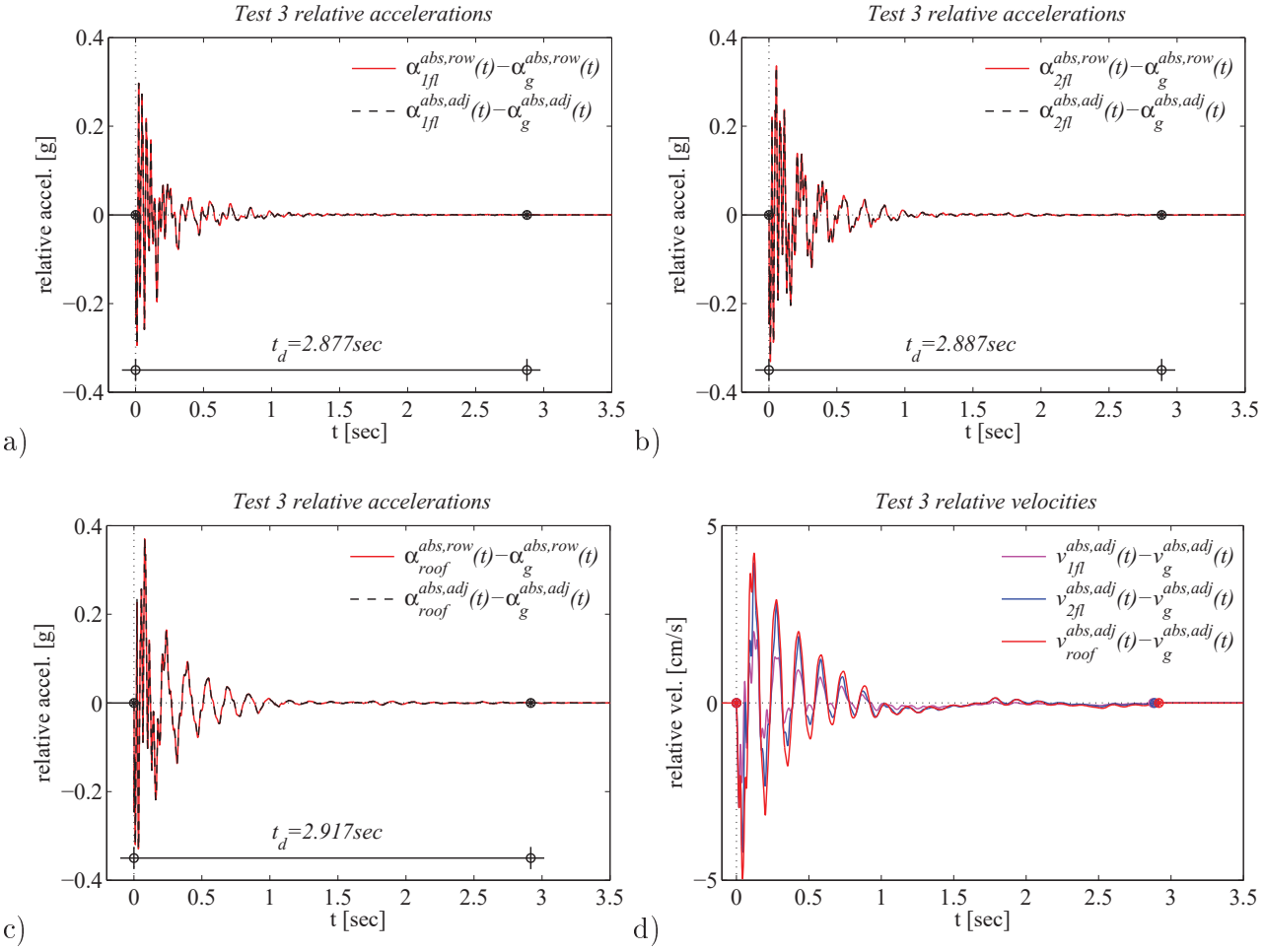

Figure A.10: Relative acceleration response at the Augusta superstructure under test 6 at first floor, second floor and roof; sub-plots a), b), c) respectively. The row signals are represented by red lines while the baseline fitted signals are shown by black lines. Sub-plot d) shows the relative floor velocities. The times when motion starts and ceases are indicated by markers. *('abs': absolute response, 'row': unprocessed response, 'adj': adjusted response, '1fl, 2fl, roof': first floor, second floor and roof response)*

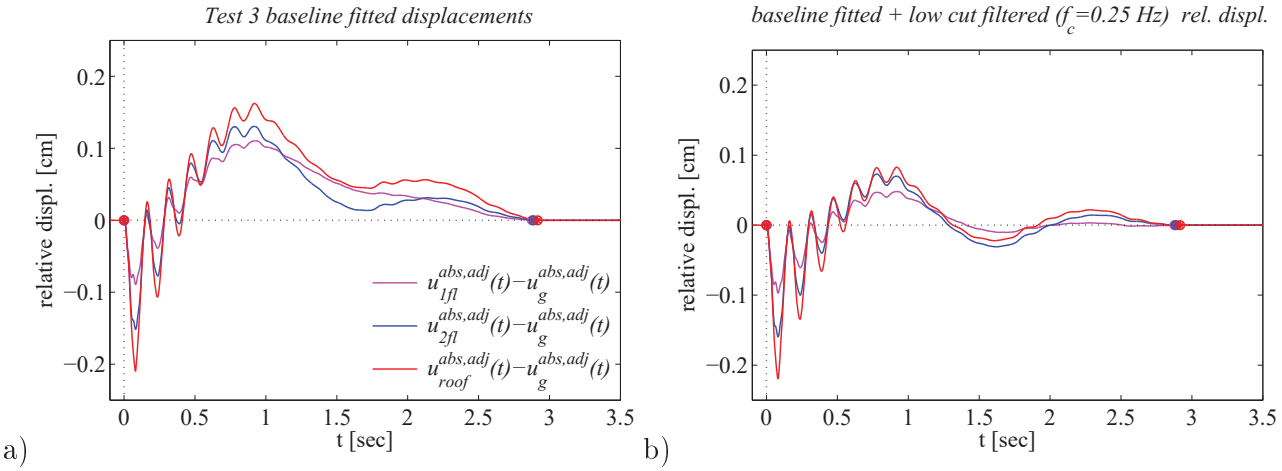

Figure A.11: Relative displacements at the Augusta superstructure during test 3; sub-plot a). Sub-plot b) shows the relative floor displacements of sub-plot a) after application of a low cut filter with corner frequency equal to $f_c = 0.30Hz$. The times when motion starts and ceases are indicated by markers. *('abs': absolute response, 'row': unprocessed response, 'adj': adjusted response, '1fl, 2fl, roof': first floor, second floor and roof response)*

A.5.3 Test 3: Relative superstructure response evaluated from the baseline fitting of the row relative motion

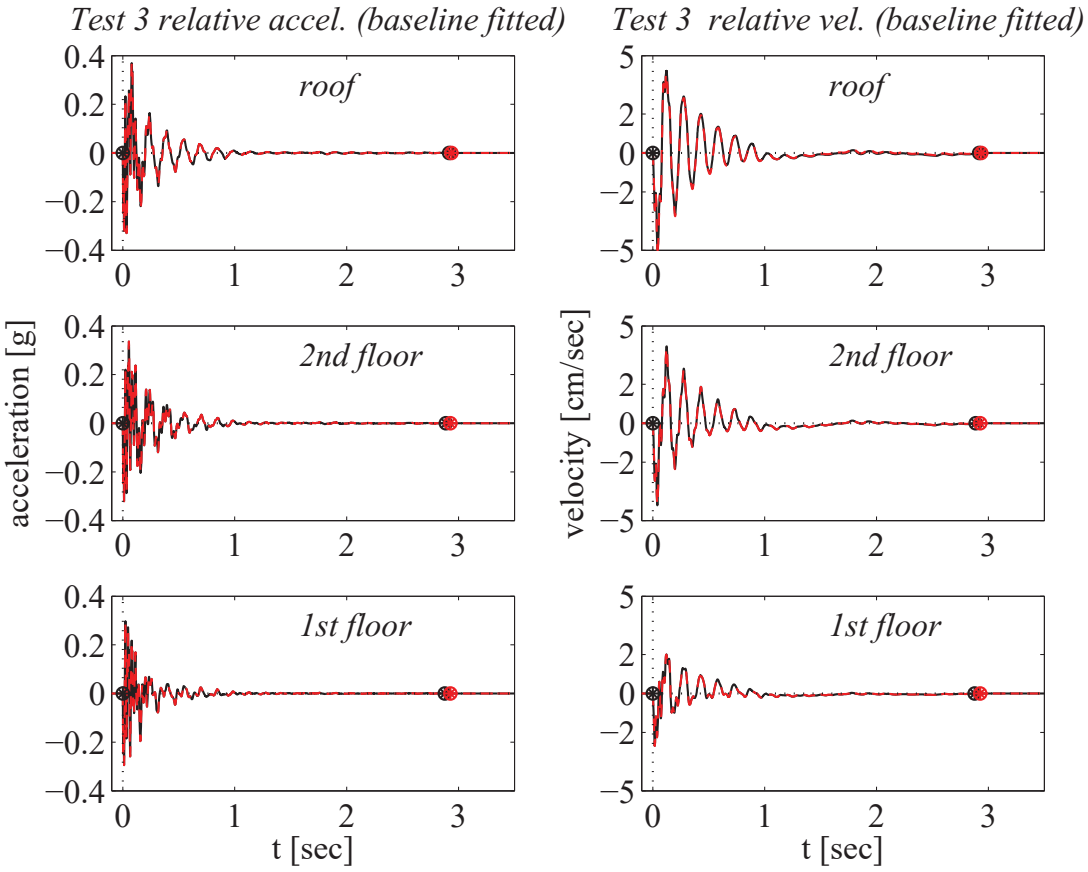

Figure A.12: Relative floor accelerations and velocities for the Augusta free vibration test 3, as evaluated from the adjusted absolute response (continuous black lines) and the adjusted relative response (dashed red lines); left sub-plots and right sub-plots respectively. The relative response is zero at the beginning and end of motion, since the superstructure is expected to respond in the linear range under such a small excitation. The times when motion starts and ceases are indicated by markers.

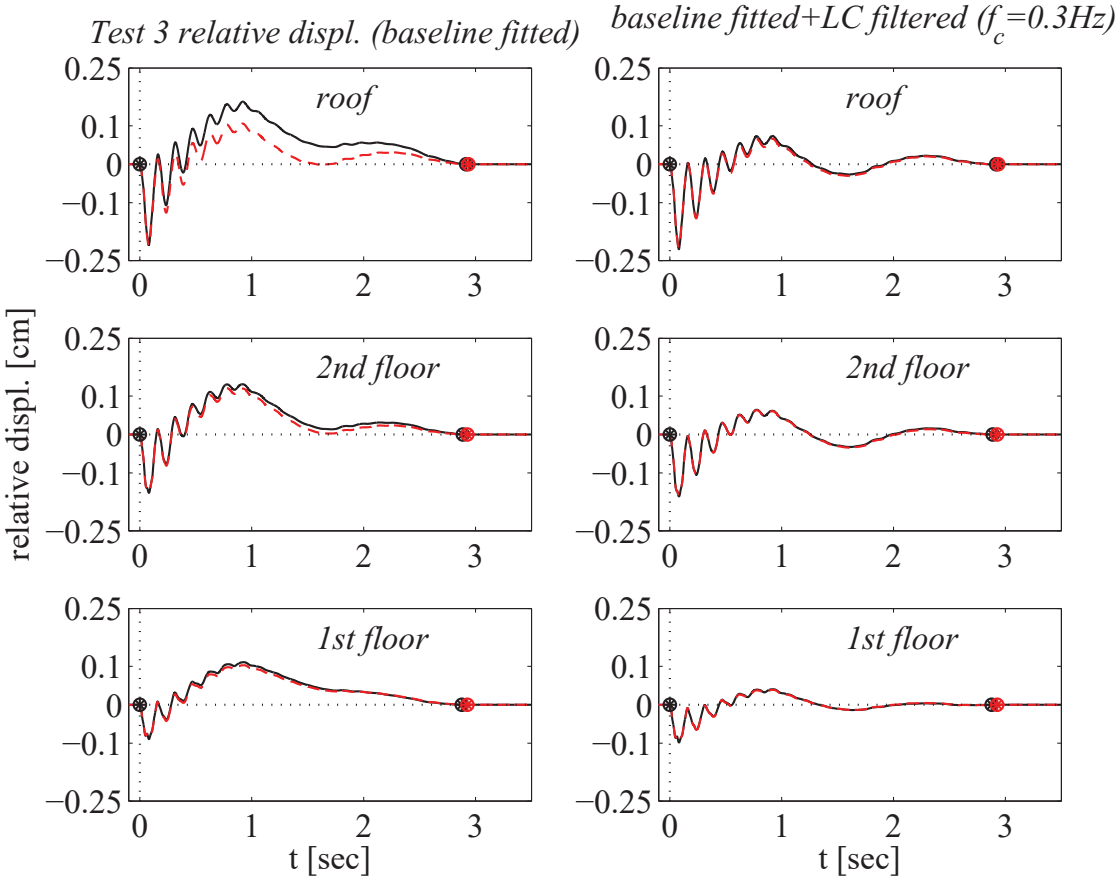

Figure A.13: Relative floor displacement histories for the Augusta free vibration test 3, as evaluated from the adjusted absolute response (continuous black lines) and the adjusted relative response (dashed red lines); left sub-plots. The relative displacements are zero at the beginning and end of motion, since the superstructure is expected to respond in the linear range under such a small excitation. The right sub-plots represent the same displacements after implementation of a low cut filter with corner frequency $f_c = 0.30Hz$. After filtering the relative displacement responses obtained by the two procedures become essentially the same. The times when motion starts and ceases are indicated by markers.

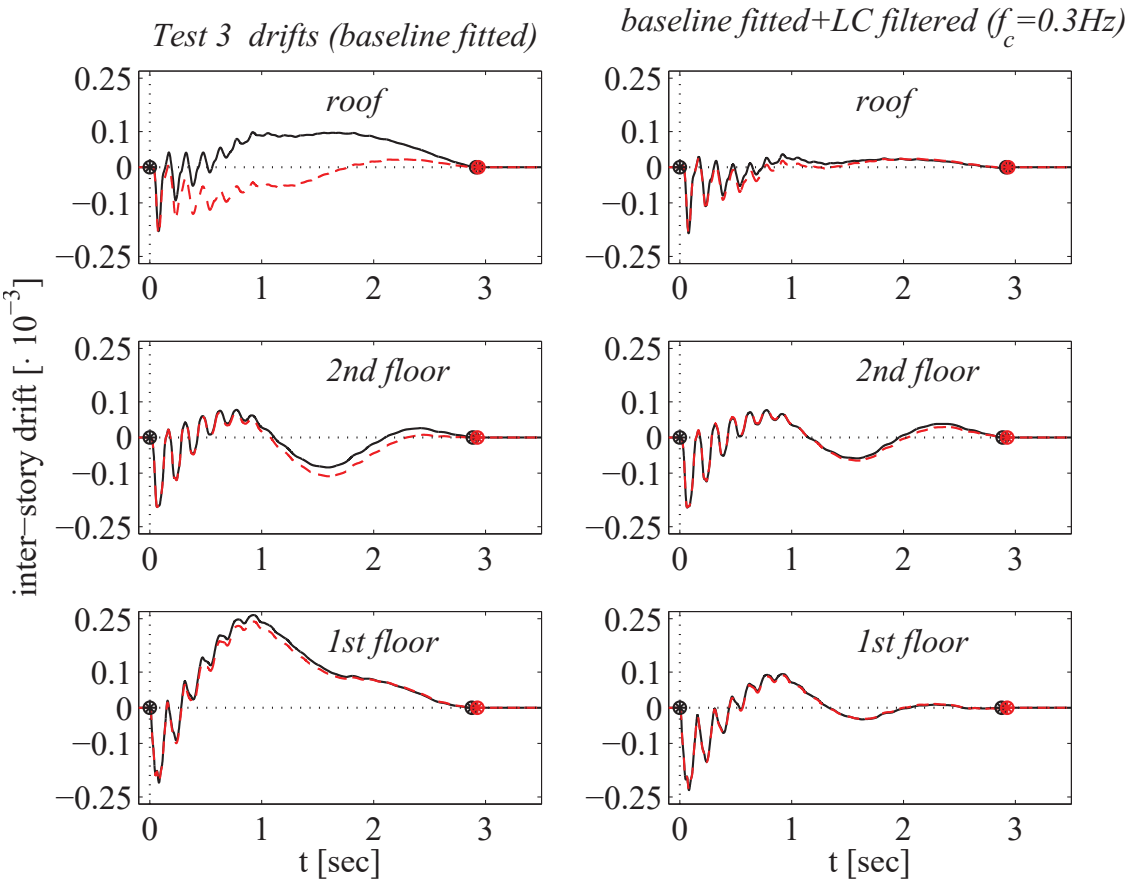

Figure A.14: Inter-story drift histories for the Augusta free vibration test 3, as evaluated from the adjusted absolute response (continuous black lines) and the adjusted relative response (dashed red lines); left sub-plots. The drifts are zero at the beginning and end of motion, since the superstructure is expected to respond in the linear range under such a small excitation. The right sub-plots represent the drifts evaluated from the corresponding filtered displacements. After filtering, the drifts obtained by the two procedures become essentially the same. The times when motion starts and ceases are indicated by markers.

A.6 TEST 4-graphs

A.6.1 Baseline fitted absolute free vibration response

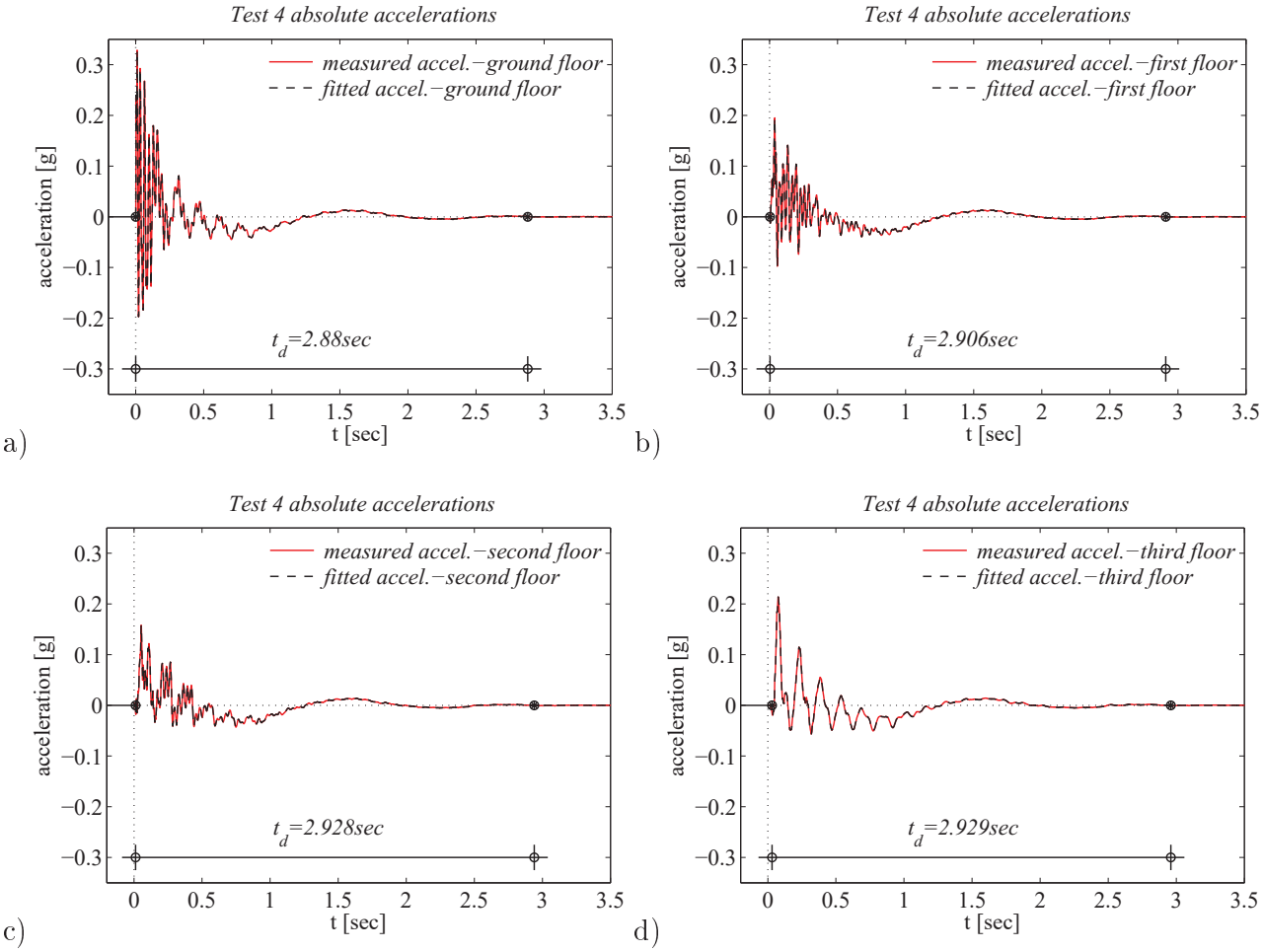

Figure A.15: Absolute acceleration response of the Augusta building during test 4: ground floor, first floor, second floor and roof response; sub-plots a), b), c), d) respectively. The row signals are represented by red lines while the baseline fitted signals are shown by black lines. The times when motion starts and ceases are indicated by black markers. The duration of strong motion is given.

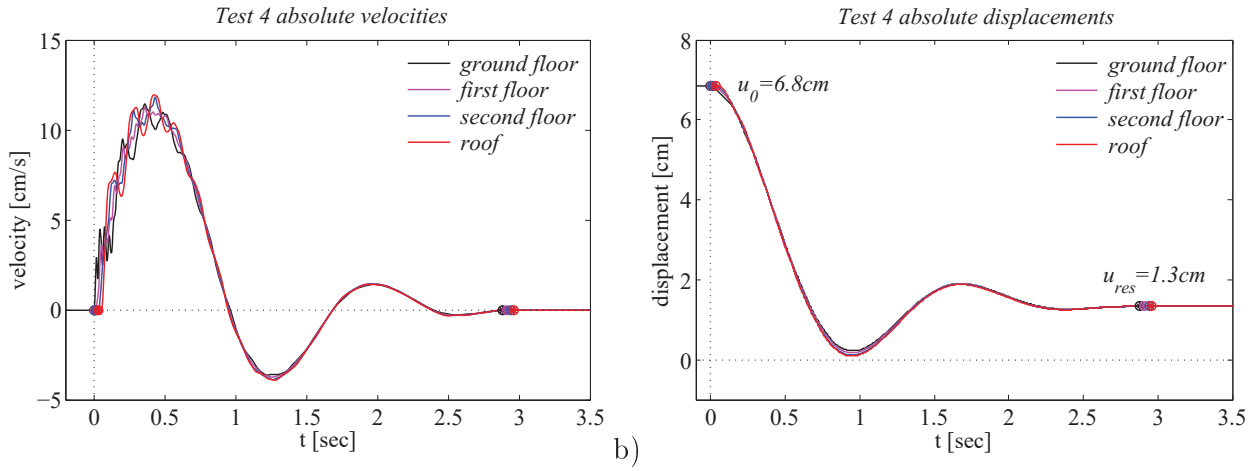

a) b)

Figure A.16: Adjusted absolute velocities and displacements at the ground floor, first floor, second floor and roof of the Augusta building during test 4; sub-plots a) and b) respectively. The times when motion starts and ceases are indicated by markers. The motion starts and ends somewhat later at the upper floors.

A.6.2 Test 4: Relative superstructure response evaluated from the processed absolute response

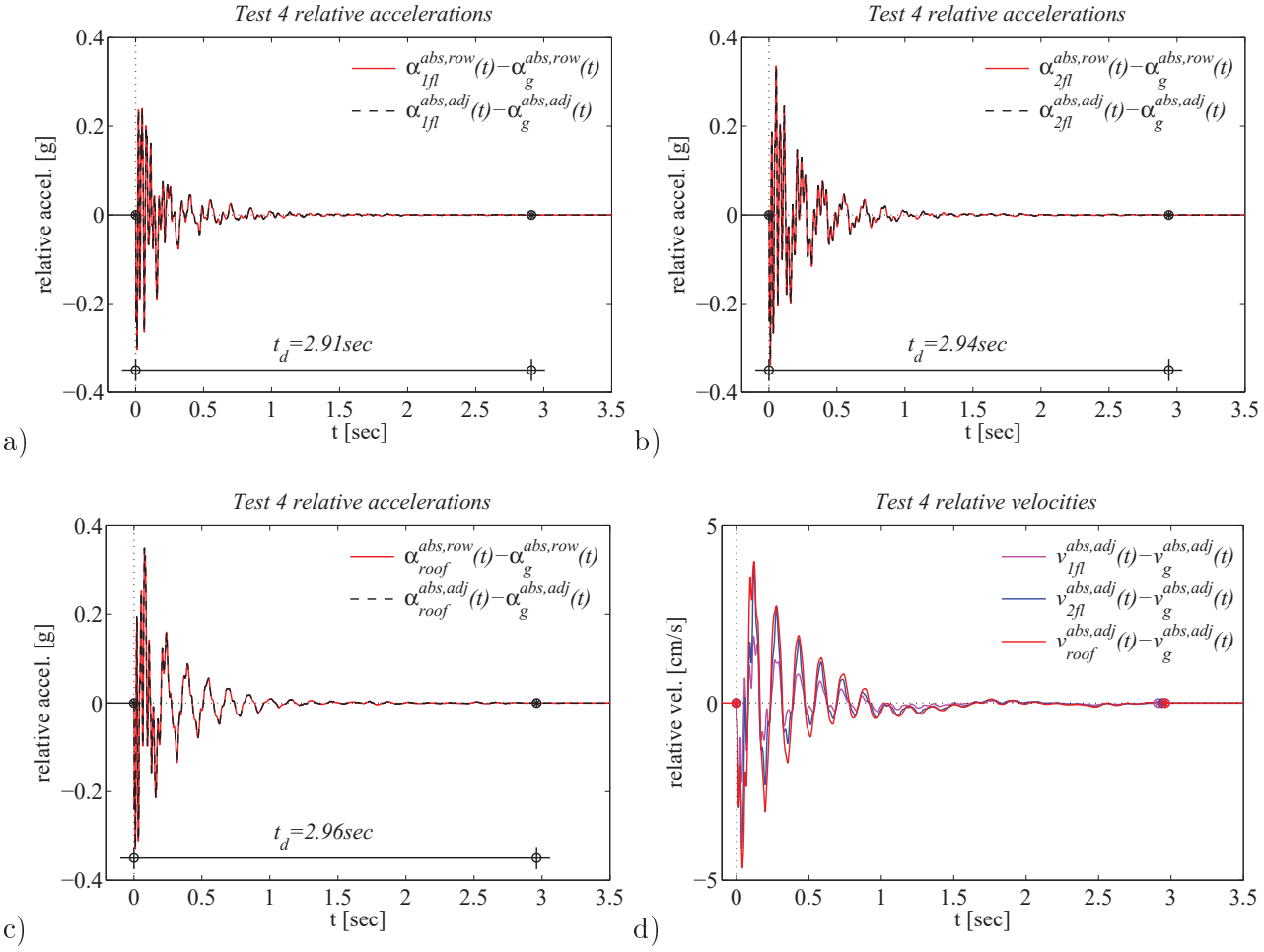

Figure A.17: Relative acceleration response at the Augusta superstructure under test 6 at first floor, second floor and roof; sub-plots a), b), c) respectively. The row signals are represented by red lines while the baseline fitted signals are shown by black lines. Sub-plot d) shows the relative floor velocities. The times when motion starts and ceases are indicated by markers. *('abs': absolute response, 'row': unprocessed response, 'adj': adjusted response, '1fl, 2fl, roof': first floor, second floor and roof response)*

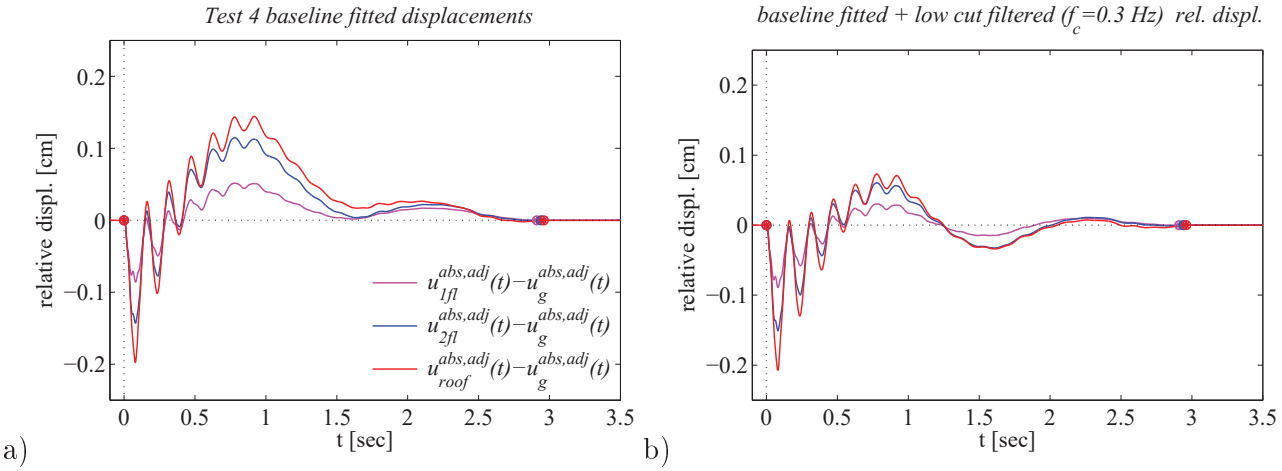

Figure A.18: Relative displacements at the Augusta superstructure during test 4; sub-plot a). Sub-plot b) shows the relative floor displacements of sub-plot a) after application of a low cut filter with corner frequency equal to $f_c = 0.30Hz$. The times when motion starts and ceases are indicated by markers. *('abs': absolute response, 'row': unprocessed response, 'adj': adjusted response, '1fl, 2fl, roof': first floor, second floor and roof response)*

A.6.3 Test 4: Relative superstructure response evaluated from the baseline fitting of the row relative motion

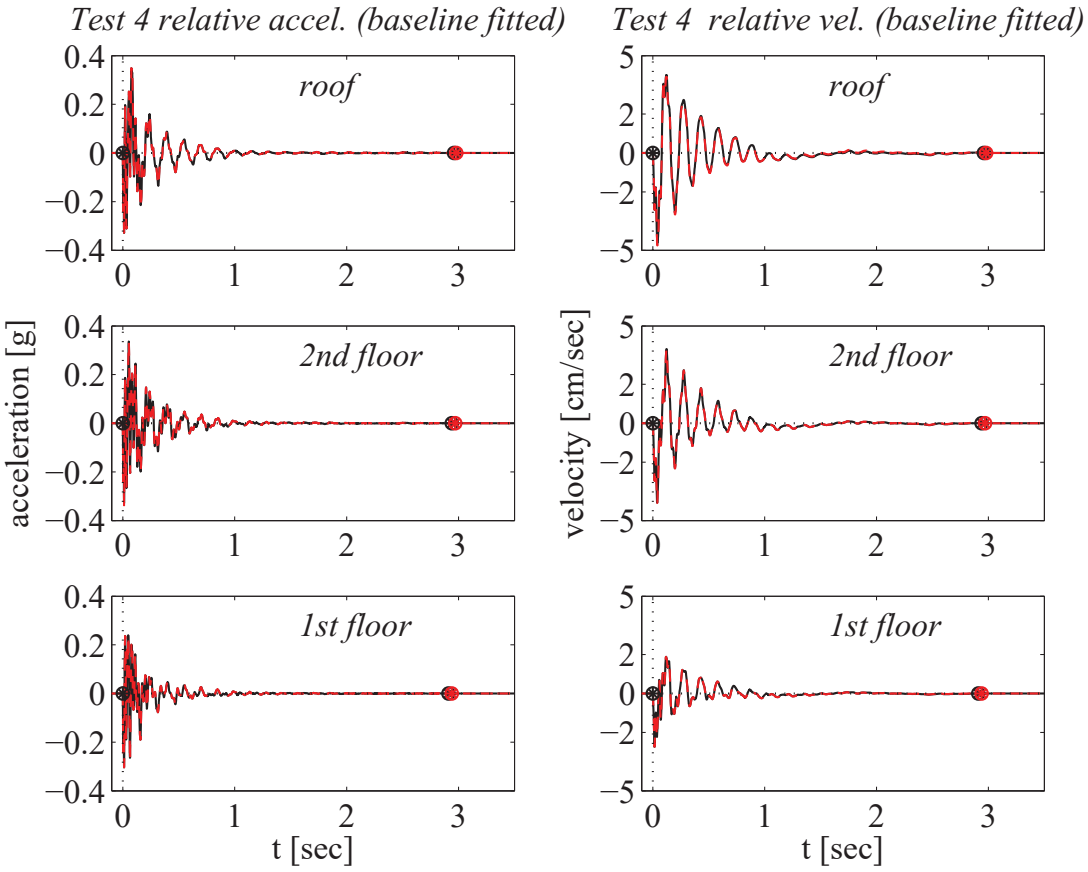

Figure A.19: Relative floor accelerations and velocities for the Augusta free vibration test 4, as evaluated from the adjusted absolute response (continuous black lines) and the adjusted relative response (dashed red lines); left sub-plots and right sub-plots respectively. The relative response is zero at the beginning and end of motion, since the superstructure is expected to respond in the linear range under such a small excitation. The times when motion starts and ceases are indicated by markers.

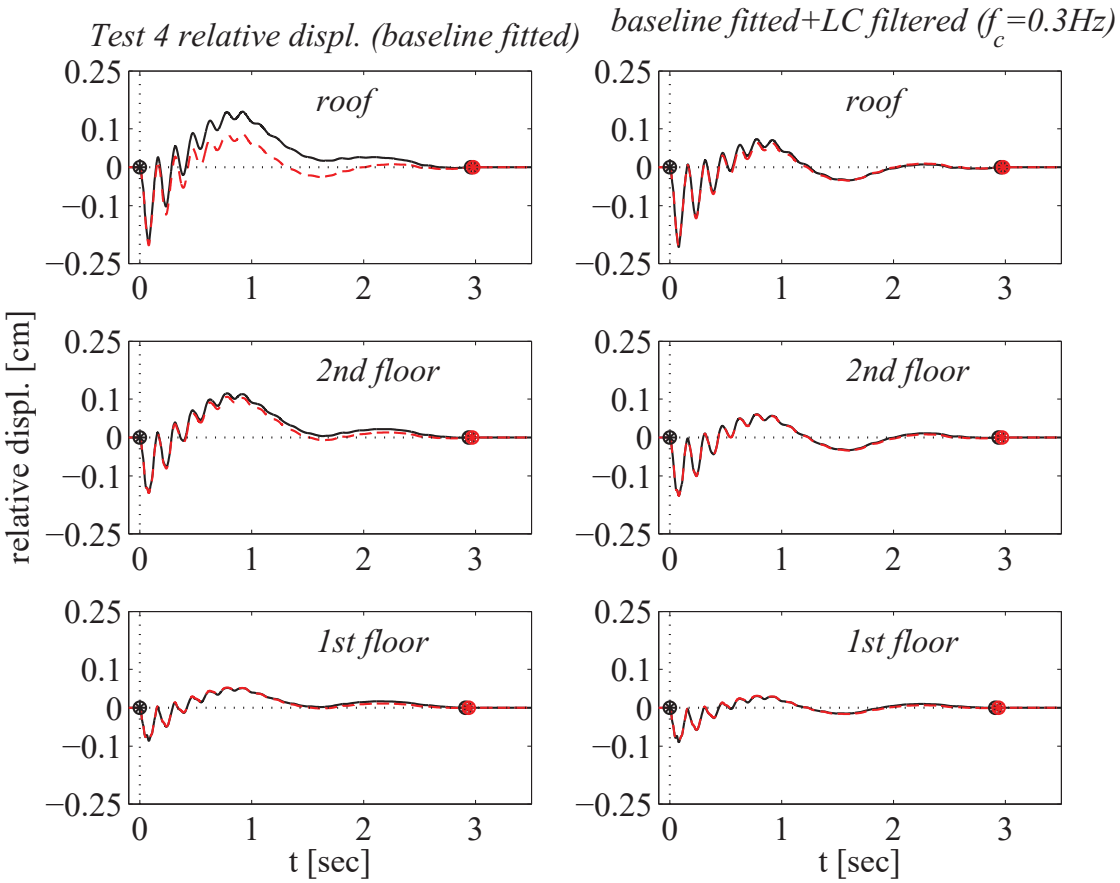

Figure A.20: Relative floor displacement histories for the Augusta free vibration test 4, as evaluated from the adjusted absolute response (continuous black lines) and the adjusted relative response (dashed red lines); left sub-plots. The relative displacements are zero at the beginning and end of motion, since the superstructure is expected to respond in the linear range under such a small excitation. The right sub-plots represent the same displacements after implementation of a low cut filter with corner frequency $f_c = 0.30Hz$. After filtering the relative displacement responses obtained by the two procedures become essentially the same. The times when motion starts and ceases are indicated by markers.

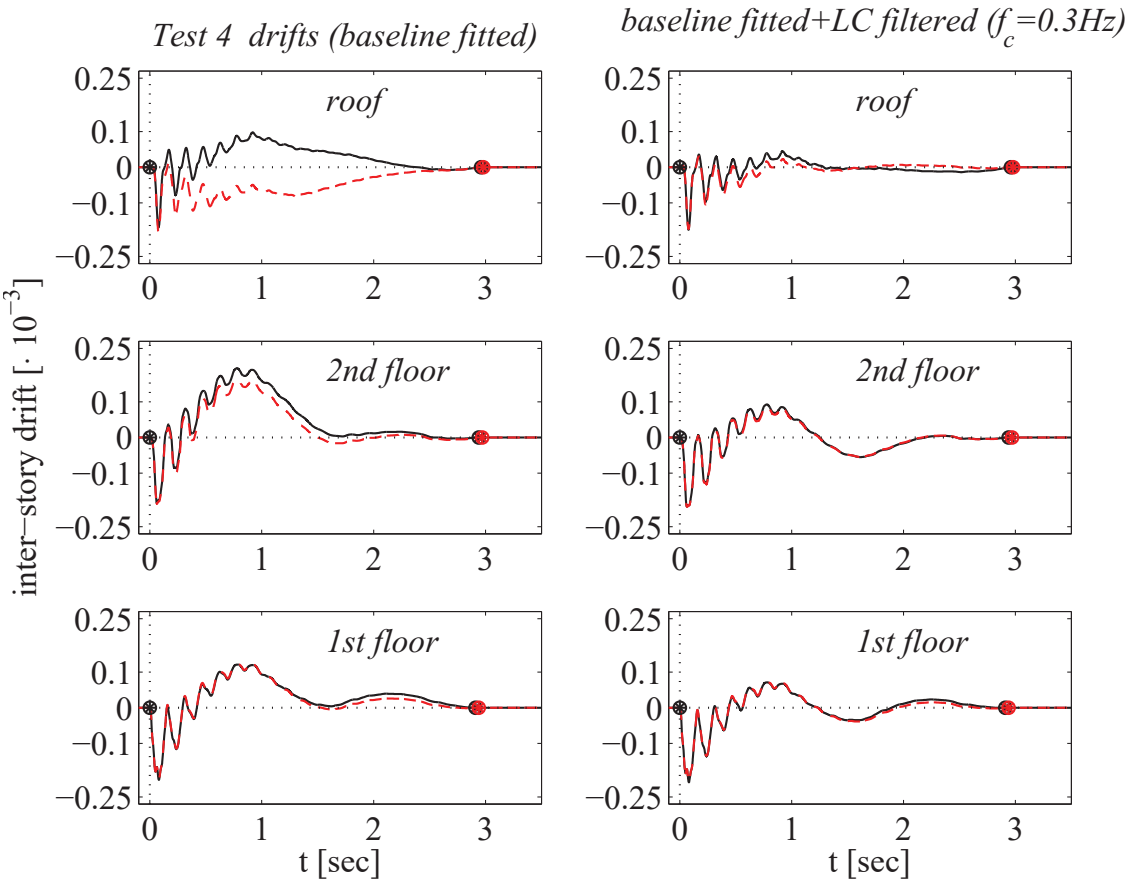

Figure A.21: Inter-story drift histories for the Augusta free vibration test 4, as evaluated from the adjusted absolute response (continuous black lines) and the adjusted relative response (dashed red lines); left sub-plots. The drifts are zero at the beginning and end of motion, since the superstructure is expected to respond in the linear range under such a small excitation. The right sub-plots represent the drifts evaluated from the corresponding filtered displacements. After filtering, the drifts obtained by the two procedures become essentially the same. The times when motion starts and ceases are indicated by markers.

A.7 TEST 5-graphs

A.7.1 Baseline fitted absolute free vibration response

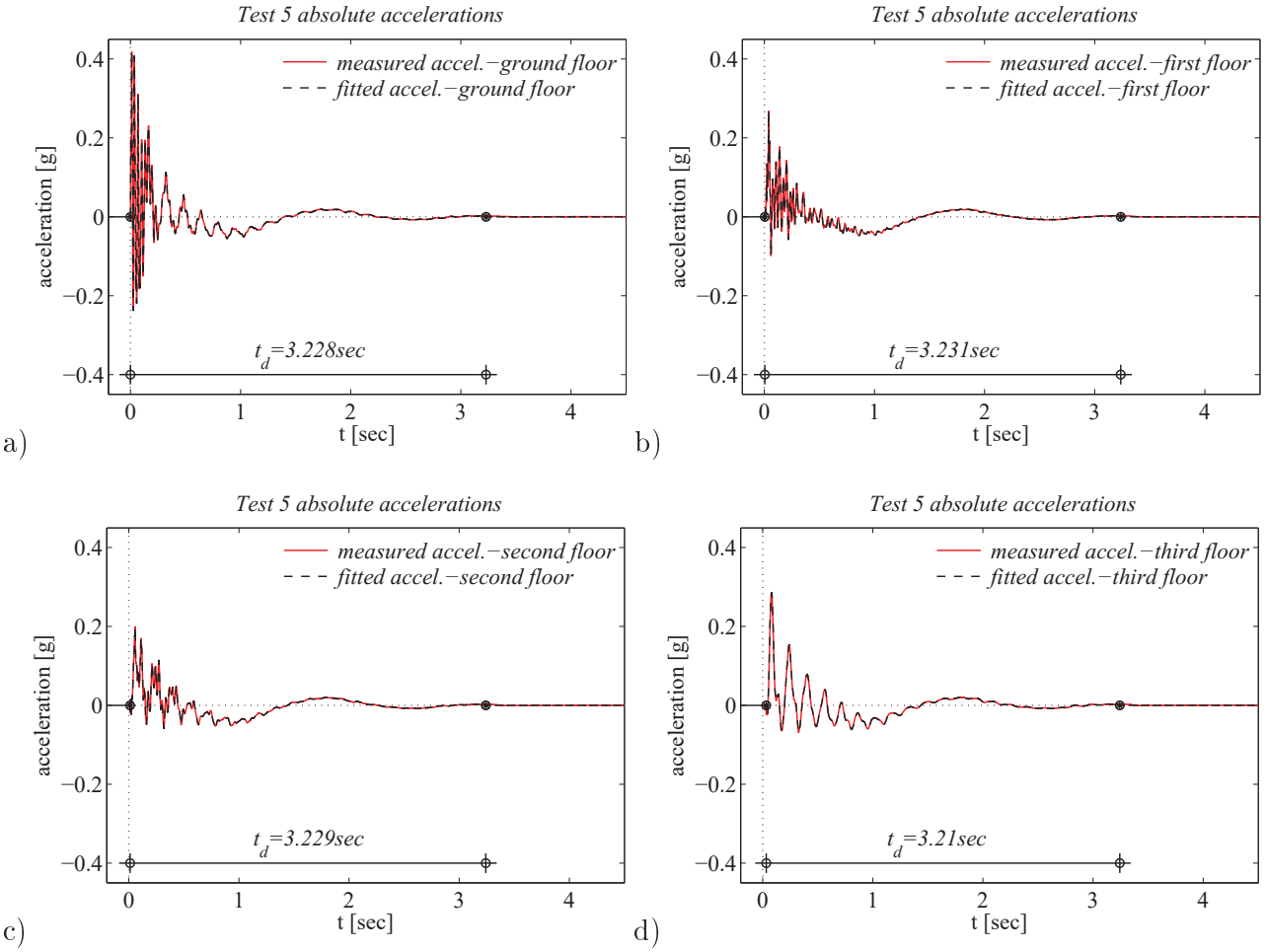

Figure A.22: Absolute acceleration response of the Augusta building during test 5: ground floor, first floor, second floor and roof response; sub-plots a), b), c), d) respectively. The row signals are represented by red lines while the baseline fitted signals are shown by black lines. The times when motion starts and ceases are indicated by black markers. The duration of strong motion is given.

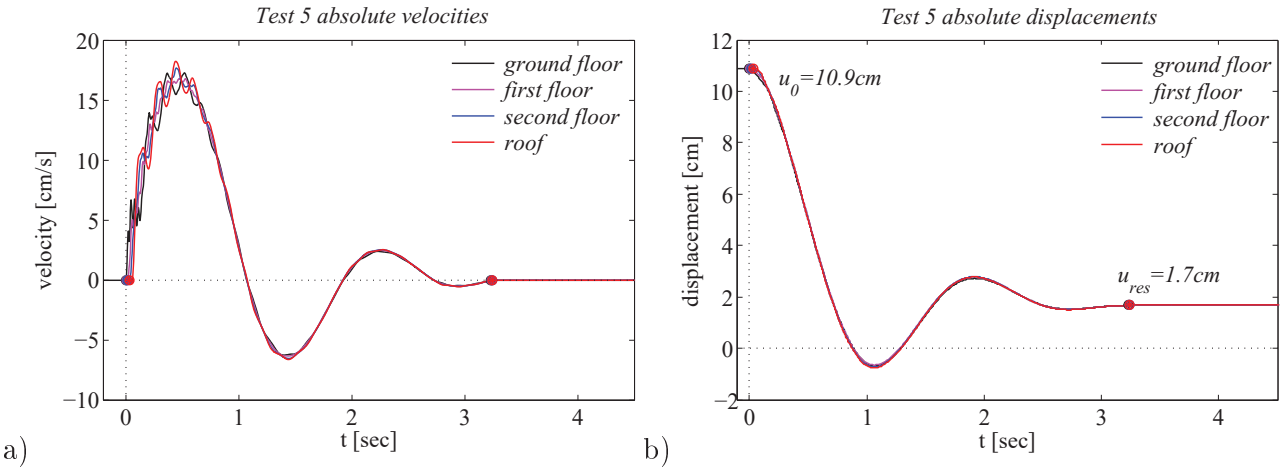

a) b)

Figure A.23: Adjusted absolute velocities and displacements at the ground floor, first floor, second floor and roof of the Augusta building during test 5; sub-plots a) and b) respectively. The times when motion starts and ceases are indicated by markers. The motion starts and ends somewhat later at the upper floors.

A.7.2 Test 5: Relative superstructure response evaluated from the processed absolute response

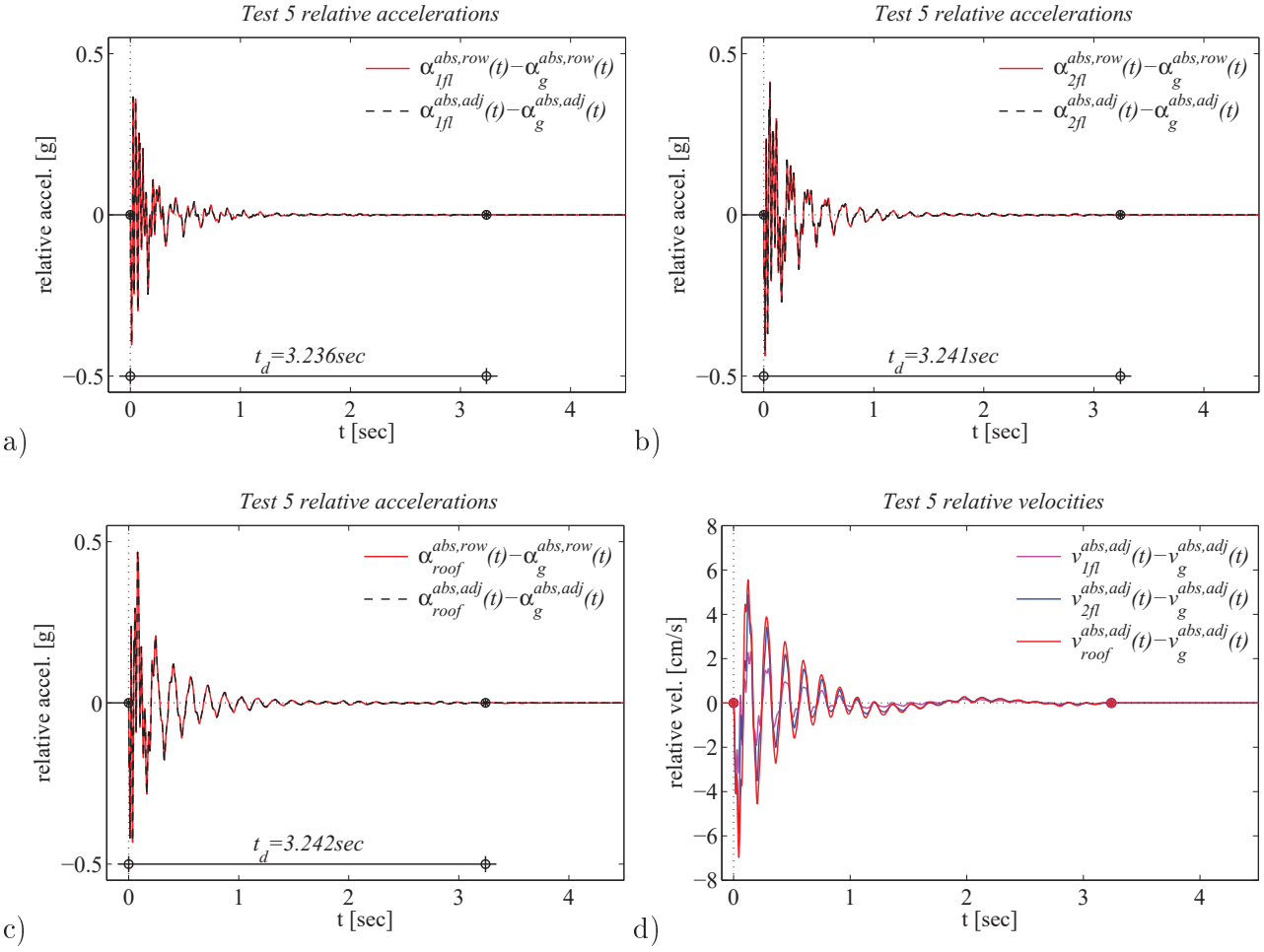

Figure A.24: Relative acceleration response at the Augusta superstructure under test 5 at first floor, second floor and roof; sub-plots a), b), c) respectively. The row signals are represented by red lines while the baseline fitted signals are shown by black lines. Sub-plot d) shows the relative floor velocities. The times when motion starts and ceases are indicated by markers. *('abs': absolute response, 'row': unprocessed response, 'adj': adjusted response, '1fl, 2fl, roof': first floor, second floor and roof response)*

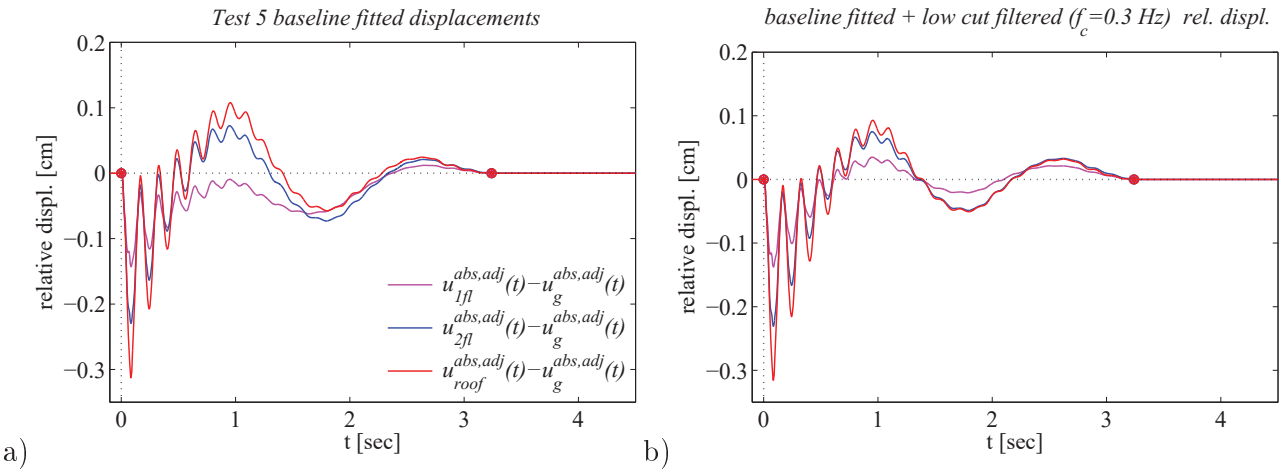

Figure A.25: Relative displacements at the Augusta superstructure during test 5; sub-plot a). Sub-plot b) shows the relative floor displacements of sub-plot a) after application of a low cut filter with corner frequency equal to $f_c = 0.30Hz$. The times when motion starts and ceases are indicated by markers. *('abs': absolute response, 'row': unprocessed response, 'adj': adjusted response, '1fl, 2fl, roof': first floor, second floor and roof response)*

A.7.3 Test 5: Relative superstructure response evaluated from the baseline fitting of the row relative motion

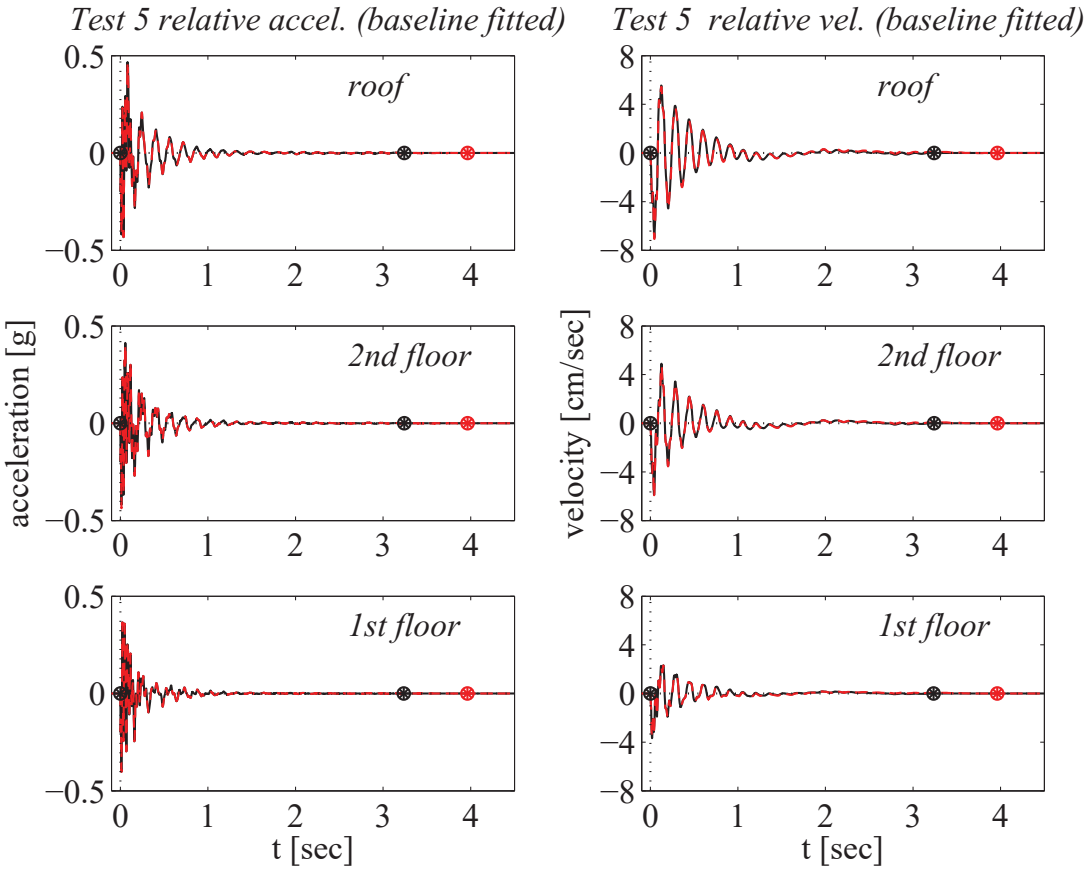

Figure A.26: Relative floor accelerations and velocities for the Augusta free vibration test 5, as evaluated from the adjusted absolute response (continuous black lines) and the adjusted relative response (dashed red lines); left sub-plots and right sub-plots respectively. The relative response is zero at the beginning and end of motion, since the superstructure is expected to respond in the linear range under such a small excitation. The times when motion starts and ceases are indicated by markers.

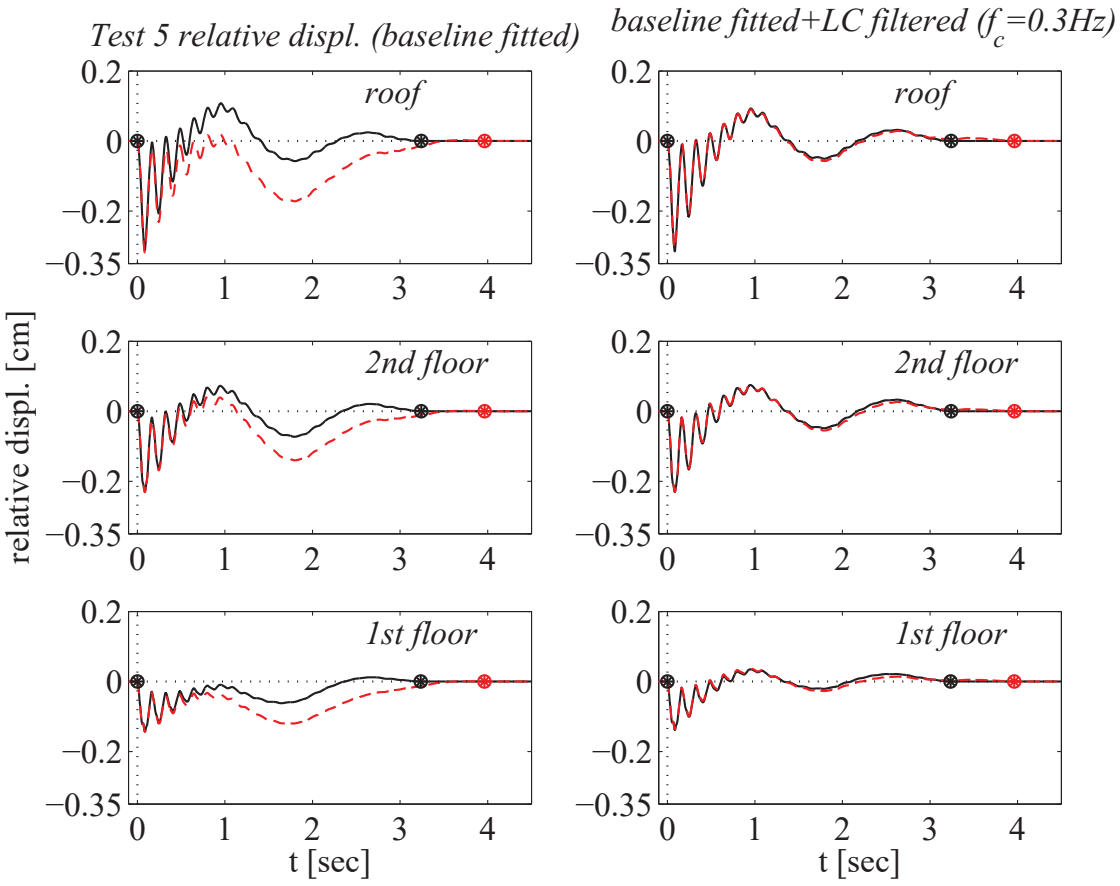

Figure A.27: Relative floor displacement histories for the Augusta free vibration test 5, as evaluated from the adjusted absolute response (continuous black lines) and the adjusted relative response (dashed red lines); left sub-plots. The relative displacements are zero at the beginning and end of motion, since the superstructure is expected to respond in the linear range under such a small excitation. The right sub-plots represent the same displacements after implementation of a low cut filter with corner frequency $f_c = 0.30Hz$. After filtering the relative displacement responses obtained by the two procedures become essentially the same. The times when motion starts and ceases are indicated by markers.

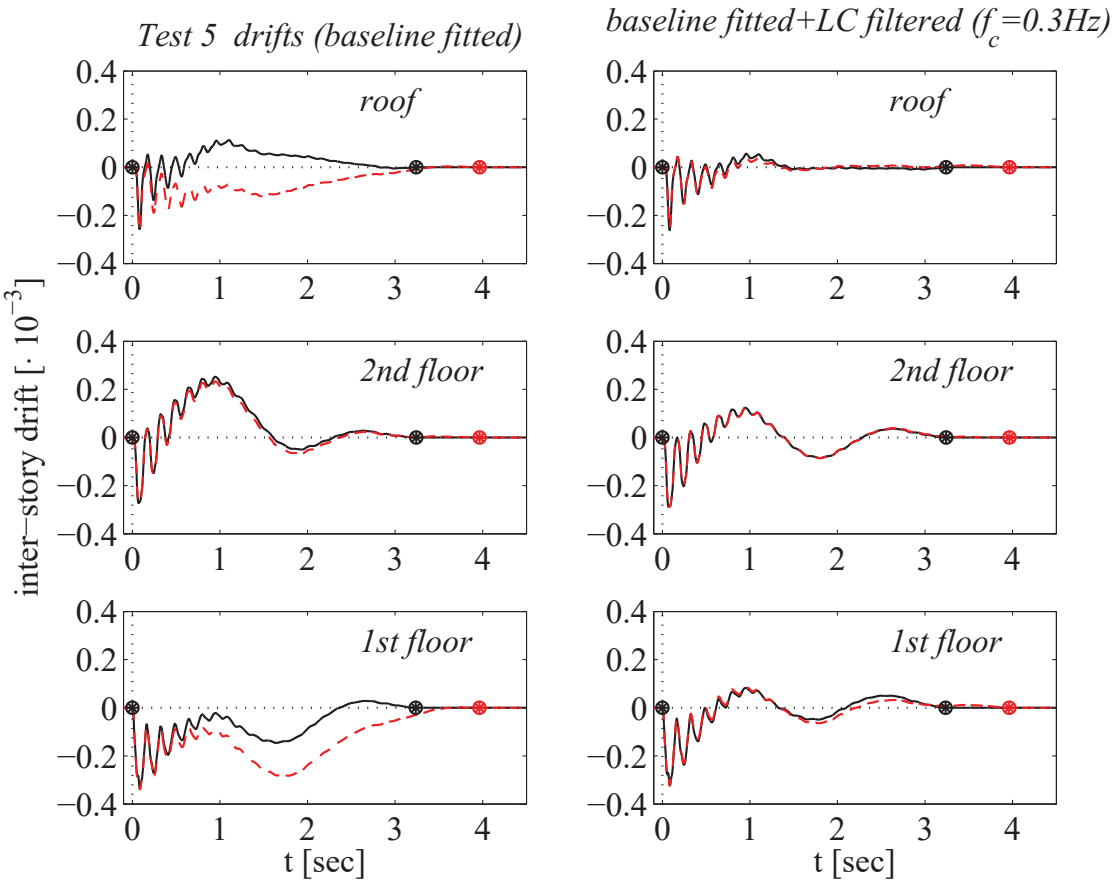

Figure A.28: Inter-story drift histories for the Augusta free vibration test 5, as evaluated from the adjusted absolute response (continuous black lines) and the adjusted relative response (dashed red lines); left sub-plots. The drifts are zero at the beginning and end of motion, since the superstructure is expected to respond in the linear range under such a small excitation. The right sub-plots represent the drifts evaluated from the corresponding filtered displacements. After filtering, the drifts obtained by the two procedures become essentially the same. The times when motion starts and ceases are indicated by markers.

A.8 Test 6-graphs

A.8.1 Baseline fitted absolute free vibration response

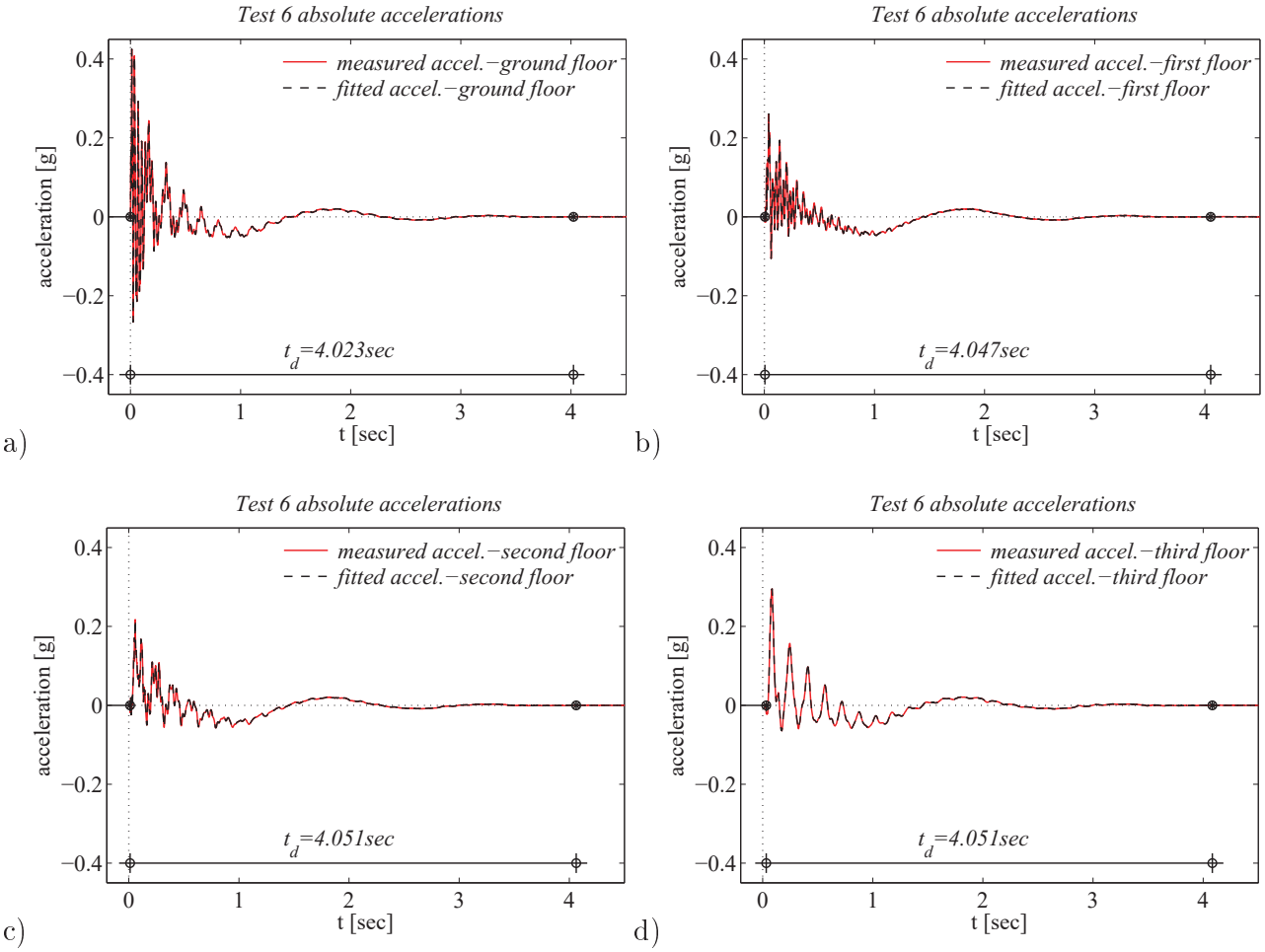

Figure A.29: Absolute acceleration response of the Augusta building during test 6: ground floor, first floor, second floor and roof response; sub-plots a), b), c), d) respectively. The row signals are represented by red lines while the baseline fitted signals are shown by black lines. The times when motion starts and ceases are indicated by black markers. The duration of strong motion is given.

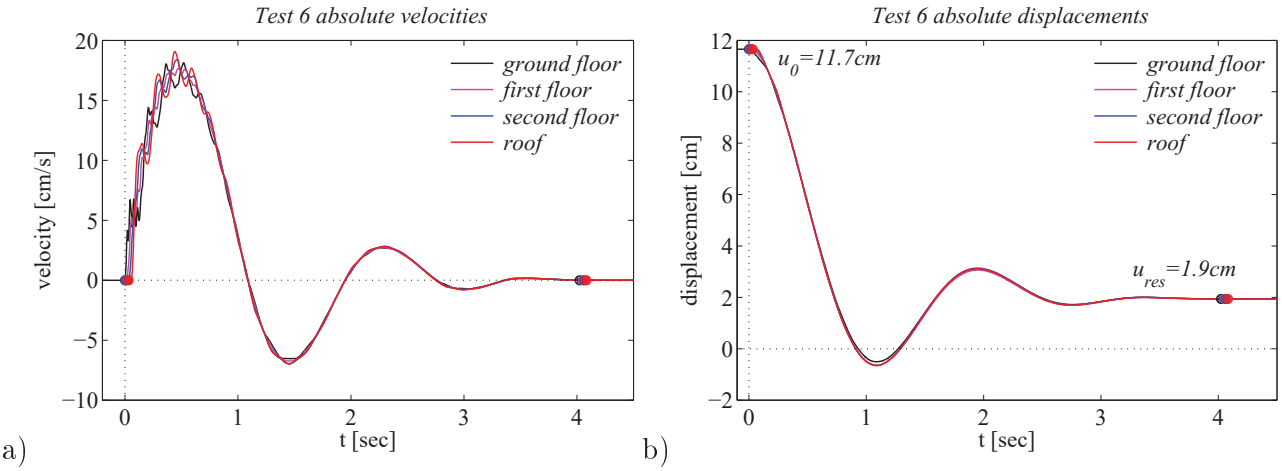

a) b)

Figure A.30: Adjusted absolute velocities and displacements at the ground floor, first floor, second floor and roof of the Augusta building during test 6; sub-plots a) and b) respectively. The times when motion starts and ceases are indicated by markers. The motion starts and ends somewhat later at the upper floors.

A.8.2 Test 6: Relative superstructure response evaluated from the processed absolute response

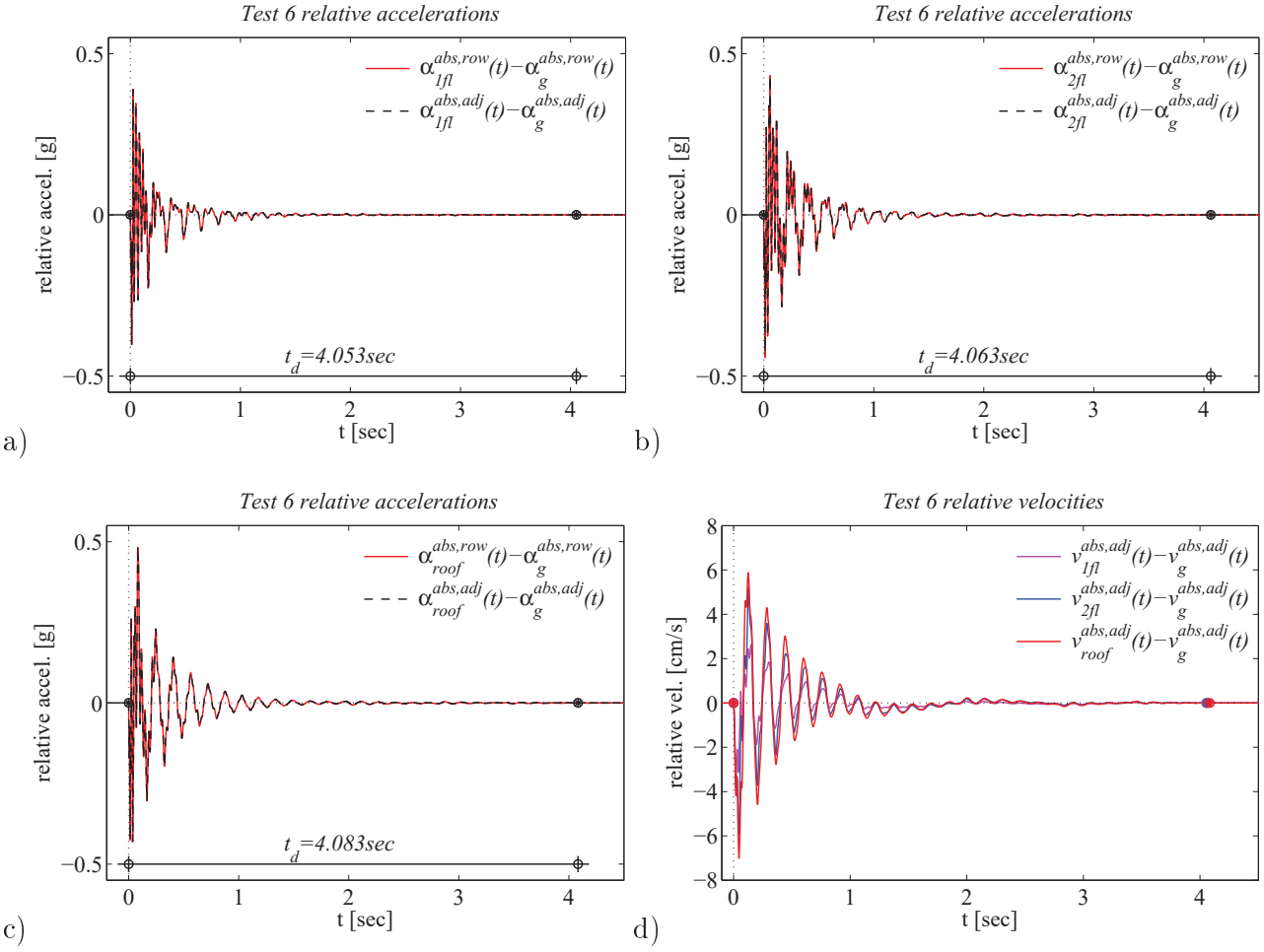

Figure A.31: Relative acceleration response at the Augusta superstructure under test 6 at first floor, second floor and roof; sub-plots a), b), c) respectively. The row signals are represented by red lines while the baseline fitted signals are shown by black lines. Sub-plot d) shows the relative floor velocities. The times when motion starts and ceases are indicated by markers. *('abs': absolute response, 'row': unprocessed response, 'adj': adjusted response, '1fl, 2fl, roof': first floor, second floor and roof response)*

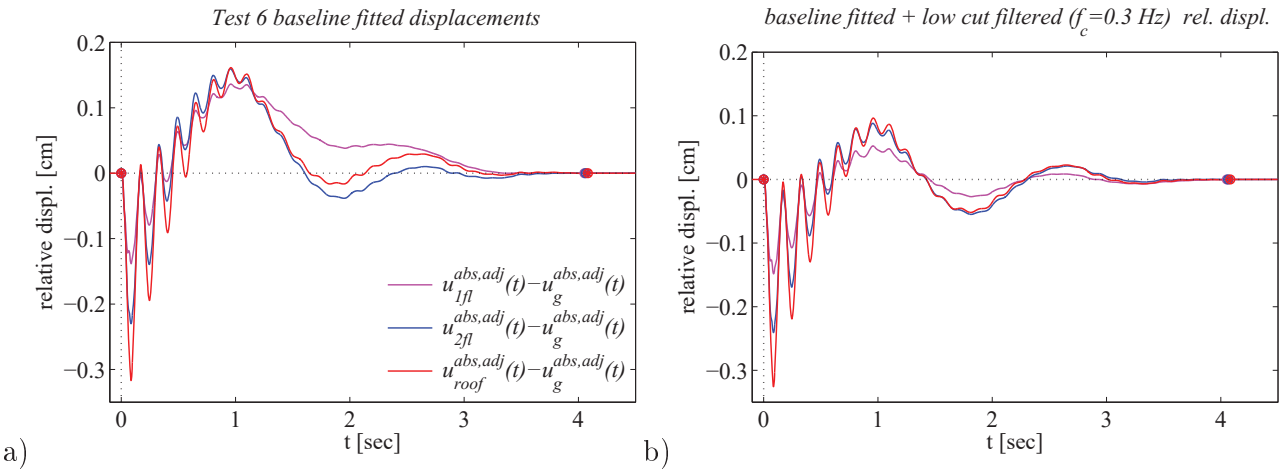

Figure A.32: Relative displacements at the Augusta superstructure during test 6; sub-plot a). Sub-plot b) shows the relative floor displacements of sub-plot a) after application of a low cut filter with corner frequency equal to $f_c = 0.30Hz$. The times when motion starts and ceases are indicated by markers. *('abs': absolute response, 'row': unprocessed response, 'adj': adjusted response, '1fl, 2fl, roof': first floor, second floor and roof response)*

A.8.3 Test 6: Relative superstructure response evaluated from the baseline fitting of the row relative motion

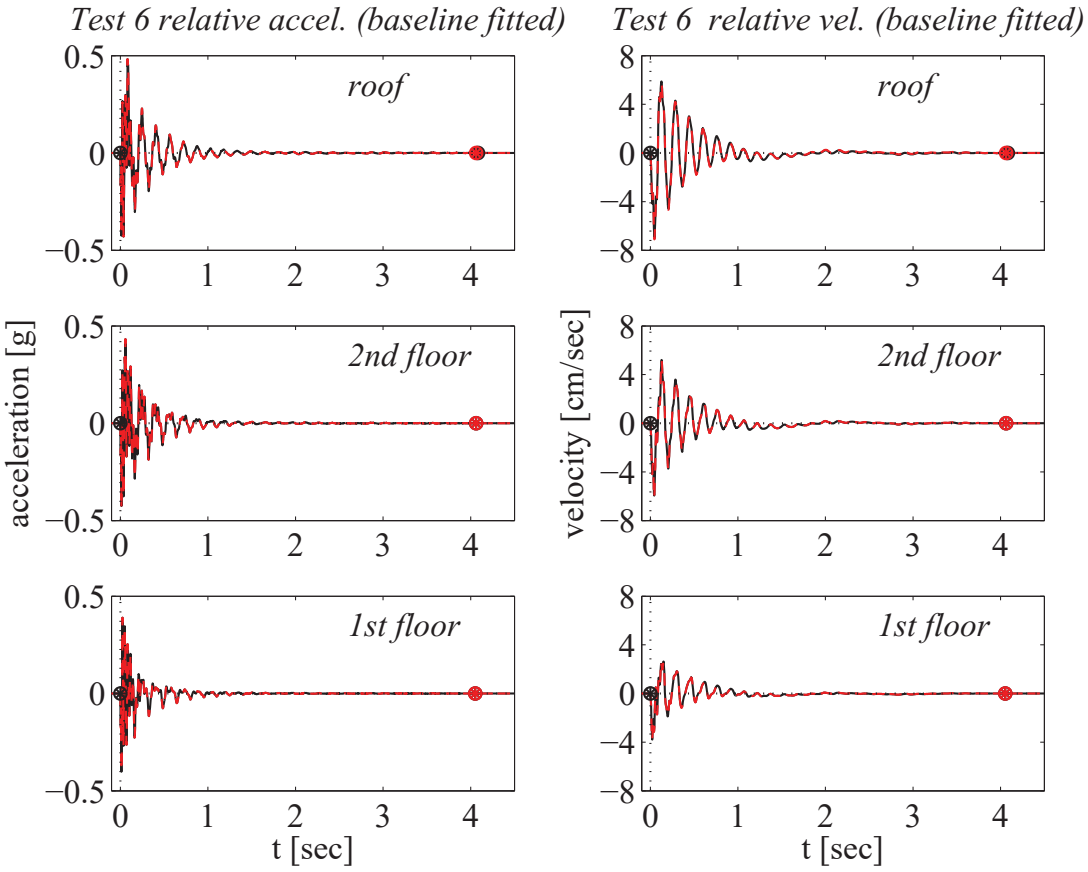

Figure A.33: Relative floor accelerations and velocities for the Augusta free vibration test 6, as evaluated from the adjusted absolute response (continuous black lines) and the adjusted relative response (dashed red lines); left sub-plots and right sub-plots respectively. The relative response is zero at the beginning and end of motion, since the superstructure is expected to respond in the linear range under such a small excitation. The times when motion starts and ceases are indicated by markers.

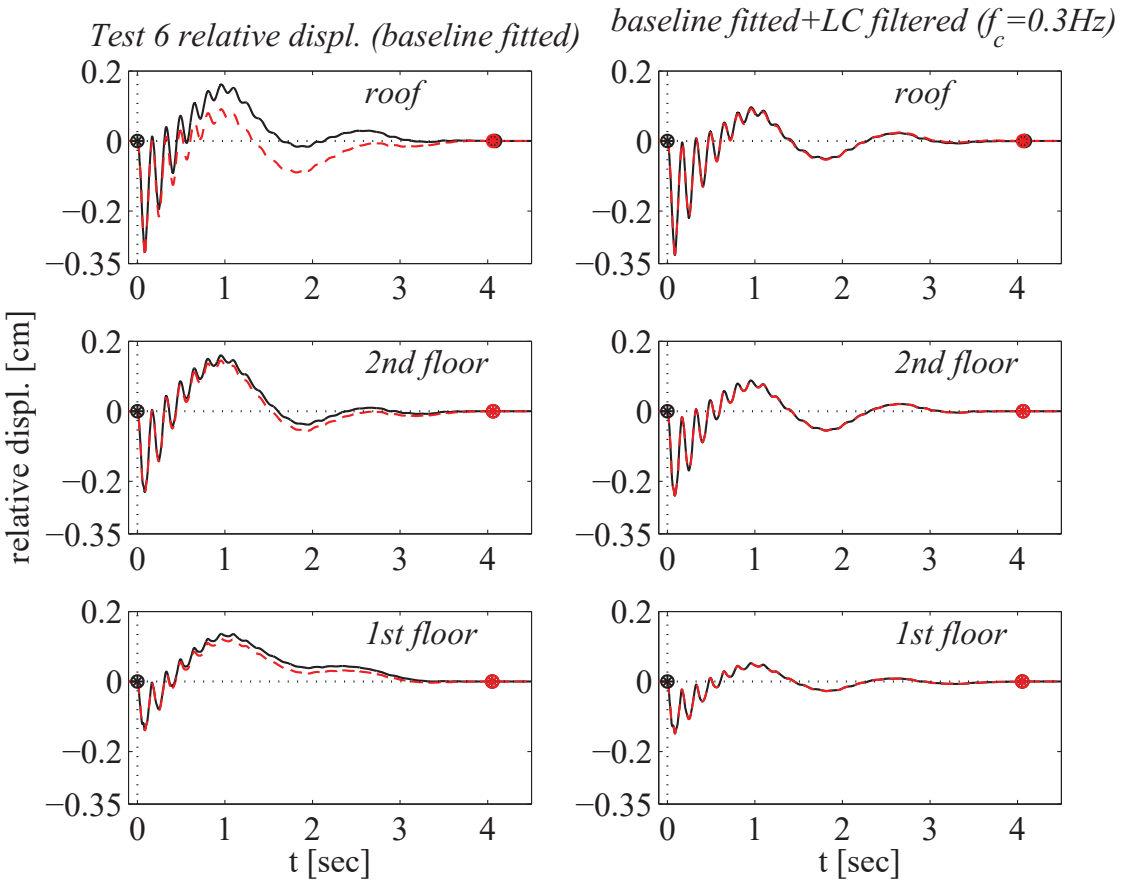

Figure A.34: Relative floor displacement histories for the Augusta free vibration test 6, as evaluated from the adjusted absolute response (continuous black lines) and the adjusted relative response (dashed red lines); left sub-plots. The relative displacements are zero at the beginning and end of motion, since the superstructure is expected to respond in the linear range under such a small excitation. The right sub-plots represent the drifts evaluated from the corresponding filtered displacements. After filtering the drifts obtained by the two procedures become essentially the same. The times when motion starts and ceases are indicated by markers.

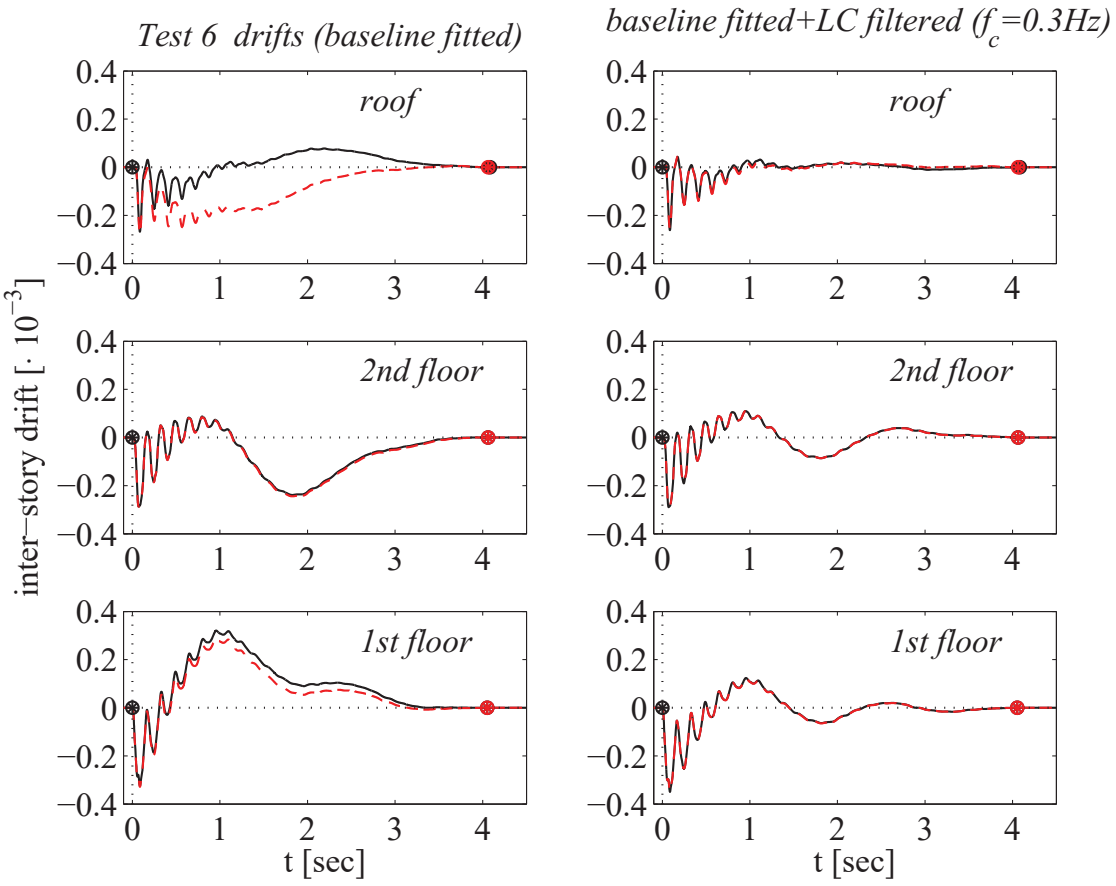

Figure A.35: Inter-story drift histories for the Augusta free vibration test 6, as evaluated from the adjusted absolute response (continuous black lines) and the adjusted relative response (dashed red lines); left sub-plots. The drifts are zero at the beginning and end of motion, since the superstructure is expected to respond in the linear range under such a small excitation. The right sub-plots represent the drifts evaluated from the corresponding filtered displacements. After filtering, the drifts obtained by the two procedures become essentially the same. The times when motion starts and ceases are indicated by markers.

A.9 TEST 8-graphs

A.9.1 Baseline fitted absolute free vibration response

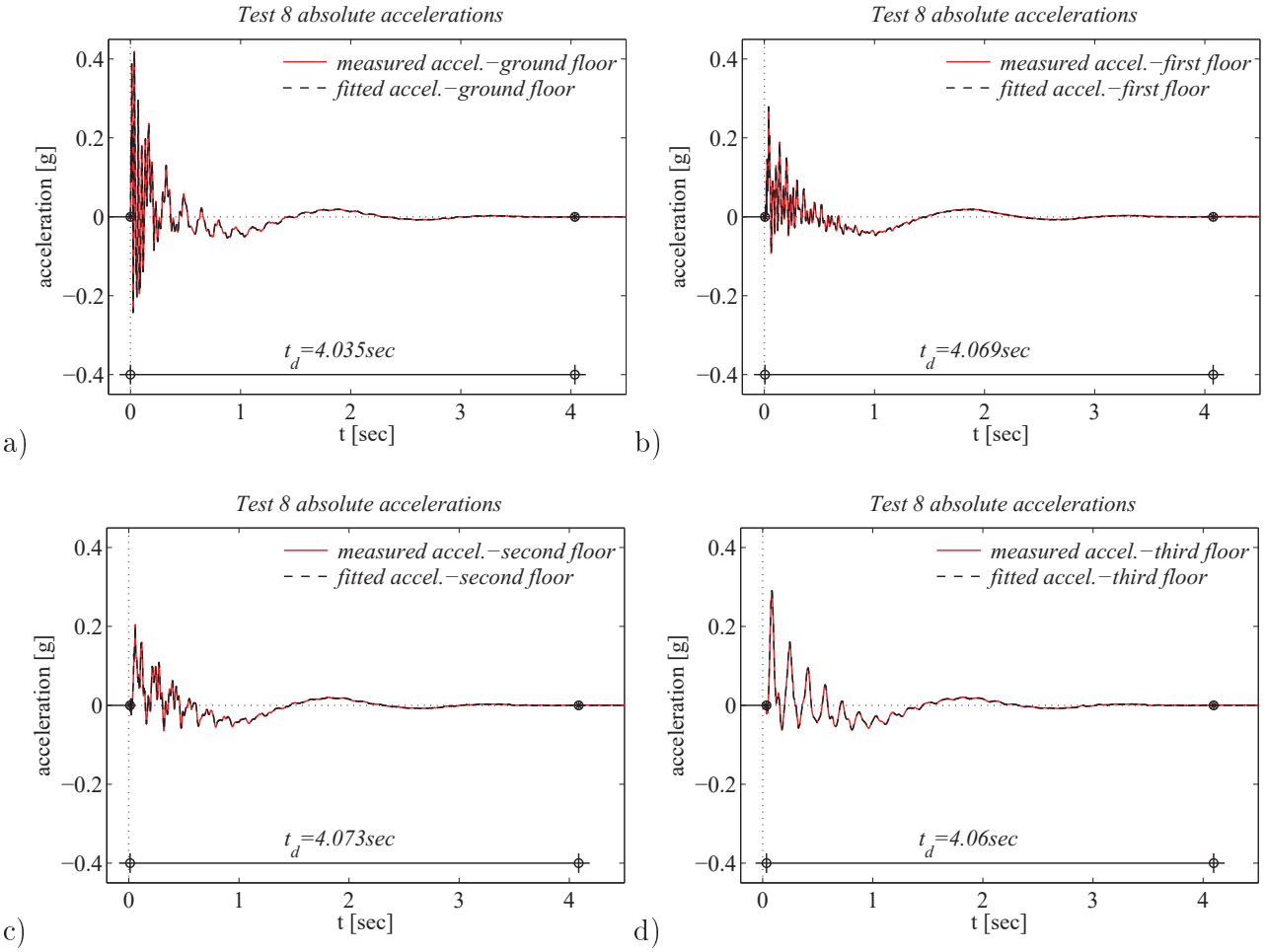

Figure A.36: Absolute acceleration response of the Augusta building during test 8: ground floor, first floor, second floor and roof response; sub-plots a), b), c), d) respectively. The row signals are represented by red lines while the baseline fitted signals are shown by black lines. The times when motion starts and ceases are indicated by black markers. The duration of strong motion is given.

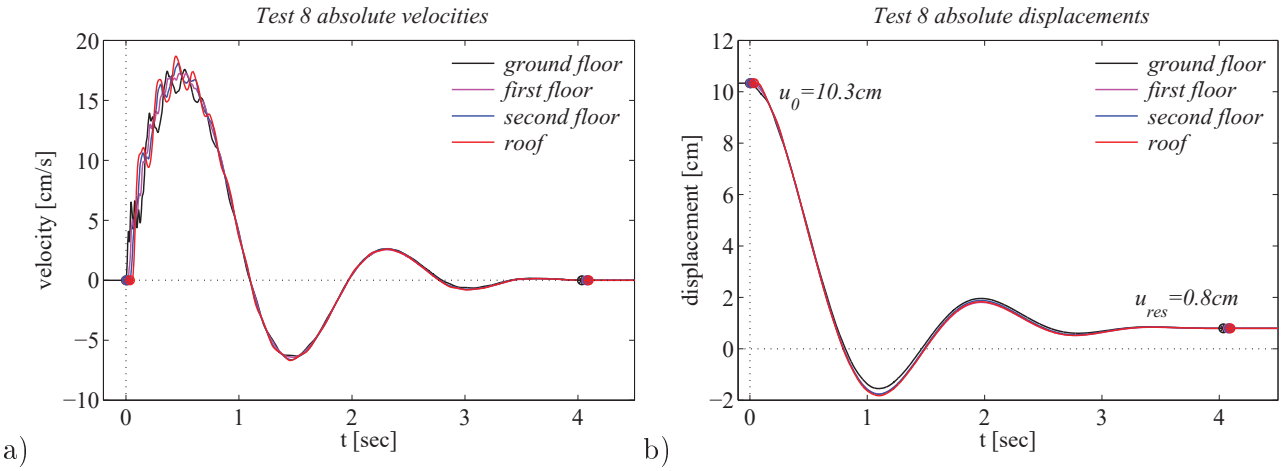

a) b)

Figure A.37: Adjusted absolute velocities and displacements at the ground floor, first floor, second floor and roof of the Augusta building during test 8; sub-plots a) and b) respectively. The times when motion starts and ceases are indicated by markers. The motion starts and ends somewhat later at the upper floors.

A.9.2 Test 8: Relative superstructure response evaluated from the processed absolute response

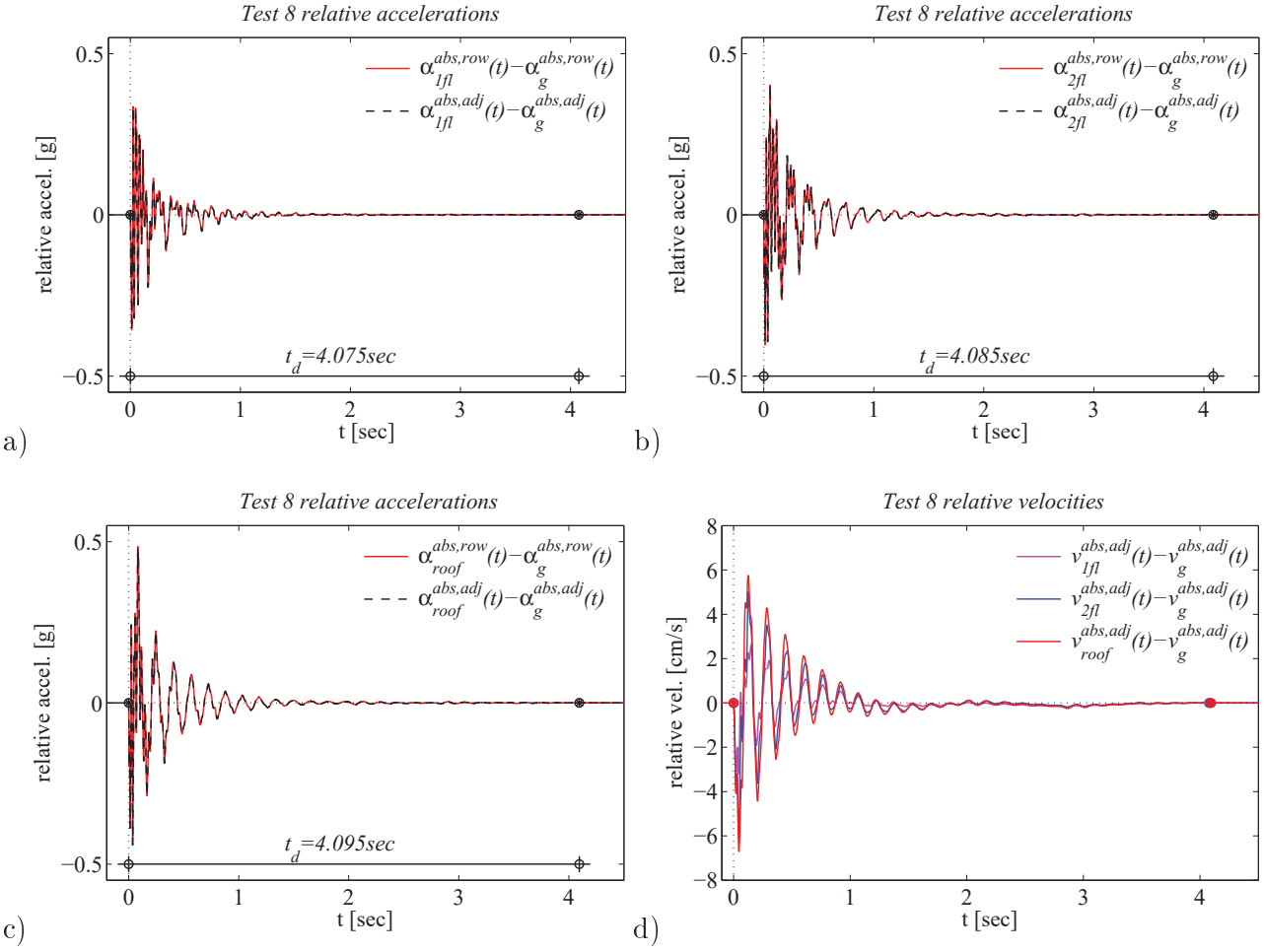

Figure A.38: Relative acceleration response at the Augusta superstructure under test 5 at first floor, second floor and roof; sub-plots a), b), c) respectively. The row signals are represented by red lines while the baseline fitted signals are shown by black lines. Sub-plot d) shows the relative floor velocities. The times when motion starts and ceases are indicated by markers. *('abs': absolute response, 'row': unprocessed response, 'adj': adjusted response, '1fl, 2fl, roof': first floor, second floor and roof response)*

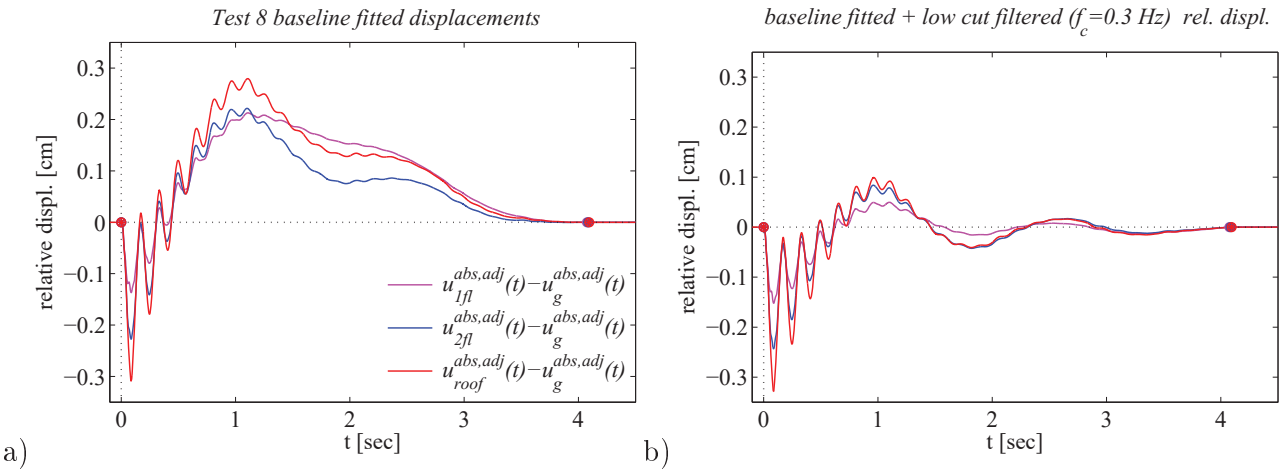

Figure A.39: Relative displacements at the Augusta superstructure during test 8; sub-plot a). Sub-plot b) shows the relative floor displacements of sub-plot a) after application of a low cut filter with corner frequency equal to $f_c = 0.30Hz$. The times when motion starts and ceases are indicated by markers. *('abs': absolute response, 'row': unprocessed response, 'adj': adjusted response, '1fl, 2fl, roof': first floor, second floor and roof response)*

A.9.3 Test 8: Relative superstructure response evaluated from the baseline fitting of the row relative motion

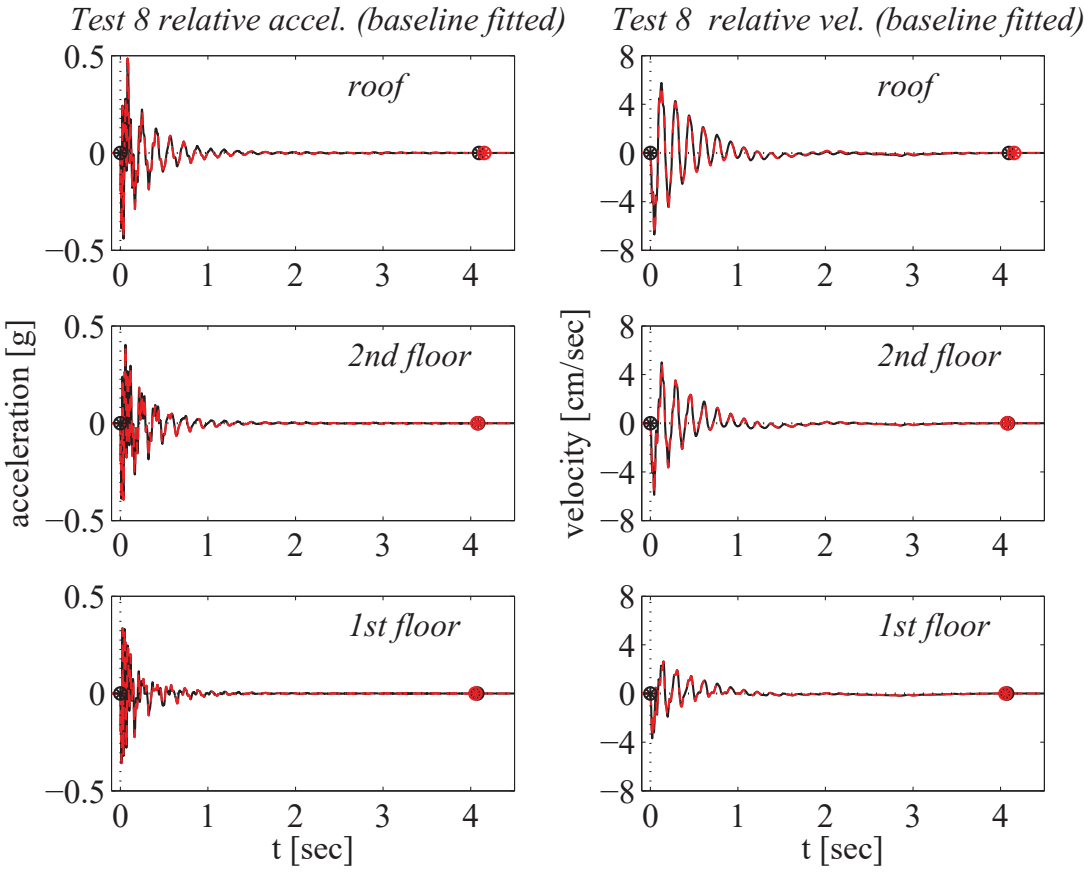

Figure A.40: Relative floor accelerations and velocities for the Augusta free vibration test 8, as evaluated from the adjusted absolute response (continuous black lines) and the adjusted relative response (dashed red lines); left sub-plots and right sub-plots respectively. The relative response is zero at the beginning and end of motion, since the superstructure is expected to respond in the linear range under such a small excitation. The times when motion starts and ceases are indicated by markers.

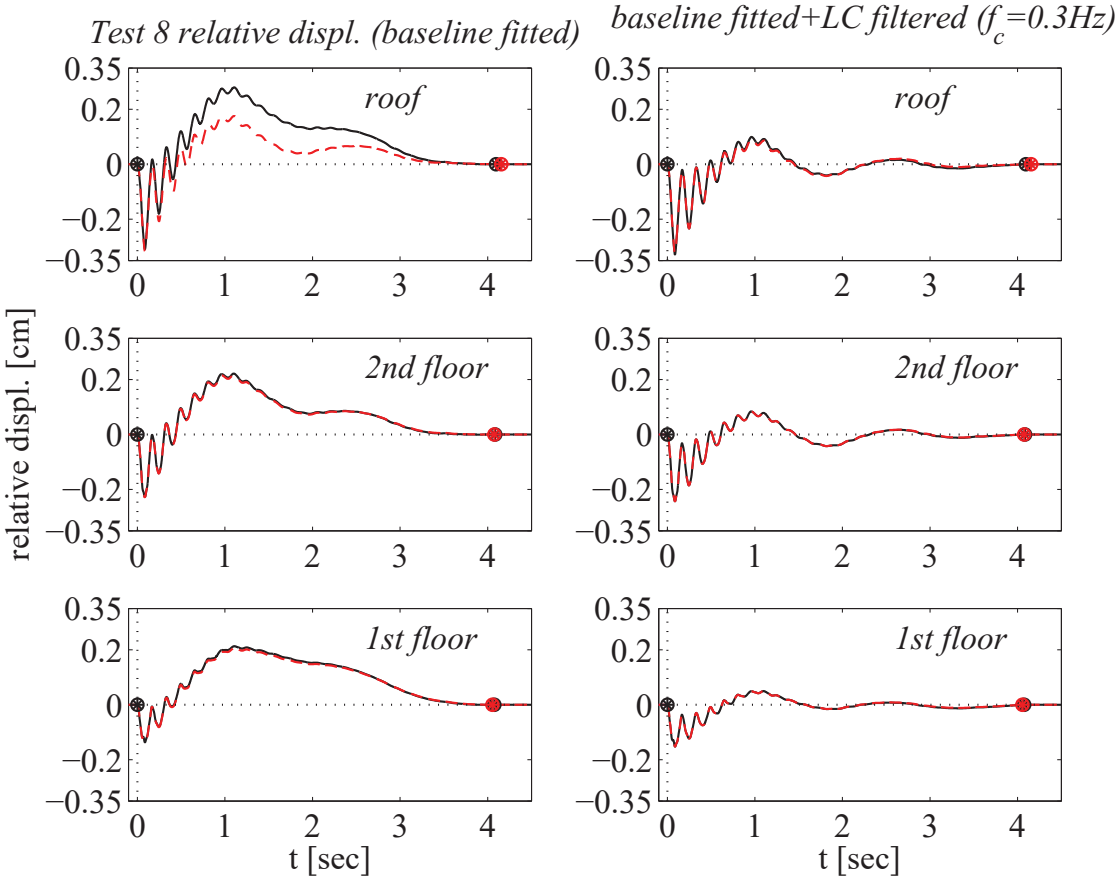

Figure A.41: Relative floor displacement histories for the Augusta free vibration test 8, as evaluated from the adjusted absolute response (continuous black lines) and the adjusted relative response (dashed red lines); left sub-plots. The relative displacements are zero at the beginning and end of motion, since the superstructure is expected to respond in the linear range under such a small excitation. The right sub-plots represent the same displacements after implementation of a low cut filter with corner frequency $f_c = 0.30Hz$. After filtering, the relative displacement responses obtained by the two procedures become essentially the same. The times when motion starts and ceases are indicated by markers.

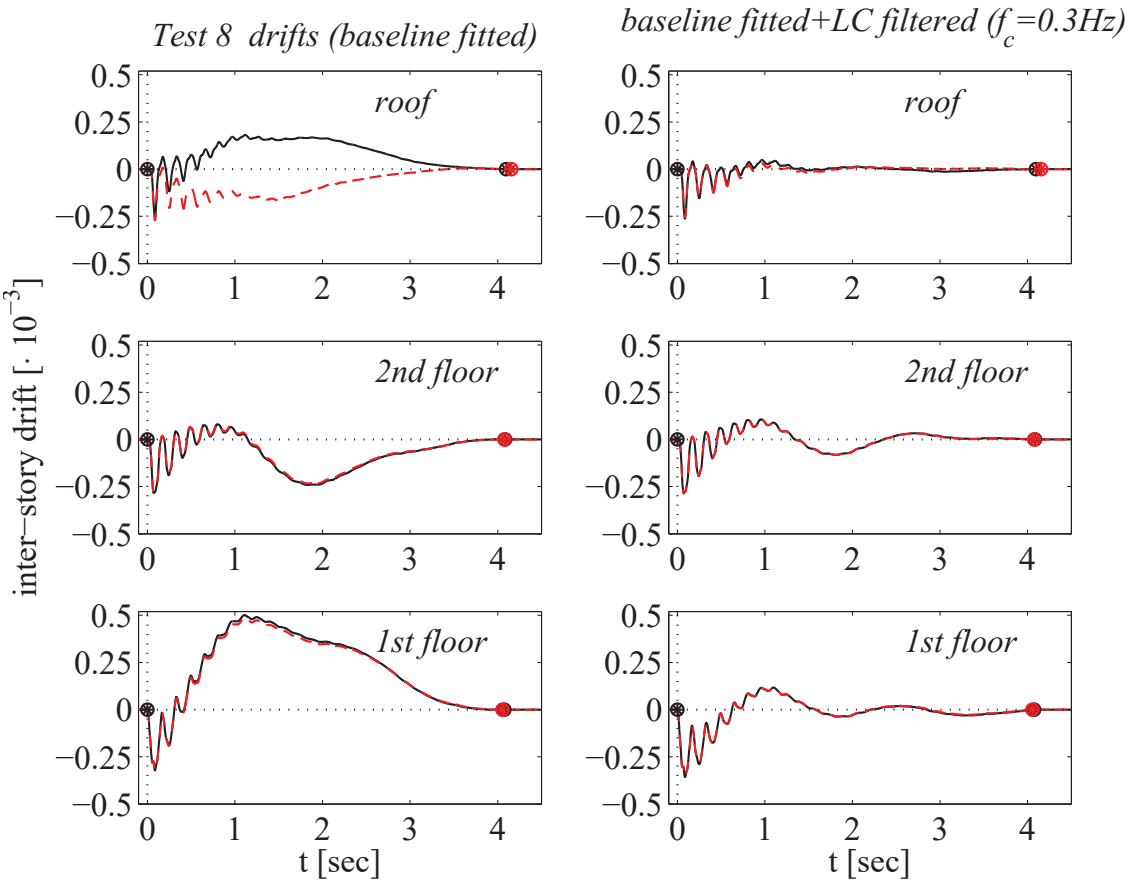

Figure A.42: Inter-story drift histories for the Augusta free vibration test 8, as evaluated from the adjusted absolute response (continuous black lines) and the adjusted relative response (dashed red lines); left sub-plots. The drifts are zero at the beginning and end of motion, since the superstructure is expected to respond in the linear range under such a small excitation. The right sub-plots represent the drifts evaluated from the corresponding filtered displacements. After filtering, the drifts obtained by the two procedures become essentially the same. The times when motion starts and ceases are indicated by markers.

A.10 TEST 10-graphs

A.10.1 Baseline fitted absolute free vibration response

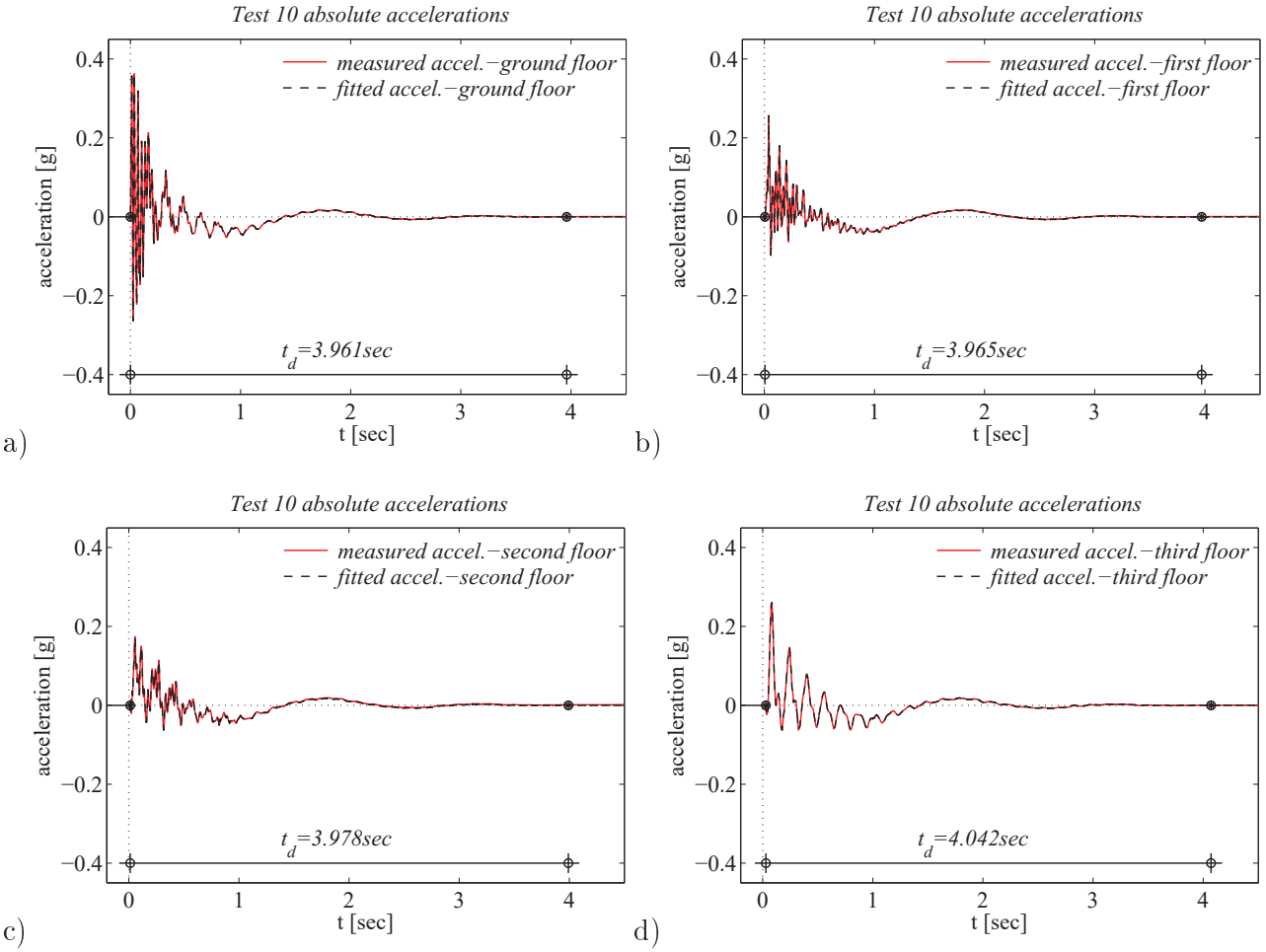

Figure A.43: Absolute acceleration response of the Augusta building during test 10: ground floor, first floor, second floor and roof response; sub-plots a), b), c), d) respectively. The row signals are represented by red lines while the baseline fitted signals are shown by black lines. The times when motion starts and ceases are indicated by black markers. The duration of strong motion is given.

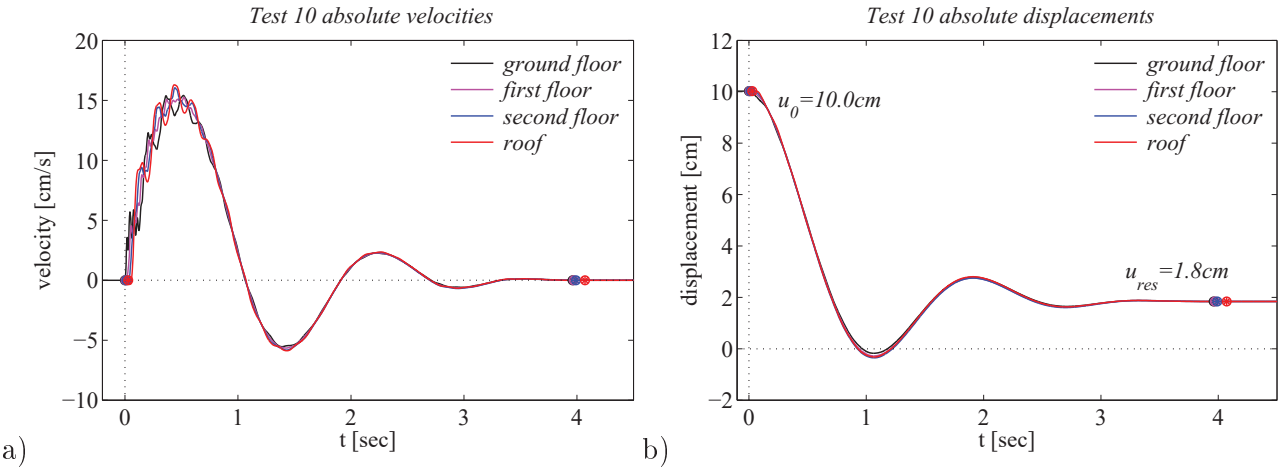

a) b)

Figure A.44: Adjusted absolute velocities and displacements at the ground floor, first floor, second floor and roof of the Augusta building during test 10; sub-plots a) and b) respectively. The times when motion starts and ceases are indicated by markers. The motion starts and ends somewhat later at the upper floors.

A.10.2 Test 10: Relative superstructure response evaluated from the processed absolute response

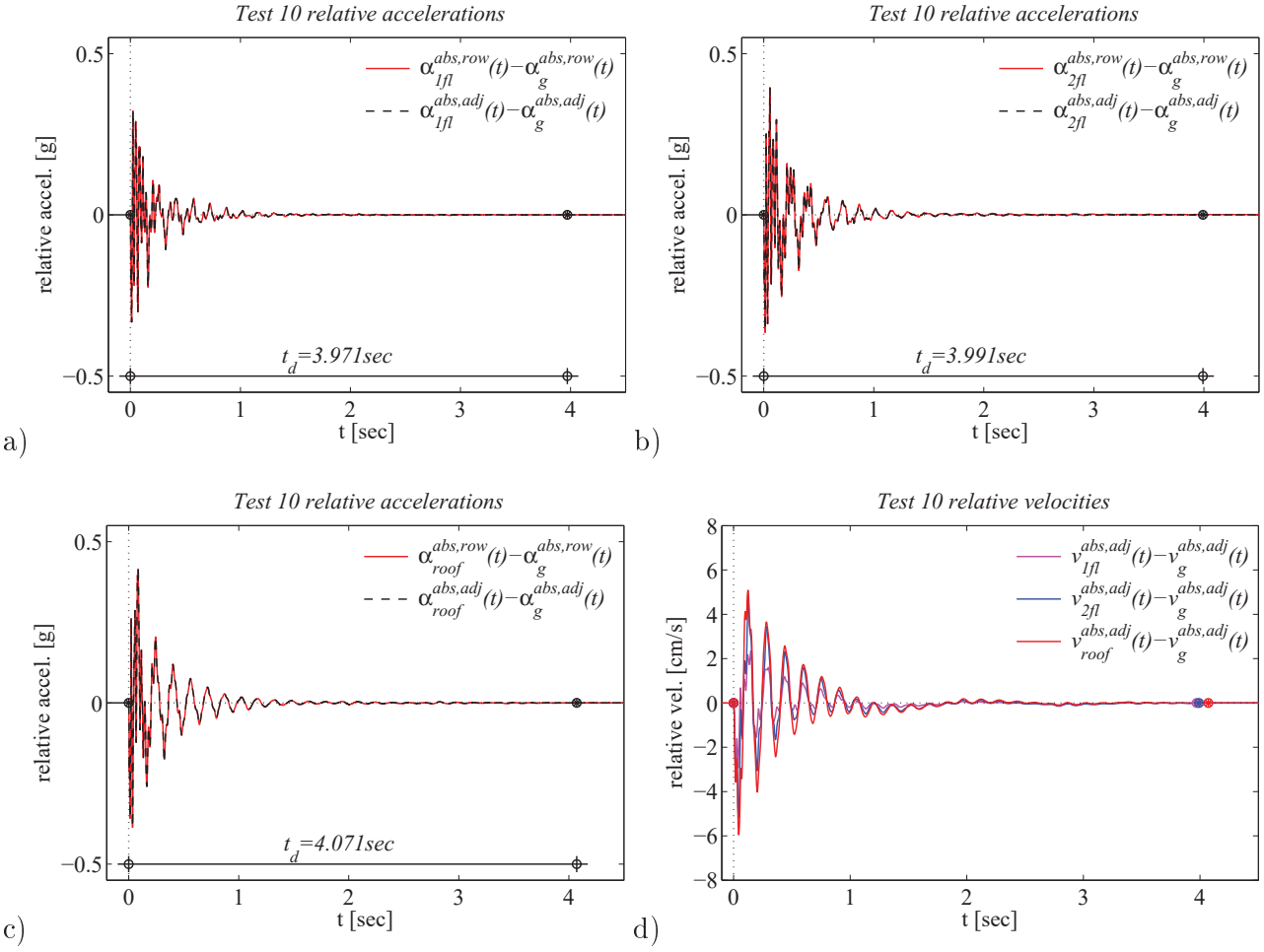

Figure A.45: Relative acceleration response at the Augusta superstructure under test 10 at first floor, second floor and roof; sub-plots a), b), c) respectively. The row signals are represented by red lines while the baseline fitted signals are shown by black lines. Sub-plot d) shows the relative floor velocities. The times when motion starts and ceases are indicated by markers. *('abs': absolute response, 'row': unprocessed response, 'adj': adjusted response, '1fl, 2fl, roof': first floor, second floor and roof response)*

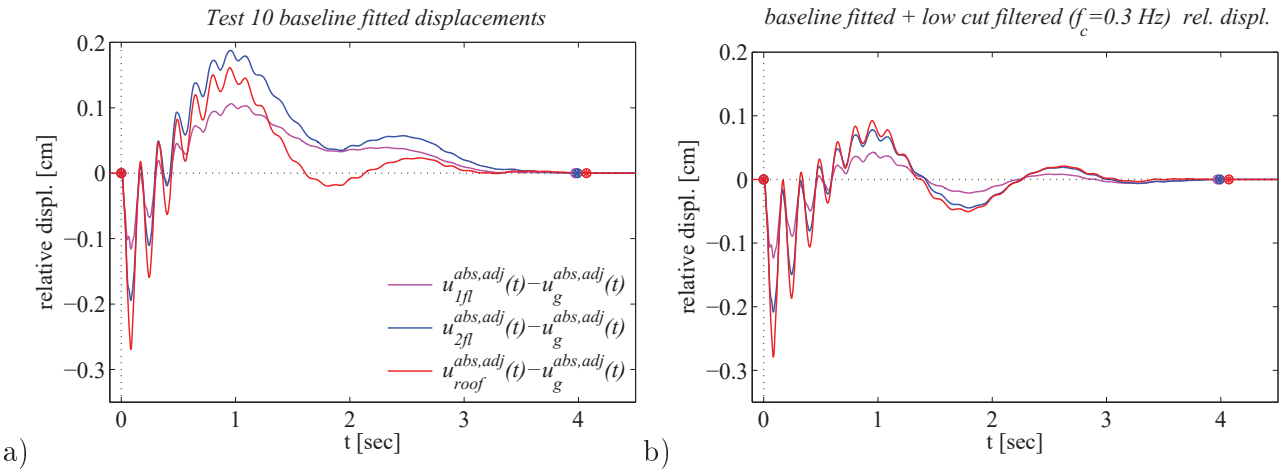

Figure A.46: Relative displacements at the Augusta superstructure during test 10; sub-plot a). Sub-plot b) shows the relative floor displacements of sub-plot a) after application of a low cut filter with corner frequency equal to $f_c = 0.30Hz$. The times when motion starts and ceases are indicated by markers. *('abs': absolute response, 'row': unprocessed response, 'adj': adjusted response, '1fl, 2fl, roof': first floor, second floor and roof response)*

A.10.3 Test 10: Relative superstructure response evaluated from the baseline fitting of the row relative motion

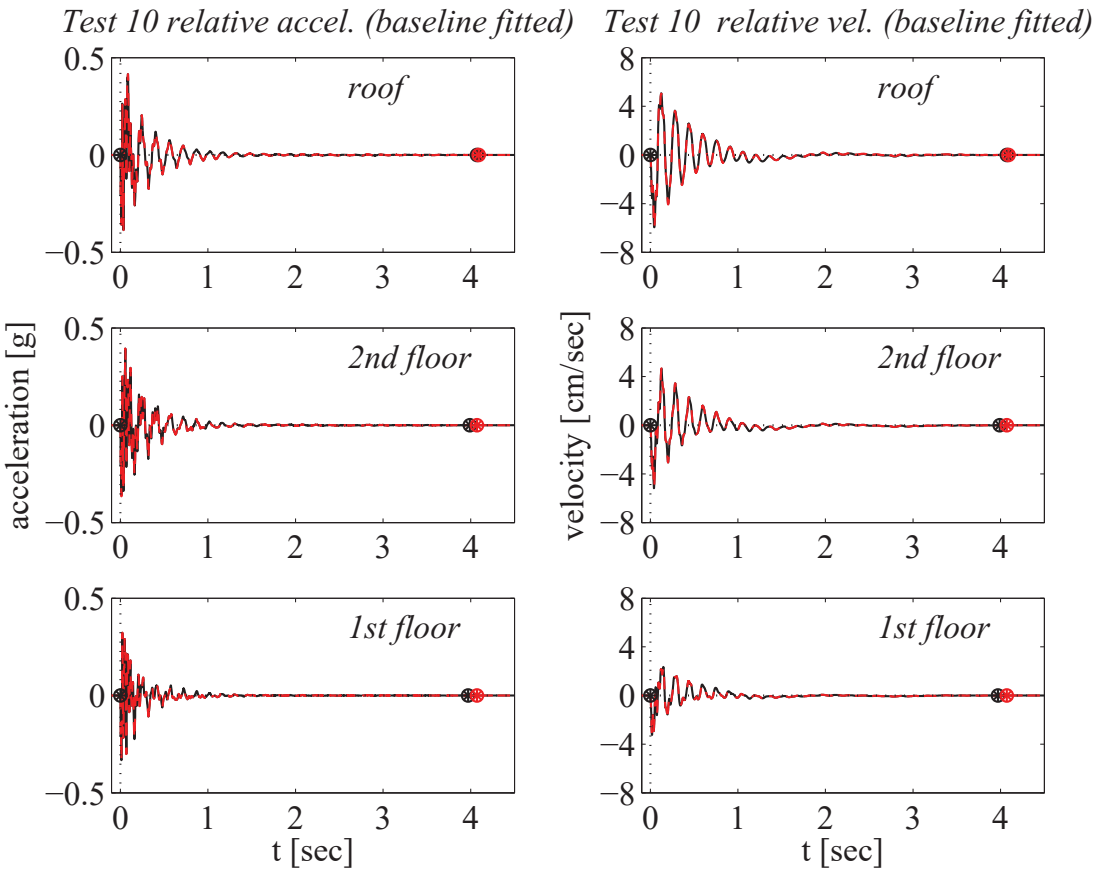

Figure A.47: Relative floor accelerations and velocities for the Augusta free vibration test 10, as evaluated from the adjusted absolute response (continuous black lines) and the adjusted relative response (dashed red lines); left sub-plots and right sub-plots respectively. The relative response is zero at the beginning and end of motion, since the superstructure is expected to respond in the linear range under such a small excitation. The times when motion starts and ceases are indicated by markers.

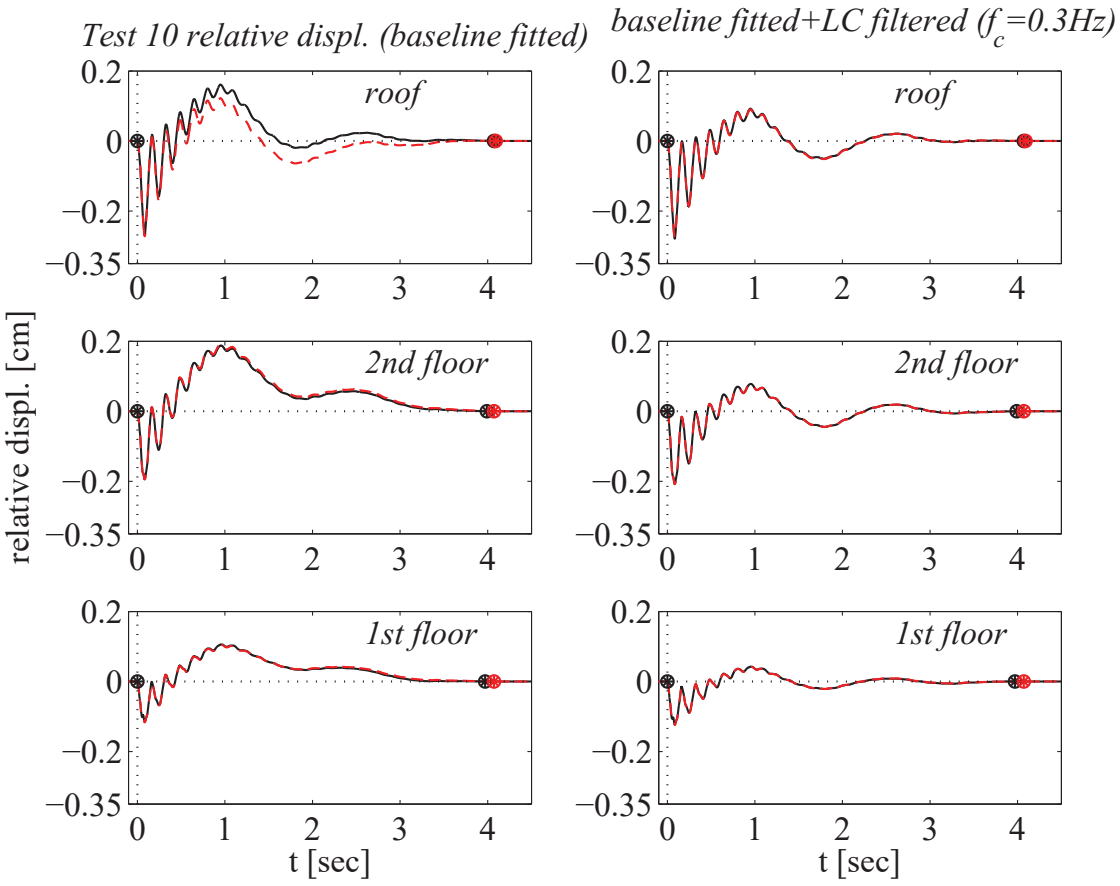

Figure A.48: Relative floor displacement histories for the Augusta free vibration test 10, as evaluated from the adjusted absolute response (continuous black lines) and the adjusted relative response (dashed red lines); left sub-plots. The relative displacements are zero at the beginning and end of motion, since the superstructure is expected to respond in the linear range under such a small excitation. The right sub-plots represent the same displacements after implementation of a low cut filter with corner frequency $f_c = 0.30Hz$. After filtering the relative displacement responses obtained by the two procedures become essentially the same. The times when motion starts and ceases are indicated by markers.

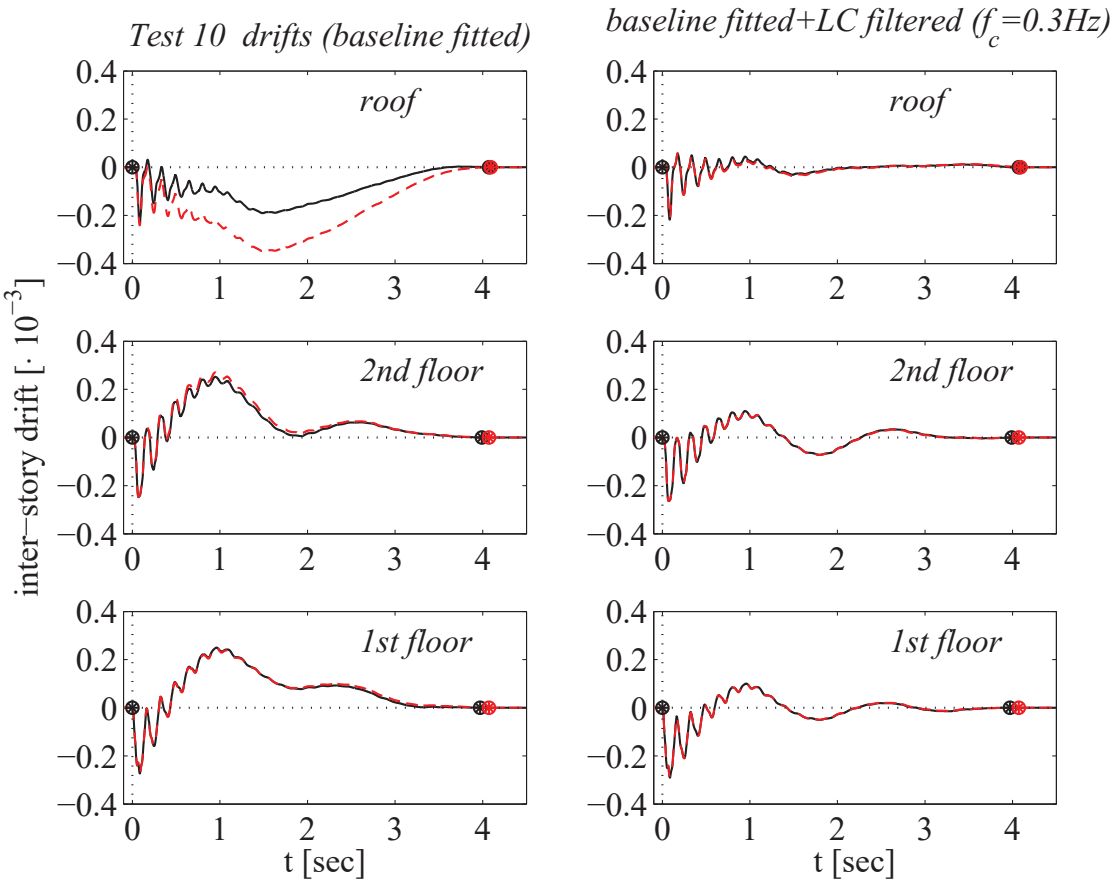

Figure A.49: Inter-story drift histories for the Augusta free vibration test 10, as evaluated from the adjusted absolute response (continuous black lines) and the adjusted relative response (dashed red lines); left sub-plots. The drifts are zero at the beginning and end of motion, since the superstructure is expected to respond in the linear range under such a small excitation. The right sub-plots represent the drifts evaluated from the corresponding filtered displacements. After filtering, the drifts obtained by the two procedures become essentially the same. The times when motion starts and ceases are indicated by markers.